Process Modelling and Experimental Validation of Residual Stress in Metal Additive Manufacturing

Wenyou Zhang M.Sc, B.Sc

Supervisors: Dr. Noel M. Harrison and Dr. Mingming Tong

A thesis submitted to the National University of Ireland, Galway as fulfilment of the requirements for the Degree of Doctor of Philosophy

Mechanical Engineering, National University of Ireland, Galway.

2021

Table of Contents

Abstract

Additive Manufacturing (AM) is an increasingly attractive advanced manufacturing technology that manufactures three-dimensional (3D) components, usually in a layer-by-layer manner, as opposed to subtractive or formative processes. Comparing with the traditional metal manufacturing techniques, AM has unrivalled capability for manufacturing complex structures and customised metal parts on an industrial scale and thus industries such as medical-device and aviation are adopting AM as a manufacturing method. However, the layer-by-layer approach, as well as indeed the continuous fine melt pool tracing process at each layer, leads to a complex sequence of repeated localised heating, melting, cooling and solidification steps. At any given time in a metal AM process, a microscale volume of the material will be exposed to rapid heating, whilst other regions will either be molten, solidifying, or cooling and solidified. As a result of this, the thermal residual stress (RS) within AM parts is intricate and is considered to be limiting a wider uptake of metal AM in industry. AM RS and the prediction thereof, is the focus of this thesis.

Finite element modelling (FEM) is capable of simulating aspects of the multi-physics AM process, but when applied to complete AM processes and parts, conventional FEM techniques accrue prohibitive computational expenses and thus are generally applied to simulating basic phenomena on small single components in basic AM representations. This thesis aims to build thermo-mechanical models for AM, to improve RS predictive capability and then inform RS mitigation strategies in additively manufactured metal components. In this content, coupled thermo-mechanical FEM capabilities for multi-processes, multi-laser beam and multi-part build were developed.

Powder bed fusion (PBF) is the most popular and widely used method to additively manufacture 3D metallic components. Ti-6Al-4V titanium alloy is one of the most popular metallic materials for PBF due to its favourable properties and is therefore utilised in this thesis. A novel computationally-efficient thermo-mechanical coupled laser beam powder bed fusion (PBF-LB) process model for part-scale Ti-6Al-4V components were developed. The influences of resolution, energy input and heating step time and cooling

step time were characterised, which provide guidelines for the 'layer scaling' technique in PBF-LB process modelling for macroscale component. The results indicate that the 'layer scaling' method was effective when scaling up to 4 times the physical layer thickness and scaling the cooling step time. To validate the developed thermo-mechanical PBF-LB prediction model, RS measurement was performed by synchrotron high energy X-ray diffraction on parts with different heights and manufactured by different scanning strategies. The computational modelling results of directional stresses were compared with the experimental measurements.

To improve the production rate of metal PBF, multi-laser beam powder bed fusion (PBF-MLB) technology has been proposed as the next generation of PBF-LB technology. Thus, a computational multi-laser beam model was developed and presented in a study on RS in PBF-MLB. To investigate the optimum multi-laser scanning strategies in PBF-MLB, the influence of twelve different scanning strategies on temperature, the final resulting RS, and the *z*- (build) direction deflection by dual laser beams were investigated. The prediction indicates that the more laser beams are employed in PBF-MLB manufacturing, the lower RS and deflection resulted. The four-laser beam PBF-MLB build can mitigate RS by 9.39 % compared to the single laser beam PBF-LB.

Most of the existing FEM is focused on single part manufacturing, which is inconsistent with the practical multi-part (full build plate) printing observed in industry. Therefore, multi-part build process PBF-LB model was developed by the layer-by-layer modelling method for mitigating RS of the manufactured parts. Effects of the number of parts per build and part spacing on temperature and RS were investigated on prism sample in PBF-LB. It was found that RS decreased with the number of parts per build and RS of four-part build was 94 % of the single part build.

The final studies within this thesis apply the computational techniques to the electron beam variety of PBF (PBF-EB), to another metal AM process- directed energy deposition (DED), and to a new titanium alloy Ti2448 and aluminium alloy. The predicted temperature evolution during PBF-EB was indirectly compared to microstructure evolution of material performed by collaborators. Preheating temperature of the base plate

was shown to be a key factor to reduce RS in PBF-LB. To interpret the *in-situ* RS characterisation of practical DED, process modelling of a thin trapezoidal plate was performed by using a bead-by-bead modelling method. The higher the numbers of layers fabricated in DED, the higher the temperature of the part during the manufacturing process, giving a 21.93 % lower temperature gradient and hence lower RS. The computational DED process modelling proved to be an effective tool to investigate temperature and RS state evolutions in macroscale components.

This work reveals further insights into AM RS mechanics and will inform metal AM part designers and process operators of optimum process configuration in order to minimise RS of metal parts in AM.

Acknowledgements

First and foremost, I would like to express my sincere gratitude to Dr. Noel M. Harrison and Dr. Mingming Tong, for their immense knowledge, guidance, and patience throughout my doctoral study. I am also grateful to Dr. Catrin M. Davies for her supports during my visit to Imperial College London. Without their support, I would not be able to finish my doctoral project.

I am grateful to Dr. Rory Monaghan, Dr. Nathan Quinlan and Dr. Padraig Molloy for their encouragements and significant contributions as members of my GRC committee.

I would like to thank the funding agencies and institutions that have supported me throughout my Ph.D., including Government of Ireland Postgraduate Scholarship from Ireland Research Council, Hardiman Scholarship and College of Science and Engineering Scholarship from NUI Galway. I would also like to thank the Erasmus Scholarship for supporting my visit to Imperial College London.

I would also like to sincerely thank all my friends and colleagues, both in China and Ireland, for their support and encouragements in this journey.

Finally, I would like to express my deepest gratitude to all members of my beloved family. Special thanks to my beloved wife Huimin Tang, to whom this thesis is dedicated.

List of publications

Papers published

Wenyou Zhang, Mingming Tong, Noel M. Harrison. Resolution, energy and time dependency on layer scaling in finite element modelling of laser beam powder bed fusion additive manufacturing. Additive Manufacturing. 2019, 28:610-620. (**Chapter 3**)

Wenyou Zhang, Mingming Tong, Noel M. Harrison. Part powder conduction approximation as part surface free convection for Powder Bed Fusion process modelling. Data in Brief. 2019, 27. (**Chapter 3**)

Wenyou Zhang, Mingming Tong, Noel M. Harrison. Scanning strategies effect on temperature, residual stress, and deformation by multi-laser beam powder bed fusion manufacturing. Additive Manufacturing. 2020, 36:101507. (**Chapter 5**)

Papers ready for submission/In preparation

Finite element modelling and experimental validation of residual stress in laser beam powder bed fusion additive manufacturing. Draft completed. (**Chapter 4**)

Influences of multi-part build on temperature and residual stress by laser beam powder bed fusion simulation. Under review. (**Chapter 6**)

Material characterisation and multi-physics computational modelling of electron beam powder bed fusion additive manufacturing of Ti2448 Titanium alloy. Ready to submit. (**Chapter 7**)

Dynamic evolution of crystalline structure during metal additive manufacturing. Draft completed. (**Chapter 8**)

Conferences presented

Wenyou Zhang, Mingming Tong, Noel M. Harrison. Part number effects on temperature and residual stress by laser beam powder bed fusion simulation. 14th WCCM-ECCOMAS Virtual Congress, Jan. 2021.

Wenyou Zhang, Mingming Tong, Noel M. Harrison. Dual laser beam thermomechanical modelling with variable scanning strategies. II International Conference on Simulation for Additive Manufacturing, Pavia, Italy, Sep. 2019.

Wenyou Zhang, Mingming Tong, Noel M. Harrison. Process thermo-mechanical modelling of powder bed fusion manufacturing. 10th European Solid Mechanics Conference, Bologna, Italy, July 2018.

Wenyou Zhang, Mingming Tong, Noel M. Harrison. Multiscale thermomechanical modelling of powder bed fusion manufacturing. 21st Sir Bernard Crossland Symposium, UCD, Dublin, Ireland, April 2018.

Nomenclature

Symbol	Definition	Unit
C_p	Specific heat	J/(kg·K)
k_s	Thermal conductivity of solid	W/(m^2·K)
k_p	Thermal conductivity of powder	W/(m^2·K)
ρ_s	Density of solid	kg/m^3
ρ_p	Density of powder	kg/m^3
σ_y	Yield strength	MPa
σ	Stress	MPa
σ_{xx}	Stress along *x* direction (S11)	MPa
σ_{yy}	Stress along *y* direction (S22)	MPa
σ_{zz}	Stress along *z* direction (S33)	MPa
E	Young's Modulus	MPa
ν	Poisson's ratio	
p	Porosity	%
h	Heat transfer coefficient	W/(m^2·K)
ε	Emissivity coefficient	
σ_S	Stefan-Boltzmann constant	W/(m^2 ·K^4)
T_m	Melting temperature	K
T_{sur}	Surface temperature	K
T_r	Chamber temperature	K
T_p	Peak temperature	K
T_S	Sodius temperature	K
T_L	Liquidus temperature	K

t_p	Preheating step time	s
t_m	Heating step time	s
t_c	Cooling step time	s
t_{tot}	Total step time	s
t_i	Cooling time interval	s
A	Heat source absorption coefficient	
P	Energy beam power	W
R	Heat source spot radium	m
r	Distance to the laser beam centre	m
H_s	Hatch spacing	m
d_m	Melt pool depth	m
d_s	Heat source spot diameter	m
v_s	Laser beam scanning speed	m/s
q	Heat flux	W/m^2
q_{cond}	Conduction heat flux	W/m^2
q_{conv}	Convection heat flux	W/m^2
q_{rad}	Radiation heat flux	W/m^2
α	Thermal expansion coefficient	1/K
$\dot{H}$	Rate of enthalpy change	W/m^3
$\dot{D}_{mech}$	Thermal-stress dissipation rate	W
η	Inelastic heat fraction	%
$\dot{\varepsilon}^p$	Plastic strain rate	1/s
f	Liquid fraction	wt %
Q	Power density	W/m^3

m_f	Mesh factor	m
L_h	Layer height	m
L	Latent heat of fusion	J/kg
l_f	Layer scaling factor	
∇T	Temperature gradient	K
ΔT	Temperature change	K
ε_e	Elastic strain	
ε_p	Plastic strain	
ε_T	Thermal strain	
ε_{Total}	Total strain	
ε_{hkl}	Strain along *hkl* crystal plane	
ε_{xx}	Strain along *x* direction	
ε_{yy}	Strain along *y* direction	
ε_{zz}	Strain along *z* direction	
d	Lattice spacing	Å
d_0	Stress-free lattice spacing	Å
λ	Wavelength	Å
θ	Reflection angle	º
m	Mass of material	Kg
E_t	Thermal energy	J
L_b	Bead increment length	m
W_b	Bead increment width	m
H_b	Bead increment height	m

1 Introduction

1.1 Metal additive manufacturing

According to the International Organization for Standards (ISO), additive manufacturing (AM or 3D printing) is defined as a "*process of joining materials to make parts from 3D model data, usually layer upon layer, as opposed to subtractive manufacturing and formative manufacturing methodologies*" [1]. AM is at the core of Industry 4.0 and has experienced significant growth in recent years [2, 3], particularly in medical device and aerospace sectors. Compared with traditional manufacturing techniques (e.g. casting or welding), AM offers crucial advantages including, ability to manufacture complex geometries, porous or lattice structures, near net-shape metal 'assemblies', highly customized or bespoke design parts, in a relatively rapid and automated process that also minimises material wastage [4-6].

Powder bed fusion (PBF) is among the seven AM technologies [7]. PBF is defined as the "*additive manufacturing process in which thermal energy selectively fuses regions of a powder bed*" [1]. The PBF technology was invented at the University of Texas at Austin in the early 1980s and the first patent of PBF was awarded at 1989 [8]. Significantly advances have been made in PBF since then, allowing PBF to be the most popular and widely used method to additively manufacture 3D metallic components [3, 9, 10]. Non-metallic PBF technologies also exist, allowing similar fabrication capacity in polymer [11] and ceramics [12]. The thermal energy beam used in metal PBF can either be laser beam (PBF-LB) or electron beam (PBF-EB).

The PBF-LB process works by a machine first depositing a thin layer of powders over a build platform (powder bed), and then the finely rastered laser beam is activated to melt the powders rapidly and fully in a localised manner. The laser beam rapidly moves around the powder layer, tracing out the relevant 2D cross section of the 3D parts. After one layer is complete, the build platform moves down by one-layer thickness, and a new thin layer of powders is added on top of the previous layer. These processes are repeated until the final 3D parts are manufactured [13, 14]. The in house PBF-LB printer (ProX® DMP100,

3D Systems) at NUI Galway and a schematic of a typical PBF-LB manufacturing process [10] are illustrated in Figure 1.1. The main commercial metal PBF-LB system manufacturers include EOS (EOS GmbH Electro Optical Systems, Krailling, Germany), Concept Laser (Concept Laser GmbH, Lichtenfels, Germany, now part of GE (General Electric Company, Boston, USA)), SLM Solutions (SLM Solutions Group AG, Lübeck, Germany), 3D Systems (South Carolina, USA) and Renishaw (Renishaw UK Sales Ltd, Gloucestershire, UK) [9, 15, 16]. Arcam (Arcam AB, Mölndal, Sweden, now belongs to GE Additive group) is the only manufacturer for PBF-EB system as of today [17, 18].

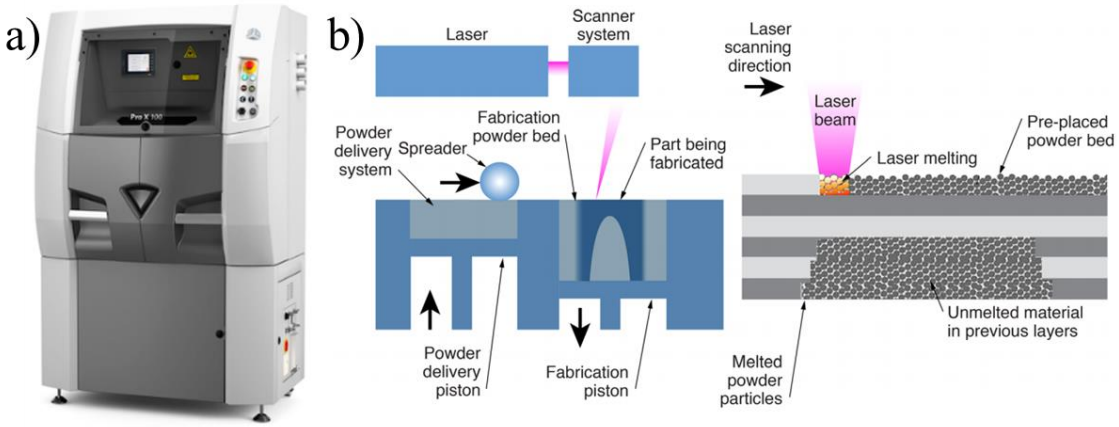

Figure 1.1. The PBF-LB manufacturing: a) An in house printer (3D Systems) and b) Illustration of manufacturing process [10].

The manufacturing process of PBF-EB is similar to the PBF-LB but key differences include:

a) PBF-LB manufacturing applies laser beam as energy while electron beam is utilised as the energy beam for PBF-EB.
b) For PBF-EB manufacturing, there is a process of preheating the metallic powders to slightly bond the powders [19-21]. However, PBF-LB process does not necessarily have a pre-heating step. When pre-heating steps are applied in PBF-LB it typically is to a lower temperature than in PBF-EB.
c) The PBF-LB manufacturing normally operates in an inert gas atmosphere (e.g. nitrogen atmosphere or argon gas) to protect the material from oxidation, while the typical PBF-EB manufacturing operates within a vacuum condition to avoid deflection of the electron beam [22].

Directed energy deposition (DED) is another one of the seven AM technologies [7]. DED is defined as an "*additive manufacturing process in which focused thermal energy is used to fuse materials by melting as they are being deposited*" [1]. Variants of DED include laser beam (DED-LB), electron beam (DED-EB) and electric arc (plasma arc, DED-PA or gas metal arc, DED-GMA), depending on the energy source applied [23]. Figure 1.2 illustrates a typical DED manufacturing process such as DED-LB [24]. The metallic powders are melted by a heat source and form a melt pool, which adheres to the fixed substrate or previously deposited layer [25]. In DED-LB manufacturing, the metal powders are delivered coaxially with the energy beam [26], which is different with the manufacturing process of PBF (where a whole layer of powder is spread on the powder bed before sintering of the active top layer). The wire feeding DED systems (DED-EB, DED-PA and DED-GMA) are based on the deposition and welding of a metallic wire into the previously deposited layer [22]. This procedure is repeated until the layer is completed and is then followed by the deposition of the next layer(s) until the 3D part is manufactured. DED manufacturing enables to directly fabricate parts with complex geometries and can also be used for repairing of damaged parts [27, 28]. The commercial DED system manufacturers including Optomec (Optomec Inc., Albuquerque, USA), Trumpf (TRUMPF GmbH, Ditzingen, Germany), Sciaky (Sciaky, Inc., Chicago, USA) and Norsk Titanium (Norsk Titanium AS, Hønefoss, Norway) [29]. The overall comparison of PBF and DED AM is summarised in Table 1.1 [23].

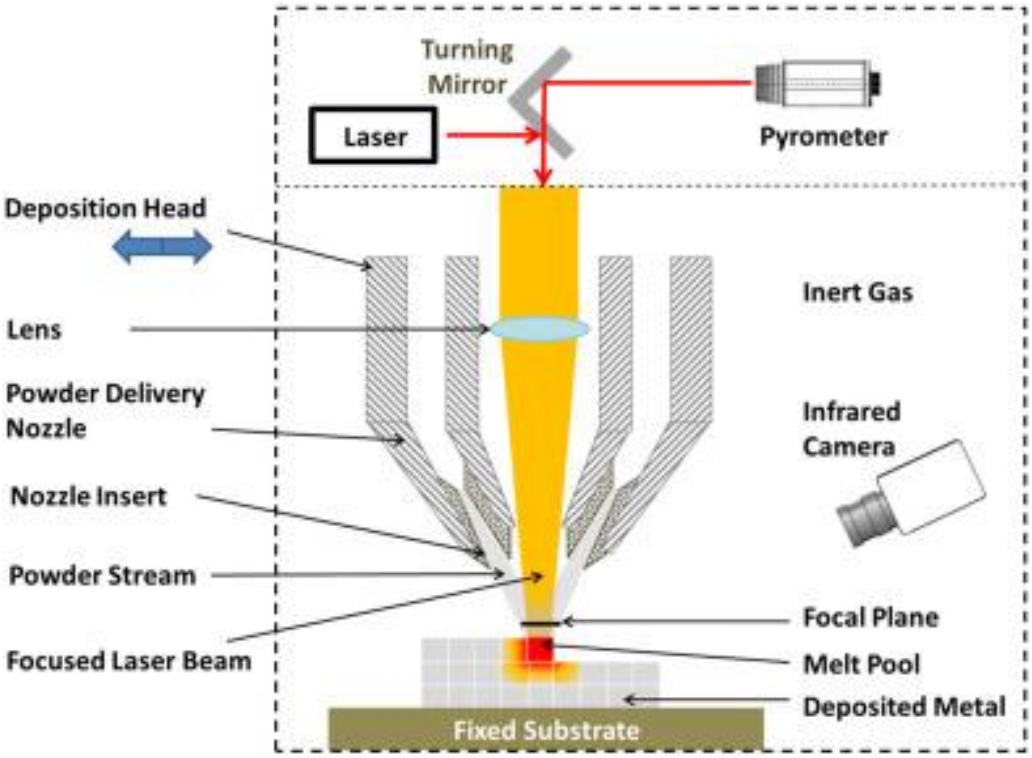

Figure 1.2. Illustration of the DED-LB manufacturing process [24].

Table 1.1. Comparison of PBF and DED AM, adapted from study [23].

Technology	PBF		DED		
Nomenclature	PBF-LB	PBF-EB	DED-LB	DED-EB	DED-PA or DED-GMA
Heat source	Laser beam	Electron beam	Laser beam	Electron beam	Electric arc
Feedstock	Powder	Powder	Powder	Wire	Wire
Environment	Shielding gas	Vacuum	Shielding gas	Vacuum	Shielding gas
Material feeding	Pre-spreading before sintering	Pre-spreading before sintering	Coaxial with the energy beam	Coaxial with the energy beam	Coaxial with the energy beam
Powder preheating?	No	Yes	No	No	No
Power (W)	50-1000	50-1000	100-3000	500-2000	1000-3000
Max. build size (mm)	500×280×320	500×280×320	2000×1500×750	2000×1500×750	5000×3000×1000

Due to the advantages at manufacturing complex geometries and high-quality metallic components, AM has a variety of industrial applications, such as aerospace and medical devices (e.g. orthopaedic implants) [3, 7, 30, 31]. This has enabled a new era of product innovation in sectors such as orthopaedic medical devices (e.g. OsteoAnchor [32, 33]) by providing new design freedoms into the design-for-manufacture stage of product

development. Other examples include personalised (patient-specific) spinal implants were PBF-LB manufactured by the commercial medical implant device manufacturers, such as Stryker (Stryker Corporation, Michigan, USA) and Zimmer Biomet (Indiana, USA) [30]. The PBF manufactured products, such as inlet temperature sensor housing for jet turbine engine, acetabular cup, bracket, and GE LEAP engine Co-Cr fuel nozzle, are shown in Figure 1.3. The market for all AM products and services worldwide is expected to be $ 23.9 billion in 2022, and $ 35.6 billion in 2024, respectively [34]. Among this, the metal AM makes up the largest proportion. Therefore, there is a current need for further AM material research and next generation of AM process design to understand and minimise process defects, optimise process parameters and overall improve industry's ability to exploit metal AM technology.

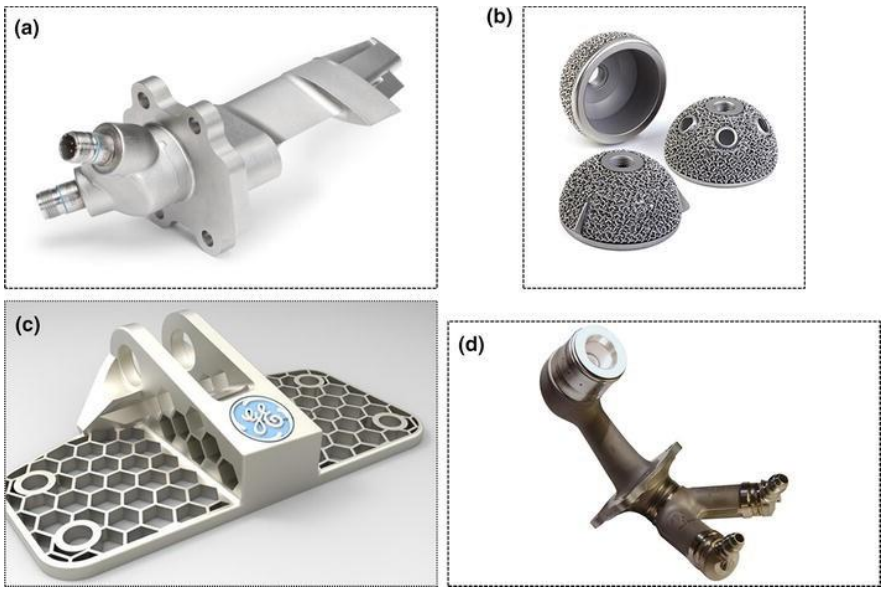

Figure 1.3. PBF manufactured industrial products: a) Inlet temperature sensor housing for jet turbine engine produced for GE Aviation. b) Acetabular cup manufactured by PBF-EB (Arcam). c) Bracket produced by PBF-LB (EOS) and d) GE LEAP engine Co-Cr fuel nozzle manufactured by PBF-LB (EOS) [9].

Despite the rapid industrial adoption of metal AM, this advanced manufacturing process is, like all manufacturing process, susceptible to undesirable process defects and artefacts. This is limiting confidence in the in-service performance of AM manufactured products [3, 9, 35]. Principal among these artefacts is thermal residual stress (RS), voids, geometric distortion, relatively poor surface smoothness, crack, and layer delamination (Figure 1.4) [35-38]. In addition, RS induced deflection of part influences the final parts quality and

performance [39]. Such phenomena can lead to an impression that metal AM produces comparatively poor quality components and is limiting the wide application of AM [40]. Current efforts to investigate such artefacts and relatively poor in-service mechanical behaviour include analysis of manufacturing process parameters, material properties and characteristics, [41, 42]. A key tool in this effort is computational process modelling, which provides the ability to fundamentally understand RS and distortion mechanisms of the manufactured components [10]. Due to the multiple spatial scales involved (manufacturing macroscale components in microscale layers) and disparate time scale for thermodynamic and heat transfer mechanisms, AM process modelling for macroscale part is computational expensive [10, 41]. Specialist simulation software such as Simufact Additive (Simufact Engineering GmbH, Germany) [43], ABAQUS AM Modeler (Dassault Systems, USA), Additive Print (Ansys inc., USA) and Netfabb (Autodesk, USA) [44] have been developed for the AM process modelling, and are commercially available. Most metal AM process modelling efforts using standard general purpose finite element simulation software (e.g. ABAQUS or ANSYS). A considerable chasm exists between the current state-of-the-art modelling studies, which generally include single laser beam PBF fabricating single small parts [41, 45] and the next generation multi-laser beam and multi-part AM technologies now entering the market.

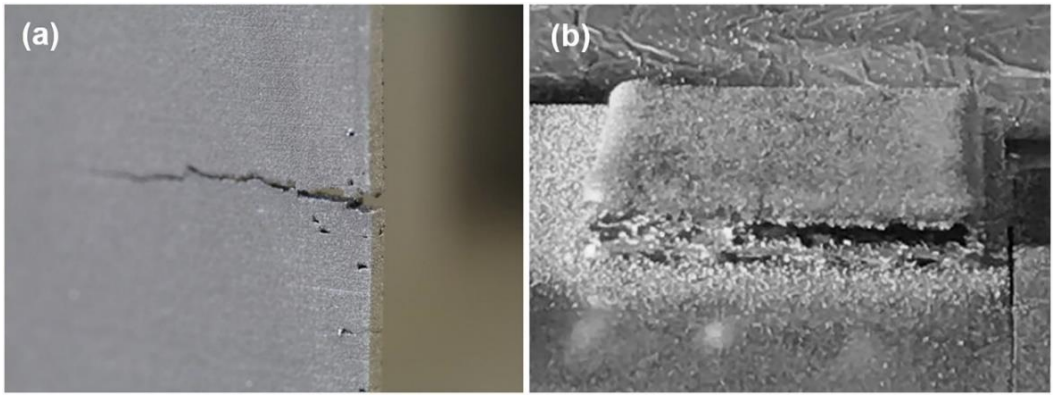

Figure 1.4. Formation of crack induced by RS in AM occurs at: a) Macroscale Ti-6Al-4V component and b) Interface of part with the build plate [37].

1.2 Residual stress in metal additive manufacturing

This thesis is focused on one of the artefacts mentioned above: residual stress in metal AM. RS is defined as stress which remains inside a body that is stationary and at equilibrium with its surroundings [46]. It is generated as a result of temperature gradient induced plastic deformation [3] or strain incompatibility of adjacent layers of material [47]. As RS in AM is mainly induced by the thermal gradient from heating, melting, cooling and solidification of material, the thermal type of RS is thus the focus of this thesis. RS can be classified into three types depending on the length scale in which it exists [3, 48]. The type I RS is a macroscale stress and acts on a large part-scale and influences bulk distortion of the manufactured part. The type II RS is a micro-stress that acts at the individual grain scale (i.e. microscale and nanoscale) [3]. The type III residual stress is at the atomic scale. As this work is focused on the macroscale AM part, RS in the main content of this thesis refers to the type I macroscopic RS.

RS in AM significantly influences mechanical performances of the manufactured bulk components, and it is therefore necessary to fully understand the development mechanisms of RS in AM. The complex RS evolution during an AM process is caused by steep temperature gradient (highly non-uniform temperature distribution), rapid cooling rates (CR) and repeated heating- melting-solidification-remelting-solidification steps [42, 49]. At any given time during an AM build process, only a portion of the component is molten (a melt pool region (shown in Figure 1.5) within the active layer, and immediately beneath that region in previous layer(s)), other regions are just below melting temperature (most recent layers), while the first deposition layer (nearest the build plate) is the coolest (though still well above room temperature). The change of temperature during AM manufacturing process induces variations of thermal and mechanical material properties (e.g. conductivity, density, specific heat, elastic modulus and yield stress) with temperature. RS remains in the parts after the AM process and has been found to cause distortion of the final manufactured parts [35, 50]. Li et al. [51] predicted that the maximum distortion of a PBF manufactured cantilever (e.g. $55 \times 5 \times 12$ mm^3) was 1.5 mm by using FEM approach, while the experimentally measured maximum distortion of the cantilever was 2.1 mm. RS is non-uniformly distributed in additively manufactured

components [23], i.e. compressive stress was formed at the interior while tensile stress occurred at the side surfaces of the additively manufactured components [52], providing ideal conditions for harmful surface phenomenon such as crack initiation and crack growth. It is recommended that the maximum RS (i.e. at the interface of the part and the base plate) be lower than the yield strength of material and RS at other areas of components be lower than 300 MPa for Ti-6Al-4V material.

Figure 1.5 indicates RS and deformation formation mechanisms of a part during the repeated heating and cooling manufacturing processes of AM [3, 53]. When the top new layer is melted on top of the previously solidified layer or the build plate, the temperature of this new layer is far above the temperature of the underlying part. Thus, the non-uniformly distributed heating causes the newly added top layer (shown in Figure 1.5a) to expand, but the underlying solidified material (with much lower temperature) restricts the expansion of the newly added layer. Therefore, during the heating and melting processes of a layer during manufacturing, the compressive and tensile residual stresses will be developed in the top layer and the underlying solidified part, respectively, as shown at Figure 1.5a. The plastic deformation will occur at the top layer if stress exceeds the elastic regime of the metallic material. After a layer is complete the new top layer begins to cool at a rapid rate however its contraction is constrained by the surrounding material, thus resulting in tensile RS at the top new layer and compressive stress at the underlying material [3, 38, 53], as shown in Figure 1.5b. This iterative heating and cooling processes lead to repeated patterns of tensile and compressive stresses formation during the AM process and a complex non-uniform stress state upon completion of the entire build and cool-down.

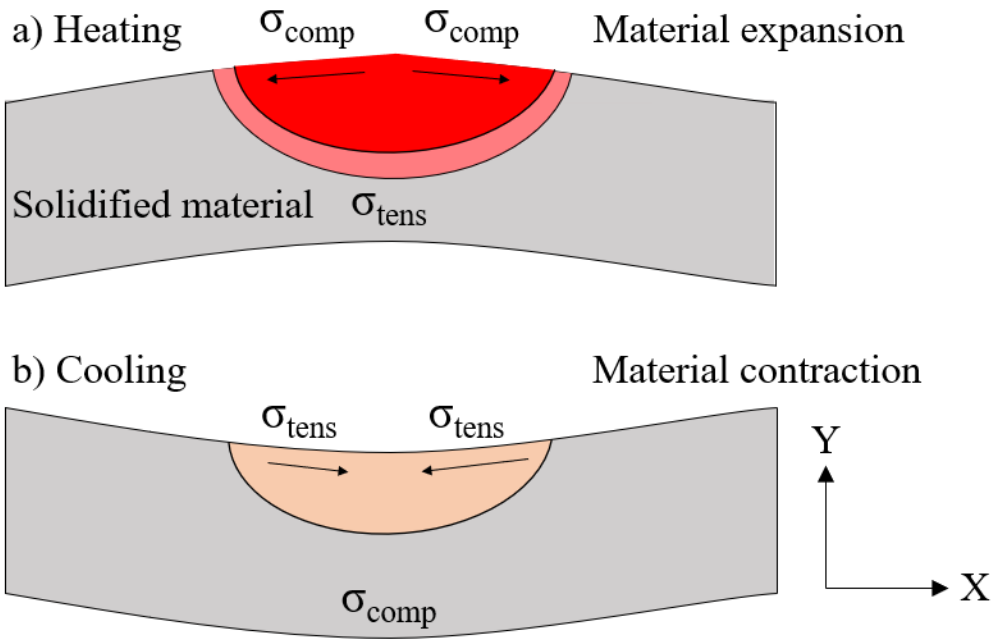

Figure 1.5. Illustration of RS and deformation formation mechanisms during AM process: a) Thermal expansion of a newly added top layer and b) Thermal contraction of the top layer [3, 53]. Compressive stress in melt pool is negligible but exists in the solid regions below the melting temperature of material.

Multiple factors influence the magnitude and distribution of RS in additively manufactured parts. Scanning strategies can significantly affect RS and mechanical performance of the final parts manufactured by PBF [10, 54]. Levkulich et al. [42] investigated process parameters effect on RS and the results showed that an increase of the laser power led to a decrease of RS at the top surface of part by PBF-LB. Therefore, there is a current need to develop FEM strategies for improving understanding of RS evolution during AM process and thus informing RS control and mitigating strategies in the manufactured parts.

To mitigate RS formed in metal AM in industry, AM equipment operators and build plate designers can minimise the potential for build failure due to RS induced deformation. In order to limit warping and distortion of the parts and aid dissipation heat from parts, build supports are added to securely anchor the part to the build plate, provide a path for heat transfer to the build plate, as well as supporting overhanging structures [55-57]. Once the AM process is complete, manufacturers can then employ post-build processes such as heat treatment and hot isostatic pressing (HIP) etc. [58]. In the case of PBF, the build plate is

removed from the PBF machine, loose powder is removed from the plate and parts, before the build plate and parts are placed in a heat treatment oven for stress relieving, annealing or other microstructural modification purposes. It has been shown that the tensile RS of as-built Ti-6Al-4V parts manufactured by PBF were reduced by 90 % via a 3 hours heat treatment at a constant temperature of 680 ℃ [59]. It has also been demonstrated that heat treatment approach can lead to increases of elongation and fatigue behaviours due to the elimination of internal defects (e.g. pores) in the manufactured parts [60, 61]. However, post AM heat treatment can reduce the ultimate tensile strength (UTS) of part [60, 61]. Some additively manufactured parts are further hot isostatic pressed, e.g. subjected to 920 ℃ and 103 MPa for 4 hours, followed by furnace cooling, and the main purpose of HIP is to reduce porosity of the manufactured parts [62, 63]. Typically, after the post-build heat treatment is complete, the parts are removed from the build plate by sacrificing the build supports. Further cleaning operations such as polishing, or surface smoothing may be required at the location of the build supports. The build plates are then usually reused in a later build, after a surface grinding or milling operation is performed to eliminate any build support remnants. If a lower level of RS can be achieved during the AM build process, the requirement for post-build heat treatment may be reduced, saving on manufacturing cost and time. It is acknowledged that in some structural application, RS is desirable and indeed manufacturing processes can be configured in order to ensure stress profiles are created [64] , however in the context of this thesis, RS is considered as a undesirable manufacturing process artefact.

1.3 Thesis aims and objectives

The overall aim of this thesis is to assess RS by developing AM process modelling tools and then utilise this knowledge to minimise RS formation of Ti-6Al-4V parts in AM, such as providing insights into critical process parameters and optimum build layouts. The approach adopted includes computational finite element modelling and experimental RS measurements. This work should provide guidelines for the computational efficient AM process modelling of macroscale parts. To achieve these aims, the key objectives of this work are as follows:

1) Development of a rapid automated and computational efficiency thermo-mechanical finite element modelling capability for predicting temperature and residual stress behaviours of PBF manufactured macroscale metal component.
2) Experimental measurement of RS for a range of scanning strategies in metal PBF to validate the computational finite element model and the predicted RS.
3) Development of optimised process parameters and strategies for next generation of PBF technology, i.e. multi-laser beam powder bed fusion (PBF-MLB). Exploring approaches to improve the build rate and optimize fabrication quality of PBF-MLB manufactured parts.
4) Development of the modelling capability for multi-part build in PBF-LB and investigate multi-part effects on thermal and stress behaviours of the manufactured macroscale components.
5) Exploration of applications of PBF-LB for Ti-6Al-4V alloy to other AM techniques and materials, such as PBF-EB and DED, Ti2448 titanium alloy and aluminium material. By adapting the developed PBF-LB thermo-mechanical model to PBF-EB and DED to interpret microstructure characterisations (e.g. phase and grain) in PBF-EB and *in-situ* RS measurement of the practical DED manufacturing, which were performed by collaborators.
6) Development of instructions for AM machine operators in RS minimisation strategies when configuring build plates for additively manufactured metallic components.

1.4 Thesis layout

This thesis consists of nine chapters. The core contents of **Chapter 3** and **Chapter 5** have been published at peer-reviewed journals. Other four manuscripts are in preparation based on contents of **Chapter 4**, **Chapter 6**, **Chapter 7**, and **Chapter 8**. An outline of the thesis is described as below:

Chapter 1 presents an overview of AM technology and process categories, origin and formation mechanisms of RS in AM, thesis aims and objectives and layouts of the thesis.

Chapter 2 presents a review of literature. This covers the commonly used metal materials for AM, the process AM modelling state-of-the-art, including finite element modelling fundamental features, thermal and mechanical mechanisms, computational efficiency AM modelling methods for macroscale component, multi-laser beam build PBF-LB modelling, multi-part build PBF-LB process modelling, temperature history effects on microstructure evolution, current challenges in AM process modelling and experimental measurement techniques for RS in AM.

Chapter 3 presents the finite element modelling fundamentals for PBF-LB AM, i.e. the thermal and mechanical mechanisms and interdependencies of resolution, energy, and time of Ti-6Al-4V alloy in PBF-LB. An in-house Python code was programmed to section the part-scale model into thin layers for PBF-LB process modelling. A novel thermo-mechanical PBF-LB process model including a computational efficiency powder-interface heat loss mechanism was proposed and developed. The effects of variations in layer height (i.e. 'layer scaling'), energy and time on temperature and RS state evolution were investigated. An effective and computational saving 'layer scaling' technique was finally presented for the process simulation of part-scale Ti-6Al-4V component in PBF-LB. This chapter provides fundamental understanding and thermal and mechanical setups for the thermo-mechanical PBF-LB FEM and computational efficiency method for part-scale model in PBF-LB.

Chapter 4 predicts and experimentally measures RS of Ti-6Al-4V part varying scanning strategies in single laser beam PBF-LB. The hatch-by-hatch simulation method was developed and applied for the thermo-mechanical model for prediction RS of part varying scanning strategies in PBF-LB. Square plates were additively manufactured by six different scanning strategies. RS of plate was experimentally measured by using the non-destructive high energy X-ray diffraction method at Diamond Light Source in UK. The results indicate a good match between the experimentally measured directional RS and the FEM predicted RS of part with different scanning strategies. This chapter validates the computational finite element model for AM, which is adapted to be employed for computational modelling of **Chapter 5** – **Chapter 8**.

Chapter 5 presents a series of computational process simulations of multi-laser beam powder bed fusion for Ti-6Al-4V alloy and investigates optimum multi-laser scanning strategies by using a 3D coupled thermo-mechanical model. The DFLUX subroutine (Gaussian distributed heat source) in the format of Fortran was combined with ABAQUS for PBF-MLB process modelling. The influences of twelve different scanning strategies on temperature, RS and deformation by dual laser beams PBF-MLB were investigated. The strategies to mitigate RS and deflection in PBF-MLB were proposed. The predicted findings in this chapter provide an insight and application of PBF-MLB finite element process simulation in improving industrial AM of metal components.

Chapter 6 investigates influences of the number of parts per build and inter-layer dwell time on temperature and RS of Ti-6Al-4V alloy in PBF-LB. The multi-part PBF-LB process thermo-mechanical modelling framework was proposed for the first time. The layer-by-layer modelling method to simulate geometry varies cross sections along the build direction was presented for the multi-part build. The process modelling consists of different numbers of prisms (1, 2 and 4) were simulated in the same build plate, respectively. Effect of part spacing on RS was also investigated in the two-part PBF-LB process modelling. This research could be beneficial for informing PBF-LB machine operators of optimum printing setup for minimising component RS.

Chapter 7 presents application of PBF-LB to PBF-EB process modelling of a novel Ti2448 alloy for medical device applications. The layer-by-layer modelling approach was adopted to computationally predict the thermal process and RS of PBF-EB AM at the scale of the overall additively manufactured component. This PBF-EB work is the result of collaboration with Institute of Metal Research, Chinese Academy of Sciences (IMR-China). The thermo-mechanically coupled process modelling of PBF-EB was used to investigate the temperature evolution and cooling rate along both the build direction and the radial direction. Residual stress of PBF-EB manufactured Ti2448 part was predicted for the first time. IMR-China completed experiments regarding AM trial and material microstructure characterisation. Finally, strategies to effectively mitigate PBF AM resulting RS were recommended.

Chapter 8 presents application of PBF-LB to another metal AM and material: DED process modelling for macroscale aluminium alloy part. This is the result of collaboration with the University of Manchester, in which the *in-situ* characterisation of the DED manufacturing process and RS measurement were conducted. The DED thermo-mechanical process modelling was performed by using the bead-by-bead modelling method to interpret the experimental RS results. The influence of bead increment length on RS was computationally predicted. Temperature, temperature gradient, cooling rate and RS state evolutions with time along both the build direction and scanning direction of part were investigated.

Chapter 9 concludes main results obtained from **Chapters 3 – Chapter 8** and outlines recommendations for the future developments of metal AM technology following the results of this work.

2 Literature review

2.1 Introduction

The entire metal AM (PBF or DED) process can be summarised as repeated sequential localised heating, melting and solidification processes involving high energy spot tracing within each thin layer. The material thermal history is complicated by subsequent repeated heating, remelting and solidification, as subsequent layers are added to create the 3D form. The resulting residual thermal stress state of the component is therefore complex. Process FEM provides the ability to assess and predict the complex RS profiles in AM materials. Due to the multi-physics and multi-scale characterises of AM process, careful model construction and understanding of FEM capabilities are needed to accurately simulate the complex process of AM, whist maintaining computational efficiency. The main sections of this literature review chapter are broken down into three key considerations:

a) Section 2.2 details the commonly used materials for metal AM in industry, such as titanium alloy, stainless steel, aluminium alloy, and nickel alloys. The characteristic of metallic power is also reviewed.
b) Section 2.3 provides a review of the state-of-the-art of finite element process modelling for metal AM, including the theory of thermal and mechanical phenomena, finite element based approaches to thermo-mechanical modelling of macroscale components, computationally efficient approaches for macroscale part modelling, multi-laser beam build effects, multi-part build process modelling, temperature history effect on microstructure evolution, and finally current challenges in AM process modelling.
c) Section 2.4 presents experimental measurement techniques for RS of additively manufactured metal parts, including hole drilling, contour method, surface-based X-ray diffraction, neutron diffraction and the high energy X-ray diffraction. Experimental RS measurement is necessary to validate the developed finite element models.

2.2 Metal materials for additive manufacturing

The range of materials available for PBF and DED-LB manufacturers is limited primarily by its supply in powder form. For DED-EB, DED-PA and DED-GMA, the raw material can be in wire (or filler) form, as shown in Table 1.1. The gas atomisation technique is the most commonly used method to produce powder formatted materials for PBF and DED-LB AM [65], where the alloy in molten status is atomized by the high-pressure flow of argon or nitrogen gas [23]. The powder material production methods such as gas atomisation and plasma atomisation are summarised in other studies [65, 66].

Alloy powder particles are common materials in both PBF-LB, PBF-EB and DED-LB techniques, due to their ease of feeding and controlled melting [37]. Alloy powder properties (e.g. shape, size distribution, surface morphology, composition and flowability) can significantly influence in-process material behaviour and the mechanical performance of additively manufactured metal parts [23, 67]. In PBF AM, the raw material of powder particles is spread by a machine blade, roller, or brush over the build platform. During the PBF-LB manufacturing process, the metallic powders absorb heat energy from laser beam to be melted, whereas in PBF-EB, electrons penetrate into the powder bed and transfer their energy to thermal energy of the powder bed to elevate powder temperature above the melting temperature [22].

To date, Ti-6Al-4V titanium alloy is one of the most popular materials for AM and has been heavily utilised across many industries adopting AM [37, 68-73]. Scanning electron microscope (SEM) morphology of typical Ti-6Al-4V powder for PBF-LB is shown in Figure 2.1 [22]. The chemical composition of Ti-6Al-4V powder for PBF is shown in Table 2.1 [74]. Ti-6Al-4V is a dual phase ($\alpha + \beta$) titanium alloy with favourable properties, for many applications, such as high strength-to-weight ratio, high corrosion resistance, heat treatability suitable for marine, automotive, and aerospace products and high biocompatibility in the range required for medical devices [75, 76].

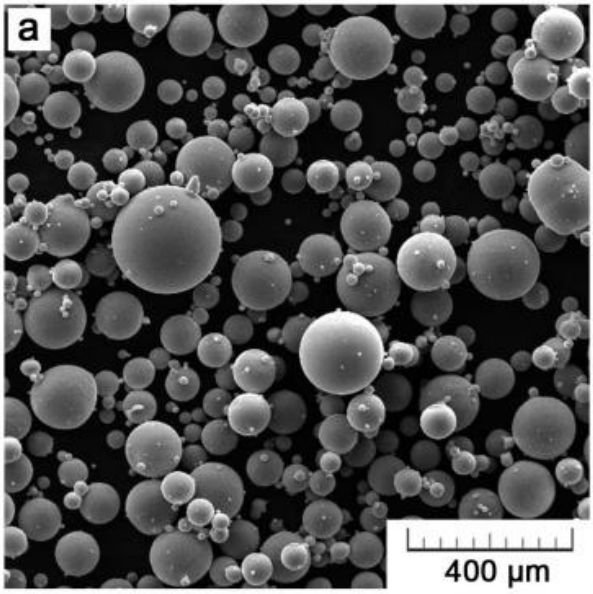

Figure 2.1. SEM morphology of Ti-6Al-4V powders used for PBF-LB manufacturing [22].

Table 2.1. Chemical composition (wt %) of the typical Ti-6Al-4V powder used for PBF [74].

Technology	Aluminium (Al)	Vanadium (V)	Iron (Fe)	Oxygen (O)	Nitrogen (N)	Hydrogen (H)	Carbon (C)	Titanium (Ti)
PBF-LB	6.02%	3.82%	0.17%	0.11%	0.01%	<0.0019%	0.01%	Bal
PBF-EB	6.35%	3.98%	0.18%	0.13%	0.01%	0.002%	0.02%	Bal

Ti-6Al-4V accounts for more than 50 % of all titanium alloy usage worldwide [77, 78], and its readily availability in powder form has ensured significant AM production to date. Ti-6Al-4V metallic powders are divided into different grades depending on the particle size (e.g. the typical powder size for PBF is 15 - 45 µm [67]) and purity. The distribution of powder size influences porosity of the non-sintered powders, PBF manufacturing process and performance of the final manufactured parts [79]. To additively manufacture parts with desirable mechanical performance, a high level of purity of metallic powder is required [80]. Ti-24Nb-4Zr-8Sn (Ti2448) is a next-generation titanium alloy, which has relatively improved compatibility with natural bone compared with Ti-6Al-4V, due to its lower Young's modulus (~ 42 GPa [81]) in conjunction with high fatigue strength etc. [18]. Ti2448 was developed specifically to be used for orthopaedic medical devices [82]. Liu et al. [82] compared microstructure and mechanical performances of PBF-LB and PBF-EB manufactured porous Ti2448 component, and the results indicated that the

microstructure of parts manufactured by PBF-LB and PBF-EB consists of single β phase and dual phases (α and β), respectively. Chemical composition and particle size of the typical Ti2448 powder used for PBF are shown in Table 2.2 [82].

Table 2.2. Chemical composition and particle size of the typical Ti2448 powder used for PBF [82].

Composition (wt %)					Particle size (μm)		
Ti	Nb	Zr	Sn	O	d_{10}	d_{50}	d_{90}
Bal	23.90	3.90	8.20	0.19	47.2	79.4	130.2

Apart from Ti-6Al-4V alloy, 316 L stainless steel is another commonly used material for PBF [83-86], due to its characteristics of good ductility and good corrosion resistance [86]. Wu et al. [87] experimentally measured RS of 316 L stainless steel parts varying process parameters by PBF-LB and revealed that an increase of laser power or a decrease of scanning speed could reduce RS. Williams et al. [88] investigated the heat treatment influences on RS for PBF-LB manufactured 316 L stainless steel and showed that heat treatment could effectively reduce RS by 10 % to 40 % compared with as-built 316 L stainless steel.

Other commonly used metal materials for AM including nickel alloys (e.g. Inconel 718 and Inconel 625), aluminium alloy, and copper alloy etc. [86, 89-92]. Since nickel alloys can retain good mechanical properties even at high temperature, they are mainly used for aerospace (e.g. turbine blade shown in Figure 2.2a) [93-96]. Barros et al. [97] investigated RS of as-built Inconel 718 alloy parts and the results indicated that tensile RS was formed at the surfaces while compressive RS occurred at the central area of the manufactured parts. Aluminium alloy has the characteristics of high thermal conductivity and high strength-to-weight and stiffness-to-weight ratios [98, 99]. Svetlizky et al. [99] manufactured the dense aluminium alloy blocks by DED and the mechanical properties were comparable to those of wrought aluminium parts. AM copper alloys have excellent thermal conductivity and thus have a variety of applications in industry (e.g. combined heat exchanger and combustion chamber as shown in Figure 2.2b) [100].

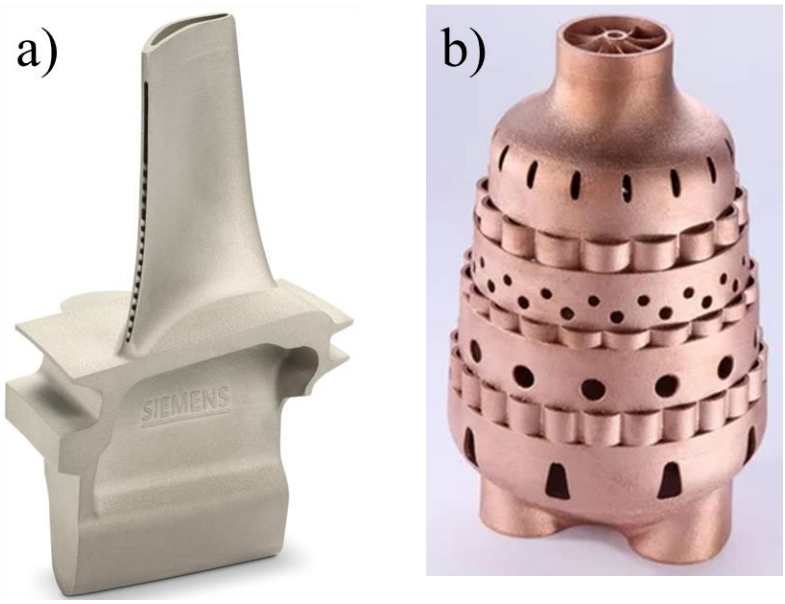

Figure 2.2. Additively manufactured metallic parts: a) Turbine blade manufactured by Siemens (nickel superalloy CM247) [94] and b) Copper combustion chamber fabricated by EOS [101].

2.3 Process modelling for metal additive manufacturing

A series of multi-scale and multi-physics process modelling efforts have been made in simulating the physical metal AM process, including FEM, discrete element method (DEM), computational fluid dynamics (CFD), molecular dynamics (MD) and cellular automata (CA) [102, 103]. FEM subdivides a large continuum domain into smaller and simpler finite elements, which makes it easier to analyse than the actual structure [104]. FEM is widely used for investigating thermal and mechanical behaviour of metal AM [26, 36, 105]. The DEM approach is suitable for particle level simulation, e.g. powder flow dynamics during laser heating of the powder bed, and the powder spreading during the recoating process of metal AM [106-108]. CFD is suitable for metal AM process modelling considering effects of fluid flow and melting of powder material [109]. MD modelling is capable of capturing the sintering kinetics of powders at a short time and nanoscale [106]. The CA method is suitable for investigating the microstructure evolution (e.g. grain) during the metal solidification process of AM [109, 110]. As this thesis aims to investigate thermo-mechanical behaviour in macroscale components in AM, the main content is focused on a solid mechanics approach using FEM (i.e. not explicitly modelling melt pool fluids).

Computational FEM is an essential tool to simulate the thermo-mechanical process of AM. Firstly, FEM is a powerful and most popular tool to simulate the practical thermal and mechanical AM processes and avoid the costly trial-and-error efforts of experiments to improve the final part quality [45, 111-113]. Secondly, it is difficult to track the practical temperature evolution during the practical metal AM process due to the high peak temperature in very small volumes and high moving speed of the energy beam [114]. AM process modelling has been shown to be an effective method to predict the complex temperature field and the resulting final RS condition of additively manufactured parts [45, 111].

To fully understand the complex multi-scale and multi-physics process in AM, and the resulting final RS condition of AM parts, the scientific community are developing computational models to simulate AM process [111, 115, 116]. Wei et al. [117] reviewed the process modelling strategies for the metal PBF technology, including different types of heat sources, heat transfer and fluid flow mechanisms, computational methodologies and temperature and RS results. Roberts et al. [118] investigated effects of a number of process variables on the resulting RS of Ti-6Al-4V parts by using FEM methods and the results indicated that RS increased with number of layers.

Recent years have also seen advances in computational process simulation tools that allow the addition or removal of solid material (i.e. finite elements) from a model during the finite element analysis (e.g. in ABAQUS [85, 119-121] and ANSYS [116, 122, 123]). Such new capability, coupled with the provision for custom-written macros and subroutines, have advanced AM modelling capability in general purpose computational software suites [124, 125]. By definition, such tools are particularly convenient for simulating AM processes, allowing the gradual build-up of solid material in a model. Two kinds of techniques are commonly used for simulating the addition of newly born material: ‘quiet elements’ and ‘element birth’ (or inactive element) [126]. The ‘quiet elements’ technique [127], where low values of material properties are applied for the layers that have not been deposited and are then modified mid-solution to realistic material properties once sintering occurs at the deposited materials in PBF. However, this method is numerical sensitive, and it can cause numerical problem of reducing the convergence ratio

of solvers. Thus, it is not recommended for the macroscale modelling [127, 128]. The 'model change' function (i.e. element birth) in the finite element software ABAQUS allows gradual activation of solid material and is commonly employed to simulate the addition of materials for AM process [36, 129].

A computationally efficient plug-in "AM Modeler" has recently been developed by Dassault Systems for ABAQUS/Standard [130-133]. Song et al. [131] predicted RS and distortion by using the "AM Modeler" add-on and the results indicated that high RS at the corner (the interface of part with the base plate) was the main factor causing cracking in DED manufacturing. This plug-in was released during this PhD project and after work was well progressed on a custom written alternative. However, the plug-in was evaluated as part of this work. Due to unavoidable computational cost limitation, it is not possible to capture the temperature or RS state evolution for large models by using the small-time increment (i.e. 10^{-5} s). So, larger time scales should be used for part level thermo-mechanical coupled models in "AM Modeler" and only the average heat input in a specific time increment and volume can be obtained. This is because that the toolpath intersection module computes how many elements are intersected by the toolpath in that time increment and assigns the heat input computed from the power input and time to that particular element. Song et al. [131] simulated the PBF-LB process modelling of a 120 mm long overhang structure by setting one time increment for each whole layer in AM Modeler. Thus it is unable to capture the local process temperature and stress state evolutions in AM for large models by using the "AM Modeler" plugin in ABAQUS [131].

Finite element analysis software companies are also developing such tools for simulating the real physical AM process, such as ANSYS Additive Print [134, 135], Simufact Additive [136, 137] and Autodesk Netfabb [138, 139]. Wang et al. [136] proposed a RS prediction method and utilised 'Simufact Additive' investigated effects of the process parameters on RS and the results showed that stress state gradually increased with the printing height of PBF manufacturing. However, there are limited studies regarding accuracy of these commercial packages [140] and the 'inherent strain' approach used in these tools need to be calibrated by the test coupons such as a cantilever beam for the part-

scale component process modelling [141]. Therefore, AM users are developing their own programs and subroutines to simulate the real physical AM process.

As described in **Chapter 1**, multiple process parameters influence the temperature history during AM, and temperature evolution further affects the performance of the manufactured components. Several thermal FEM models (uncoupled) have been developed to predict temperature behaviour in AM [142-144]. As the mechanical behaviour (e.g. RS and distortion) in AM process is mainly induced by the thermal phenomenon, the mechanical process simulations should be closely linked with the thermal process model. Therefore, coupling simulations (both the sequentially coupled thermal-stress (or thermo-mechanical) analysis and the fully coupled thermal-stress analysis or staggered analysis) are commonly used in the process modelling of PBF and DED to get the temperature and RS information [23, 36]. In sequentially coupled thermal-stress analysis, the temperature field is independent of the stress field. The thermal analysis and stress analysis are run separately, first conducting the heat transfer analysis and then importing the calculated temperature field into the stress analysis. The fully coupled thermal-stress analysis performs the thermal analysis and stress analysis simultaneously and can obtain the temperature and stress results by a single analysis. However, this approach is typically more computationally expensive due to a large un-symmetric system of equations to be solved and it is more prone to convergence issues caused by the nonlinear material properties [145]. The staggered analysis performs the thermal and mechanical analysis simultaneously, and the difference between staggered and fully coupled thermo-mechanical analysis is insignificant [146], but there is no staggered option in ABAQUS. Lu et al. [26] predicted RS of DED manufactured macroscale parts by fully coupled thermal-stress analysis. Williams et al. [36] investigated the RS and distortion of PBF manufactured macroscale parts using sequentially coupled thermal-stress modelling. The fully coupled thermal-stress modelling has the advantage of setting one model while the sequentially coupled approach requires two separately models. The advantages of sequentially coupled thermal-stress analysis are computational modelling, easier to get convergence and less memory requirement. In summary, as AM is a thermal driven process and the plastic strain energy is insignificant compared with the

laser or electron beam energy [133], the sequentially coupled modelling can be regarded as valid for AM process modelling.

To accurately simulate the real practical AM process, temperature dependent material properties (both thermal and mechanical) are required [142]. This is due to the presence of large temperature gradients during the repeated heating and solidification processes of AM process. Some studies ignored the temperature dependent material properties, employing constant mechanical and thermal properties. However, inaccurate thermal results were obtained in PBF without considering the temperature dependent Ti-6Al-4V material properties [147]. Therefore, the temperature dependent material properties of metal material are applied for the AM process modelling in the main content (**Chapter 3** to **Chapter 8**) of this work.

2.3.1 Thermal and mechanical model of metal AM modelling

Fully coupled thermal-stress modelling can be implemented by solving the following governing equations using finite element method with ABAQUS computer-aided engineering (CAE). The energy equation that is employed in fully coupled thermal-stress modelling for the AM process is [114, 148-150]:

$$\dot{H} + \nabla \cdot \boldsymbol{q} = Q + \dot{D}_{mech} \tag{2.1}$$

where $\dot{H}$ is the rate of enthalpy change (per unit volume), $\boldsymbol{q}$ is the heat flux, Q is the power density of energy beam heating and $\dot{D}_{mech}$ is the thermal-stress dissipation rate caused by plastic deformation [149, 151, 152]. The fully coupled thermal-stress modelling was conducted in **Chapters 3**, **4, 5** and **8**.

In sequentially coupled thermal-stress modelling, the heat transfer process is independent of the mechanical behaviour of material and the energy equation can be simplified to:

$$\dot{H} + \nabla \cdot \boldsymbol{q} = Q \tag{2.2}$$

Sequentially coupled thermal-stress modelling was performed in **Chapters 6** and **7**. For both fully coupled and sequentially coupled thermal-stress modelling, the enthalpy rate can be stated as:

$$\dot{H} = \rho_s C_p \frac{dT}{dt} + \rho_s \frac{d(fL)}{dt} \tag{2.3}$$

where ρ_s for density of solid material, C_p for specific heat capacity, T for temperature, t for time and L for latent heat of fusion. The liquid fraction f is assumed to be a linear function of temperature as [153]:

$$f = \begin{cases} 0 & T < T_S \\ \frac{T - T_S}{T_L - T_S} & T_S \leq T \leq T_L \\ 1 & T > T_L \end{cases} \tag{2.4}$$

where T_S and T_L are the sodius and liquidus temperature, respectively.

Inputting the energy source into the FEM model is essential to heat and melt the newly added material in AM. One approximation approach is to define a predefined temperature on the newly added material, and the predefined temperature is equal to or above the melting temperature of material. Alternatively, a power density of energy beam could be applied to newly deposited material in the process modelling of metal AM, which can be approximated based on energy balance and the AM process build parameters, such as laser spot size and power. Williams et al. [36] investigated stress and displacement of a bridge structure in PBF-LB by depositing the 316L stainless steel material with a predefined melting temperature, and the displacement of the part was validated by experiments. There are two commonly used power densities in metal AM process modelling: the moving heat source and the uniformly distributed (equivalent) heat source [45]. Most of the moving heat sources are in the format of volumetric Gaussian profile and can simulate the moving of the energy beam with time and scanning paths, which is normally applied at the PBF process modelling with several layers of material [41, 144, 154]. The uniformly distributed heat source method is commonly used to simulate AM modelling in a layer-by-layer manner, where each whole layer is melting and cooling simultaneously [36, 143]. The Gaussian distributed volumetric power density is defined as [154]:

$$Q = \frac{4\sqrt{2}AP}{\pi\sqrt{\pi}R^3} e^{\frac{-2r^2}{R^2}} \tag{2.5}$$

where A is heat source absorption coefficient, P is laser beam power, R is laser spot radium and r is the distance to the laser beam centre.

The volumetric power density for the uniformly distributed volumetric heat source used in the finite element simulation can be approximated based on the build process parameters of AM [155, 156]:

$$Q = \frac{AP}{d_s d_m H_s} \tag{2.6}$$

where d_s is the heat source spot diameter, d_m is the melt pool depth and H_s is the hatch spacing. The total energy density can be determined by multiplying the power density by the heating step time t_m.

The heating step time t_m is the time when the energy beam operates in melt mode heating the newly added layer of powder to above the liquidus temperature. The heating step time of the uniformly distributed volumetric power density for the active layer for AM process modelling can be simplified as [143, 157]:

$$t_m = \frac{d_s}{v_s} \tag{2.7}$$

where v_s is the energy beam scanning speed during the material melting process.

The predefined temperature of material for simulating energy input in the computational AM process modelling is calculated based on energy balance:

$$C_p m \Delta T = E_t \tag{2.8}$$

where C_p for specific heat, m for mass of material, ΔT for change in temperature comparing with the initial room temperature and E_t for thermal energy. The total energy input into the computational model can also be calculated by:

$$APt_m = E_t \tag{2.9}$$

The heating time for each element increment is simplified to be calculated based on the bead increment length in the computational AM modelling and the moving speed of the deposition nozzle:

$$t_m = \frac{L_b}{v_s} \tag{2.10}$$

where L_b is the bead increment (or element) length that is along the scanning direction and v_s is the moving speed of the deposition nozzle. The mass for a single computational bead increment of material can be calculated as:

$$m = \rho_s L_b W_b H_b \tag{2.11}$$

where ρ_s for density of solid material, W_b for width of specific bead increment and H_b for bead increment height. Combing Eq. 2.8 to Eq. 2.11, the temperature change ΔT caused by energy input can be calculated as:

$$\Delta T = \frac{AP}{C_p \rho_s W_b H_b v_s} \tag{2.12}$$

The predefined temperature of material T_P for the computational model is the sum of the temperature increment for each layer and room temperature:

$$T_P = \Delta T + T_R \tag{2.13}$$

where T_R for room temperature.

The thermo-mechanical dissipation rate $\dot{D}_{mech}$ for fully coupled thermal-stress analysis is defined as [151, 152, 158]:

$$\dot{D}_{mech} = \eta \boldsymbol{\sigma} : \dot{\boldsymbol{\varepsilon}}^p \tag{2.14}$$

Where η is the inelastic heat fraction and is assumed as 1 in the ABAQUS solution, $\boldsymbol{\sigma}$ is the stress tensor and $\dot{\boldsymbol{\varepsilon}}^p$ is the plastic strain rate tensor. The thermo-mechanical dissipation rate is not involved in the sequentially coupled thermal-stress analysis due to the independence of thermal and mechanical fields. AM is mainly a thermal induced process, and the heat due to plastic deformation D_{mech} is negligible if compared to the laser input.

The heat losses that are commonly involved in the macroscale thermal PBF modelling are as follows (more details shown in Figure 3.2a):

i. Heat conduction between the active layer (i.e. the newly added layer of material, which is always the top layer of material) and the solidified material of the previous layer or the base plate.
ii. Heat conduction from the solidified material to the surrounding powders.
iii. Heat radiation and convection at the top surface of the active layer to the chamber / surrounding atmosphere.

The heat flux due to conduction can be formulated as [159]:

$$q_{cond} = -k_s \nabla T \tag{2.15}$$

where k_s is the temperature dependent thermal conductivity of the solid material. The active layer radiation heat loss can be defined by Stefan-Boltzmann's law before the next layer is added [149]:

$$q_{rad} = \varepsilon \sigma_S \left({T_{sur}}^4 - {T_r}^4 \right) \tag{2.16}$$

where q_{rad} is the heat flux due to active layer radiation, ε is the emissivity, σ_S is the Stefan-Boltzmann constant, T_{sur} is the surface temperature of the part and T_r is the build chamber temperature [115].

In AM process modelling, as the solid part is surrounding by atmosphere, the heat convection between the side surface of part and surrounding environment is included. The active layer convection heat dispersion can be expressed by Newton's law of cooling [149, 160]:

$$q_{conv} = h(T_{sur} - T_r) \tag{2.17}$$

where *h* is the heat transfer coefficient [161].

The equilibrium for the finite element mechanical analysis is given by:

$$\nabla \cdot \boldsymbol{\sigma} = 0 \tag{2.18}$$

where $\boldsymbol{\sigma}$ is the stress tensor. The mechanical constitutive law for the elastic problem is defined as:

$$\boldsymbol{\sigma} = \boldsymbol{C}: \boldsymbol{\varepsilon_e} \tag{2.19}$$

where $\boldsymbol{C}$ is the material stiffness tensor and $\boldsymbol{\varepsilon_e}$ is the elastic strain tensor. The total strain rate can be represented as:

$$\dot{\boldsymbol{\varepsilon}}_{\boldsymbol{Total}} = \dot{\boldsymbol{\varepsilon}}_{\boldsymbol{e}} + \dot{\boldsymbol{\varepsilon}}_{\boldsymbol{p}} + \dot{\boldsymbol{\varepsilon}}_{\boldsymbol{T}} \tag{2.20}$$

where $\boldsymbol{\varepsilon_{Total}}$, $\boldsymbol{\varepsilon_p}$ and $\boldsymbol{\varepsilon_T}$ are the total, the plastic, and the thermal strain, respectively. The thermal strain component is given by:

$$\boldsymbol{\Delta\varepsilon_T} = \boldsymbol{\alpha}\Delta T \tag{2.21}$$

where $\boldsymbol{\alpha}$ is the coefficient of thermal expansion of material. ΔT is the change of temperature between at time increment Δt and at the beginning.

Coupling strategies are used if the thermal and mechanical solutions are interdependent and thus determined simultaneously. The transient fully coupled thermal-stress analysis in ABAQUS/Standard software can be represented as [26]:

$$\begin{bmatrix} K_{uu} & K_{u\theta} \\ K_{\theta u} & K_{\theta\theta} \end{bmatrix} \begin{Bmatrix} \Delta u \\ \Delta\theta \end{Bmatrix} = \begin{Bmatrix} R_u \\ R_\theta \end{Bmatrix} \tag{2.22}$$

where Δ_u and Δ_θ are the corrections to the incremental displacement and temperature, respectively. K_{ij} are submatrices of the fully coupled Jacobian matrix. R_u and R_θ are the mechanical and thermal residual vectors, respectively [162].

2.3.2 Fundamentals for macroscale part process powder bed fusion modelling

One of the chief motivations for PBF-LB process simulation is to predict the manufacturing induced RS. Zhao et al. [115] calculated the RS evolution, focusing specifically on von Mises stress, and concluded that the maximum von Mises stress occurred in the middle layer of the printed part. Yang et al. [163] predicted the maximum principal stress distribution in a block model during the PBF process and it was found that RS at the outer surface of the part was tensile with compressive stress inside the block. Up to now, there are few experiments that study the stress state evolution during the PBF-LB process, with one validation experiment involving a single scanning track of simple

geometry [164]. Zaeh et al. [164] computationally studied the influence of layer thickness on deformation and found that a decreased layer thickness would increase the deformation of a layer. Contrary to this, Mukherjee et al. [121] showed that RS could be decreased by reducing the layer thickness. Roberts et al. [165] illustrated that the average residual stresses increased with the number of melted powder layers.

Various multi-scale and multi-physics computational models of PBF-LB process have been reported [111, 115, 116]. Raghavan et al. [166] stated that the repeated thermal loading caused by the dynamic heat flux as well as heat transfer from subsequent layers have significant effects on local transient temperature distribution and temperature gradient. Khairallah et al. [167] simulated the PBF-LB process and thermal diffusion when using powders with a layer thickness of 35 μm. Chen et al. [168] investigated the influence of parameters on the sintering depth and shape of the melt pool by formulating a novel temperature-transforming model.

PBF-LB process temperature history determines the resulting RS and thus influences the in-service performance of the final parts. Hodge et al. [169] developed a continuum thermo-mechanical model for part-scale (macroscale) PBF-LB manufacturing and investigated the resulting RS and deformation. The predicted stress and deformation fields were further experimentally validated in a later study [170]. To date, significant progress has been made in the area of melt pool geometry, RS, microstructure, build distortion, and the effects of various PBF-LB process parameters [111, 121, 171, 172]. However, most finite element models are limited to simulating small build volumes, or low numbers of layers, e.g. a 0.6 mm height cuboid [173-175].

Macroscale PBF-LB modelling for part at the (microscale layer) resolution at which it is built is computationally expensive. In terms of simulating the manufacturing process of macroscale part in PBF, custom developed efficient AM simulation software has also recently emerged (e.g. Simufact Additive [43]) and been utilised to investigate RS [136]. Pal et al. [176] presented a novel framework for a dynamic mesh transition approach to capturing a moving heat flux in their thermo-mechanical process model. Denlinger et al. [177] predicted the thermal history of Inconel 718 on a single layer build during the PBF-LB process via a novel software (CUBE). Chiumenti et al. [125] presented a FEM

framework for the heat transfer analysis of AM by using the COMET software with the Common Layer Interface (CLI) file and the “element birth” method on a 50 mm height model. While technically advanced, such new dedicated AM software may be beyond the reach of industry due the requirements of additional licencing and upskilling on new software.

One of the primary considerations in finite element modelling is specification of minimum element size (i.e. overall nodal quantity and thus total number of degrees of freedom). This practical limitation often forces decisions such as whether loose powder should be included in the simulation, and the layer height in each model. The layer height for each layer is the thickness of each newly added material in the computational modelling domain. It has been shown that failure to include loose Inconel 718 powder can result in a 30 % underprediction of temperature using the custom software CUBE [177]. However, including powder material in the model can significantly increase the computational cost and limit achievable resolution in layer height.

Specifying model layer height is not a trivial task - it has consequences for the entire model configuration and application of multiple boundary conditions. In particular, it will influence the selection of appropriate model resolution, energy input and time factors and more crucially: understanding their interdependencies (Figure 2.3), which is regularly missed in research publications in the literature to date [178].

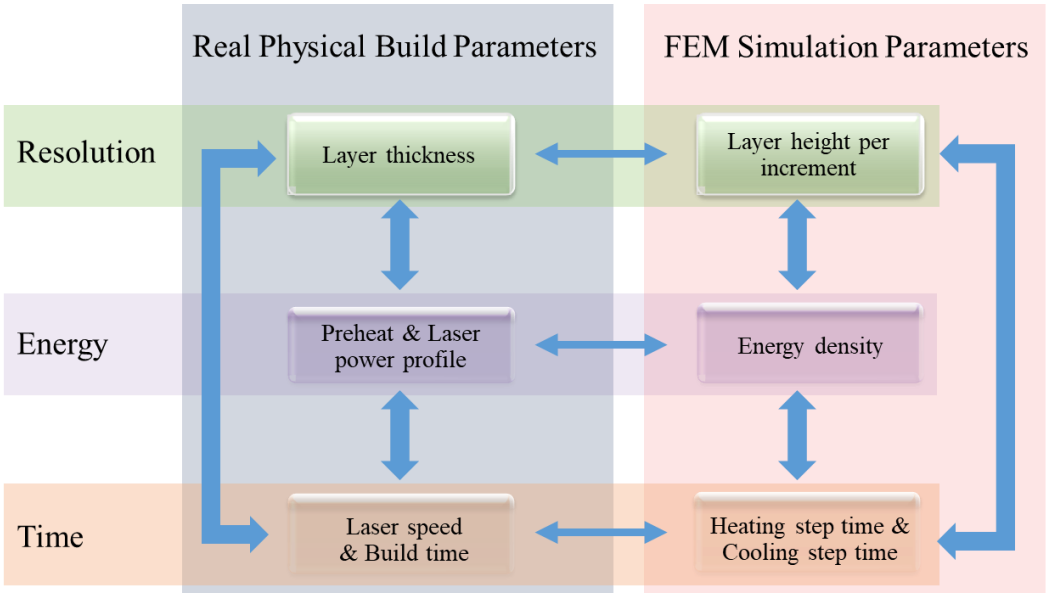

Figure 2.3. Interdependencies of resolution, energy and time in the real physical domain and computational model domain of AM.

A typical PBF-LB build process could take > 20 hours of build time. This period consists of a laser exposure time step and target material cooling time step, for every layer. In simulating this thermal process, researchers must determine appropriate energy input times and cooling step times (where the material solidifies, cools, and partially reheats) in the computational domain. The cooling step time is the step in which the energy beam deactivates, and the roller/coater spreads a new thin layer of powders on the powder bed. This is particularly important for computational microstructural modelling where cooling rate determines the microstructure. The energy input time and material cooling time per layer depend on the build parameters such as laser scan speed, hatch spacing, layer height, and part dimension etc. [179]. However, it is unclear what, if any, adjustments should be made to the step times when 'layer scaling' technique (which using much larger layer thickness in FE model than in manufacturing domain) is used.

Michele et al. [125] investigated the validity of process PBF-LB modelling on macroscale Ti-6Al-4V walls with deposition volume of 107 cm^3 by using the layer-by-layer modelling approach. However, they did not investigate the effects of process parameters of heat input and heating step time on RS. Li et al. [180] showed that distortion could be predicted on the L-shaped part by scaling up the layer height from 30 μm to 1500 μm (layer scaling factor of 50), but did not investigate temperature evolution during manufacturing.

Rubenchik et al. [181] investigated ‘ layer scaling’ laws for different materials and parameters with respect to the temperature distribution around the melt pool, but did not explore the macroscale effects.

A simple approach to model the heating effect of the laser could involve directly specifying a material temperature boundary condition [182]. More commonly, the power density of the laser is applied based on laser power and spot size, and directly input to the model. Cunningham et al. [183] used energy densities ranging from 48.61 J/mm^3 to 194.44 J/mm^3 in a process parameter study of PBF-LB manufacturing of Ti-6Al-4V components. Kasperovich et al. [184] employed a uniformly distributed energy density of 117 J/mm^3. Gusarov et al. [185] proposed a volumetric heat source formulation via laser radiation absorption in a powder layer. Some researchers have thoroughly investigated the local profile of the energy field associated with a laser beam, and developed Gaussian distribution profiles, in both 2D [186] and 3D [50, 187]. Regardless of the input format, it is important that the energy generates a physically realistic thermal field, i.e. that the resulting temperature is momentarily above the melting point of the material. RS is based on the overall temperature history and temperature gradient.

The resolution, energy and time parameters are inextricably linked, in the real build parameter domain and in the computational simulation domain. This interdependency has yet to be fully defined, and as a result no guidelines / standards exist for PBF-LB computational simulation of macroscale components. Examining PBF-LB FEM studies in the literature, it can be seen that different scales of resolution, energy and time have been adopted, and this is summarised in Table 2.3. To the best of the author’s knowledge, no macroscale PBF-LB component has been simulated at model layer heights equal to the build layer thickness. Few studies illustrate the relationship of resolution, energy, and time, and no prior work has been found on a specific framework for balancing these three key facets in PBF-LB modelling. The interdependencies of resolution, energy and time is investigated in **Chapter 3** of this work.

Table 2.3. AM process modelling parameters review.

Methods	Material	Solid size (mm)	Volume (mm^3)	Layer Height (mm)	Mesh size (μm)	Scan speed (m/s)	Power (w)	Spot diameter (μm)	Hatch Spacing (μm)
PBF-EB [188]	Ti-6Al-4V	2×1.5×0.65	1.95	0.05	62.5×62.5×12.5	0.1, 0.5			
PBF-LB [175]	Steel	5×0.3×0.5	0.75	0.15	50×50×37.5	0.05	300	600	100
PBF-LB [175]		35×15×0.15	78.75		250×250×50				
PBF-LB [174]		6×1.4×0.037	0.31	0.037	16.7×16.7×12.3	0.8	195		
DED [187]	Steel	58×24×8	11136		317.5×200×200				
PBF-LB [50]	Ti-6Al-4V			0.05, 0.03		0.1, 0.5	20-50	70	200
PBF-LB [186]	Ti-6Al-4V			0.05	50×50	4.5			
PBF-LB [189]	Nickel alloy			1.6		0.004		750	750
PBF-LB [190]	Ti18Zr14Nb			0.06		0.7,0.95,1.2	125,200,280		80,140, 200
PBF-LB [191]		5×3×0.9	13.5	0.1					
PBF-LB [192]	Inconel 718	9×3×0.9			20				
DED-LB [121]	Ti-6Al-4V			0.9		0.01	2000	1500	

2.3.3 Scanning strategy and heat profiles for AM process modelling

Scanning strategy (or scanning pattern) is the energy beam moving path on the powder bed to trace out the designed geometry of the 3D part in each layer. It is one of the most important factors that influence the process temperature, RS, microstructure (e.g. grain), porosity, surface roughness and mechanical performances of component in PBF-LB manufacturing [193]. Scanning strategy can vary greatly between different layers of the 3D parts. Multiple different scanning strategies are commonly used in PBF, including parallel scanning (0° layer rotation scanning), 90° layer rotation scanning (alternating 90°), 67° layer rotation scanning (strips), 45° layer rotation scanning, island scanning strategy (chess) and out-in scanning etc. [41, 180]. Illustration of different scanning strategies used in metal AM is shown in Figure 2.4 [194]. The appropriate scanning strategy can be selected by the AM designers and operators depending on the process parameters, part geometry, dimension or the specific PBF machine etc.

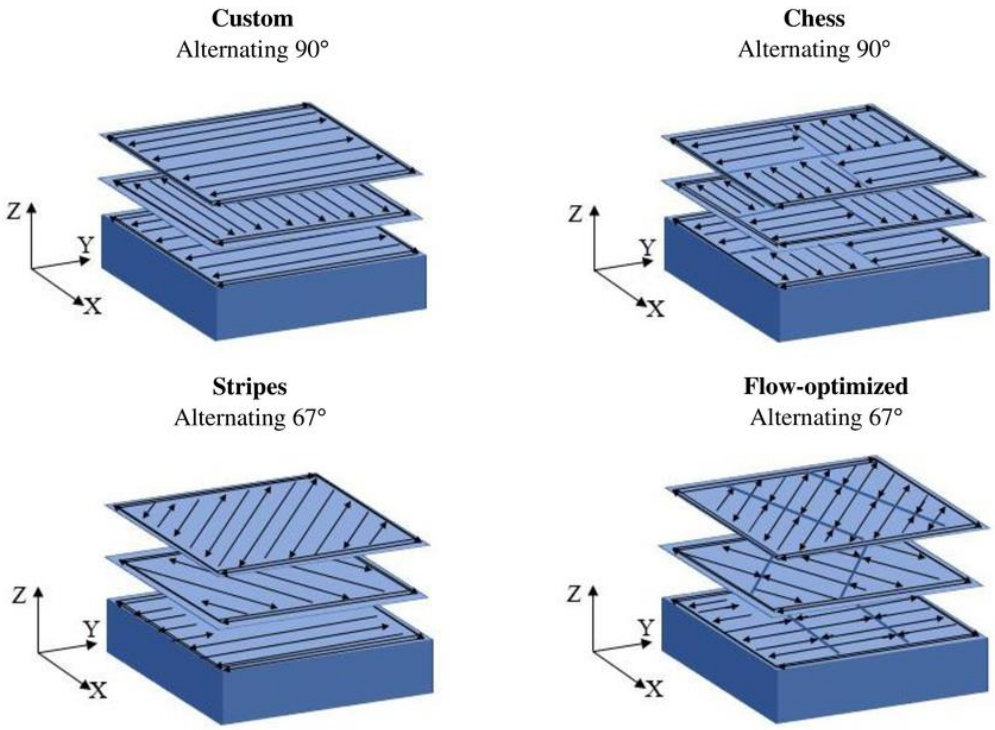

Figure 2.4. Different scanning strategies used in metal AM [194].

The dynamic microscale laser spot characteristic for different scanning strategies and the layer-by-layer features of PBF manufacturing results in a non-uniform temperature distribution, RS, and deflection in the PBF manufacturing [38, 41, 71, 195]. The study by Li et al. [38] revealed that the horizontal and vertical sequential scanning strategy (Figure 2.4a) generated a relatively uniform RS distribution in the *x* and *y* directions. Robinson et al. [195] experimentally demonstrated that the *XY* alternative scanning strategy (where the scan direction rotates 90° after finishing one layer) caused a more uniform and lower average RS compared with that of the no layer (0°) rotation. Masoomi et al. [50] illustrated island scanning was an effective strategy to reduce the final component RS. Cheng et al. [41] numerically studied the influences of eight different scanning strategies on temperature, stress and deformation by the single laser beam PBF-LB and the results showed that 45° line scanning had the lowest build direction deformation compared with other scanning strategies and the island scanning produced the maximum peak temperature due to the residual heat effect within the short scanning path.

There are a variety of modelling methods for simulating the practical PBF process. Depending on the type of the applied heat source, the commonly used process modelling methods in PBF include [36, 45]:

i. Moving heat source modelling method.
ii. Element-by-element (i.e. spot-by-spot or bead-by-bead).
iii. Hatch-by-hatch (i.e. track-by-track).
iv. Layer-by-layer modelling method.

The moving heat source modelling method applies a moving heat source as energy to melt materials, which offers an advantage of obtaining the accurate temperature history for simulating the real physical AM process. The Gaussian distributed heat source profile described in Eq. 2.5 is one of the most commonly used heat sources for the moving heat source modelling method. The overall summary and comparison of different moving heat sources for simulating the PBF manufacturing can be found in literature [154]. However, the moving heat source modelling method is computationally sensitive and expensive, thus it is only suitable for modelling of small volumes or several layers of material, i.e. 5 × 0.3 × 0.5 mm^3 [41, 95, 175].

The element-by-element method slices the macroscale part into different numbers of elements or beads, which are not specifically finite elements in FE models, but a small volume of material to be deposited. The element-by-element method is one of the commonly used techniques for macroscale part modelling in AM and it enables to simulate the scanning strategy by gradually activating element following the predefined moving paths. Lu et al. [105] performed process modelling of a wall structure in DED by using the element-by-element method, and the ‘element birth’ technique to activate elements sequentially in their in-house software COMET. Chiumenti et al. [125] predicted the thermal behaviour of PBF-LB manufacturing by using the element-by-element approach, which was validated by experiments. It should be noted that the element-by-element approach still costs a large number of time steps and a long computational time [125]. For instance, there are 1,280,000 time steps for simulating one single layer of a thin wall structure in PBF [125].

To further simply the macroscale PBF process modelling, hatch-by-hatch modelling method (shown in Figure 2.5) can also be applied for the AM process modelling [157, 180]. In the hatch-by-hatch method, the whole FEM model is sliced into different layers and each layer is then sliced into different numbers of hatches (i.e. strip of material, as shown in Figure 2.5b) depending on the part dimension, process parameters and scanning strategies (Figure 2.5a) in AM. To simulate the PBF manufacturing process, each hatch is sequentially activated by simulating the physical manufacturing process. The hatch-by-hatch modelling method is a compromise between the element-by-element method and the layer-by-layer modelling method. Li et al. [180] applied the hatch-by-hatch modelling method and investigated the effects of four different scanning strategies on RS and distortion of part in PBF-LB. Chiumenti et al. [128] using the hatch-by-hatch method simulated the DED manufacturing process; the results indicated that although the hatch-by-hatch method lost the oscillation of temperature during the real DED manufacturing, it could capture the average temperature. Details regarding process modelling using the hatch-by-hatch method can be found in literature [125].

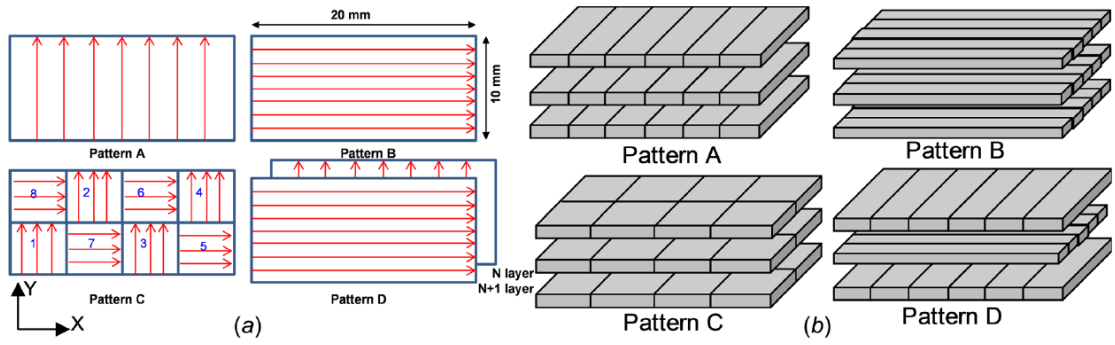

Figure 2.5. AM process modelling illustration: a) Top view of scanning strategies and b) Hatch-by-hatch modelling method towards different scanning strategies [180].

To save computational cost, some modelling strategies do not attempt to simulate all the laser scans [114, 180, 196]. PBF models can be simplified into a layer-by-layer format, rather than the physically realistic laser spot tracing, when it is not necessary to simulate details such as scanning strategy of each layer [36]. It applies a uniformly distributed (equivalent) heat source for all FEM elements in the same whole layer of a component, and all the material at the whole layer is heating and cooling simultaneously. The heat source (described by Eq. 2.6) and heating step time (defined by Eq. 2.7) etc. applied for

each layer are approximated based on the build process parameters in PBF, such as energy beam power, moving speed, hatch spacing, spot diameter and melt pool depth [155]. William et al. [36] simulated a cuboid geometry process modelling by using the layer-by-layer method in PBF-LB and proved that layer-by-layer method can provided suitable accuracy; for instance, the predicted displacement of a cuboid component was within 10 % comparing with that of the experiments. Prabhakar et al. [196] simulated the PBF-EB manufacturing process of a Inconel 718 part (e.g. 50 layers) by the layer-by-layer method in ABAQUS. For a symmetric model, half or quarter of the computational model can be used in the layer-by-layer modelling method to further reduce the computational cost but is not feasible for the hatch-by-hatch or the moving heat source method due to the variation of scanning strategies. The layer-by-layer method is the most common approach for macroscale PBF process modelling [36].

Lindwall et al. [157] investigated PBF process thermal modelling of a 0.64 mm height bulk metallic glass part using the "MSC.Marc" software and by the moving heat source, hatch-by-hatch and layer-by-layer method, respectively. The results showed that the computational time for the layer-by-layer method was only 0.2 % of that for the moving heat source method. Chiumenti et al. [125] revealed that the CPU time for the layer-by-layer approach was 17 % of the hatch-by-hatch method for two walls modelling in PBF-LB. Although a portion of thermal history and profile (within each layer) of PBF manufacturing is not captured, the layer-by-layer remains a viable computational approach [157].

For the above-described PBF modelling techniques (moving heat source method, element-by-element, hatch-by-hatch and layer-by-layer), the majority of the metal PBF models include the base plate as substrate to constrain the part via the bottom layer. The base plate also has a role as a powerful heat sink that effectively extracts heat by conduction from the part to cool the solid part during the AM process, so that the melted deposition materials can solidify rapidly. A selection of computational modelling methods and sample model details applied in the PBF process simulation found in the literature are summarised in Table 2.4.

Table 2.4. The computational methods and model details applied in PBF modelling.

Modelling approach	Dimension of model (mm)	Dimension of base plate (mm)	Heat source distribution
Moving heat source modelling [197]	2 × 1 × 0.02	2 × 1 × 0.5	Gaussian
Moving heat source modelling [41]	6 × 6 × 0.09	8 × 8 × 1	Gaussian
Element-by-element modelling [198]	30 × 3.8 × 3	32 × 4 × 50	Uniform
Hatch-by-hatch modelling [199]	20 × 10 × 2	100 × 20 × 10	Uniform
Layer-by-layer modelling [200]	55 × 10 × 20	-	Uniform

For the computational process modelling of metal AM in this study, the moving heat source method is applied for investigating scanning strategy effects on temperature and RS in the process PBF-MLB modelling of **Chapter 5**. The bead-by-bead (i.e. element-by-element) method is used for the macroscale thin wall process modelling of DED in **Chapter 8**. Hatch-by-hatch modelling is used for the square shaped part modelling in **Chapter 4**. The layer-by-layer modelling method is used for the macroscale PBF modelling in **Chapters 3**, **4**, **6**, and **7**.

2.3.4 Computational efficient strategies in finite element methods

A typical 50 mm high metal orthopaedic implant can be manufactured using 1667 layers of 30 μm thick via PBF-LB [201]. If every 30 μm thick layer is to be defined in the computation of the thermo-mechanical process, a fine mesh with prohibitive computational cost is needed [38, 178]. It is shown that there were 1.28×10^6 finite elements with an element size of $50 \times 50 \times 30$ μm^3 within a single layer of a thick specimen (i.e. $40 \times 80 \times 50$ mm^3) [125], and it is approximated that there would be 2.13×10^9 finite elements for the entire specimen if using the same uniformly distributed stationary meshes. One common approach is to approximate the 3D process modelling by 2D simulation [157]. However, 2D modelling is only suitable for geometries with uniform shapes, not for complex geometries [126].

Other computational cost saving techniques in PBF modelling, include the layer scaling, the inherent strain method and adaptive meshing approaches [95, 202, 203]. 'Layer scaling' is a technique where the deposition of multiple thin layers is represented by the deposition of fewer, thicker layers in the computational model. It assumes that the heating

and cooling processes occurs simultaneously in multiple layers, i.e. a multilayer-by-multilayer modelling method. Both Papadakis et al. [203], Hodge et al. [169] and Zaeh et al. [164] have demonstrated the layer scaling approach which involves modelling the process with much larger layer thicknesses (e.g. × 20) than in manufacturing domain to predict the temperature and RS distribution. This approach can significantly save computational cost. Even when layer scaling is employed, long model preparation and computational solution times can still be required for simulating macroscale parts, and it is thus essential to simplify or automate the model generation stage for large objects in PBF.

The 'inherent strain' method estimates distortion of parts by simplifying the FEM model as linear elastic by imposing the inherent strain, which can be obtained either by FEM simulations or experimental measurements [204]. The inherent strain method can significantly reduce the computational calculation time by simulating macroscale component thermo-mechanical modelling in a layer-by-layer static equilibrium [205, 206]. However, this method assumes that each whole layer of material at different heights of components experiences the same thermo-mechanical history, which does not represent the real practical PBF manufacturing process [205]. Details and summary of the inherent strain method can be found in [204].

Adaptive remeshing is a method to always retain fine mesh resolution at region where temperature and strain gradients are high (i.e. close to the melt pool) while coarsening the mesh elsewhere [146]. An example and illustration of the adaptive remeshing is shown in Figure 2.6. By using fewer elements and nodes at any given time, the computational time can be significantly reduced. Olleak et al. [207] developed an adaptive remeshing ability for PBF manufacturing. Gouge et al. [208] performed thermo-mechanical process modelling of PBF using the layer-wise adaptive remeshing approach in the commercial software of 'Autodesk Netfabb'. The results indicated good agreement between predicted distortion and the experiment (within 13% difference), but with a significant time saving (computational time one-tenth of production time). However, complex programming code is necessary for the adaptive remeshing strategy. The review of computational efficiency methods for AM are summarised by Lindgren et al. [95].

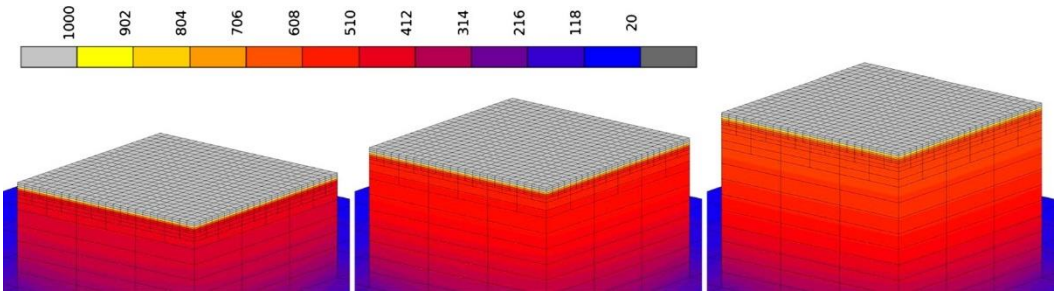

Figure 2.6. Illustration of adaptive remeshing method [95]: gradient meshes for the computational model, i.e. fine mesh close to the active layer (top several layers) and coarse mesh further below. The legend shows temperature (ºC) during AM process modelling.

The commercial general-purpose finite element package ABAQUS /Standard is a most commonly used software for thermo-mechanical process modelling of PBF [36, 180]. Three kinds of mesh refinement techniques are provided by ABAQUS/Standard to obtain accurate results [209]: adaptive remeshing (varying topology adaptivity), arbitrary Lagrangian-Eulerian (ALE) adaptive remeshing and mesh-to-mesh solution mapping. The adaptive remeshing technique is typically used for determining the optimized mesh of the model and it works by running the same model multiple times, with different mesh sizes. ALE adaptive remeshing is a tool to maintain a high-quality mesh throughout a FEM analysis, even when a large deformation occurs. The mesh-to-mesh solution mapping technique aims to control element distortion and works by mapping the temperature and stress results from the old mesh to a new mesh. The overall comparisons of the three remeshing techniques in ABAQUS can be found elsewhere [210]. The above three mesh refinement techniques in ABAQUS/Standard can be directly used for the PBF modelling process, for purposes of validating mesh convergence or improving accuracy of the final results [210]. However, none of the above three techniques are immediately applicable to macroscale AM process modelling due to the dynamic heat source, small layer resolutions and the overhead costs associated with a remeshing step. Therefore, AM users need to program their own codes and subroutines for computational efficient metal AM process modelling.

2.3.5 Multi-laser beam build powder bed fusion modelling

A major issue limiting the wider adoption of PBF-LB is the productivity rate and associated costs [40, 103, 211, 212], particularly for large 3D components. Strategies to

improve the PBF-LB build rate include modifying process parameters, such as enlarging the laser beam diameter, layer thickness and laser power to be 1 mm, 200 μm and 1000 W, respectively [213]. However, such methods can result in a 10 % loss of density and poor component geometry accuracy and inability to capture fine design details [213, 214]. PBF-MLB, with additional laser beams acting on different regions of the same active layer, is a next generation of PBF technology that has been introduced primarily to reduce build times and improve overall productivity rates. The PBF-MLB has the potential to obtain high manufacturing efficiency in conjunction with high precision [214].

Two kinds of PBF-MLB technologies were developed [215]: single trajectory lasers with multi-beam and multiple trajectory lasers with multi-beam (Figure 2.7). The single trajectory lasers with multi-beam technique utilises the secondary beam as an auxiliary heat source. Heeling et al. [83] noted that the secondary beam could heat the region surrounding the melt pool, thus decreasing the cooling speed. Multiple trajectory lasers with multi-beam involve all beams acting as powder melting heat sources. Li et al. [214] studied the resulting microstructure and mechanical performance when the laser overlap was varied during the dual laser beams PBF-MLB and found that PBF-MLB could obtain uniform part properties. Heeling et al. [40] investigated the influence of scanning strategies on the melt pool dimensions, dynamics and temperature gradients in the PBF-MLB and the results showed that PBF-MLB could reduce the temperature gradients by up to 20 %. Masoomi et al. [216] reported a dependence of temperature, microstructure, defect occurrence and mechanical performance on scanning strategies in PBF-MLB, which indicated that temperature gradients were highly sensitive to scanning strategies and the number of laser beams. Commercial development of multi-beam systems is currently underway, including PBF-MLB technologies and systems from SLM Solutions (SLM Solutions Group AG, Lübeck, Germany) [217], Renishaw (Renishaw UK Sales Ltd, Gloucestershire, UK) [218], EOS (EOS GmbH Electro Optical Systems, Krailling, Germany) [219] and Concept Laser (Concept Laser GmbH, Lichtenfels, Germany, now part of GE (General Electric Company, Boston, USA)) [220].

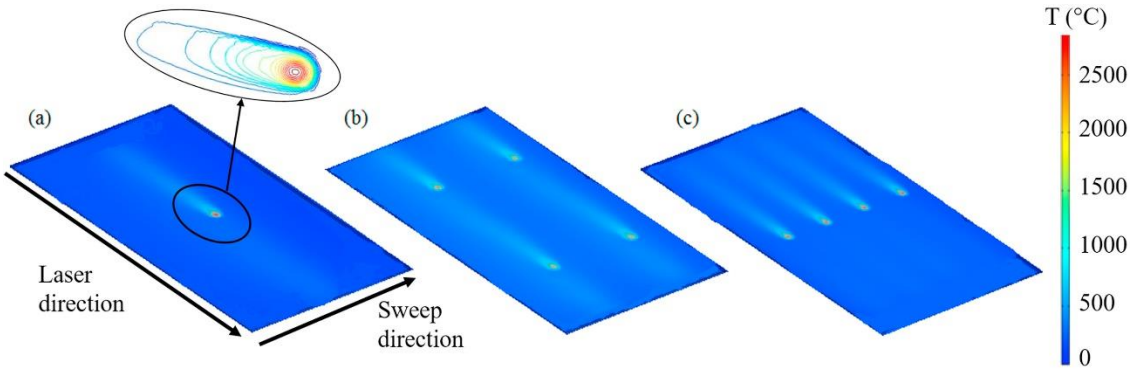

Figure 2.7. Temperature contours for different numbers of laser beams PBF process modelling: a) Single laser beam. b) Four laser beams by island scanning strategy and c) Four laser beams by parallel scanning strategy [50].

The dual laser beams PBF-MLB manufacturing is not only effective in improving the build rate and reduced cycle times for standard PBF parts [214, 216], but also makes it more practical for the larger macroscale components. In dual laser beams PBF-MLB manufacturing, the total exposure time can be shortened up to a factor of 2 compared with single laser beam while the production rate could be improved to ~ 60 cm^3 per hour, comparable to that of the PBF-EB [211].

Computational process modelling can provide insights into the optimum PBF-MLB configuration and process parameters, enabling consistent high build quality, greater part complexity and design freedom [10]. The ability to accurately simulate the physical PBF-MLB process and predict the thermal history and the final residual state stress would constitute a considerable advancement in AM and further empower product and process design.

PBF-MLB has also been found in practice to give lower RS in components. The reason for this is not fully understood. Most of the current PBF modelling studies found in literature are based on the single laser beam PBF machines [36, 41, 221], with the PBF-MLB yet to be fully investigated [40, 216]. A detailed understanding of the PBF-MLB process is required to obtain the RS information and inform the AM designers and operators of the optimum setup during the physical PBF-MLB printing.

Several researchers investigated the effects of the number of laser beams on temperature and RS in PBF-LB. Masoomi et al. [50] investigated the influences of laser beam number

(1, 2 and 4) on temperature and properties of the manufactured parts and included that the production times, cooling rates and RS magnitudes decreased when increasing the number of laser beams. The dimension of the model was $10 \times 5 \times 0.06$ mm^3 and the formation of only two layers was simulated. Zhou et al. [222] investigated the effects of the number of laser beams and scanning strategy on RS of Ti-6Al-4V material by the PBF-MLB method. The hatch-by-hatch method is also utilised in simulating the process modelling of PBF-MLB for Ti-6Al-4V material [223]. Apart from Ti-6Al-4V material, multi-laser systems were also developed for manufacturing Inconel 625 alloy [224] and AlSi10Mg alloy [225] component.

To date, there is still a lack of systematic investigation on the effectiveness of PBF-MLB over single laser beam PBF-LB in terms of RS. To overall quantify the multi-laser effects, the temperature, RS, and deflection behaviours are required. In addition, the effects of different scanning strategies should be systematically studied in the PBF-MLB in order to provide effective strategies for AM designers and operators to improve properties of the final manufactured parts. The PBF-MLB effects on thermal and mechanical behaviours are systematically investigated in **Chapter 5**.

2.3.6 Multi-part build powder bed fusion modelling

The manufacturing process parameters, part geometry and scanning strategy effects on the temperature evolution have been widely investigated by process modelling or experiments in PBF-LB [41, 226, 227]. However, the research outcomes of the current investigations are mainly based on a single part on a large build plate, which is not reflective of the industrial scale batch manufacturing of the PBF-LB manufacturing process, where typically large batch sizes of samples are arranged for simultaneous manufacturing in a single build [200, 228], as shown in Figure 2.8. In some instances, a single large component or small numbers of prototype parts are printed within the same build plate [173, 221]. However, the multi-part build effect on RS and the influence of batch size on the in-service properties of the manufactured component are still poorly understood.

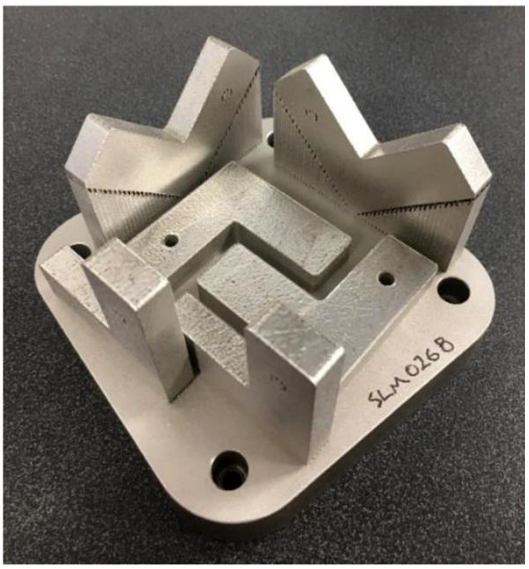

Figure 2.8. Multi-part build by PBF-LB [200].

The multi-part PBF-LB build has advantages of faster build time and increased production rate for each part [44]. Yılmaz et al. [44] investigated the influences of the number of cubic shaped samples on temperature and stress by using the commercial 'Netfabb' software and the results demonstrated that temperature increased while stress reduced with the increase in the number of samples. Yadollahi et al. [229] investigated the number of samples effects on mechanical performance and microstructure and found that longer inter-layer dwell time (ILDT) resulted in higher cooling rate and higher strength. Conversely, Mahmoudi et al. [230] indicated that the number of samples had an insignificant influence on the mechanical properties of tensile and compressive strengths of 17-4 PH stainless steel parts.

When printing different numbers of 3D components in a single build in PBF-LB, the ILDT between successive layers changes and can affect the process temperature history of each layer and thus the resulting RS of the manufactured parts. The ILDT is defined as the time from when the laser beam first starts in layer n, to when the laser beam first starts in layer n +1, which includes the time for all laser sintering, laser repositioning, roller movement, powder spreading and compaction of a layer [84]. The influences of ILDT on properties of additively manufactured parts have been widely investigated in DED [112, 229, 231, 232] or wire arc AM [233, 234]. Denlinger et al. [231] studied ILDT effects on distortion of Ti-6Al-4V components in DED, and found that an ILDT of 40 s had a 122.45 % higher

RS than the RS with ILDT of 0 s. Babu et al. [235] predicted that larger ILDT caused higher RS and larger displacement in DED of Ti-6Al-4V, which was experimentally validated. However, there are currently limited publications investigating ILDT effects on thermal and mechanical behaviours in PBF-LB. Mohr et al. [84] investigated the influences of ILDT (by varying scanning speed) on sub-grain size, melt pool geometry and hardness of 316L stainless steel by varying ILDT of a prism model, and the results demonstrated that an increase of ILDT via reducing the scanning speed caused an decrease of the melt pool depth for PBF-LB. Williams et al. [221] investigated the influences of ILDT on microstructure and porosity and the results revealed that a reduction of ILDT caused a higher (i.e. up to 200 ℃) surface temperature at the end of PBF-LB manufacturing and before cooling. Different with DED or wire arc AM, which is typically limited to manufacture a single part per build, PBF-LB manufacturing is capable of manufacturing multiple parts in a single build. Compared with single part build in PBF-LB, there is more heat input to the powder bed and a longer ILDT for multi-part printing, which alters temperature history. However, ILDT effects on RS of PBF manufactured parts have yet to be investigated. Therefore, the overall influences of ILDT on temperature and mechanical performance (e.g. RS) of Ti-6Al-4V components by variation in the number of parts per PBF-LB manufacturing need to be investigated [84, 221].

The part geometry influences ILDT and further significantly influences the temperature histories and properties of the manufactured parts [236]. When printing a batch of components simultaneously, the cross sections of the PBF-LB manufactured samples often vary greatly throughout the build [196, 237], which means the laser time per layer is not a constant [221]. Therefore, variation in cross sections while building different layers causes different ILDTs for each layer. Wu et al. [87] experimentally measured RS of a 316L stainless steel prism and investigated process parameter effects. Li et al. [45] predicted RS of a bridge structure model with an equivalent body heat source technique and validated RS by experiments. However, the same energy source and cooling and heating step times were applied for each layer with variation in cross-sectional areas and there is a lack of a guideline for the PBF-LB process modelling of part with geometry varies cross sections.

To date, significant progress has been made on process modelling of PBF-LB. However, most FEM simulation models are focused on optimisation of a single part build [36, 238], which is contradictory with the multi-part build in the real physical PBF manufacturing. To better simulate the real multi-part PBF printing process, the multi-part process FEM model is required and multi-part fabrication effects on the thermal and mechanical behaviour of parts should be investigated, which is shown in **Chapter 6** of this study.

2.3.7 Temperature-microstructure relationship in powder bed fusion

As microstructure significantly affects mechanical properties of additively manufactured parts [239], understanding the microstructure is important to obtain high quality parts. The thermal field during PBF manufacturing process not only determines the resulting RS, but also influences the microstructure such as phase, grain size, morphology, and crystallographic orientation [5, 240]. To obtain optimum microstructure of manufactured components, it is necessary to establish the link between AM process and the resulting complex microstructure [241]. Microstructure evolution is not modelled specifically in this thesis; however, the computational simulation strategies developed could be extended to also simulate microstructure evolution. This in turn could enhance the RS prediction by including microstructural dependant mechanical and thermal properties.

The complex temperature history (i.e. extreme temperature gradient and high cooling rate) and layer-by-layer build format cause a characteristic microstructure in PBF manufactured parts [242, 243]. Zhang et al. [132] stated that the morphology of the as-built additively manufactured Ti-6Al-4V typically consisting of acicular α' martensite. Sames et al. [244] indicated that the size of precipitates changed gradually in Inconel 718 alloy during PBF manufacturing, which could be used to optimise mechanical behaviour of the alloy. By optimising the process parameters, PBF 316L stainless steel exhibited better mechanical properties and density than the same material manufactured by using powder metallurgy process (i.e. HIP) [245].

In order to better control mechanical performances of PBF parts, it is necessary to understand the process-microstructure relationship and the microstructure formation mechanisms by the thermal simulation technology in PBF [243]. Microstructure is

strongly dependent on the thermal history in PBF and the microstructure and phase fraction (e.g. alpha phase) change with the PBF process temperature history [240]. As each phase has different mechanical properties, predicting phase fraction is important in determining the properties of the additively manufactured part [240]. The phase fraction transitions with the temperature history and cooling rate. Yang et al. [5] developed a process-structure model to predict phase transition based on the temperature history in PBF-LB for Ti-6Al-4V. The microstructures of Ti-6Al-4V material manufactured by PBF-LB, PBF-EB and DED are shown in Figure 2.9. Details of the PBF process and microstructure finite element modelling framework for Ti-6Al-4V can be found in other studies [5, 240, 246].

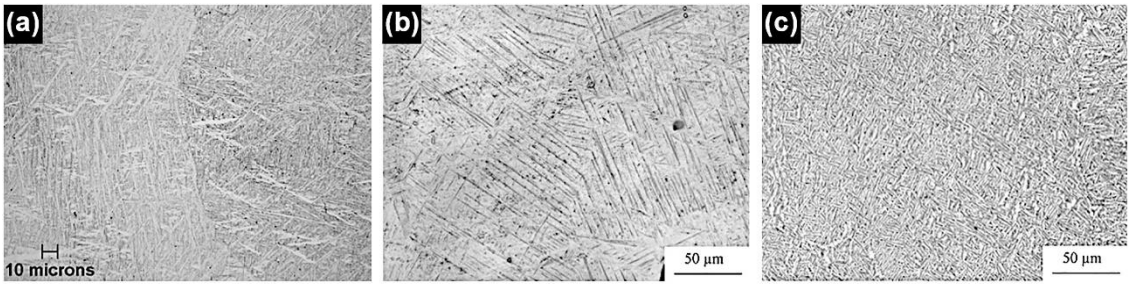

Figure 2.9. Optical microstructures of Ti-6Al-4V manufactured by different AM methods: a) Acicular α' martensite phase produced by DED. b) α' martensite by PBF-EB. c) Fine α and β dual phases manufactured by PBF-LB. Adapted from [37].

The cooling rate (CR) from the PBF temperature history can significantly influence the evolution of microstructure during PBF manufacturing [247]. It was found that columnar grains were formed at the centre of the additively manufactured Ti-6Al-4V sample, which was caused by the high CR and the heat transfer direction which was reversed with the build vertical direction [248]. Letenneur et al. [249] stated that CR influenced grain size of IN625 alloy in PBF-LB, and the higher scanning speed, the larger the CR and the smaller the grain size by both modelling and experiments. For Ti-6Al-4V material, the high cooling rates (i.e. > 10^5 K/s) produce a α' martensitic phase in the as-solidified material [69]. For instance, the martensite of Ti-6Al-4V material forms if CR is over 410 K/s [250]. The temperature history and CR caused solid-state phase transition (α phase, β phase, and alpha prime (α') martensite phase) diagram of Ti-6Al-4V material during PBF-LB manufacturing is shown in Figure 2.10.

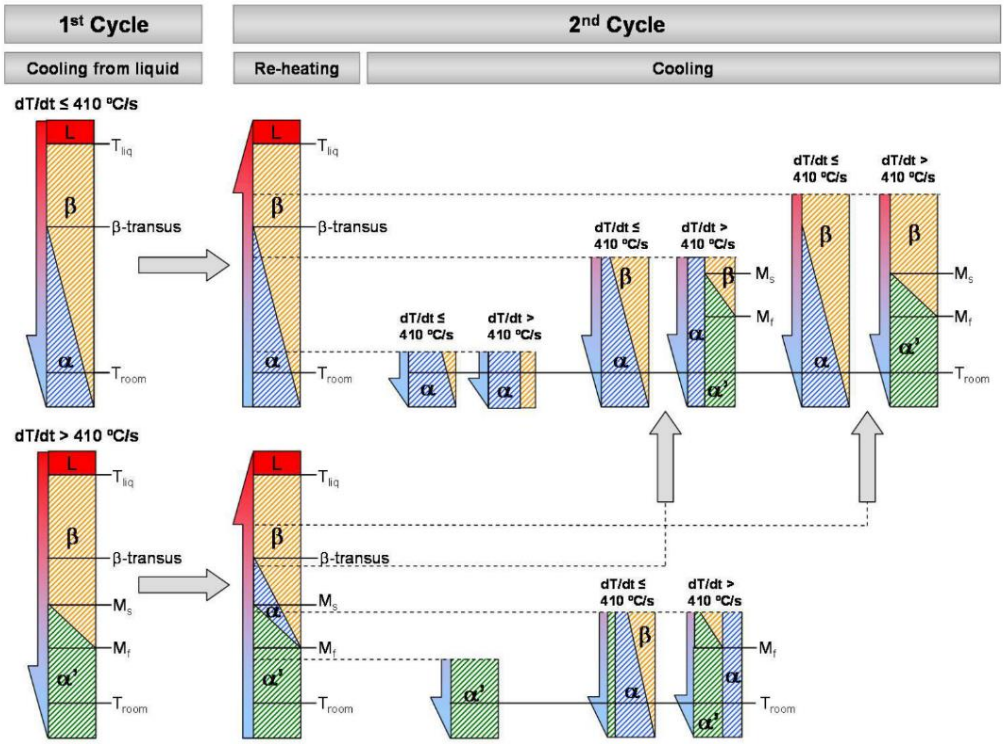

Figure 2.10. Phase transition diagram of Ti-6Al-4V [251].

The temperature time transformation (TTT) diagram of Ti-6Al-4V for calculating the cooling rate based on the temperature history of PBF manufacturing is shown in Figure 2.11.

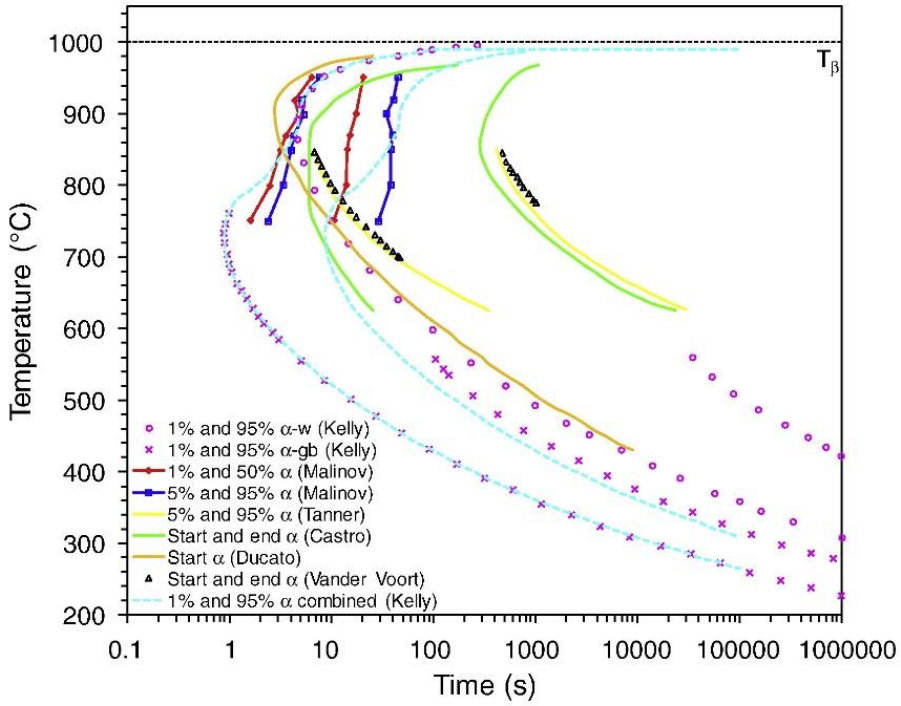

Figure 2.11. Time temperature transformation diagram of Ti-6Al-4V calculated by JMaPro [250].

The geometry of the part influences heat dispersion mechanisms and heat transfer direction, which further influences the final microstructure [221, 252]. The first several deposition layers (i.e. at part bottom areas) are directly contacted with the build plate, thus a lower temperature and higher cooling rate are observed than that at the top of sample in PBF manufacturing [243]. For the deposition layers close to the build plate in PBF, the build plate is typically much larger than the cross sectional area of the part, causing the heat to disperse in different directions and thus causing randomly crystallographic orientation grains [253]. With addition of sequential layers of part (i.e. far away from the build plate), the heat transfer direction is mainly opposite to the vertical build direction, and the preferred grain growth direction is shown in the build direction [254]. Karimi et al. [243] investigated wall thickness effects on microstructure evolution and indicated that fine grains were formed in the top and side surfaces of alloy 718 walls and a higher cooling rate was observed at the bottom of the part than that of the top layers in PBF-EB.

In summary, the temperature history of PBF in the simulation domain can be beneficial for predicting formation of microstructure and further prediction properties of the manufactured part. Therefore, it is necessary to simulate the process PBF thermal history. The thermal behaviour and temperature effects on microstructure evolution in PBF are

investigated in **Chapter 7**; however, this thesis does not explicitly model microstructural evolution.

2.3.8 Challenges of computational AM process modelling

Even though significant processes have been made in PBF process modelling, there are still a series of computational challenges existing at the PBF modelling, as listed below [10, 178, 255]:

1) There is currently no framework on macroscale component process modelling in AM to investigate the complex interdependencies of resolution, energy and time, such as significant dimension mismatch between the thin layers (in the order of microns) manufacturing and the constructed 3D macroscale parts (in the order of 10's of mm), the power density, heating step time, cooling step time on temperature and RS during AM.
2) Strategies to balance the computational efficiency with the high-fidelity of the part-scale model are under development. On the one hand, extremely thin layers are required in the manufacturing of a part, which makes the process PBF modelling expensive and sensitive. On the other hand, capturing the high process temperature and temperature gradient are essential for the thermal and mechanical PBF process modelling. Therefore, it is technically challenging to accurately predict the temperature and RS at part-scale.
3) Multi-laser beam build PBF process modelling capability. A multi-laser strategy is assumed to improve the productivity rate and decrease the RS. However, most of the current PBF modelling investigated single laser beam PBF and there is only limited research on multi-laser beam PBF process simulations or experimental measurements.
4) Multi-part PBF process simulations in a single build. The current PBF systems print different numbers of parts in a single build. However, most of the current modelling research is focused on single part build. The multi-part effects on RS are poorly understood. In addition, it is not sure if the results acquired from the single part build are suitable for the multi-part PBF process modelling.

2.4 Experimental methods for residual stress measurements

Stress, unlike strain, is difficult to visually identify and to measure directly. Both destructive methods and non-destructive techniques have been used to measure RS. The destructive methods including hole drilling and the contour method, which rely on measuring strain and back-calculating stress. Non-destructive experimental RS measurement methods include X-ray diffraction, neutron diffraction and high energy X-ray diffraction (HE-XRD) etc. [23, 256]. Other RS measurement methods such as layer removal, Barkhausen noise, ultrasonic and ring-core method are summarised in study [256].

2.4.1 Hole drilling

The hole drilling method is the most popular RS measurement method [256]. It operates by drilling a hole at the location of the part where RS is to be measured. The resulting strain of the component due to the stress relief induced by the hole formation is measured by a stain gauge [124]. The RS is back-calculated from the measured strain using the integral method. Marchese et al. [257] measured surface RS of PBF-LB manufactured cubic samples by hole drilling method and the measurements showed that RS increased with depth below the top surface and a ~ 600 MPa RS was measured at location where 0.6 mm below the top surface of sample. Illustration of the typical hole drilling facility and setups are shown in Figure 2.12a. The diagram of the principle of hole drilling method for RS measurement is shown in Figure 2.12b. The hole drilling facility is generally available in labs and easy to use. However, the limitation of the hole drilling technique is its low accuracy (i.e. ± 50 MPa [258]). More details in terms of the hole drilling method for stress measurements can be found in studies [258-260].

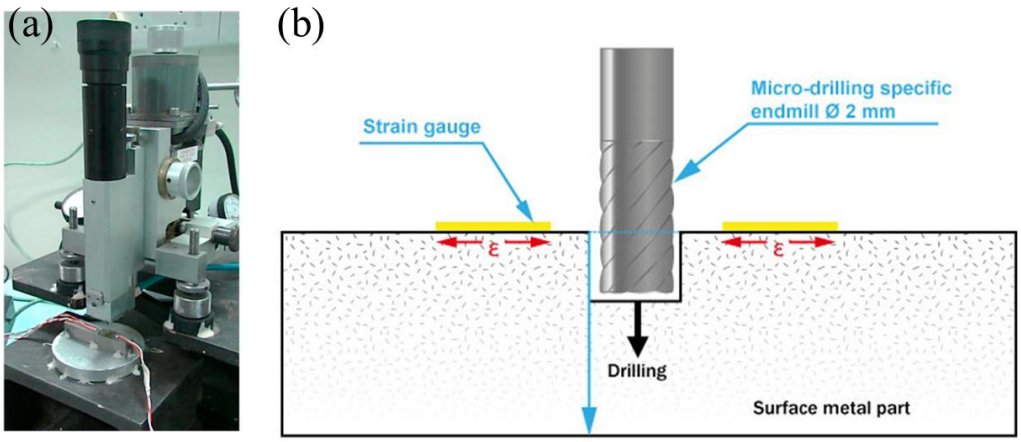

Figure 2.12. Hole drilling technique for RS measurement: a) The typical setup of the hole drilling method [259] and b) Schematic of principle of hole drilling method [260].

2.4.2 Contour method

The contour method enables to obtain a 2D RS contour of an interior surface of a part. It works by first cutting a sample into two along the plane to be measured. Vrancken et al. [261] measured residual stresses of PBF-LB manufactured Ti-6Al-4V parts by the contour method and found that the maximum RS was close to the yield strength of the material in PBF. As the quality of the cutting determines the final RS, often the wire electric discharge machining (EDM) process is used to cut the sample [256]. The RS (which is normal to the cut plane) is released after the above cutting operation. Methods such as coordinate measuring machines (CMM) are then used to measure the surface deformations of the two contoured surfaces. The surface RS can be obtained by applying the reverse deformations on the same geometry via finite element modelling [256]. The contour method can provide high fidelity RS results and is suitable for a wide range of materials but is a destructive measurement process. The principle of RS measurement by contour method is shown in Figure 2.13 [52]. However, by using the contour method, it is not possible to make successive slices close to each other [256]. Details in terms of the contour method can be found in studies [52, 256].

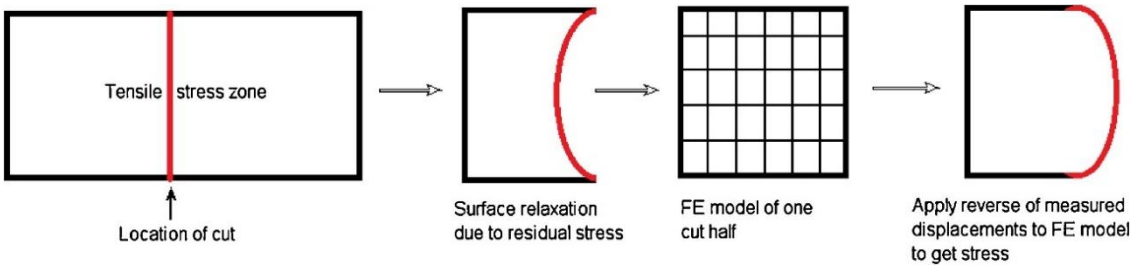

Figure 2.13. The principle of RS measurement by contour method [52].

2.4.3 Surface-based X-ray diffraction

The surface-based X-ray diffraction (XRD) is a non-destructive method that can measure RS at the surface (i.e. penetration depth of 3 – 10 μm) of a sample. Levkulich et al. [42] measured surface RS of PBF-LB manufactured Ti-6Al-4V samples and the results revealed that top surface RS decreased with the printing height. The principle of surface-based XRD is the lattice spacing (d-spacing) (shown as the distance from line A to line B in Figure 2.14) will change if RS exists in the samples compared to the unstressed (stress-free) status. When the material is under a tensile state, the lattice spacing increases while the lattice spacing decreases when the material is under a compressive stress state [262]. The lattice spacing is related to deflection angle by the Bragg's Law [263]:

$$n\lambda = 2d \sin\theta \tag{2.23}$$

where n is an integer, λ is wavelength, d is lattice spacing and θ is reflection angle.

The peak of the diffracted X-ray angle (at which the maximum diffraction intensity takes place) shifts with the lattice spacing. The strain and RS are calculated based on the peak shift [262, 264].

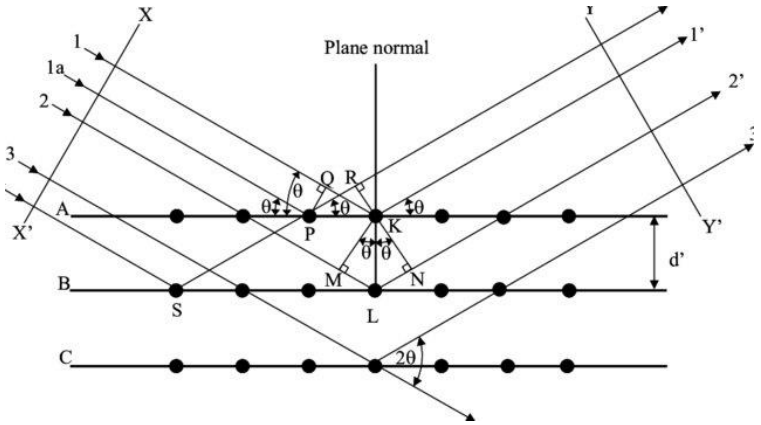

Figure 2.14. Illustration of Bragg's Law [265].

The surface-based XRD is generally available and suitable for a range of materials. However, this technique is limited to measuring surface RS (i.e. 3 – 10 μm depth). As the surfaces of the as-built parts by PBF normally have roughness in the range of 6 - 20 μm (Ra) [266], it is not suitable for surface RS measurement directly. Consequently, electro-polishing of the additively manufactured metallic parts surfaces is necessary before RS measurement using the surface-based XRD technique.

2.4.4 Neutron diffraction

Neutron Diffraction (ND) is one of the non-destructive stress measurements methods that can measure the interior stress of a sample. It is able to produce a 3D RS map inside a solid part. Wu et al. [87] measured RS of a PBF manufactured 316 L stainless steel part by the ND method and the results indicated that higher σ_{xx} and σ_{yy} stresses were formed at top surface of sample while stress at side surface of sample was mostly tensile (Figure 2.15). The typical ND set up is shown at Figure 2.16. To calculate the RS, the strain is first calculated based on Bragg's Law described in Eq. 2.23. The strain on the *hkl* plane, which is the relative change compared with the reference value from the stress-free sample, can be calculated as [267, 268]:

$$\varepsilon_{hkl} = \frac{d_{hkl} - d_{0hkl}}{d_{0hkl}} \tag{2.24}$$

where *hkl* are Miller indices, ε_{hkl} is the strain along the *hkl* crystal plane, d_{hkl} is the lattice spacing along the *hkl* plane and d_{0hkl} is the unstressed (stress-free) lattice spacing along the *hkl* plane.

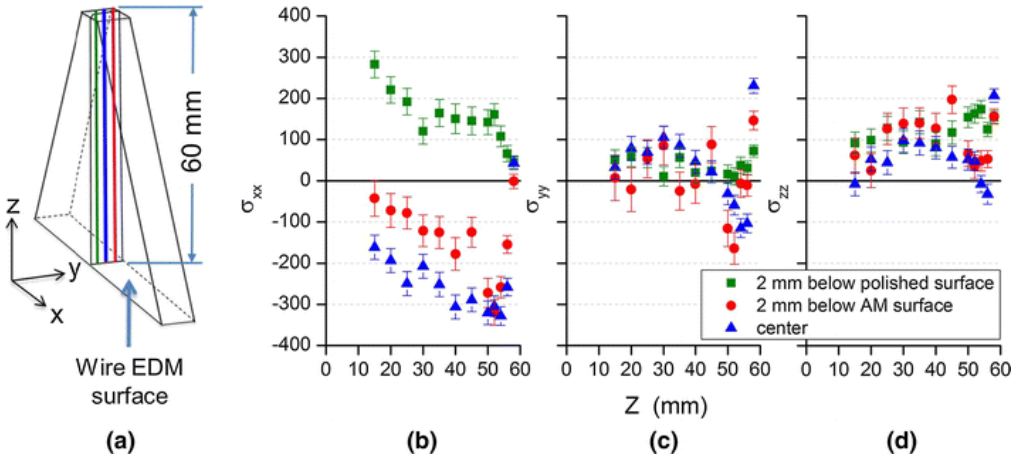

Figure 2.15. RS of additively manufactured sample measured by neutron diffraction: a) Prism sample. b) σ_{xx}. c) σ_{yy} and d) σ_{zz}. [87].

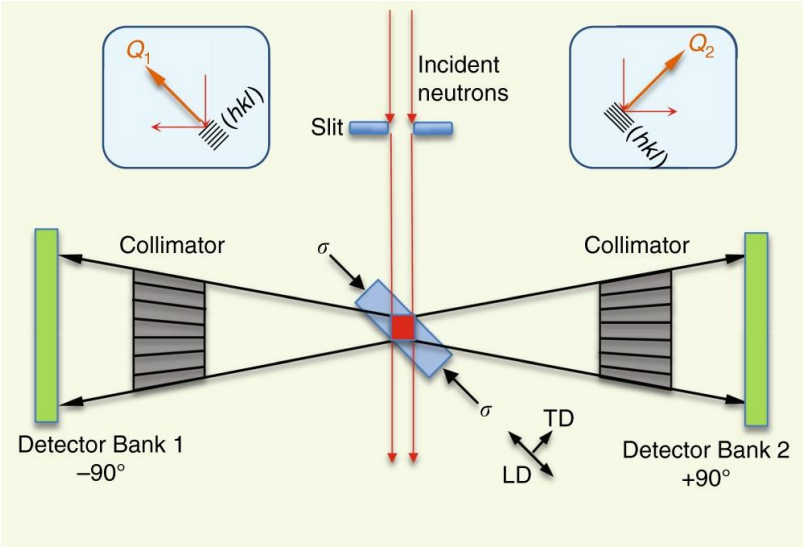

Figure 2.16. Illustration of Neutron Diffraction for RS measurement [269].

Combining Equation 2.17 and Equation 2.18, the strain ε_{hkl} can be calculated as [270]:

$$\varepsilon_{hkl} = \frac{sin\ \theta_{0hkl}}{sin\ \theta_{hkl}} - 1 \tag{2.25}$$

To determine the full strain and stress tensors, a minimum of six independent strain components must be measured [271]. Hooke's law can be used for calculation of both principal and shear stresses [272]:

$$\sigma_{ij} = \frac{E}{(1+\nu)}(\varepsilon_{ij} + \frac{\nu}{(1-2\nu)}\delta_{ij}\,\varepsilon_{kk}) \tag{2.26}$$

where E is elastic modulus, ν is Poisson's ratio, ε_{ij} the strain tensor, σ_{ij} the stress tensor, δ_{ij} the Kronecker delta (i.e. $\delta_{ij} = 1$ when $i = j$, and $\delta_{ij} = 0$ when $i \neq j$) and ε_{kk} the sum of over all kk.

The focus of this thesis is on normal residual stresses, thus shear stresses were not measured and calculated. Based on the assumption that the measurements were made along the principal directions [273], simplified form of Hooke's law is employed to calculate the RS components [267, 273]:

$$\sigma_{xx} = \frac{E}{(1+\nu)(1-2\nu)}[(1-\nu)\varepsilon_{xx} + \nu(\varepsilon_{yy} + \varepsilon_{zz})] \tag{2.27}$$

$$\sigma_{yy} = \frac{E}{(1+\nu)(1-2\nu)}[(1-\nu)\varepsilon_{yy} + \nu(\varepsilon_{xx} + \varepsilon_{zz})] \tag{2.28}$$

$$\sigma_{zz} = \frac{E}{(1+\nu)(1-2\nu)}[(1-\nu)\varepsilon_{zz} + \nu(\varepsilon_{xx} + \varepsilon_{yy})] \tag{2.29}$$

where σ_{xx}, σ_{yy} and σ_{zz} are the stress along the x, y, and z directions, ε_{xx}, ε_{yy} and ε_{zz} are the strains along the x, y, and z directions, respectively.

Even though the ND method is able to provide an accurate 3D map of RS, it is time intensive, and the costs of the equipment and measurement are higher than for other RS measurement methods. Furthermore, the ND facilities are limited worldwide, in part because this technique requires a nuclear reactor to supply the neutrons [274]. The beamline times for stress measurements by the ND method can be applied from agencies such as ISIS Neutron and Muon Source (Oxfordshire, UK), Institut Laue-Langevin (ILL, Grenoble, France), Research Neutron Source Heinz Maier-Leibnitz (FRM-II, Garching, Germany), Paul Scherrer Institute (PSI, Villigen, Switzerland) [275].

2.4.5 High energy X-ray diffraction

The high energy X-ray diffraction is a non-destructive RS measurement technique; thus, this method does not affect the RS state of the samples. Strantza et al. [276] measured RS of Ti-6Al-4V parts by the HE-XRD method and validated the RS results in the simulation domain. The principle of the HE-XRD method is that the sample to be measured is exposed to the X-ray and a detector is utilised to collect the Debye-Sherrer pattern, which is "caked" into equal azimuthal-width portions [277]. Each sector provides strain information along the related azimuthal direction. The principle of HE-XRD method is illustrated at Figure 2.17.

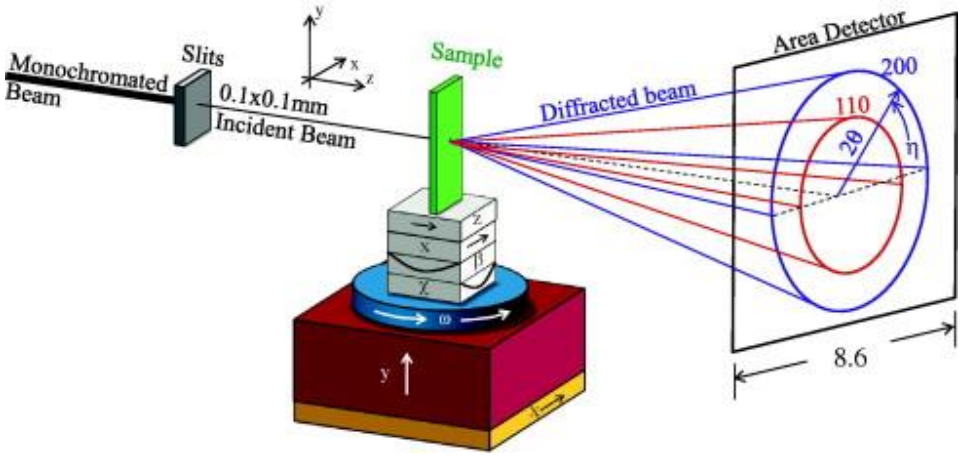

Figure 2.17. Illustration of the high energy X-ray diffraction method [278].

The lattice spacing and RS measured by the high energy XRD technique can be calculated based on Bragg's Law in Equations 2.17 - 2.22. Table 2.5 lists a comparison of the above RS measurement techniques.

Table 2.5. Comparisons of different RS measurement techniques in AM [256, 258].

Technique	Advantage	Disadvantage	Accuracy	Ability
Hole drilling	Fast; Easy to use; Wide range of materials	Semi destructive; Interpretation of data; Limited strain sensitivity and resolution	± 50 MPa, limited by reduced sensitivity with increasing depth	Generally available
Contour method	High-resolution maps of the stress normal to the cut surface; Wide range of materials; Larger components	Destructive; Interpretation of data; Impossible to make successive slices close together		
Surface-based X-ray diffraction	Ductile; Wide range of materials; Macro and Micro RS	Small components; Only basic measurements	± 20 MPa, limited by the surface condition	Generally available
Neutron diffraction	Macro and Micro RS; Optimal penetration and resolution; 3D maps	Only specialist facility	$\pm 50\times10^{-6}$ strain, limited by counting statistics and reliability of stress-free references	Not available
High energy X-ray diffraction				Available

Experimental measurement of RS is vitally important for validation of the predicted stress results by finite element AM process modelling. To date, most experimental RS measurement for metallic parts manufactured by AM is focused on a single part, but variation in measurement locations [88, 200]. As different conditions (i.e. manufacturing systems and process parameters) were applied for each separate study, it is difficult to compare experimental findings and achieve consistent conclusions. As scanning strategies influence parts RS in AM, RS measurement on a set of samples varying manufacturing patterns (i.e. scanning strategy) by the same PBF machine and process parameters is required to accurately validate the FEM predictions.

2.5 **Summary**

This chapter reviews recent developments and technologies of both finite element modelling and experiments in AM technologies. Finite element modelling is an effective tool to predict the thermal and mechanical behaviour of the complex process of AM. Experimental validation, especially non-destructive techniques for RS should be used to validate the accuracy of the developed finite element model for AM. The summary of **Chapter 2** is as follows:

a) It is computational expensive for the part-scale AM process modelling and layer scaling method is an effective method to accelerate the thermo-mechanical AM modelling and save the computational costs. However, its effects on time and energy input need to be better understood.
b) RS measurements on a set of parts are important to validate the predicted residual stress of additively manufactured components.
c) To improve the productivity rate and properties of the final PBF manufactured components, the PBF-MLB technologies are needed. However, there is limited study in terms of PBF-MLB manufacturing and modelling. It is thus necessary to build the process modelling capability for the PBF-MLB build.
d) There is currently a gap between the real multi-part build and computational single part process PBF modelling. To better understand the multi-part PBF manufacturing, process modelling capability for multi-part PBF is necessary to be developed.
e) The process PBF thermal modelling can be used to predict microstructure, which can further improve the final parts performance.

This work will help inform AM product designers and AM operators the optimum set up for the additive manufacturing system in order to minimising RS of the final manufactured parts.

3 Framework of finite element thermo-mechanical process modelling in laser beam powder bed fusion additive manufacturing

3.1 Introduction

As described in Section 2.3.2 and Figure 2.3, the precise representation of resolution (i.e. layer height and mesh size), energy (i.e. power density) and time (i.e. heating step time and cooling step time) in the simulation domain should closely embody real physical PBF-LB manufacturing setup and parameters. These three key aspects are interdependent (both in the simulation and real domains). However, as listed in Table 2.3, the literature contains studies employing vastly different resolutions, energies, and times, without a standard framework of PBF-LB process modelling, leading to difficulties in interpreting and comparing computational findings. Apart from accounting for the complex process parameters, PBF-LB process modelling is challenging due to the multiple size scales at play (i.e. microscale manufacturing of macroscale components). The consequences of common practices such as the layer scaling technique are not fully addressed in the literature.

One of the primary heat transfer mechanisms in PBF-LB is heat loss from the solidified part to the surrounding non-solidified powders [177]. Powder in-plane depth (i.e. thickness of surrounding loose powder within the active layer) has a significant influence on both the cooling rate as well as the steady-state temperature. To date, most finite element simulations of PBF-LB component manufacturing include the powder elements in the finite element model, and are limited to small volumes [175], due to computational cost. For macroscale component PBF modelling, the computational efficiency technique to representing solid part-powder conduction (heat conduction from printed part to surrounding powder material) is necessary. In addition, to accurately simulate the physical manufacturing process, how depth of powder material (i.e. build volume) should be included in the PBF-LB process modelling is still poorly understood.

The aim of this study is to investigate the computational efficiency technique for macroscale component modelling and interdependencies of resolution, energy, and time in PBF-LB FEM for Ti-6Al-4V alloy. The objectives of this chapter are as follows:

a) Developing a process PBF-LB modelling capability for macroscale components by using thin layer height.
b) To develop a computational efficiency approximation strategy to account for heat conduction loss from solidified part to the surrounding powder material for PBF-LB process modelling.
c) To investigate layer scaling effects on temperature and RS of macroscale component in PBF-LB modelling.
d) Investigation of interdependencies of resolution, energy, and time and their effects on temperature and RS.

The results of this work will facilitate efficient and accurate layer scaling, by providing guidance on the required mesh resolutions, and appropriate modifications to the energy and time inputs. This will also contribute FEM simulation guidelines to the modelling community for PBF-LB process. Finally, this study will serve as a reference document for design and manufacturing engineers in efficiently and accurately simulating the PBF-LB manufacturing induced residual stresses in their parts and optimising their build configurations.

3.2 Methods

In this chapter, a PBF-LB process computational modelling framework was developed using the general-purpose finite element software ABAQUS (Dassault Systems, USA, 2017) [85, 119, 120]. Firstly, a Python script for ABAQUS was created to section CAD macroscale models in a microscale layer-by-layer manner. The (computational) layer height was predefined by the user. The flowchart of Python code for ABAQUS thermo-mechanical analysis is presented in Figure 3.1. Secondly, heat transfer mechanisms were automatically applied to each layer by the Python script to account for solid part-base plate conduction, solid part-powder conduction, active layer free surface convection and radiation. A computationally efficient approximation to capture the heat loss due to solid

part-powder conduction was developed and applied. This PBF-LB modelling framework was utilised to study the model sensitivities and interdependences described above.

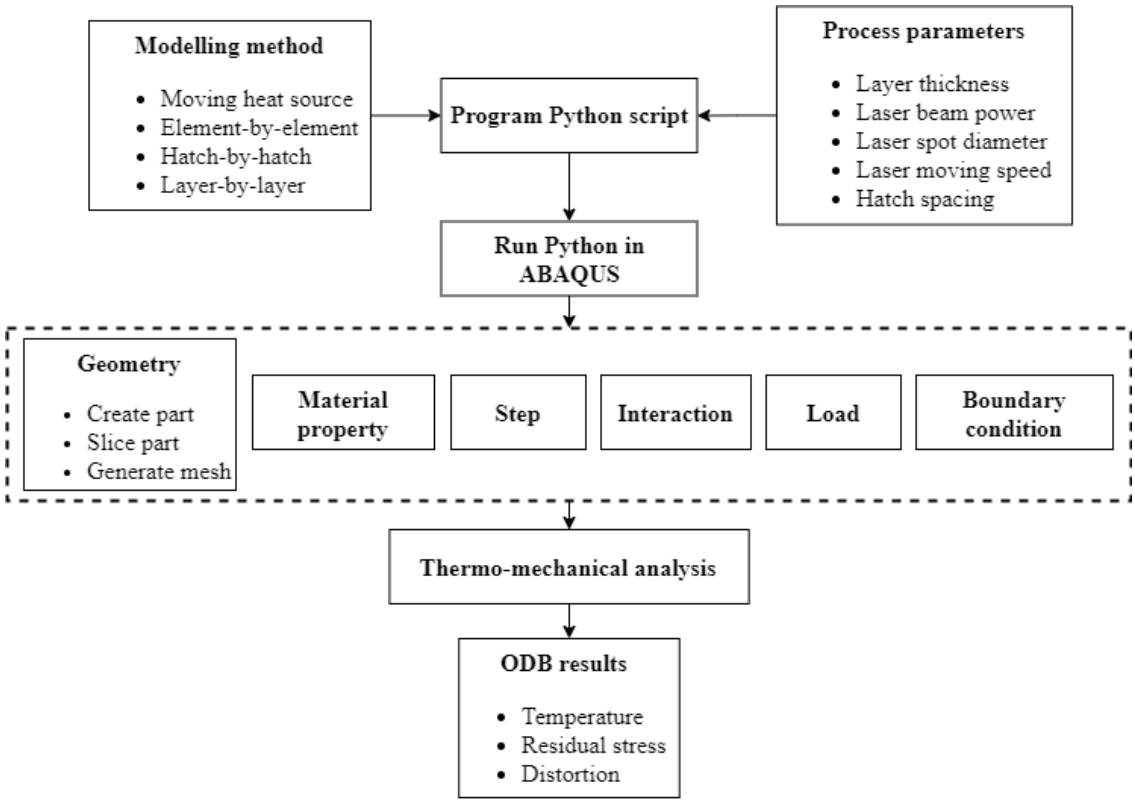

Figure 3.1. Flowchart of Python script for ABAQUS analysis.

3.2.1 Thermal and mechanical analysis

The PBF-LB thermal cycle includes the laser heating and material cooling by heat conduction (Eq. 2.15), radiation (Eq. 2.16) and convection (Eq. 2.17). In this study, the addition of each layer is captured in an individual step, and it begins with the addition of a new active layer (of fixed layer height L_h) and lasts for a total step time of (t_{tot}). A uniformly distributed power density (W/m^3) (Eq. 2.6) is applied to the entire active layer for a fixed heating step time of t_m. The uniformly distributed heat source in this study is determined by the build process parameters such as energy beam power, beam spot diameter and beam moving speed and has been described in Eq. 2.6. The model is then allowed to cool via the heat transfer mechanisms for a fixed cooling step time t_c. The total step time t_{tot} is the sum of the heating step time t_m and cooling step time t_c. After finishing one step, a new step begins to simulate the next new layer. The governing equation for the

thermal analysis is given in Eq. 2.1. The equilibrium for the mechanical analysis has been given in Eq. 2.18.

The laser scanning speed also strongly influences temperature of the target material. Therefore, in computational simulation of PBF-LB, the heating step time over which power density is applied will influence temperature and RS. The heating step time was calculated by dividing the laser spot diameter by the laser scanning speed, as described in Eq. 2.7. For the remainder of this chapter, a laser heating step time of 5×10^{-4} s (Eq. 2.7) and power density of 1.67×10^{13} W/m^3 were applied as the boundary conditions.

The main thermal dissipation mechanisms in PBF-LB are shown in Figure 3.2 and consist of:

i. Conduction (Eq. 2.15) within the solid part;
ii. Conduction between the solid part and the base plate;
iii. Conduction between the part and powder bed;
iv. Convection between the active layer and the surrounding atmosphere;
v. Radiation from the active layer to the surrounding atmosphere.

The relative importance of these thermal mechanisms has been debated in the literature, with thermal conduction varying greatly between solid material and powder (of different porosity) [73, 279]. Some researchers state that the influence of convection and radiation are negligible [279, 280] while others state that these mechanisms must be included [155, 281]. Other studies have stated that the part-powder conduction can be ignored due to the negligible powder thermal conductivity [185, 282, 283]. In the current study, all of the above mechanisms have been accounted for via material properties (i-ii), or surface thermal process definitions (iv-v). In order to remove the requirement of including the powder (i.e. powder finite elements and nodes) in the FEM model, the heat loss due to the conduction processes (iii) is approximated as convection heat loss from the solid part surface to powder bed.

Denlinger et al. [177] showed the importance of incorporating loose powder along with the solid part in FEM of PBF, due to the need to capture the solid part to powder conduction heat transfer. The heat loss profile due to part-powder conduction was first

characterised, by simulating a single layer consisting of a solid region (exposed to a heat flux) and a powder region. The powder region experiences heating due to conduction from the solid part only. In practice, the total heat loss due to this mechanism will depend on the powder in-plane depth, i.e. how densely packed the build volume is with parts, and how close the parts are to the chamber walls. Therefore, a range of powder in-plane depths were simulated (20.5 mm, 41 mm, 102.5 mm, 205 mm, 410 mm, 615 mm) for a 20.5 mm wide solid part (Figure 3.2b), and the temperature at the part-powder interface was monitored.

A new model (Figure 3.2c) was prepared with the powder removed and powder-interface convection was defined at the part surface (formerly the powder-part interface). The convection coefficient was calibrated to produce the same cooling profile as the converged cooling profile (i.e. with powder explicitly included).

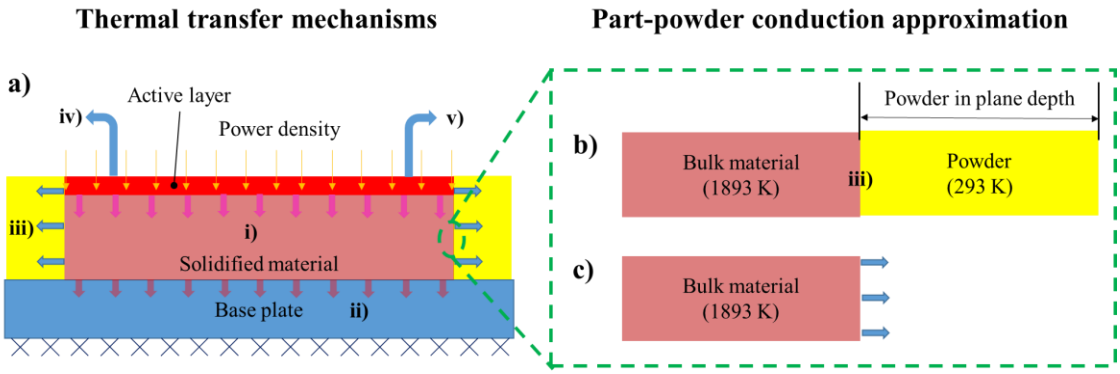

Figure 3.2. Thermal transfer mechanisms and powder in-plane depth research during the PBF-LB process of Ti-6Al-4V: a) Heating by power density, heat losses include: i) Solid conduction, ii) Base plate conduction, iii) Part-powder conduction, iv) Active layer convection and v) Active layer radiation. b) Part-powder conduction requiring bulk material elements and powder elements and c) Equivalent interface convection without including powder elements.

Active layer convection and radiation (Eq. 2.16) and (Eq. 2.17) occur at the top surface of the (newly added) active layer to the surrounding atmosphere. Here, the chamber temperature was 293 K, which was the same with the initial temperature of powder and the characteristic heat transfer coefficient h was found to be 12.7 W/(m^{2}K) with assuming that h is independent of temperature [161]. The emissivity of the active layer surface was set as 0.35 [161] and the Stefan's constant was defined as σ_s = 5.669 ×10^{-8} W/(m^{2}K^4)

[111]. Between two subsequent layers, a layer cooling step time of 10 s was used to model the time needed by the coater to spread the new powder layer [193].

3.2.2 Finite element process modelling

The following basic model configuration was used in all subsequent simulations in this chapter. A simple 54.72 mm high, 41 mm wide block of Ti-6Al-4V material was simulated in 2D plane RS. The structure was built on a fully constrained 5 mm thick Ti-6Al-4V base plate, 7 mm from the edge of the block. Due to the layer-by-layer modelling approach (described in **Chapter 2**) and the symmetry of the 2D model in Figure 3.2a, half of the geometry was modelled to minimise computational cost. Symmetry boundary conditions were specified on the centre line (the yellow line in Figure 3.3). The custom-written Python code based on Etienne and co-authors' research [156] was adapted and programmed to automatically section the macroscale model into microscale layers of predefined thickness and specified a new model step with the associated interactions, boundary conditions and loads for each layer (Figure 3.3).

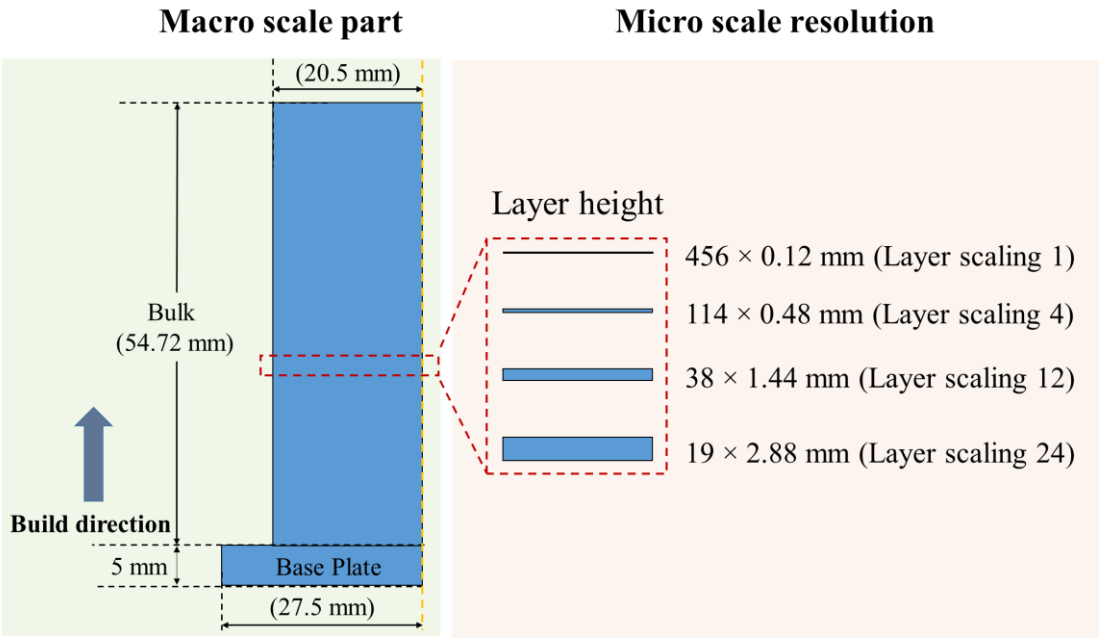

Figure 3.3. Model illustration for macroscale modelling of PBF-LB components at a microscale resolution.

In each step, the new layer was added via ‘model change’ (element birth) in ABAQUS and a power density was applied for the predefined heating step time and allowed to cool for the predefined cooling step time. For the newly added material in this work, the powders were not exactly simulated, and the bulk material properties were applied [157]. The convection approximation for part-powder conduction heat loss (shown in Figure 3.2) was applied to each step, along with surface convection and radiation from the current active layer. The element size was defined in the code as a fraction of the layer height, known as the ‘mesh factor’ (e.g. layer height of 0.48 mm and a mesh factor of 0.5 gives a default element size of 0.24 mm). This provides a facility to determine mesh convergence for each layer scaling. Coupled temperature-displacement elements (type CPE4T) were used. The initial temperatures of both the powder and the base plate were set as 293 K (no preheating) [50, 175]. The complete range of modelling parameters are summarised in Table 3.1. In each simulation, the peak temperature per element, final nodal temperature and final max principal RS were determined.

Table 3.1. Parameters summary for PBF thermo-mechanical analysis [73, 111, 161, 193, 284].

Symbol	Material	Ti-6Al-4V
	Base plate size (m)	0.05472 × 0.005
T_{bp}	Base plate preheats temperature (K)	293
	Powder preheating temperature (K)	293
p	Powder porosity	40.5 %
	Solid size (m)	0.041 × 0.05472
L_h	Layer heights (mm)	Variable: 0.12, 0.48, 1.44, 2.88
m_f	Mesh factors	Variable:1, 0.5, 0.33, 0.2, 0.1, 0.05
t_m	Heating step time each layer (s)	5×10^{-4}
t_c	Cooling step time each layer (s)	10
P	Laser beam power (W)	300
A	Heat source absorption coefficient	0.4
d_s	Heat source spot diameter (mm)	0.6
v_s	Laser moving speed (m/s)	1.2
d_m	Melt pool depth (mm)	0.12
H_s	Hatch spacing (mm)	0.1
Q	Power density (W/m^3)	1.67×10^{13}
ε	Emissivity	0.35
h	Heat transfer coefficient ($W/m^2/K$)	12.7

In this chapter, it was decided that the overall energy input in every model must be the same and equal the total energy input in the real build process under simulation, i.e. that 'energy scaling' is not physically justifiable. Therefore, the following sequence of parameter studies was carried out to investigate layer and time scaling. Similar to layer scaling, time scaling is a technique to modify the real time parameter in the computational model.

i. Determine mesh factor convergence for every layer scaling. This is completed by standard finite element mesh convergence methods where the minimum node spacing required to give a mesh-insensitive solution is determined. The temperature evolution at the central top node (Figure 3.4) was examined in all mesh convergence simulations.

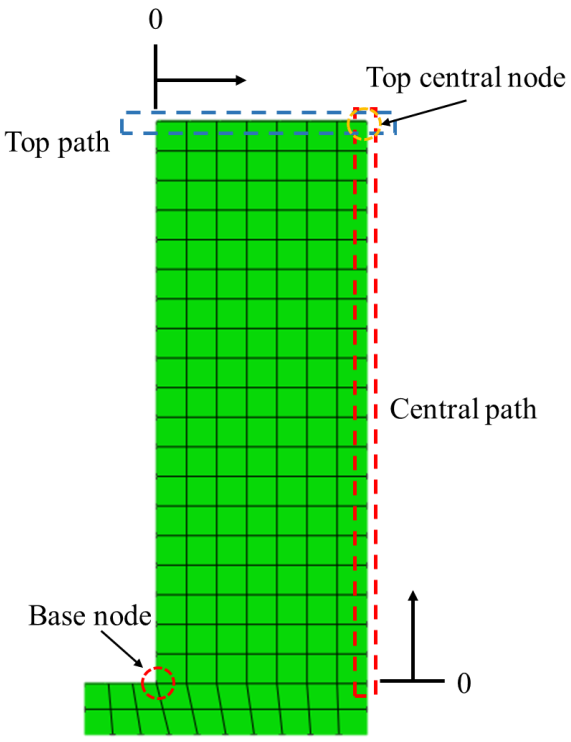

Figure 3.4. Locations illustration for the simulation results.

ii. Determine the effects of heating and cooling step time on temperature and the final RS of part.

In this study, three approaches to linking time scaling to layer scaling were considered and compared to a PBF-LB simulation of the macro-scale part with no layer scaling. In type A, the heating step t_m per layer is constant and is calculated based on Eq. 2.7. In type B, the total heat energy is constant by varying heating time and power density (Eq. 2.6). In type C, the total model cooling time is constant. The simulation process parameters are summarised in Table 3.2.

Table 3.2. Parameters applied for PBF-LB simulations. Note that model 2 and model 5 are identical.

	Model	Layer height (mm)	Layer scaling factor	Layer number	Power density ($\times 10^{12}$ W/m^3)	Heating time per layer ($\times 10^{-3}$ s)	Cooling time per layer (s)	Total cooling time (s)
No layer scaling	1	0.12	1	456	16.7	0.5	10	4560
Layer scaling A	2	0.48	4	114	16.7	0.5	10	1140
	3	1.44	12	38	16.7	0.5	10	380
	4	2.88	24	19	16.7	0.5	10	190
Layer scaling B	5	0.48	4	114	16.7	0.5	10	1140
	6	0.48	4	114	8.35	1.0	10	1140
	7	0.48	4	114	4.175	2.0	10	1140
Layer scaling C	8	0.48	4	114	16.7	0.5	40	4560
	9	1.44	12	38	16.7	0.5	120	4560
	10	2.88	24	19	16.7	0.5	240	4560

3.2.3 Material properties

The material properties were considered to be isotropic and homogeneous. An elastic-perfectly plastic model was assumed. The temperature dependent material properties of solid Ti-6Al-4V were obtained from the literature [115] (Figure 3.5) and were assumed to vary linearly between data points. The base plate was assumed to also be solid Ti-6Al-4V, thus avoiding thermal expansion mismatch with the model [285].

Material definitions for Ti-6Al-4V powder were assumed to be simply related to the solid material properties via powder bulk porosity p [115]:

$$\rho_p = \rho_s(1 - p) \tag{3.1}$$

$$k_p = k_s(1 - p) \tag{3.2}$$

where ρ_p for density of powder Ti-6Al-4V and k_p for temperature dependent thermal conductivity of the powder material. It is also recommend using thermal conductivity of looser powder material from study [125] for AM process modelling. A powder porosity p of 40.5 % was determined based on published powder (2.63 g/cm^3 [284]) and solid (4.42 g/cm^3 [73]) Ti-6Al-4V. Therefore, a porosity p of 40.5 %, thus allowing k_p to be determined based on the temperature dependant k_s. The thermal conductivity of powder Ti-6Al-4V was assumed to equal solid Ti-6Al-4V above the melting point of 1893 K. The

remaining powder thermal properties of specific heat of powders were considered to equal solid properties [119, 286, 287].

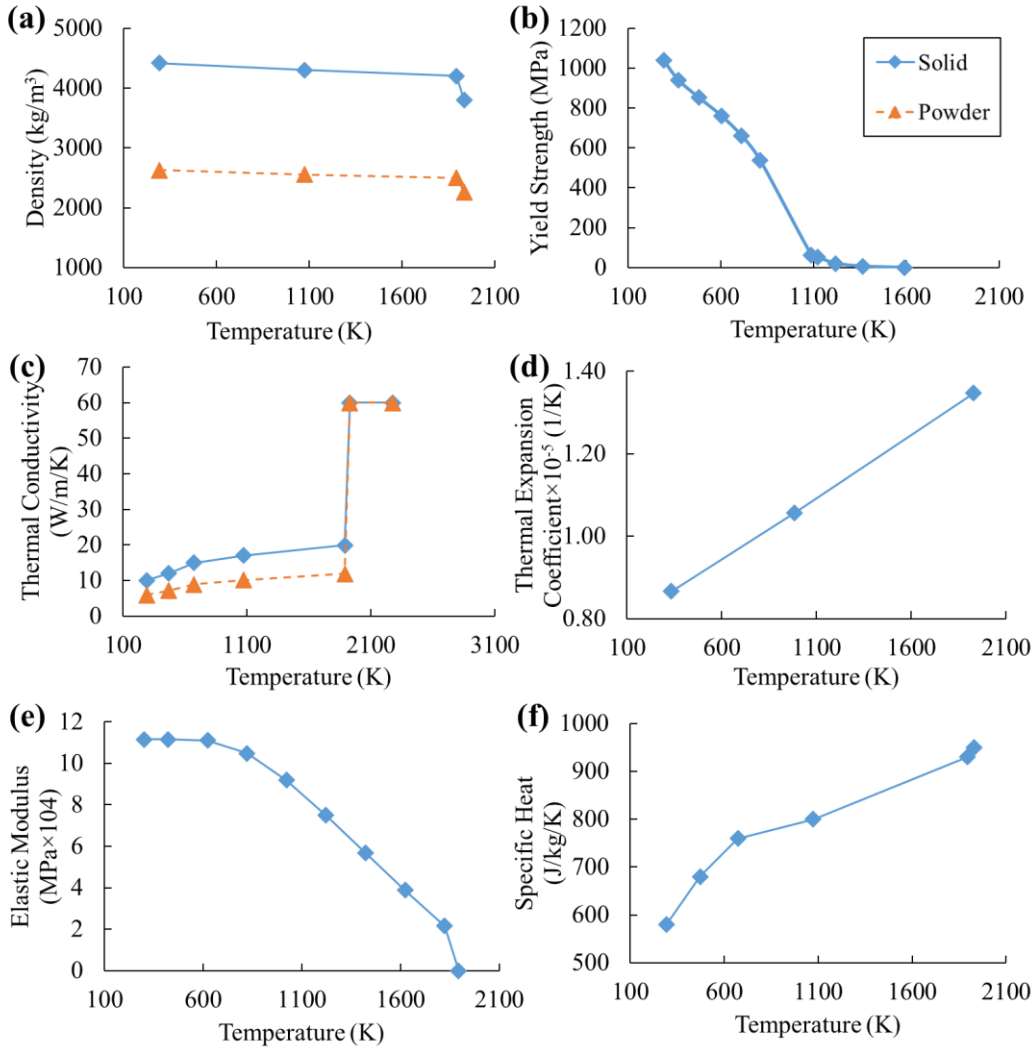

Figure 3.5. Temperature dependent Ti-6Al-4V material properties [115].

3.3 Results and discussions

3.3.1 Part-powder conduction approximation technique and results

Figure 3.6a indicates the cooling rate of part-powder conduction at the powder interface with different powder in-plane depths. In all cases, the temperature initially decreases exponentially, followed by steady state. For this model configuration, the greater the powder in-plane depth, the lower the final temperature, i.e. 600 K and 1350 K interface

temperature for powder in-plane depths of 20.5 mm and 410 mm, respectively. The heat loss rate converges at 205 mm powder in-plane depth, i.e. larger powder-in plane depths have minimal influence on surface temperature.

The time-dependant film coefficient defined for the powder-interface convection model was calibrated to fit the resulting free surface convection cooling curve to the 205 mm powder in plane depth cooling profile (Figure 3.6a). The resulting fit of the convection-based approximation (powder-interface convection) of the conduction-based cooling mechanism (part-powder conduction) is shown in Figure 3.6b. This time-dependant surface convection definition for Ti-6Al-4V could be employed for every layer, in lieu of including (heat conductive) powder elements [149].

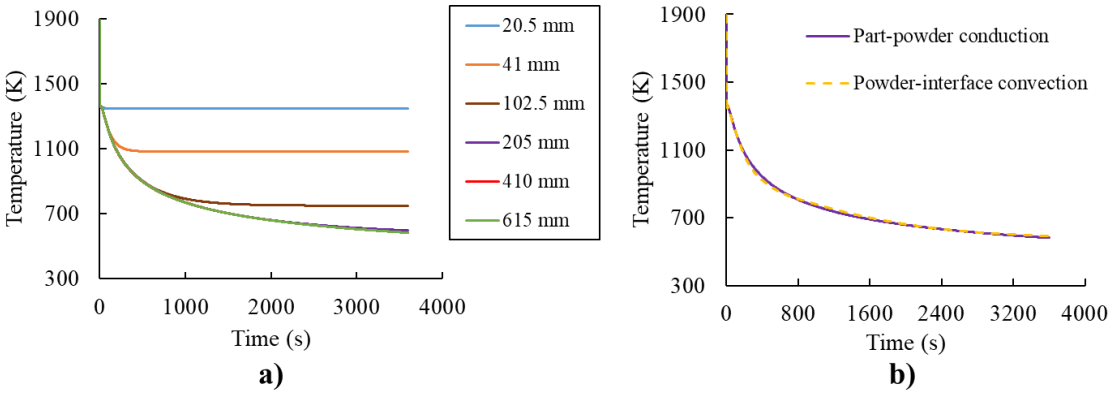

Figure 3.6. Computational modelling results of part-powder thermal loss: a) Ti-6Al-4V powder in-plane depth verification during the part-powder conduction and b) Cooling curves of part-powder conduction and powder-interface convection.

3.3.2 Mesh factor convergence

Mesh factors of 1, 0.5, 0.33, 0.2, 0.1 and 0.05 were tested in the computational modelling. In each model, the largest possible element size is equal to the computational layer height. The power density, heating step time and cooling step time were held constant. Mesh convergence plot for four-layer scaling shown in Figure 3.7 revealing that mesh sensitivity increases with layer scaling.

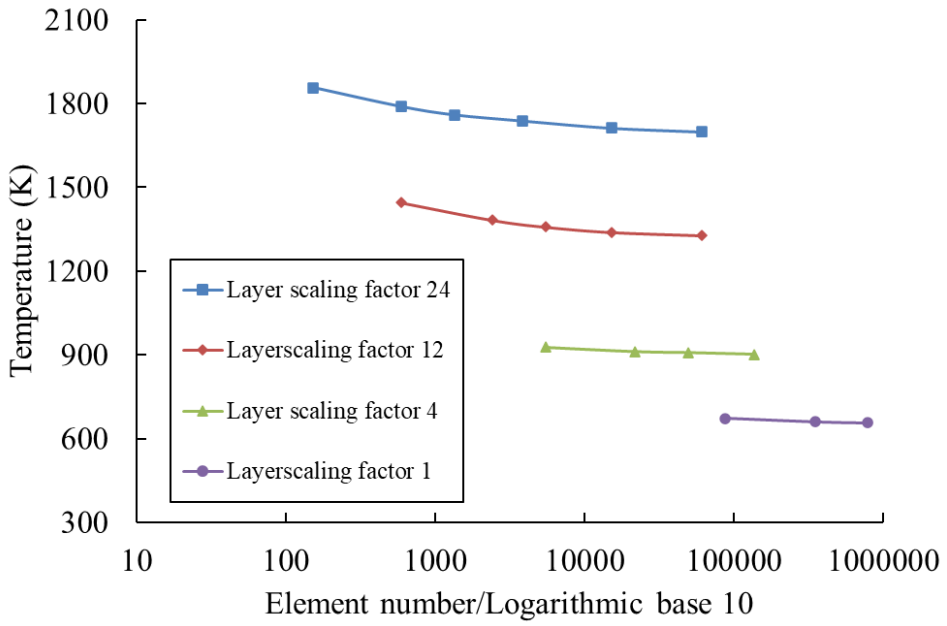

Figure 3.7. Mesh convergence verification for different layer scaling factors (final temperature at the top centre node).

It is also notable that although mesh convergence has been reached in all four-layer scaling models, their final temperature (and RS) solutions differ significantly. Figure 3.8 shows the temperature history and Figure 3.9 shows a local zoom-in of Figure 3.8. It can be seen that all temperature histories follow the same overall trend of two temperature reversals. Figure 3.8 shows the highest temperature occurred when the first layer was added to the base plate, followed by gradual reduction as a small number of subsequent layers are added, followed by a reversal and gradual increase as further layers are added, before a final temperature decrease. This trend is a consequence of competing and saturating energy input, thermal transfer and heat loss mechanisms, also observed elsewhere [288]. A similar substrate temperature trend was also experimentally observed elsewhere [289]. The final base node temperature (mesh converged solution) for the 24, 12, 4 and 1 layer scaling factor models were 942, 739, 627 and 567 K respectively. In addition, the average temperature differential (the temperature difference between one layer and another, measured at the secondary peak of Figure 3.9) for each converged solution was 94, 79, 59 and 38 K, respectively. This highlights the importance of the PBF-LB modelling community thinking beyond mesh convergence when layer scaling is employed. In all

cases, a mesh-converged solution was achieved, but the temperature and RS solutions depended on layer scaling.

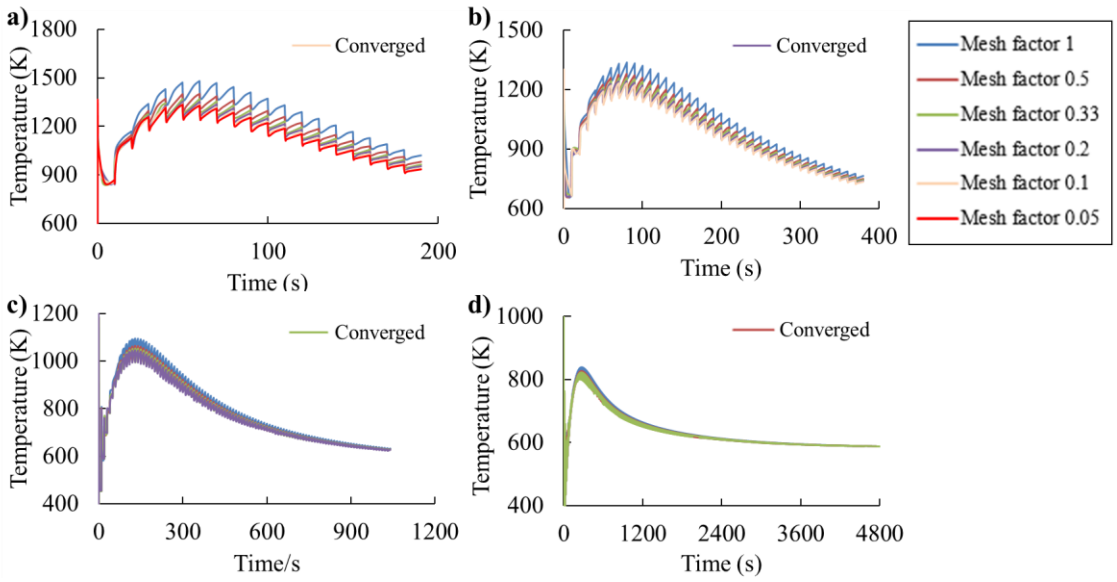

Figure 3.8. Computational temperature variations by time at the base node with different layer scaling factors and mesh factors: a) Layer scaling factor of 24 (2.88 mm). b) 12 (1.44 mm). c) 4 (0.48 mm) and d) 1 (0.12 mm).

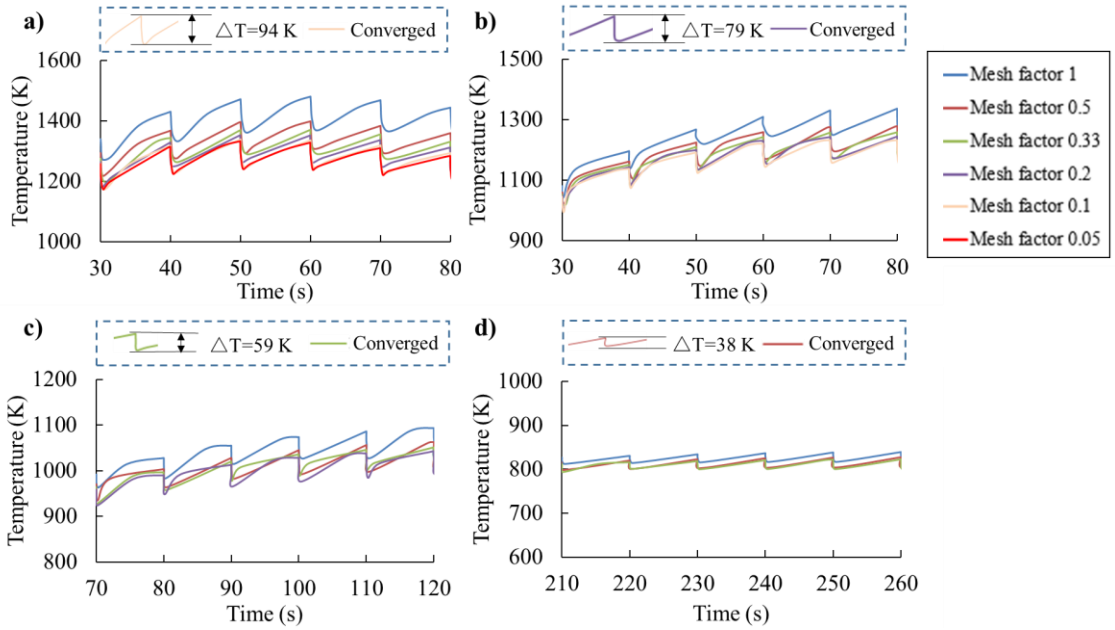

Figure 3.9. Computational temperature variations by time at the base node with different layer scaling factors and mesh factors (magnified pictures): a) Layer scaling factor of 24 (2.88 mm). b) 12 (1.44 mm). c) 4 (0.48 mm) and d) 1 (0.12 mm).

Based on the above mesh convergence studies, the recommend mesh sizes and mesh factors for different layer scaling factors are summarised in Table 3.3. Mesh convergence was achieved when the relative change in temperature obtained by a finer mesh size was less than 1 %. The RS analysis solutions had also converged. The correlation between layer scaling factor (l_f) to the mesh factor (m_f) can be fitted by the exponential equation $l_f = 0.4039{m_f}^{-1.405}$ with a R^2 = 0.9921.

Table 3.3. Layer scaling factors and mesh factors correlation for PBF-LB process modelling.

Model	Layer height (mm)	Layer scaling factor (l_f)	Mesh factor (m_f)	Mesh size (mm)
1	0.12	1	0.5	0.06
2	0.48	4	0.33	0.16
3	1.44	12	0.2	0.288
4	2.88	24	0.1	0.288

3.3.3 Influences of heating, cooling and total step times on temperature and residual stress

Using only the converged mesh resolution solution, Figure 3.10 shows that with increased layer height the final temperature increased significantly, although the same heating time was used for each layer. This is due to the shorter total cooling step time for the larger layer height models. Figure 3.10 also shows a decrease (and greater distribution) in the maximum in-plane stress (all the RS unit in this study is MPa) for the larger layer height models (i.e. using 'layer scaling' method), due to having fewer heating-cooling cycles, and potentially lower temperature gradient, and thus induces a lower RS within manufactured components.

Figure 3.11a illustrates the temperature of the top path (shown in Figure 3.4) with different layer scaling (only converged mesh sizes). The overall trend in temperature is consistent in all layer scaling cases, but it further demonstrates the dependence of final temperatures on layer scaling. Furthermore, the temperature difference increases as layer scaling increased. Figure 3.11b shows the temperature profile along the central axis (shown in Figure 3.4) of the part. In all cases, due to the occurrence of instant convection and

radiation at the topmost surface, the highest temperature occurred at a small distance below the top surface (Figure 3.11b).

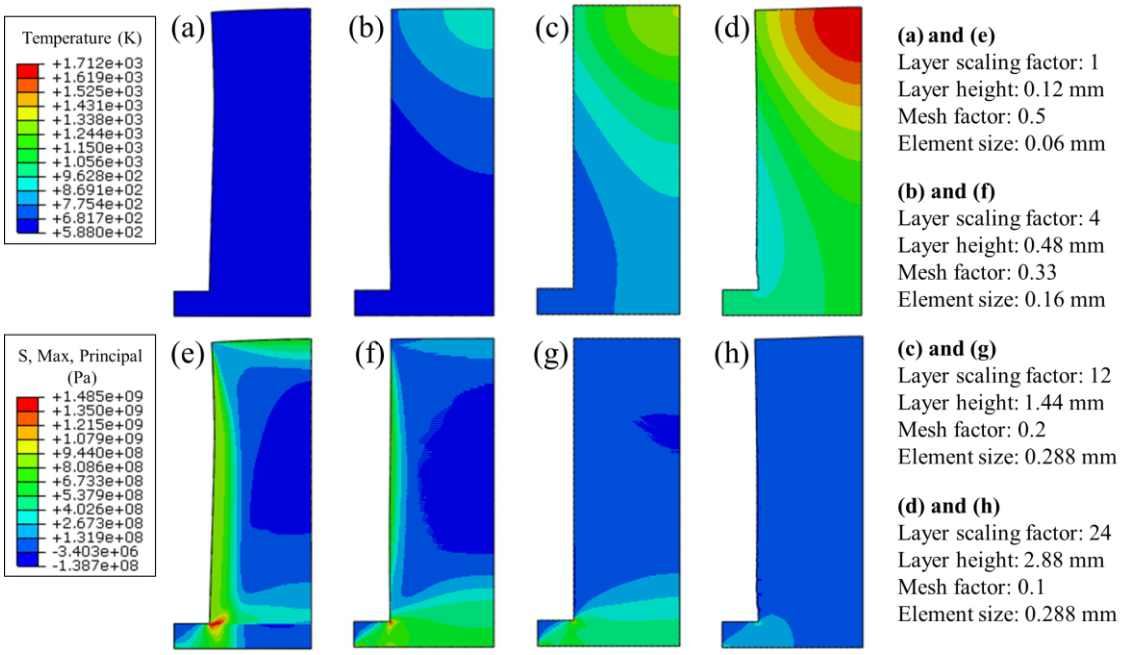

Figure 3.10. Computational modelling results of final temperature and residual stress contours with different layer scaling factors after 10 s of cooling for every layer (Layer scaling A).

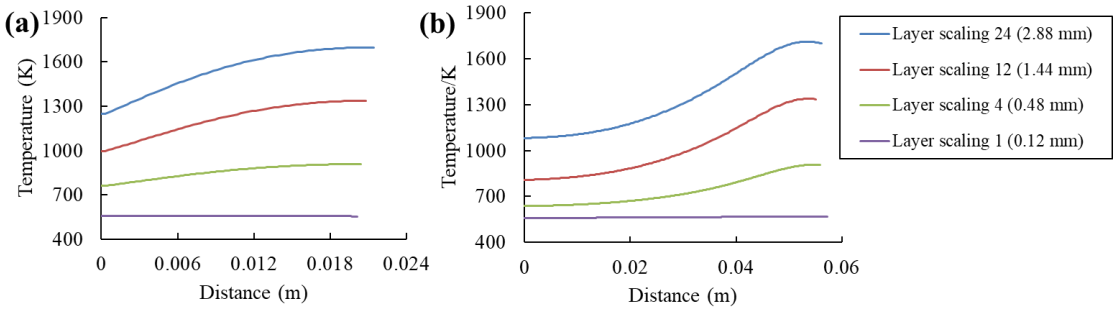

Figure 3.11. The computational final temperature distributions along: a) Top path and b) Central path with relationship of distance under different layer scaling factors.

In layer scaling B (Table 3.2), the influence of the heating step time on the final temperature and Mises stress were found to be insignificant, when keeping the overall energy (product of power density and heating step time) constant, shown in Figure 3.12.

For layer scaling type C (Table 3.2) time layer scaling, the final temperature and maximum in-plane stress on the overall part and temperature evolution with time (Figure 3.14) were

investigated. With the same total time for every layer height, the temperature and RS distributions are much closer to the reference (layer scaling 1). This is the opposite trend to layer scaling A (Figure 3.10). Overall, the differences in temperature between the layer scaling C models are much less than the type A layer scaling models. For the final temperatures, the maximum nodal temperature difference was 20 K between no layer scaling and the layer scaling factor 4 (Figure 3.13a and Figure 3.13b), but temperature by layer scaling factors of 12 (Figure 3.13c) and 24 (Figure 3.13d) was different with that of no layer scaling factor (Figure 3.13a).

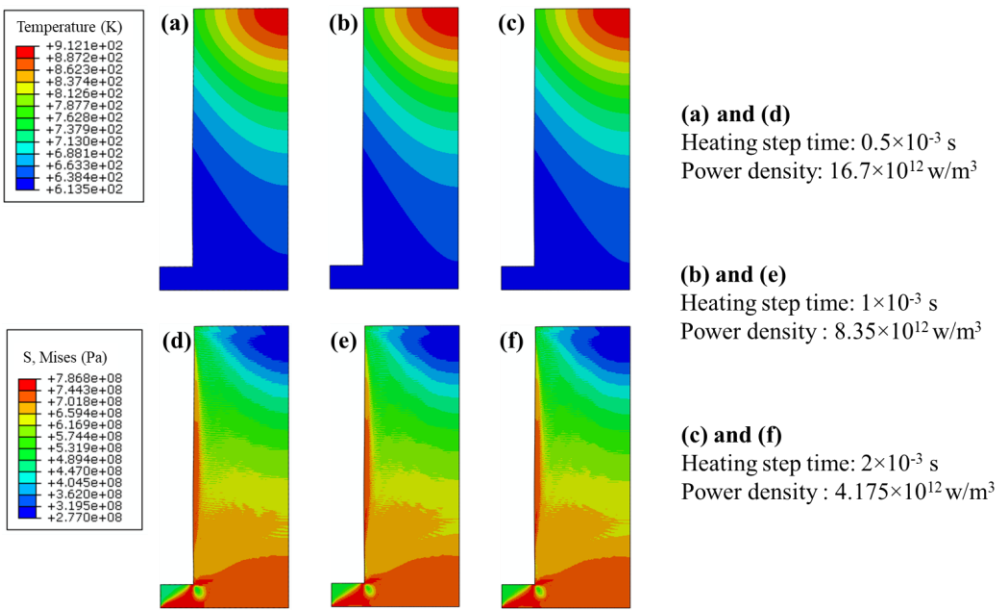

Figure 3.12. The computational modelling results of final temperature and residual stress contours with different heating step times.

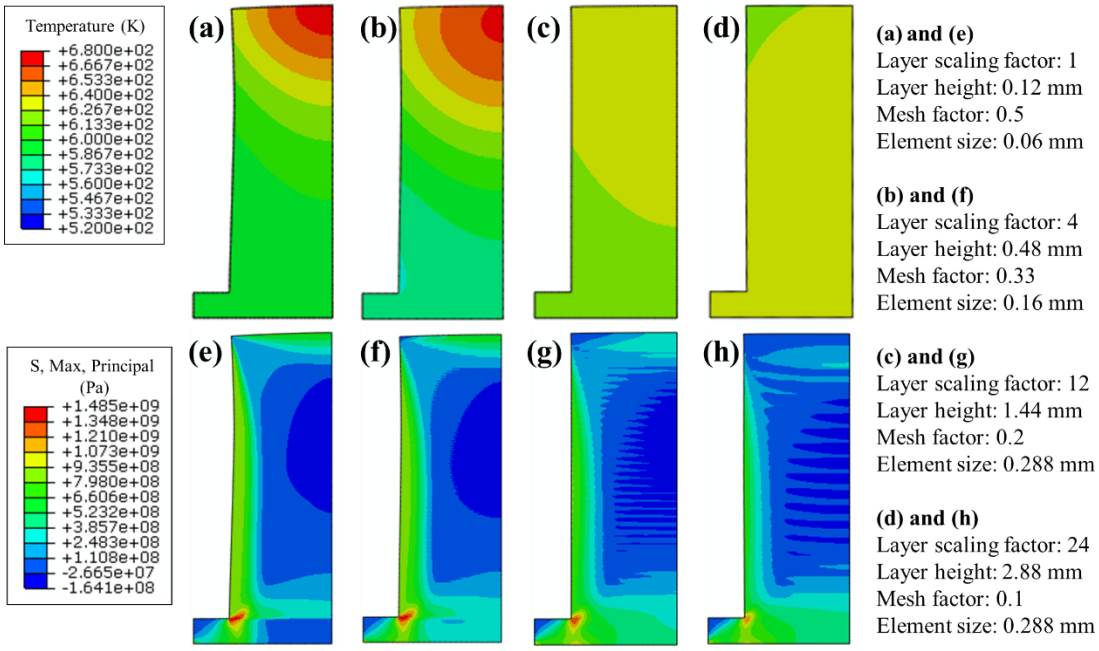

Figure 3.13. Computational final temperature and residual stress contours with different layer scaling factors and scaled layer cooling times to give the same total cooling time after completing manufacturing process and cooling for 10 s.

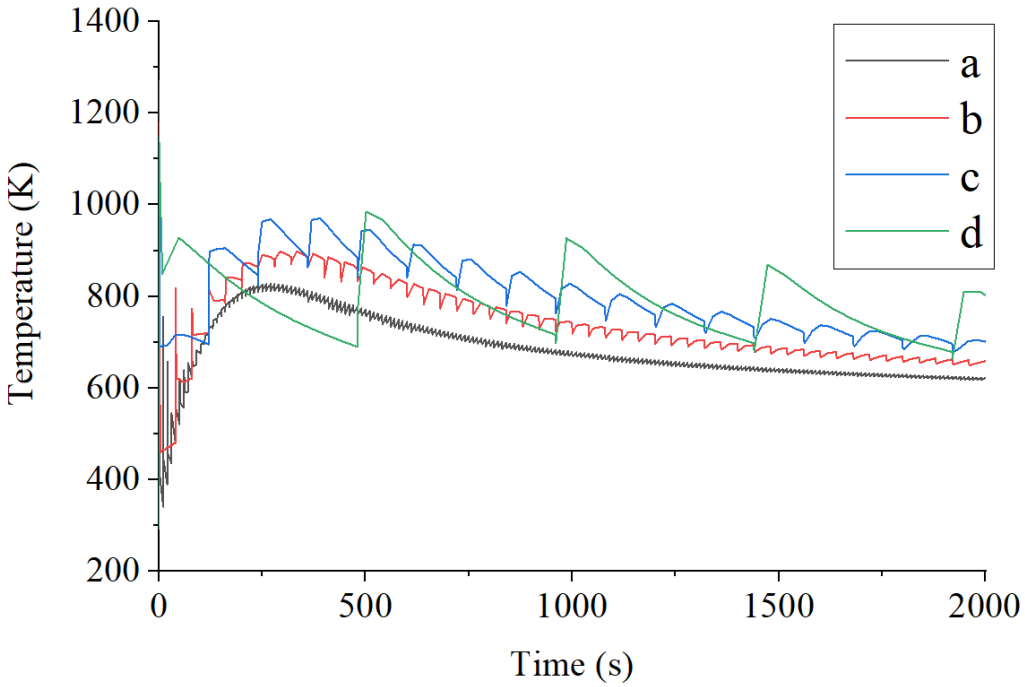

Figure 3.14. Computational temperature variations by time at the base node with different layer scaling factors and scaled layer cooling times to give the same total cooling time: a) Layer scaling factor of 24 (2.88 mm). b) 12 (1.44 mm). c) 4 (0.48 mm) and d) 1 (0.12 mm).

For layer scaling C time layer scaling, the parameters of resolutions, energy and time applied on different layer scaling are summarised on Table 3.4. As seen in Figure 3.13 and Figure 3.14, the results of the layer scaling factor of 4 (0.48 mm) are almost the same as the results of layer scaling factor of 1 (0.12 mm), but with a 95 % saving in total CPU time (Table 3.4). The correlation with the larger layer scaling models (1.44 mm and 2.88 mm) to the primary model (0.12 mm) is comparable for RS (and less so for final temperature), with considerable computational efficiencies obtained.

The cooling time per layer is the dominant factor that influences the final temperature as well as the RS distribution. Denlinger et al. [231] suggests that implementing a cooling step period between each layer can increase the final RS and distortion, and the current work concurs, and this would also negatively impact production rates.

Table 3.4. Summaries of parameters applied on simulations of layer scaling 1 by layer scaling of 4, 12 and 24.

Resolutions				Time		Energy	
Layer height (mm)	Layer scaling factor	Layer number	Mesh size (mm)	Heating step time per layer $\times 10^{-4}$ (s)	Cooling step time per layer (s)	Power density $\times 10^{13}$ (W/m^3)	CPU time (s)
0.12	1	456	0.288	5	10	1.67	1341454
0.48	4	114	0.288	5	40	1.67	62812
1.44	12	38	0.16	5	120	1.67	10881
2.88	24	19	0.06	5	240	1.67	5393

In this current research, significant differences exist in both the temperature and RS distributions for the PBF-LB process simulations with the same process parameters, same overall energy input but with different layer scaling factors. However, the results of real build resolution could be accurately replicated in lower resolution models by incorporating time scaling parameters along with layer scaling, up to a limit of layer scaling factor of 4. Above 4, considerable differences in the final RS and temperature were observed (Figure 3.13). This is caused by the complex temperature cycles and temperature gradient of different layer scaling factors.

3.4 Summary

In summary, a python-based script for the general-purpose FEM solver ABAQUS was developed to section CAD macroscale models in a layer-by-layer manner and define the thermal transfer mechanisms automatically. This tool was then employed to investigate the appropriateness of layer scaling. Model sensitives and key resolution, energy and time interdependencies were identified and characterised. The results of three approaches to time (one with the same cooling time per layer, another with different heat input times per layer but constant total heating, and finally one with different cooling times per layer but the same total cooling time) were compared. It was found that the cooling step time should also be scaled by the layer scaling factor.

In future, this work will lead to rapid modelling capability for AM product designers and manufacturers and may serve in the development of industry standards for PBF-LB process modelling. It may also provide guidance to PBF-LB machine operators for real build parameters.

- Final temperature predictions and temperature trajectories are strongly dependant on layer scaling. For a given layer scaling, the recommended element size should be based on Table 3.4. The final temperature (within 3 % difference) and RS (less than 3.36 % difference at interface of part with base plate) of layer scaling 1 could be obtained by scaling up 4 times the cooling step time under layer scaling 4.
- Cooling step time per layer is the dominant time factor affecting temperature and RS- the heating step time has negligible influence on temperature and RS within layer scaling.
- Powder-solid heat conduction can be approximated as interface surface convection.

4 Computational modelling and experimental validation of residual stress varying scanning strategies in PBF additive manufacturing

4.1 Introduction

In **Chapter 3**, the computationally thermo-mechanical finite element modelling of fundamental feature for macroscale Ti-6Al-4V part by PBF-LB AM was investigated. Experimental measurement of RS is essential for validating the predicted RS in manufactured components. Most existing AM studies are focused on the maximum residual stress in the additively manufactured part [290] or stress profile along specific path, but largely ignore the overall RS distribution on the entire part. As discussed in Section 2.3.3, scanning strategies can significantly affect temperature field and thus influence the resulting RS in additively manufactured parts [41, 195]. In addition, overall part height of the sample can also influence RS of PBF-LB manufactured parts due to resulting number of thermal heating-cooling cycles experienced by each layer during the manufacturing process [118]. However, the part height effect on RS has not been experimentally measured. Most of the existing RS measurements for PBF-LB manufactured parts are performed by destructive methods such as hole drilling, which provides limited accuracy (e.g. ± 50 MPa) [258]. As reviewed in section 2.4, where RS measurement techniques were compared, the non-destructive RS approach (e.g. ND and high energy XRD) has a greater accuracy than destructive methods. But there is limited availability of non-destructive facility worldwide, for instance, ISIS and PSI etc. [275]. The author acknowledges the support from Dr. Wajira Mirihanage and Da Guo at the University of Manchester for experimental sample testing and data analysis. In **Chapter 3**, the computational layer-by-layer modelling method was applied to a 2D macroscale geometry and ignored influences of scanning strategies on RS. In this chapter, the geometry is extended to 3D. By applying the converged solutions considering resolution, energy, and time from **Chapter 3**, the sensitivity of scanning strategy on RS in the single

laser beam PBF-LB is predicted. Parts manufactured for two different geometries and six different scanning strategies were employed for experimental RS measurement.

RS after cooling and before removing from the base plate was investigated in **Chapter 3** by thermo-mechanical process PBF-LB modelling. However, PBF-LB manufactured parts are usually cut from the base plate (e.g. by wire EDM), including experimental measurements of RS before and after deformation. The effect of releasing base plate constraints on RS has not been widely investigated in PBF-LB manufacturing. Therefore, in this work, the influence of releasing the mechanical boundary condition of the base plate on RS was computationally investigated in PBF-LB manufacturing.

The aim of this chapter is to experimentally validate the developed thermo-mechanical model for PBF-LB and investigate scanning strategy influences on RS of additively manufactured Ti-6Al-4V parts. The objectives are as follows:

a) Experimental RS validation of the developed thermo-mechanical coupled finite element prediction model in PBF-LB for macroscale Ti-6Al-4V component.
b) Non-destructive experimental investigation of the influence of scanning strategies of single laser beam PBF-LB on RS.
c) Comparison of computational RS results by different PBF-LB process modelling approaches, such as moving heat source, element-by-element, hatch-by-hatch and layer-by-layer modelling methods.
d) Computationally investigate effect of releasing constraints of the base plate on RS of the manufactured parts in PBF-LB.

4.2 Methods

4.2.1 Computational model configuration

To explore the scanning strategies influence on RS of single laser beam PBF-LB manufactured part, six different scanning strategies (scanning patterns & scanning vectors) devised from [41] are applied as shown in Figure 4.1. The six different scanning strategies are: a) island scanning, b) 0° no rotation scanning, c) 45° rotation scanning, d)

45° rotation and vertical mixed scanning, e) 90° rotation scanning and f) 67° rotation scanning strategy.

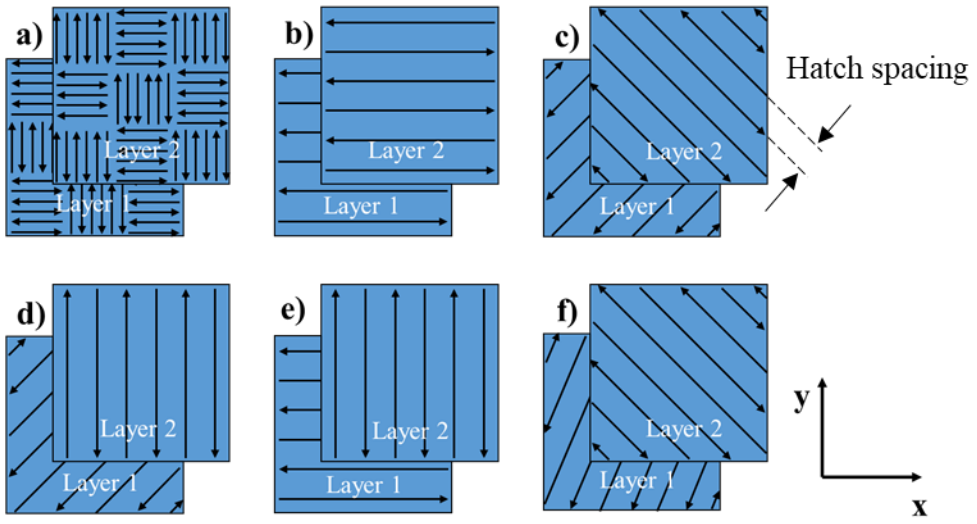

Figure 4.1. Illustration of six different scanning strategies for manufacturing part: a) Island scanning. b) 0° no rotation scanning. c) 45° rotation scanning. d) 45° rotation and vertical mixed scanning. e) 90° rotation scanning and f) 67° rotation scanning. Layer patterns repeat every two layers, for the 25 layers of the 1 mm specimen and 75 layers of the 3 mm specimen. For illustration, the hatch spacing (distance between two adjacent arrows) has been magnified. This figure is adapted from [41].

In this work, PBF-LB process modelling consists of a block of additively manufactured part and a block of build plate, using the general-purpose finite element software ABAQUS (Dassault Systems, USA, 2019), as shown in Figure 4.2a. Two sizes of 3D parts were created: 10 × 10 × 1 mm^3 and 10 × 10 × 3 mm^3. To investigate the influence of scanning strategies on RS, the hatch-by-hatch modelling method were performed for the 1 mm height model (Figure 4.2), which has been described in **Chapter 2**. Considering the computational cost and for comparison purposes, PBF-LB process modelling for the 1 mm and 3 mm models were performed by using the layer-by-layer modelling method that has been described in **Chapter 3**. In **Chapter 3**, 2D macroscale geometry and deposition layers were adopted. However, in order to investigate scanning strategies influences on the directional stresses (σ_{xx} and σ_{yy}), the 3D component and layers were employed for PBF-LB modelling. The layer height for all the computational models was set as 40 µm, corresponding to the practical PBF-LB manufacturing (i.e. no layer scaling). For all the simulations, the bottom of the build plate was fully fixed during the manufacturing process

and the post manufacturing cooling process of part. After the part was cooled to room temperature, the build plate was released (deactivated) instantaneously via the 'model change' function in ABAQUS to allow the deformation of the part [291, 292] without any further heat or energy input. The initial temperature of both the part and the build plate were set as 293 K.

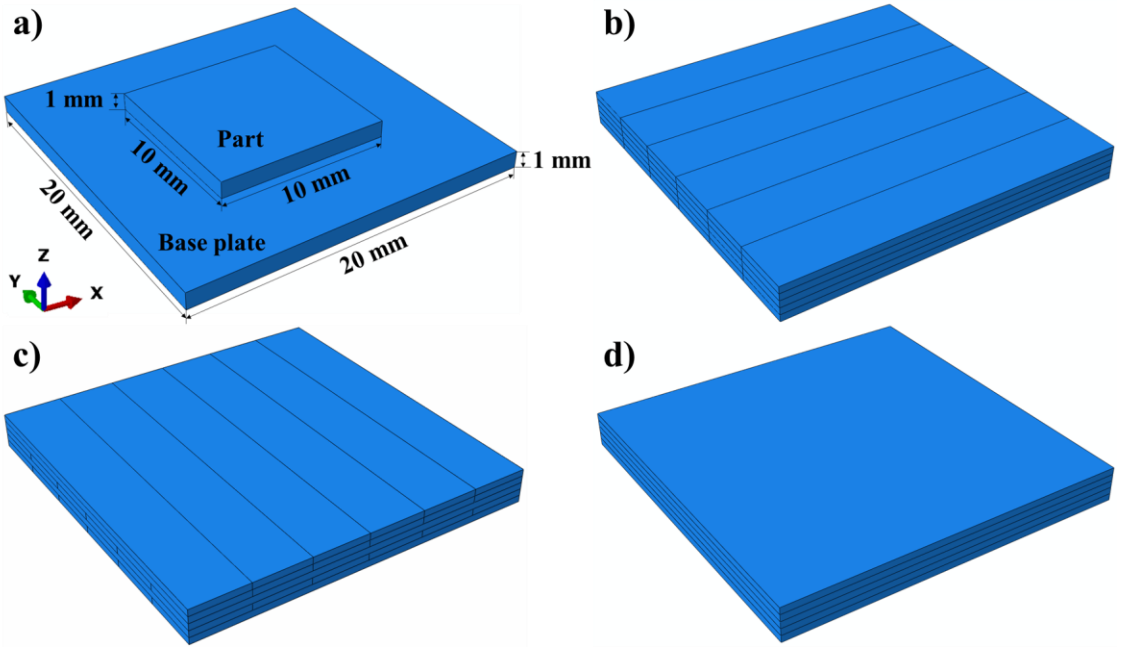

Figure 4.2. Model configuration and illustration of process modelling methods: a) Computational finite element model for PBF-LB. b) 0° hatch-by-hatch method for the 0° no rotation scanning (Figure 4.1b). c) 90° rotation hatch-by-hatch method for the 90° rotation scanning (Figure 4.1e) and d) Layer-by-layer modelling method. For illustration purpose, the layer height of model has been magnified.

To computationally investigate sensitivity of scanning strategies and RS, the hatch-by-hatch PBF modelling method was employed for the 1 mm height specimen. The 0° hatch-by-hatch (illustrated in Figure 4.2b) and 90° rotation hatch-by-hatch (Figure 4.2c) represent the 0° no rotation scanning (Figure 4.1b) and 90° rotation scanning (Figure 4.1e), respectively. To simulate the inclined scanning strategies (i.e. with an inclination angle with respective to the *x* or *y* direction in Figure 4.1) such as 45° rotation scanning (Figure 4.1c), 45° rotation and vertical mixed scanning (Figure 4.1d) and 67° rotation scanning (Figure 4.1f), the staggered hatch-by-hatch modelling method was developed, as illustrated in Figure 4.3. This is because inclining angles exist for two adjacent layers of

these three scanning strategies (Figure 4.1c, d, f) and the cuboid mesh cannot be generated, but it is feasible for the staggered hatch-by-hatch modelling method. A Python script for the layer-by-layer PBF-LB modelling in **Chapter 3** (Figure 3.1) was adapted to the hatch-by-hatch modelling, so that the 3D part could be sliced into separate hatches depending on the hatch size. All the hatches were deactivated at the initial step, and each hatch was activated sequentially by using the 'model change' function described in **Chapter 3**. In the hatch-by-hatch modelling method, all the finite elements of a single hatch were bundled together to heating and solidification simultaneously. Each hatch was heated and melted by the uniformly distributed volumetric heat source (Eq. 2.6) for a heating step time t_m (Eq. 2.7). After finishing the heating process, the active hatch began to cool for a period of cooling step time, which was calculated by the length of hatch divided by the laser beam moving speed. After the manufacturing process was completed, the part began to cool for 6 hours to room temperature. For the convenience of PBF modelling, the hatch size was 10 × 0.4 × 0.04 mm^3 and the element type of 8-node thermally coupled brick (C3D8T) was applied for the hatch-by-hatch modelling.

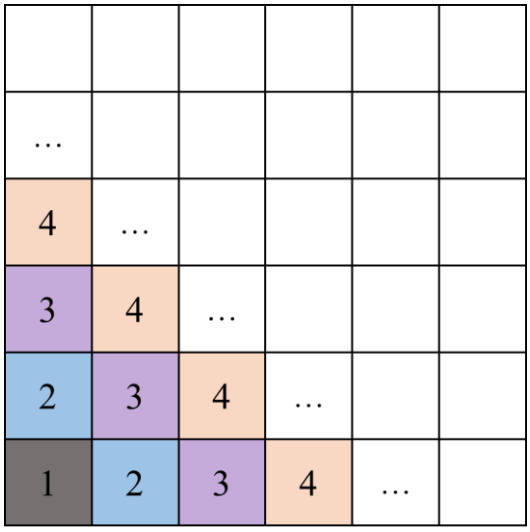

Figure 4.3. Illustration of the staggered hatch-by-hatch process modelling method for PBF-LB.

For the layer-by-layer PBF modelling (Figure 4.2d), which has been described in Section 2.3.3, the commonly used uniformly distributed volumetric power density (described in Eq. 2.6) was applied on each layer for a fixed layer heating time t_m (described in Eq. 2.7). After the material melting process of the active layer, the material was cooled for a fixed

layer cooling time (re-coater time between layers) of 10 s before the next layer was added. It should be noted that, to keep consistency, the total computational cooling time for the hatch-by-hatch and layer-by-layer method remained constant.

To compare the computational cost, the PBF process modelling by using different modelling approaches, such as Gaussian moving heat source method [154], element-by-element method, hatch-by-hatch method and layer-by-layer method (described in **Chapter 2**) were performed and compared on a single layer height model ($10 \times 10 \times 0.04$ mm^3). The volumetric Gaussian distributed heat source (Eq. 2.5) was applied for the moving heat source modelling method, by using the 'S' 0° no rotation scanning (as shown in the first layer of Figure 4.1b). The single element dimension was $0.5 \times 0.1 \times 0.04$ mm^3 for the element-by-element method and the hatch size for hatch-by-hatch method was $10 \times 0.1 \times 0.04$ mm^3. Considering the computational cost for the macroscale component, the mesh size of $0.2 \times 0.2 \times 0.04$ mm^3 (less than 0.1 % stress difference comparing with using a finer mesh) was applied for the PBF-LB modelling. After the manufacturing was finished, the single layer height part was gradually cooled for 2 hours to room temperature.

The thermal transfer mechanisms for PBF-LB process including heat conduction (Eq. 2.15) to the build plate, conduction (Eq. 2.15) from part to powder bed (simplified as part-interface convection, as described in **Chapter 3**), radiation (Eq. 2.16) and convection (Eq. 2.17) from the active layer to the surrounding atmosphere, which have been described in **Chapter 2** and Section 3.2.1.

4.2.2 Material properties for PBF-LB process modelling

The temperature dependent Ti-6Al-4V material properties were applied on both the part and the base plate for the macroscale process PBF-LB model, which have been described in Section 3.2.3 [115, 149, 292]. The temperature dependent and strain dependent plastic property (i.e. yield strength) for Ti-6Al-4V with isotropic hardening law [36] was applied (Figure 4.4), which is original from [250].

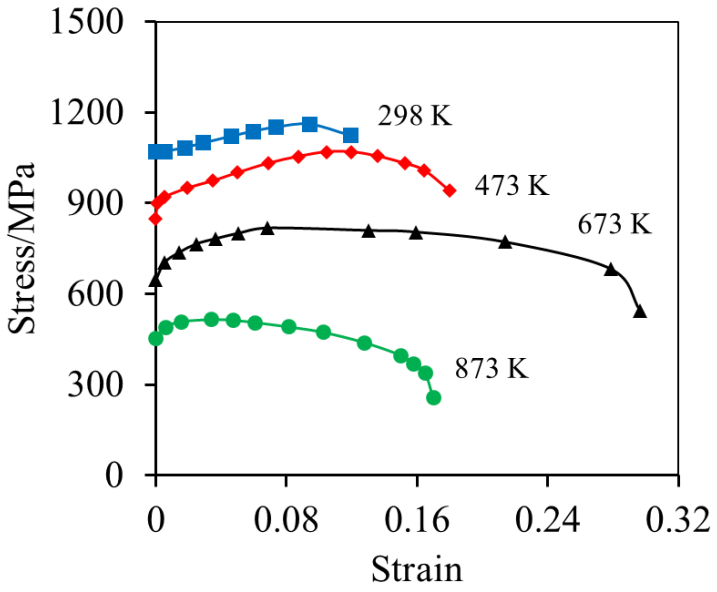

Figure 4.4. Temperature dependent tensile behaviour of Ti-6Al-4V material applied for PBF-LB process modelling [250].

4.2.3 Experimental diffraction method setup and analysis techniques

Six small square plates (10 × 10 × 1 mm^3) and six large square plates (10 × 10 × 3 mm^3) were PBF-LB manufactured in Ti-6Al-4V at Jiangsu Institute of 3D Intelligent Manufacturing (3DIMI), China on an NCL-M2150 printer. After the manufacturing process of part was complete and cooling to room temperature, a wire EDM process was employed to cut the samples from the build plate at 3DIMI. All the samples were printed using the same build process parameters, as shown in Table 4.1.

Table 4.1. Build process parameters for parts manufactured by PBF-LB [293].

Symbol	Process parameters	Value	Unit
	Layer height	0.04	mm
P	Laser power	95	W
R	Laser radius	0.05	mm
v_s	Scanning speed	0.6	m/s
H_s	Hatching space	0.1	mm
	Re-coater time between layers	10	s

RS measurement experiments were carried out by the high energy synchrotron X-ray diffraction facility at Diamond Light Source, UK with the beamline number of I12 (JEEP)

[294] and the 12 samples were sequentially measured. The incident X-ray beam was limited by slots to a size of 1 mm by 1 mm and the beam was moved along the predefined path to fully scan each whole sample in a spot-by-spot way. The applied beam energy was 70.40 keV, and the wavelength of beam was 0.17609 Å, which was recommended by Diamond technical staff for Ti-6Al-4V samples. The corresponding Debye-Scherrer diffraction ring (Figure 4.5a) for each spot was obtained in TIFF format as raw data.

RS was calculated by first converting the grey scale TIFF image to a profile of diffraction signal intensity as a function of wave vector by the open-source DAWN 2.13.0 data analysis workbench developed by the Diamond Light Source. RS was calculated based on the shift of peak diffraction angle compared with the reference (stress-free) value. Gaussian peak fitting function was implemented on MATLAB (Mathworks Inc., USA, R2014a) to find the peak diffraction intensity position for each measurement spot. To get accurate RS results, sectors of 20° from the Debye arcs (Figure 4.5a) were integrated and utilised to calculate the peak position of reflection angle along either the *x* or *y* direction [270]. For instance, 80° to 100° and 260° to 280° (Figure 4.5a) were integrated for the Gaussian peak fitting (Figure 4.5b) and calculation of stress along the *y* direction. Figure 4.5c shows an example (1 mm specimen manufactured by island scanning strategy, Figure 4.1a) of plotting of the integration of raw data with an integration angle of 20° for the diffraction pattern with different lattice planes.

To calculate elastic strain and RS, the stress-free lattice spacing d_{0hkl} (Eq. 2.24) on the specific lattice plane *hkl* is necessary. Maimaitiyili et al. [295] indicated three kinds of techniques that could be used for determining the stress-free lattice spacing: 1) measuring the raw powder used for printing part; 2) Measuring from the corner of each manufactured part and 3) Averaging lattice spacing of each sample. However, another study revealed that the lattice parameters varied with the measurement locations of the same part and differed from each other if manufactured by different process parameters [295]. Therefore, in this work, reflection angles at all the sampling points of each sample that were measured by the high energy X-ray diffraction experiments were averaged [295] and approximated as the stress-free reflection angle. Theory regarding RS calculation process has been introduced from Eq. 2.23 to Eq. 2.29 in **Chapter 2**. Strain and RS at each measurement

spot were calculated by using Hooke's law as shown in Eq. 2.27 to Eq. 2.29. Because of the limitation of I12 (JEEP) beamtime at Diamond Light Source, the specimens were not inclined in order to get σ_{zz} (stress along the build direction) value. Due to the small thickness (along the *z* direction) compared to length and width of sample, RS along the *z* direction σ_{zz} was assumed as 0. Finally, the 2D RS contour, which is the average through sample thickness (Figure 4.6), was plotted by using the programmed MATLAB code. The average through thickness stress indicates the average stress within a small volume (1 × 1 × 1 mm^3 for 1 mm sample and 1 × 1 × 3 mm^3 for the 3 mm sample, corresponding to the practical beam size) of material. The tensile and compressive stress distributions within the samples were not experimentally measured in this work.

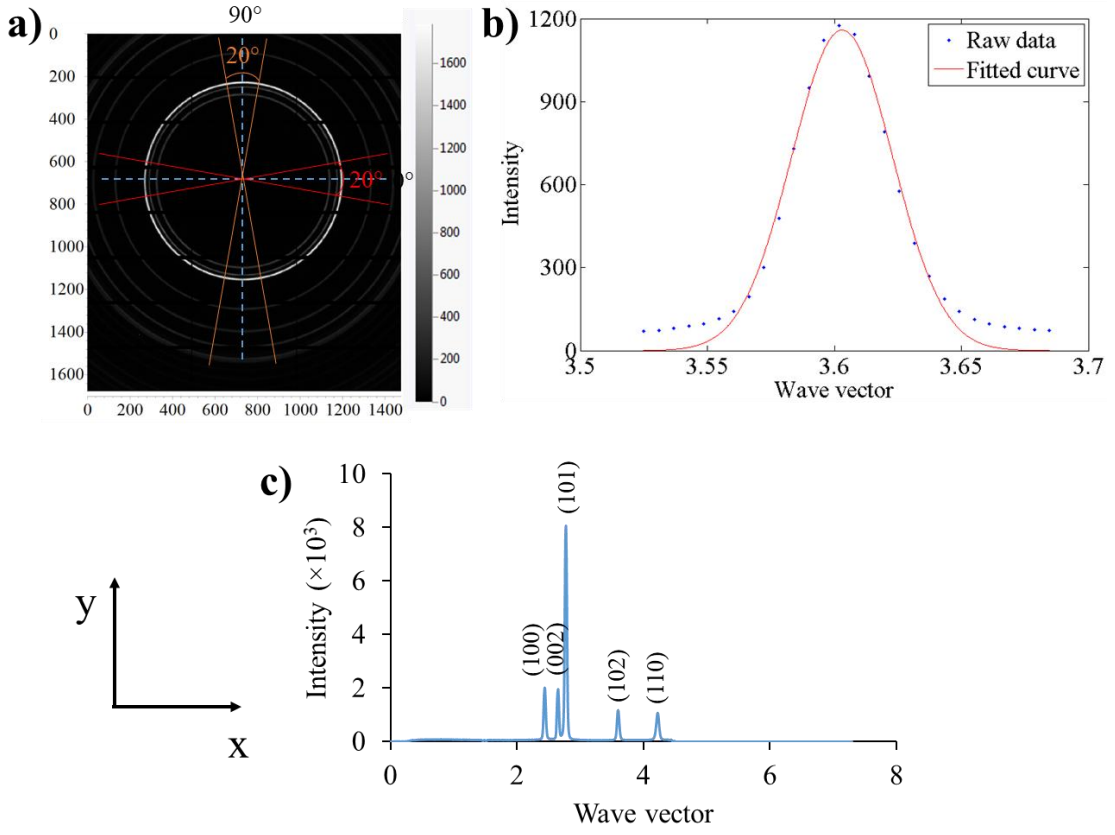

Figure 4.5. Illustration of RS calculation process: a) Raw diffraction pattern. b) Gaussian fitting and c) Plotting of the integration of diffraction pattern taken from 1 mm specimen manufactured by island scanning strategy (Figure 4.1a).

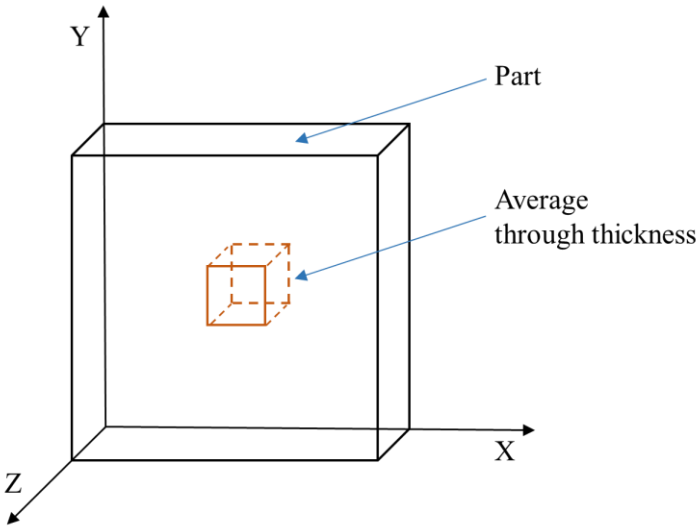

Figure 4.6. Illustration of the average through thickness stress. The average through thickness direction is along the positive Z direction.

Ti-6Al-4V alloy is a two-phase alloy that mainly contains α-phase with the hexagonal close-packed (HCP) structure [296]. At each measurement site, the lattice plane of {102} (Figure 4.5c) was employed for analysis, which is because that the {102} crystallographic plane is only weakly influenced by the crystallographic stress of Ti-6Al-4V. The elastic modulus and Poisson's ratio of Ti-6Al-4V along the {102} lattice plane were set as 121 GPa and 0.31, respectively [250].

4.3 Results and discussions

4.3.1 PBF process modelling for single layer models

Figure 4.7 indicates the computational results of the maximum principal RS distributions for the single layer height model after cooling to room temperature, which was produced by the Gaussian moving heat source, element-by-element, hatch-by-hatch (Figure 4.2b) and (single) layer-by-layer method, respectively. For the Gaussian moving heat source, element-by-element and hatch-by-hatch method, their RS contours at the bottom of the single layer model followed the scanning paths. Figure 4.7 indicates significantly larger area of RS was formed by the layer-by-layer modelling method. For all cases (Figure 4.7), the stresses were predominately tensile, and the maximum tensile stress was ~ 1200 MPa. Figure 4.7 shows RS at the bottom surface of the part (i.e. interface of part and base plate),

which is the highest within the model. This is caused by the highest cooling rate induced by heat conduction from the bottom of the part to the build plate. In addition, before the base plate removal, the cooling and shrinkage of the model is constrained by the base plate at the post manufacturing process [41]. In addition, RS produced by the element-by-element (e.g. 0.5 mm element length) in Figure 4.7b indicates a gradient of RS within each element that RS at the edges of element was lower than at the central area, replicating what is observed on the larger scale entire layer.

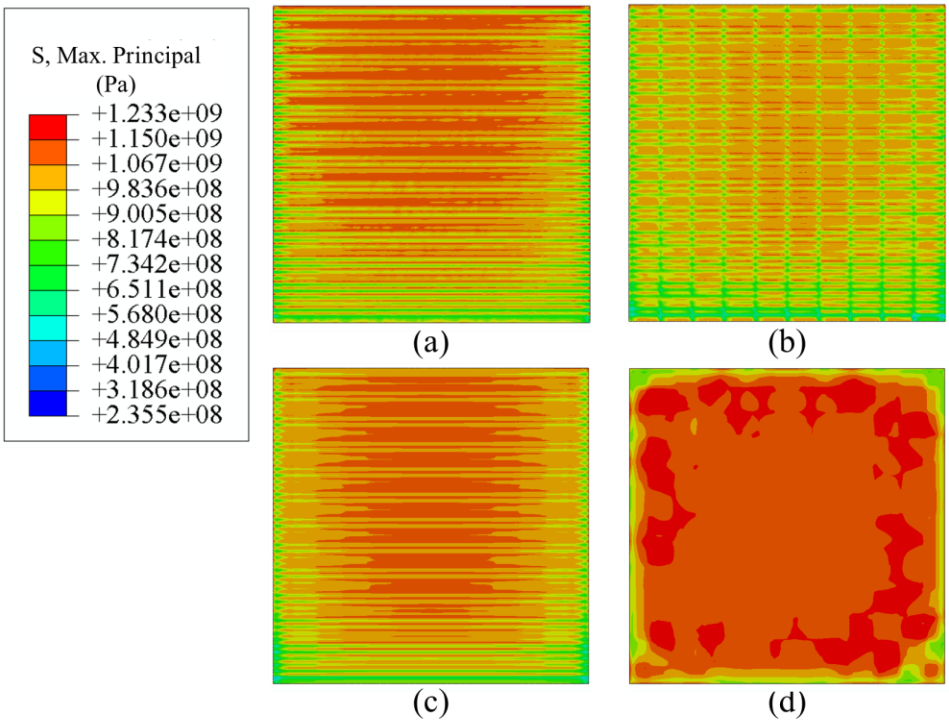

Figure 4.7. Computational RS contours for the single layer height model by different modelling methods at the bottom surface of model: a) Gaussian moving heat source method. b) Element-by-element method. c) Hatch-by-hatch method and d) Layer-by-layer modelling method.

In this chapter, it is assumed that stress produced by the Gaussian moving heat source modelling method is high fidelity and is the most representative of the practical PBF-LB manufacturing. As a uniformly distributed heat source was applied for the element-by-element, hatch-by-hatch and layer-by-layer method, their temperature difference was within 1.73 %, but was 18.68 % lower than the peak temperature of the Gaussian moving heat source (Table 4.2). The volume average stress means the average residual stress within an entire model ($10 \times 10 \times 0.01$ mm^3 in this case). The volume average maximum

principal stress over the entire single layer model by the element-by-element, hatch-by-hatch and layer-by-layer modelling method was 1.42 %, 9.46 % and 15.97 % lower than that of the Gaussian moving heat source, respectively. This is because the more uniformity distribution of the heat source, the lower average stress of model resulted.

Note that both the Gaussian moving heat source and element-by-element methods required a long computational time (Table 4.2). The moving heat source method uses 2 steps (within which the laser path is defined by the DFLUX subroutine) (1920 CPU hours) while the element-by-element method applies 1000 steps for heating and manufacturing of the single layer model (2400 CPU hours). Both models use the same number of elements; however, each additional step in a solution process adds a time and memory overhead cost. Due to the computational cost per layer (requiring a solution increment for minute movement of the gaussian heat profile within the layer), it is not feasible to use the Gaussian moving heat source or the element-by-element modelling method to model macroscale (multi-layer) PBF-LB models in this study. The hatch-by-hatch approach is employed due to: 1) its computational cost is 6.88 % of the Gaussian moving heat source method and it could simulate different scanning strategies, as have been reviewed in **Chapter 2**) The difference of the average maximum principal stress between Gaussian heat source and hatch-by-hatch methods is within 9.46 % (Table 4.2). In addition, the maximum principal stress by the layer-by-layer modelling method is 8.25 % higher than that of the Gaussian heat source method. Therefore, the computationally - efficient method of layer-by-layer modelling method was utilised for the 3 mm height macroscale part PBF-LB process modelling.

Table 4.2. Comparison of different modelling approaches for a single layer model.

Modelling method	Steps	Increments	CPU hours	Peak temperature (K)	Peak Max principal stress (MPa)	Average Max principal stress (MPa)
Gaussian heat source	2	34746	1920	3325	1236	983
Element-by-element	1000	7255	2400	2668	1162	969
Hatch-by-hatch	100	736	132	2704	1176	890
Layer-by-layer	2	33	12	2715	1338	826

4.3.2 PBF process modelling for model varying scanning strategies

As the high energy X-ray diffraction facility produced raw data of the Debye arcs is 2D format, as shown in Figure 4.5a, only the directional σ_{xx} and σ_{yy} stresses were calculated. Therefore, the corresponding computational σ_{xx} and σ_{yy} was investigated in this chapter. The computational results of σ_{xx} stress contour for the 1 mm height sample after cooling to room temperature and before base plate removal by using different hatch-by-hatch scanning strategies and layer-by-layer modelling method is shown in Figure 4.8a-e. Figure 4.8f shows the computational results of σ_{xx} stress contour for the 3 mm height sample by using the layer-by-layer modelling method. For all the modelling cases, the σ_{xx} stress at the central area of part was tensile stress while compressive stress occurred at the edges of model, which is consistent with results of studies [193, 297]. It is interesting to find that the σ_{xx} stress of part is mainly in tensile status, for both the 1 mm and 3 mm height models, which is because the shrinkage of the part is constrained by the base plate at the post manufacturing cooling process. The largest σ_{xx} stress occurred at the bottom of all models, i.e. at the interface of the part with the base plate. The layer-by-layer modelling method (Figure 4.8e) could approximately obtain the similar σ_{xx} RS contour with that of the 0° no rotation scanning (Figure 4.8b). Significantly lower σ_{xx} stress was obtained for the 90° rotation scanning (Figure 4.8d) than the 0° no rotation scanning (Figure 4.8b). This is because all the hatches for the 0° no rotation scanning modelling were along the *x* direction, while there was a 90° rotation for adjacent layers in the 90° rotation scanning (i.e. hatches were along the *x* direction for the odd number of layers and along the *y* direction for the even number of layers). At the central area of the model, the maximum tensile σ_{xx} stress decreased from the 1 mm height model (Figure 4.8e) to the 3 mm height model (Figure 4.8f) and a larger area of compressive stress was formed at the edges of 3 mm height part. This is induced by the part shrinking inwards, relieving stress, and is a

result of the base plate having a less significant constraint on the thicker (3 mm) plate compared to the 1 mm height plate [298].

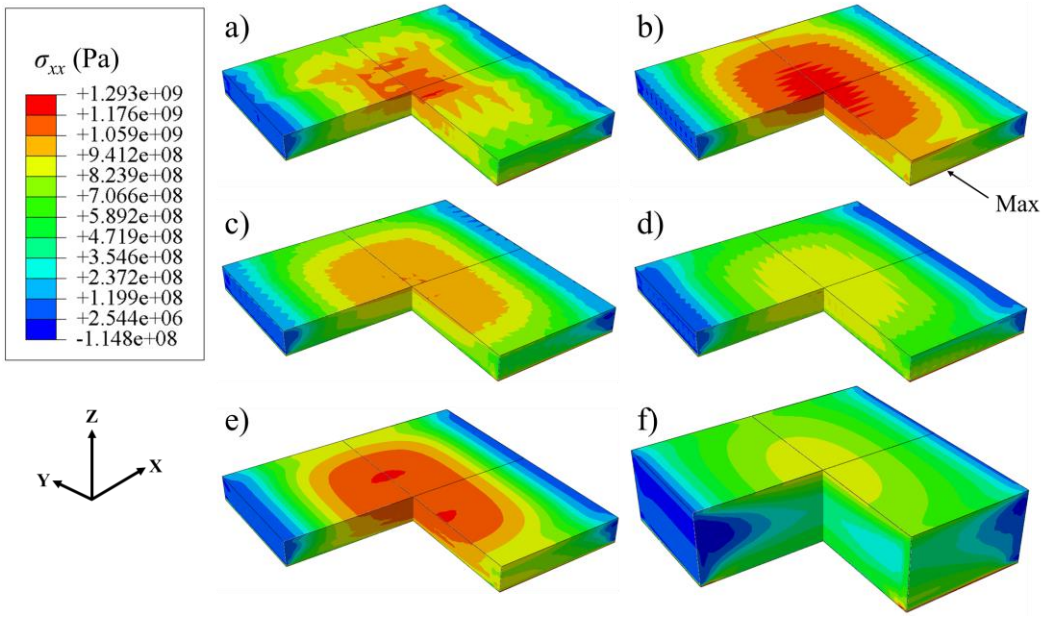

Figure 4.8. Computational results of σ_{xx} stress contour after cooling to room temperature and before removing base plate with different modelling approaches and model heights: a) Island scanning. b) 0° no rotation scanning. c) 45° rotation and vertical mixed scanning. d) 90° rotation scanning strategy. e) Layer-by-layer method for 1 mm height model and f) Layer-by-layer method for 3 mm height model.

Figure 4.9 indicates the computational results of σ_{yy} stress by using different modelling approaches and model heights before removing constraints of the base plate. It can be seen from Figure 4.9 that scanning strategy influences the σ_{yy} stress contours that significantly higher σ_{yy} stress was occurred at the 90° rotation scanning (Figure 4.9d) than the 0° no rotation scanning (Figure 4.9b), due to the 90° rotation of the hatches between two adjacent deposition layers. This result is with a good agreement with other PBF-LB study [41]. The island scanning strategy (Figure 4.9a) produced σ_{yy} was higher than that of the 0° no rotation scanning (Figure 4.9b) and 45° rotation and vertical mixed scanning (Figure 4.9c), which is caused by the energy concentration in the individual island (Figure 4.1a) [41]. The layer-by-layer modelling method (Figure 4.9e) obtained similar σ_{yy} stress contour and magnitude with that of the 90° rotation hatch-by-hatch method (Figure 4.9d). Figure 4.9 further reveals the σ_{yy} RS was higher along the direction of scanning paths [193]. Comparing RS predicted by using the layer-by-layer method for both the 1 mm

height (Figure 4.9e) and 3 mm height (Figure 4.9f) parts, more uniformity of σ_{yy} distribution was formed at the 3 mm height model, which is caused by the heat accumulation induced lower temperature gradient with increasing of the printing height.

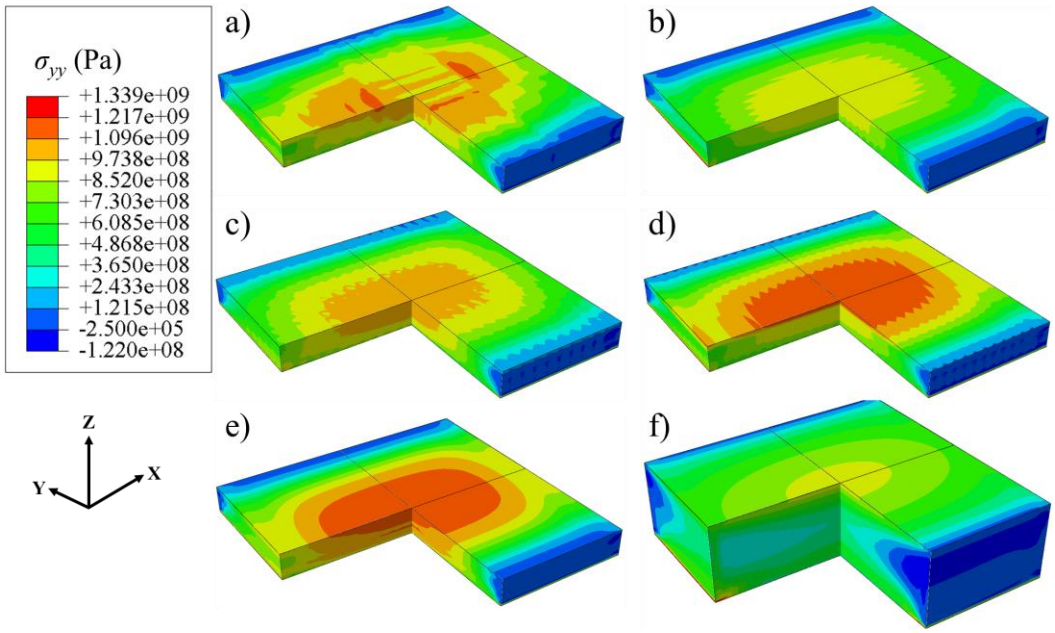

Figure 4.9. Computational results of σ_{yy} stress contour after cooling to room temperature and before removing base plate with different modelling approaches and model heights: a) Island scanning. b) 0° no rotation scanning. c) 45° rotation and vertical mixed scanning. d) 90° rotation scanning strategy. e) Layer-by-layer method for 1 mm height model and f) Layer-by-layer method for 3 mm height model.

To compare with stress before base plate removal, residual stress of part after releasing constraints of the base plate was also computationally investigated. Figure 4.10 indicates the computational results of σ_{xx} stress for the 1 mm height sample (Figure 4.10a-e) and 3 mm height sample (Figure 4.10f) after base plate removal, respectively. Figure 4.10a-d means σ_{xx} stress produced by different scanning strategies. σ_{xx} stress along the horizontal path (Figure 4.10) at the top surface of part is shown in Figure 4.11. Comparing RS before (Figure 4.8) and after (Figure 4.10) base plate removal, σ_{xx} RS field varied, and stress magnitude decreased significantly (e.g. ~ 350 MPa reduction at the bottom surface of part by 0° no rotation scanning) after removing the base plate due to stress release induced by no constraint by the base plate. As the manufactured part was removed from the base plate by wire EDM for experimental stress measurement, the RS after removing the base plate is used thereafter. At the top surface of sample, ~ 100 MPa larger σ_{xx} stress was formed at

0° no rotation scanning (Figure 4.10b) than the 90° rotation scanning (Figure 4.10d), which is consistent with σ_{xx} stress before base plate removal (Figure 4.8).

It is interesting to find that both tensile and compressive stresses were formed at the top surface of part that was manufactured by the island scanning strategy (Figure 4.10a and Figure 4.11a), this is induced by the 90° rotation of scanning between adjacent islands (Figure 4.1a). The layer-by-layer modelling method (Figure 4.10e) could accurately capture the σ_{xx} stress distribution of the 0° no rotation scanning (Figure 4.10b) after base plate removal, which is consistent with results before removing the base plate. Comparing with RS contour for the 1 mm height part by using the layer-by-layer modelling method (Figure 4.10e and Figure 4.11e), more compressive stress was observed in the central area for the 3 mm height part (Figure 4.10f and Figure 4.11f) while tensile σ_{xx} stress was found at the top and bottom surfaces of the 3 mm height part, i.e. the maximum compressive stress for the 1 height model and 3 mm height model at the central area was ~ 80 MPa and ~ 277 MPa, respectively. The predicted stress contour is in line with study elsewhere [149]. The tensile stress occurred at the top surface of the 3 mm height model was because the shrinkage of material at the top surface of part was constrained by the underlying solidified part during the final post manufacturing cooling process. The larger size sample (i.e. 3 mm height) had a greater shrinkage than the 1 mm height sample, which resulted in a higher RS on the manufactured part [299].

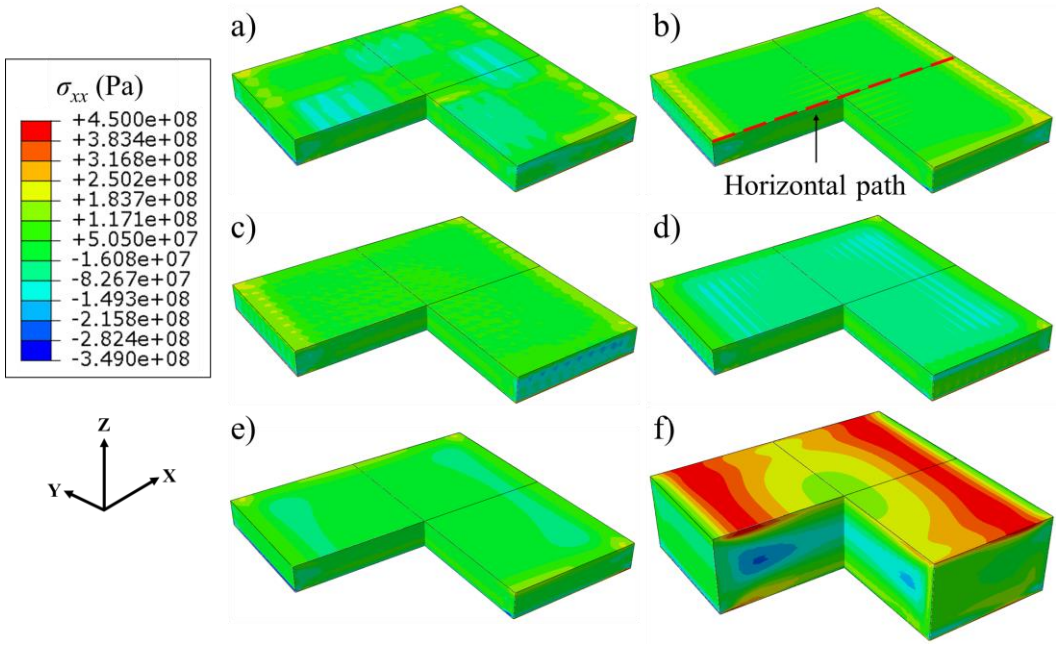

Figure 4.10. Computational results of σ_{xx} stress contour after removing base plate with different modelling approaches and model heights: a) Island scanning. b) 0° no rotation scanning. c) 45° rotation and vertical mixed scanning. d) 90° rotation scanning strategy. e) Layer-by-layer method for 1 mm height model and f) Layer-by-layer method for 3 mm height model.

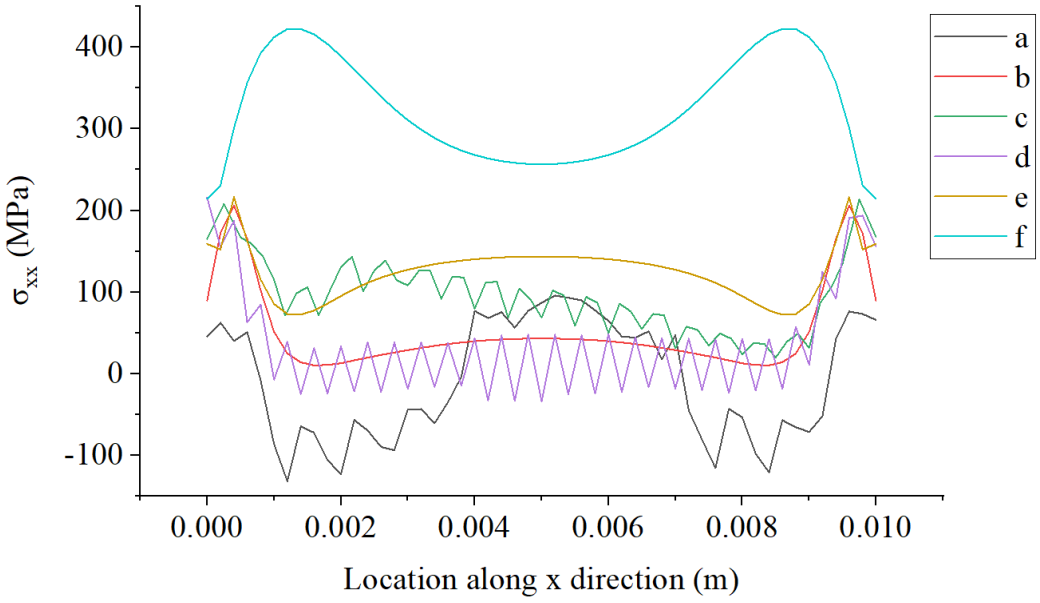

Figure 4.11. Computational results of σ_{xx} stress along the horizontal path (Figure 4.10) at top surface of the part after removing the base plate with different modelling approaches and model heights: a) Island scanning. b) 0° no rotation scanning. c) 45° rotation and vertical mixed scanning. d) 90° rotation scanning strategy. e) Layer-by-layer method for 1 mm height model and f) Layer-by-layer method for 3 mm height model.

The computational results of σ_{yy} contour for island scanning, 0° no rotation scanning, 45° rotation and vertical mixed scanning, 90° rotation scanning and layer-by-layer modelling methods for 1 mm height sample, after removing mechanical constraints of the base plate, is shown in Figure 4.12a-e, respectively. The 90° rotation scanning (Figure 4.12d) shows a higher σ_{yy} stress than the 0° no rotation scanning (Figure 4.12b), especially at the top surface of the manufactured part, due to the 90° rotation between adjacent deposition layers. This is consistent with the results before removing the base plate (Figure 4.9), but with a lower magnitude of σ_{yy} stress due to the stress relaxation. The island scanning strategy (Figure 4.12a) revealed tensile and compressive mixed σ_{yy} stress at the top surface of part, which indicates the scanning strategy has a significant influence on the surface σ_{yy} stress of PBF-LB part. Figure 4.12 reveals less uniform stress distribution was obtained for the 3 mm height model (Figure 4.12f) than the 1 mm height sample (Figure 4.12a-e), i.e. higher tensile stress at the top surface and higher compressive stress at the central area of part. The σ_{yy} stress distribution along the height direction of part is consistent with study [131].

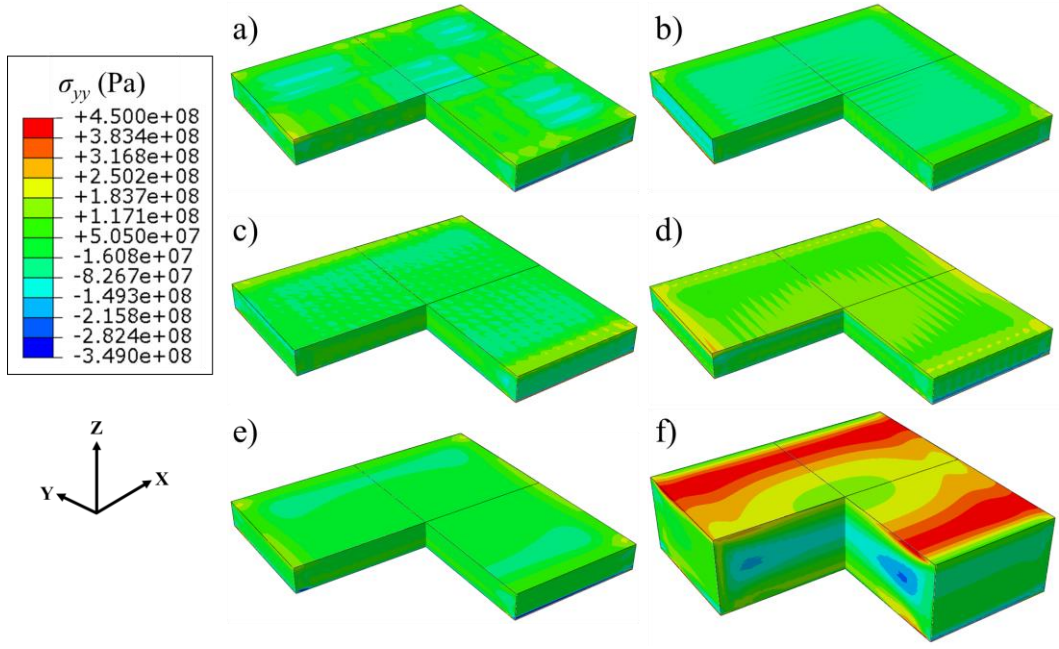

Figure 4.12. Computational results of σ_{yy} stress contour after removing base plate with different modelling approaches and model heights: a) Island scanning. b) 0° no rotation scanning. c) 45° rotation and vertical mixed scanning. d) 90° rotation scanning strategy. e) Layer-by-layer method for 1 mm height model and f) Layer-by-layer method for 3 mm height model.

Figure 4.13 shows the computational results of σ_{zz} stress (along the z direction) contour produced by different scanning strategies for 1 mm height part (Figure 4.13a-e) and 3 mm height part (Figure 4.13f), respectively. The tensile σ_{zz} stress was formed at the side surface of part while compressive stress occurred at the interior of part. This is because that the part shrinkages inward and downwards at the final cooling process during post manufacturing [300]. The same σ_{zz} stress distribution was also predicted by [131]. The σ_{zz} stress for the 1 mm height model (Figure 4.13a-e) is at a low level of magnitude, i.e. lower than 100 MPa. In addition, there is a minor difference of σ_{zz} stress between different scanning strategies for the 1 mm part modelling, due to the thin structure of part. It should be noted that there was a significantly increase of the σ_{zz} stress at the side surface of the 3 mm heigh part than the 1 mm height model. The increase of the maximum stress with the printing height has also been reported in [118]. For the 1 mm height model, its expansion and contraction are mainly constrained by the base plate. While the expansion and contraction of the material at the upper location of the 3 mm height model are mainly constrained by the underlying solidified material [298], which results higher and more area of compressive stress at the 3 mm height model.

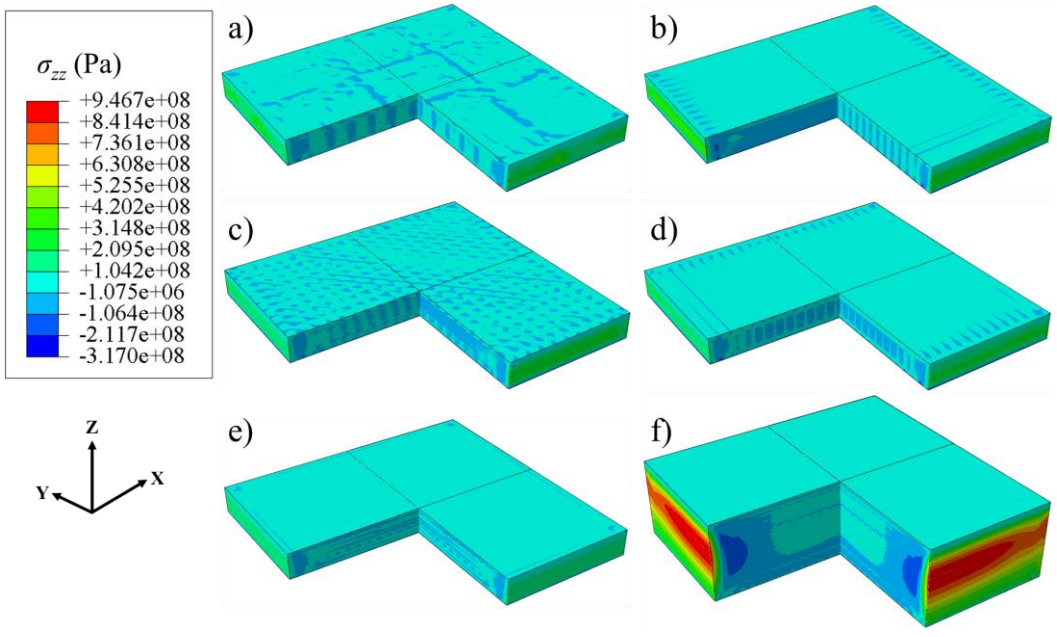

Figure 4.13. Computational results of σ_{zz} stress contour after removing base plate with different modelling approaches and model heights: a) Island scanning. b) 0° no rotation scanning. c) 45° rotation and vertical mixed scanning. d) 90° rotation scanning strategy. e) Layer-by-layer method for 1 mm height model and f) Layer-by-layer method for 3 mm height model.

Figure 4.14 shows the computational modelling results of the maximum principal stress of model, after base plate removal. For all modelling cases, peak maximum principal stress occurred at the part-plate interface with high maximum principal stresses formed at the side-faces of part, while compressive RS occurred at the central region of the part. The 0° no rotation scanning (Figure 4.14b) had a 23.56 MPa higher stress than the 90° rotation scanning (Figure 4.14d), which indicates 90° layer rotation is beneficial for mitigating RS and is consistent with the result of σ_{xx} stress (Figure 4.10). The inclined scanning strategy (e.g. 45° rotation and vertical mixed scanning, shown in Figure 4.14c) had the lowest maximum principal stress, which indicates the inclined scanning is beneficial for mitigating stress. For the 1 mm height model, the layer-by-layer method obtained a lower maximum principal stress than the hatch-by-hatch modelling method, e.g. the layer-by-layer method (844.14 MPa) had a 11.14 % lower peak maximum principal stress than the 90° rotation scanning (949.97 MPa). This is because the layer-by-layer method induces a more uniformity distribution of temperature, which is in good agreement with the results of single layer model (Table 4.2).

The RS in the 3 mm height model (Figure 4.14f) differs from the 1 mm height plate (Figure 4.14a-e), by showing a higher gradient in maximum principal stress, which is consistent with study [298]. An 13.23 % increase of the peak maximum principal stress was predicted by the 3 mm height model than the 1 mm height model, by using the same layer-by-layer modelling method. The increase of RS with the number of layers deposited is possibly induced by a greater number of thermal heating-cooling cycles for each layer in PBF-LB manufacturing. For the 3 mm height model, tensile RS formed at the top and bottom areas of the model and compressive stress occurred at the central field, same phenomenon was also observed in other PBF-LB study [301].

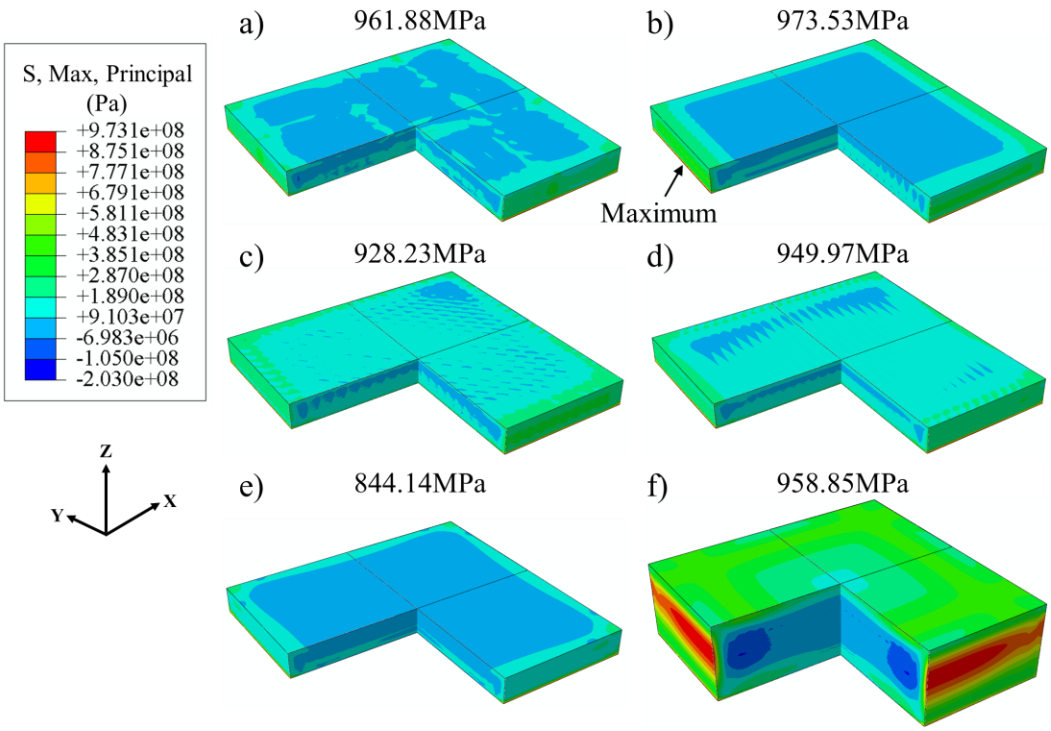

Figure 4.14. Computational results of the maximum principal stress contour after removing base plate with different modelling approaches and model heights: a) Island scanning. b) 0° no rotation scanning. c) 45° rotation and vertical mixed scanning. d) 90° rotation scanning strategy. e) Layer-by-layer method for 1 mm height model and f) Layer-by-layer method for 3 mm height model.

4.3.3 Experimental residual stress measurement

As RS obtained from the high energy synchrotron X-ray diffraction experiment represents an average value through the thickness of sample at each measurement point, the average RS within a small volume of each scanned beam field (i.e. $1 \times 1 \times 1$ mm^3 for the sample with height of 1 mm and $1 \times 1 \times 3$ mm^3 for the 3 mm sample, corresponding to the beam spot size in practical RS measurement) was used in this work [264]. Note that during the practical high energy synchrotron X-ray diffraction experimental measurements, the measurement protocol may not have ensured that the tested samples were always fully centred on the measurement platform in the experimental set-up [270]. As a result of this, and the area-averaging measurement feature of the X-ray beam, the experimental data obtained from the specimen's outer edges was not included in the analysis as shown in Figure 4.15b. If these edge effects were considered, the calculated lattice spacing at the boundary of the part would be over 10 times higher or lower than the lattice spacing at the central region of part. Thus, a 1 mm edge effect boundary was applied to all experimental

RS results and stresses at the specimen edges were not involved in RS calculation. Therefore, only the inner 8 mm by 8 mm area (within the 10 mm by 10 mm square plate) was used for plotting the 2D average RS contour of part in this work.

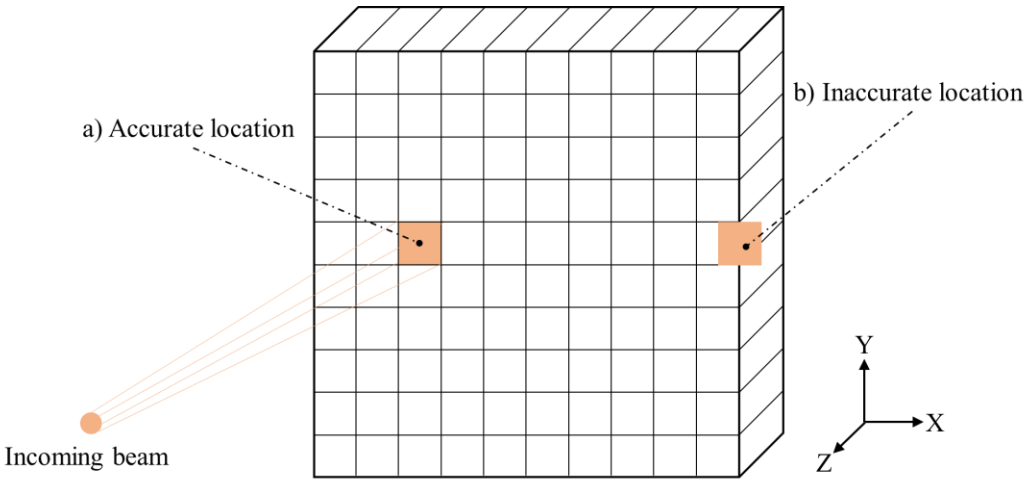

Figure 4.15. Illustration of the experimental measurement location during the high energy X-ray diffraction experiment: a) Accurate location of beam at the central area of part and b) Inaccurate location of the beam at the edges of part.

The experimentally measured *x* directional (σ_{xx}) and *y* directional (σ_{yy}) stress contour for samples with overall height of 1 mm by six different scanning strategies (Figure 4.1) are shown in Figure 4.16 and Figure 4.17, respectively. The results indicate different scanning strategies produced significantly different contours and magnitudes of the directional stresses (σ_{xx} and σ_{yy}). The island scanning (Figure 4.1a, Figure 4.16a and Figure 4.17a) had a larger average σ_{xx} and σ_{yy} RS than that of the 0° rotation scanning (Figure 4.1b, Figure 4.16b and Figure 4.17b). This is induced by the residual thermal effect on the individual island (Figure 4.1a), due to the shorter scanning vector compared with other five scanning strategies (Figure 4.1b-f). The (through-thickness average) RS distribution of components produced by the scanning strategies with an inclination angle (Figure 4.1c-d, Figure 4.16c-d, Figure 4.17c-d) were more uniform and lower than the no inclined strategy (Figure 4.1a-b, Figure 4.16a-b, Figure 4.17a-b) for the 1 mm height sample, e.g. the maximum σ_{xx} stress of 45° rotation scanning and vertical mixed scanning (inclined scanning, 59.12 MPa) was approximately half (45.27 %) lower than the maximum σ_{xx} stress for the island scanning (no inclined scanning, 108.02 MPa). This indicates the inclined scanning strategy could balance and mitigate the directional σ_{xx} and σ_{yy} stresses

of part, which is consistent with the computational results of σ_{xx} (Figure 4.10), σ_{yy} (Figure 4.12) and the maximum principal stress (Figure 4.14). Experimental measurement indicates σ_{xx} stress of the 90° rotation scanning strategy (51.78 MPa, Figure 4.16e) was 46.36 % lower than the σ_{xx} stress of the 0° no rotation scanning strategy (96.53 MPa, Figure 4.16b) for the 1 mm height model, which is in line with the predicted results that 90° layer rotation is beneficial for reducing the σ_{xx} directional stress (Figure 4.10).

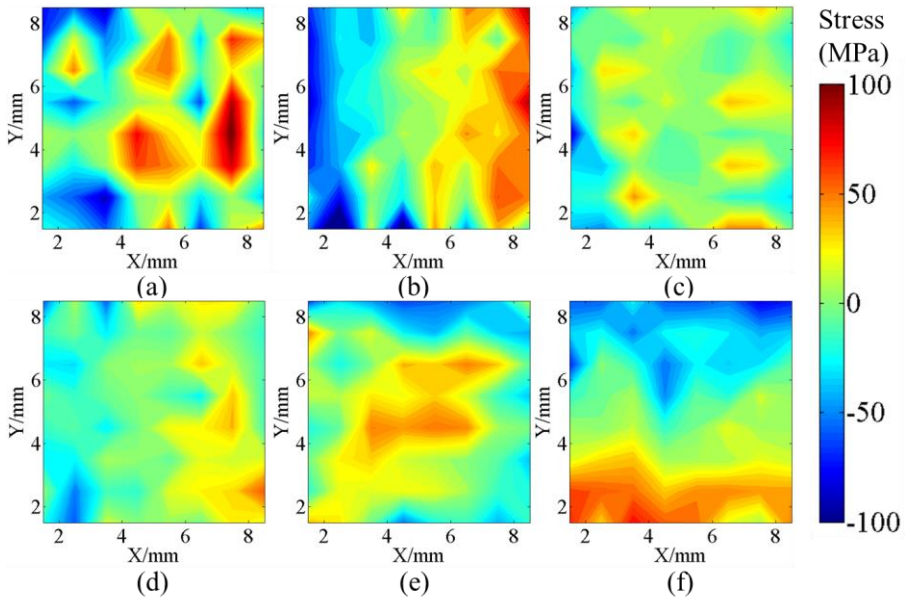

Figure 4.16. The experimentally measured average σ_{xx} stress contour of samples with overall height of 1 mm and produced by six different scanning strategies: a) Island scanning. b) 0° no rotation scanning. c) 45° rotation scanning. d) 45° rotation and vertical mixed scanning. e) 90° rotation scanning and f) 67° rotation scanning strategy.

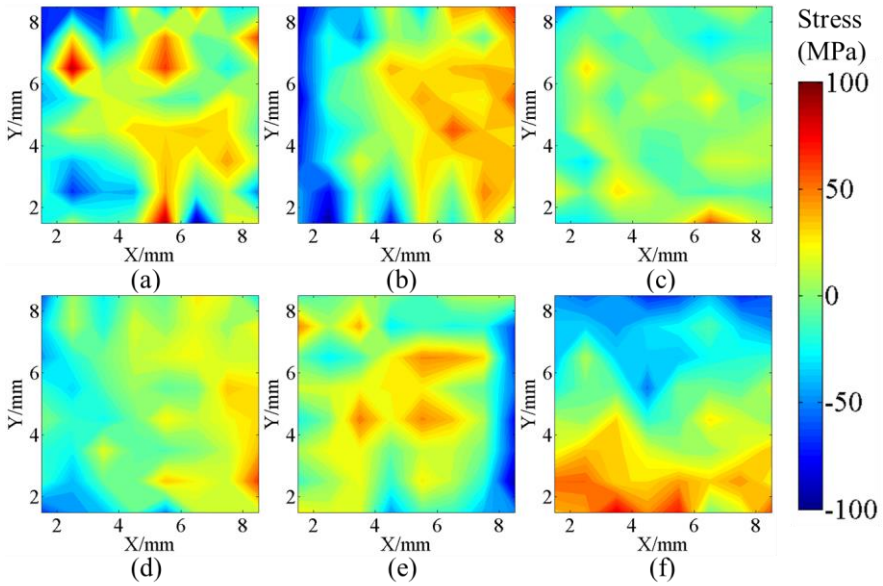

Figure 4.17. The experimentally measured average σ_{yy} stress contour of samples with overall height of 1 mm and produced by six different scanning strategies: a) Island scanning. b) 0° no rotation scanning. c) 45° rotation scanning. d) 45° rotation and vertical mixed scanning. e) 90° rotation scanning and f) 67° rotation scanning strategy.

The average σ_{xx} and σ_{yy} stress contour for 3 mm height samples by six different scanning strategies (Figure 4.1) is shown in Figure 4.18 and Figure 4.19, respectively. Figure 4.20 indicates the maximum σ_{xx} and σ_{yy} stresses statistics for the 3 mm height part. Figure 4.18 and Figure 4.19 indicate the overall stress contour of the island scanning strategy (Figure 4.1a) is higher than other scanning cases, which is assumed to be caused by the thermal concentration in the individual island and residual heat effect on the island scanning strategy (Figure 4.1a) and is consistent with the results of 1 mm height part (Figure 4.16 - Figure 4.17). Note that the 0° no rotation scanning strategy (Figure 4.1b) had the largest σ_{xx} stress for the 3 mm height part (Figure 4.20). Figure 4.20 indicates the inclined scanning strategies (Figure 4.1c, d and f) had lower maximum σ_{xx} stress than the no inclined scanning strategy (Figure 4.1a, b and e) for the 3 mm height part, e.g. the σ_{xx} stress of the 45° rotation scanning strategy (83.24 MPa) was 21.15 % lower than the island scanning strategy (105.57 MPa). This is caused by the inclined laser scanning trajectories balancing the directional σ_{xx} and σ_{yy} stresses, which is in good agreement with experimental results of the 1 mm height part (Figure 4.16 - Figure 4.17). In addition, as can be seen from Figure 4.20, the 0° rotation scanning strategy obtained the largest difference of directional stresses than other scanning strategies.

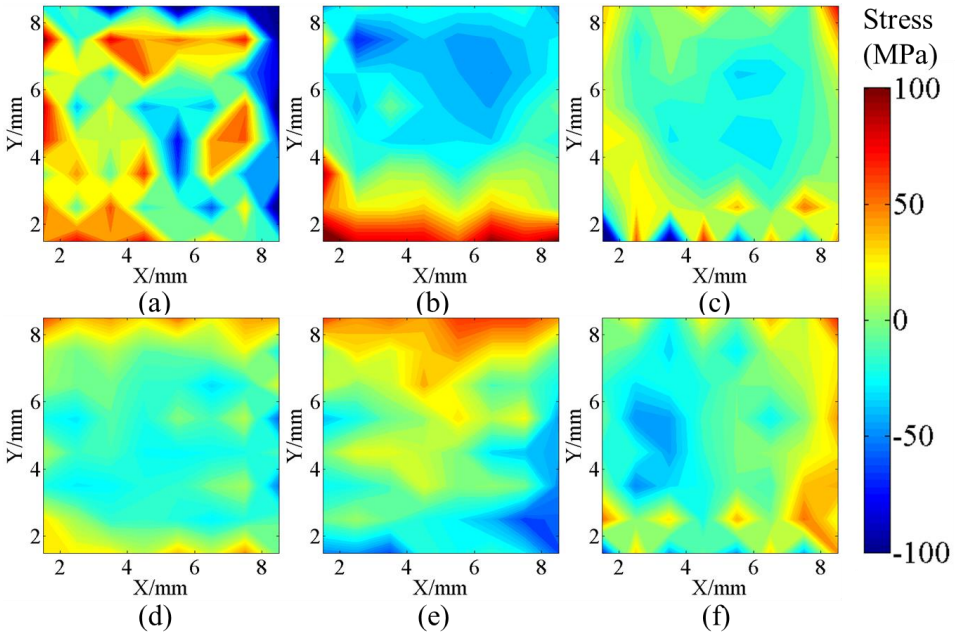

Figure 4.18. The experimentally measured average σ_{xx} stress contour of samples with overall height of 3 mm and produced by six different scanning strategies: a) Island scanning. b) 0° no rotation scanning. c) 45° rotation scanning. d) 45° rotation and vertical mixed scanning. e) 90° rotation scanning and f) 67° rotation scanning strategy.

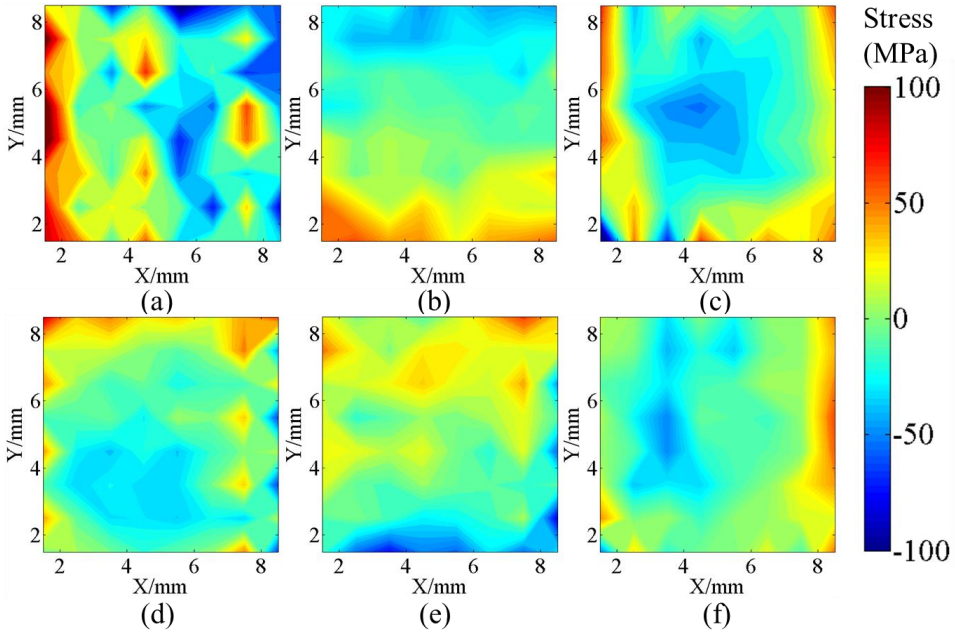

Figure 4.19. The experimentally measured average σ_{yy} stress contour of samples with overall height of 3 mm and produced by six different scanning strategies: a) Island scanning. b) 0° no rotation scanning. c) 45° rotation scanning. d) 45° rotation and vertical mixed scanning. e) 90° rotation scanning and f) 67° rotation scanning strategy.

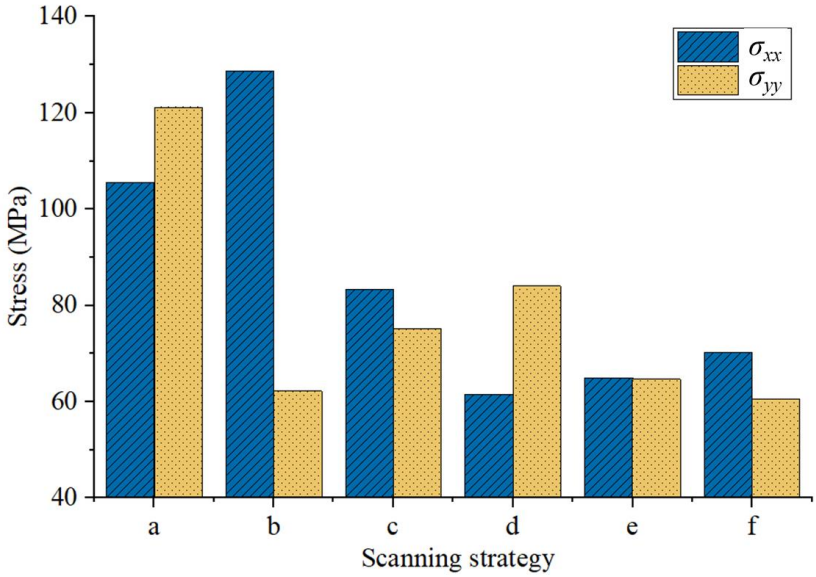

Figure 4.20. Experimentally measured maximum σ_{xx} and σ_{yy} stresses for 3 mm height component manufactured by six different scanning strategies: a) Island scanning. b) 0° no rotation scanning. c) 45° rotation scanning. d) 45° rotation and vertical mixed scanning. e) 90° rotation scanning and f) 67° rotation scanning strategy.

4.3.4 Comparison of simulation and experimental results

To compare with the experimental measurements, RS over the corresponding same volume of model from the computational PBF-LB modelling was averaged. The average RS in format of 2D contour represents the 3D stress field of each sample, both for experimental measurements and computational simulations. Figure 4.21 shows statistics of the maximum σ_{xx} and σ_{yy} stresses for the different scanning strategies, including both the computation and experiment. The experimental measurement indicates that the island scanning strategy (Figure 4.21a) generated the highest maximum σ_{xx} (108.02 MPa) and σ_{yy} (93.18 MPa) stresses for the 1 mm plate, which is caused by the energy concentration of the individual island (Figure 4.1a). While the computational modelling results show that the island scanning strategy produced the largest maximum σ_{yy} stress (50.74 MPa) and the second largest σ_{xx} stress (47.10 MPa). The computational modelling results indicate that the 0° no rotation scanning strategy (Figure 4.21b) generated the highest σ_{xx} stress (51.58 MP), due to that this scanning strategy excluding layer rotation.

Both the computational modelling and experimental measurement reveal that the 90° rotation scanning strategy (Figure 4.21e) generated a significantly lower σ_{xx} stress than the

0° no rotation scanning strategy (Figure 4.21a), which indicates 90° layer rotation could be beneficial for balancing and thus reducing the directional stresses. This is consistent with the computational modelling results of the maximum principal stress (Figure 4.14). Figure 4.21 shows that the 45° rotation scanning strategy (Figure 4.21c) obtained the lowest experimental σ_{xx} stress (49.67 MPa) for the 1 mm height part, which validated the computational modelling results that the lowest σ_{xx} stress (33.43 MPa) was formed at the 45° rotation scanning strategy. While higher σ_{xx} stress was formed at the no inclined scanning strategies, such as island scanning strategy (108.02 MPa), 0° no rotation scanning strategy (96.53 MPa) and 90° rotation scanning strategy (51.78 MPa). This confirms the inclined scanning strategy could balance the σ_{xx} and σ_{yy} stresses.

It can be seen from Figure 4.21 that the predicted σ_{xx} and σ_{yy} stresses were lower than the experimental measurements, i.e. the predicted σ_{yy} stress (45.91 MPa) of 0° no rotation scanning strategy was 35.05 % lower than the experimentally measured σ_{yy} stress (70.69 MPa). However, the majority of the computational and experimental σ_{xx} and σ_{yy} stresses produced by different scanning strategies were in the range of 30 MPa to 100 MPa. The computational RS stress with different scanning strategies was consistent with the experimental measurement. For instance, both the computational modelling and experimental measurement indicate the 45° rotation scanning strategy (Figure 4.21c) had the least σ_{xx} stress while the island scanning strategy (Figure 4.21a) and the 0° no rotation scanning strategy (Figure 4.21b) had higher σ_{xx} and σ_{yy} stresses than other four scanning strategies (Figure 4.21c-f). Therefore, in general, the experimentally measured σ_{xx} and σ_{yy} stresses had a good fit with the computational modelling results.

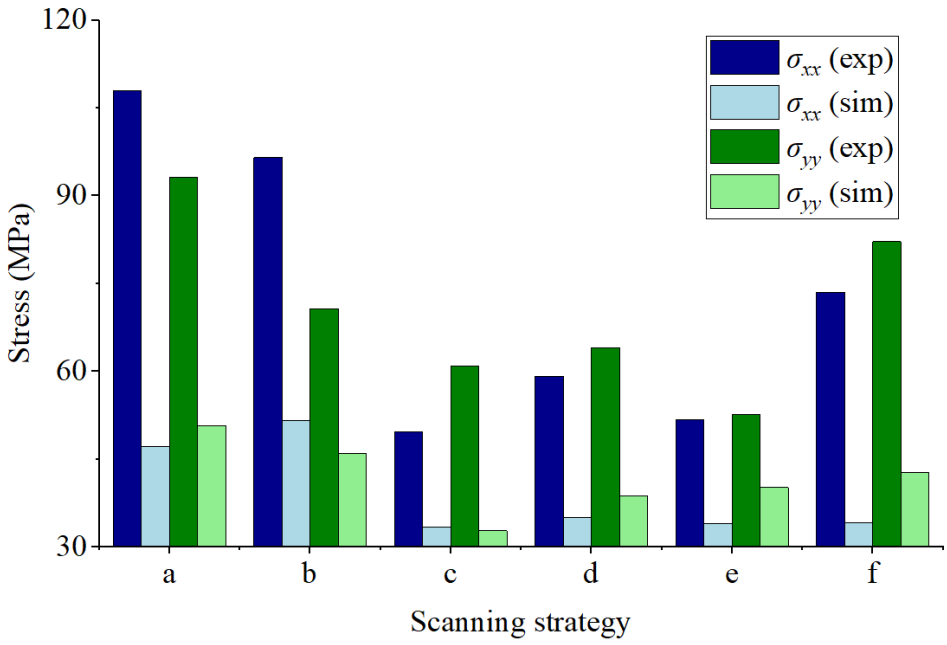

Figure 4.21. Comparison of the maximum average through thickness σ_{xx} and σ_{yy} stresses by simulation (sim) and experiment (exp) for 1 mm height component manufactured by six different scanning strategies: a) Island scanning. b) 0° no rotation scanning. c) 45° rotation scanning. d) 45° rotation and vertical mixed scanning. e) 90° rotation scanning and f) 67° rotation scanning strategy.

Figure 4.22 shows the comparison of computational results and experimentally measured σ_{xx} and σ_{yy} stresses contour for the 90° rotation scanning strategy (Figure 4.1e), which is beneficial for mitigating RS. In order to quantitatively compare the computational modelling results with the experimentally measured stress, Figure 4.23 indicates σ_{xx} and σ_{yy} stress profiles along the horizontal path (Figure 4.22b). Overall, the predicted directional stresses are more uniform than the experimental measurement (Figure 4.22 and Figure 4.23). For the 90° rotation scanning strategy, both the computational σ_{xx} and σ_{yy} stresses (including contours and magnitudes) are close to the experimental measurement (Figure 4.22), e.g. predicted σ_{xx} stress was 31.18 % lower than experimentally measured at the central area of part. The centre area of part obtained higher directional stress than at the edges of part, for both prediction and measurement. For σ_{xx} and σ_{yy} stresses along the horizontal path (Figure 4.22b), there is also an agreement (within 31.18 % difference in

σ_{xx} stress) at the central area of part between computational modelling and experimental measurement (Figure 4.23).

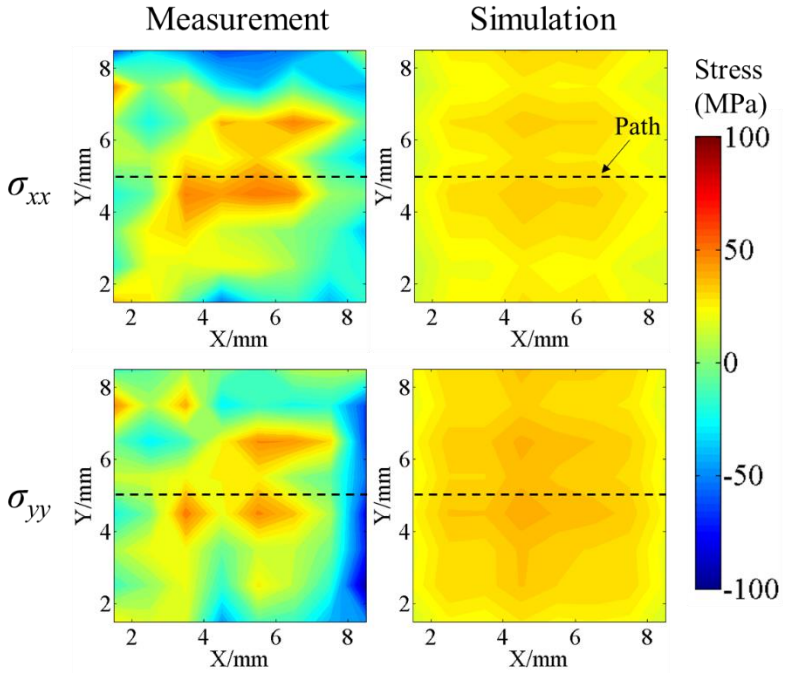

Figure 4.22. Comparison of computational modelling stress results with experimentally measured σ_{xx} and σ_{yy} stresses contour for the 90° rotation scanning strategy (Figure 4.1e) and 1 mm height model: a) Experimentally measured σ_{xx} stress. b) Predicted σ_{xx} stress. c) Experimentally measured σ_{yy} stress and d) Predicted σ_{yy} stress.

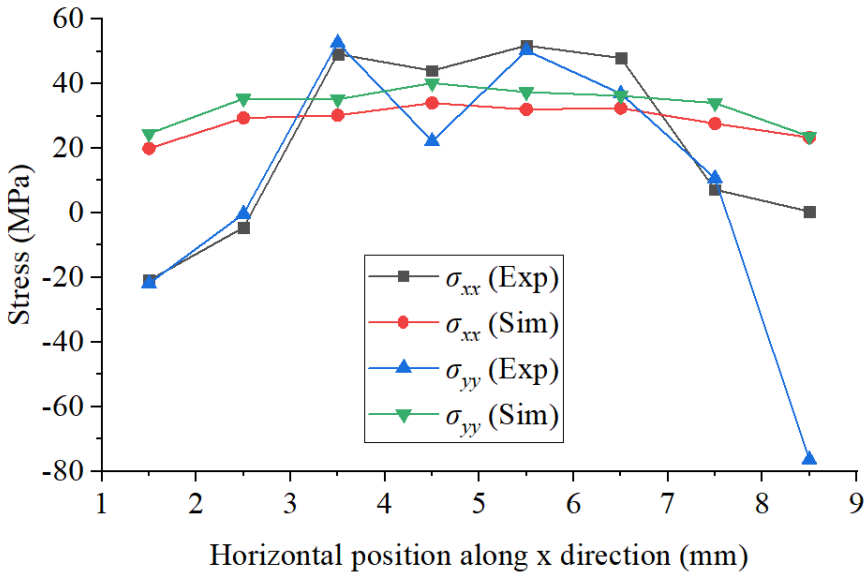

Figure 4.23. Comparison of σ_{xx} and σ_{yy} stresses by simulation (sim) and experiments (exp) along horizontal path (Figure 4.22b) for the 90° rotation scanning strategy (Figure 4.1e) and 1 mm height model.

4.3.5 Discussions

This study experimentally measured residual stress of square plate, which provided comparison data for the model predictions. By comparing computational modelling results with the experimentally measured σ_{xx} and σ_{yy} stresses (Figure 4.21 and Figure 4.22), the computational finite element model successfully predicts trends of σ_{xx} and σ_{yy} profiles (e.g. RS is higher at the central area of sample than at the edge, for both experimental measurements and computational modelling). The stress quantities are of the same order of magnitude, but the experimental measurement shows a wider range (higher maximum and lower minimum) of stress than prediction.

Different scanning strategies produced different directional σ_{xx} and σ_{yy} stresses (Figure 4.21). Both the inclining angle, layer rotation and scanning vector of scanning strategy influenced stress of PBF-LB manufactured parts. As the island scanning strategy (Figure 4.21a) and 0° no rotation scanning strategy (Figure 4.21b) produced higher directional stresses than other scanning cases (Figure 4.21c-f), it is not recommended to use these two scanning strategies in the practical PBF-LB manufacturing. Based on the computational and experimental results, to get the least residual stress in the manufactured part, it is

recommended to use the 90° layer rotation scanning strategy (Figure 4.1e) or the inclined scanning strategy (e.g. 45° rotation scanning strategy, Figure 4.1c).

This work calculated the experimentally measured σ_{xx} and σ_{yy} stresses by assuming the σ_{zz} stress equals to zero. Figure 4.24 shows the average through thickness σ_{zz} stress predicted by FEM for the island scanning strategy (Figure 4.1a) as an example. After calculation, the average σ_{zz} stress of the entire sample is 2.60 MPa. Therefore, it is considered reasonable to approximate the σ_{zz} stress of the thin square plate to be zero in the experimental stress calculation. In addition, this work employed the square plate, for better recognition of the experimental measurement positions and the *x* direction and *y* direction of part, it is recommended to consider modelling of trapezoid geometry part in the next experimental RS measurements. In future, more experiments can be performed, such as experimentally measuring the σ_{zz} stress (e.g. by tilting the incoming beamline in high energy X-ray diffraction experiment) to validate the assumption behind the stress results of this work and measuring RS distribution of part by using the neutron diffraction facility.

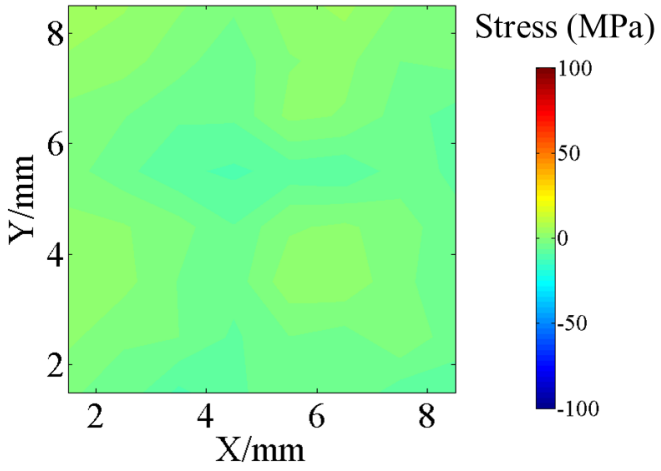

Figure 4.24. Computational results of average through thickness σ_{zz} stress contour of the island scanning strategy after base plate removal.

Note that the predicted σ_{xx} and σ_{yy} stresses are tensile while the experimentally measured RS are compressive at the edges of part (Figure 4.22). There is also a difference of magnitude of stress between the computational modelling and experiments (Figure 4.21). Multiple factors could cause the difference between the experimentally measured RS and the computationally predicted RS of part after removing constraints of the base plate. The

first possible reason is the stress-free lattice spacing of Ti-6Al-4V material was not experimentally measured by the higher energy X-ray diffraction experiment and an approximation method was used for calculating the stress-free lattice spacing in this study. Secondly, the manufactured samples were cut from the base plate by wire EDM method after the manufacturing process is finish. In this modelling work, the build plate removal was simulated as instantaneous release with no additional thermal load, but in reality the process involves progressive removal of physical material from one edge of the plate to the opposite edge using a slow high temperature cutting wire. The EDM wire process could influence redistribution of stress, future work could consider gradual removal of the part from the base plate by simulating the physical wire EDM process after the build process is complete. In addition, the inaccurate position of EDM cut caused some portion (e.g. ~ 0.1 mm thickness) of the support structure to remain on the plates, which may be included in the experimentally measured RS of part. Thirdly, the {103} lattice plane was recommended as the least sensitive lattice direction (or lattice plane) to calculate the stress-free lattice spacing for RS analysis of Ti-6Al-4V material [302]. But the peak of the {103} lattice plane in the raw data that was directly produced by the high energy X-ray diffraction facility was too weak to be observed and was invisible for RS analysis. For comparison purpose, the single peak fitting of the lattice plane {102} and {101} (Figure 4.5c) was separately utilised for RS calculation of the same sample. Figure 4.25 indicates RS calculated by different lattice planes for the same sample did not change the distribution but changed the magnitude of the maximum RS. For instance, for the 1 mm heigh sample manufactured by the island scanning strategy (Figure 4.1a), the calculated average σ_{xx} for the {102} and {101} lattice plane was 108.02 MPa (Figure 4.25a) and 90.10 MPa (Figure 4.25b), respectively. The experimentally measured stress could fit better with the prediction by using the {103} lattice plane if its peak is visible. Fourthly, the hatch-by-hatch and layer-by-layer modelling methods were employed for the process modelling of PBF-LB, as shown in Figure 4.7 and Table 4.2, which is not identical to the spot-by-spot manufacturing manner (more nonuniformity of the heat source) in the practical PBF-LB manufacturing and this may affect the accuracy of the predicted RS. Finally, the lattice plane can have positive or negative effects on the true macroscale elastic strain (Figure 4.26) [303], which could cause more tensile or compressive RS on

the measured part. Due to the existence of the intergranular stress, the experimentally measured RS, which is calculated by using the lattice plane of {102} or {101}, is not exactly equal to the thermal process induced stress in PBF-LB manufacturing.

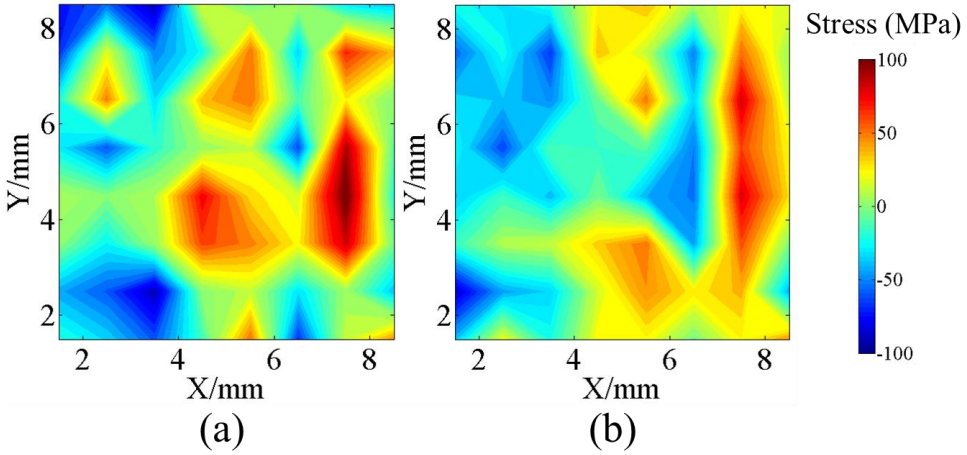

Figure 4.25. Experimentally measured average residual σ_{xx} stress contours for 1 mm sample height manufactured by the island scanning strategy (Figure 4.1a), which was calculated by different lattice planes: a) {102} lattice plane and b) {101} lattice plane.

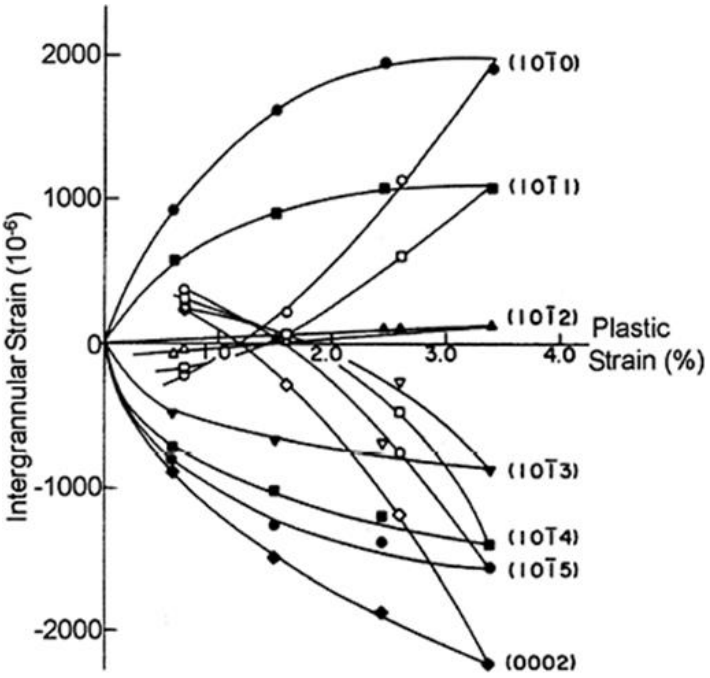

Figure 4.26. Effect of different lattice planes on intergranular strain on HCP structure of material [303].

The experimentally measured RS magnitude and contour are largely depending on the stress-free lattice spacing (d_0) on the specific lattice plane of material. One solution for measuring d_0 is to cut the samples (which is the same with samples for stress measurement) into small cubes (e.g. $3 \times 3 \times 3$ mm^3) by wire EDM technique [200]. However, due to the limitation of the I12 beamtime at the Diamond Light Source in UK and Covid-19, the stress-free lattice spacing d_0 for PBF-LB manufactured Ti-6Al-4V sample was not experimentally measured. The experimentally measured stress-free lattice spacing is specimen specific and is also influenced by factors such as the kind of alloy, chemical composition and phase transformation of material etc. [250]. For instance, it is reported that the measurement of the unstrained lattice parameters for Ti-6Al-4V material is largely dependent on the measurement position of sample [304, 305]. Therefore, it is required to experimentally measure the specimen specific stress-free lattice spacing d_0 at multiple positions of each sample that was manufactured by PBF-LB for calculation of residual stress. However, this requirement remains difficult to achieve, as there is limited availability and beamtime of the high energy X-ray diffraction or Neutron Diffraction facility worldwide, and the fabrication of truly stress-free components is challenging.

4.4 Summary

In summary, the experimental RS measurement of Ti-6Al-4V part was performed by the high energy X-ray diffraction technique on a series of samples manufactured by different scanning strategies in PBF-LB AM. The scanning strategies and part heights effects on the average directional residual stresses of parts were investigated. The computational layer-by-layer and hatch-by-hatch modelling approaches were developed and applied for predicting RS in PBF-LB. The main conclusions are as follows:

- Both the experimental measurement and computational prediction show that the 90° rotation scanning strategy had a lower σ_{xx} stress than the no rotation scanning strategy, which indicates 90° layer rotation is beneficial for mitigating stress of PBF-LB manufactured component.
- The high energy X-ray diffraction experiments indicate the inclined scanning strategy (e.g. 45° rotation scanning strategy) is beneficial for reducing the

directional stress (σ_{xx} and σ_{yy}) than the no inclined scanning strategy (e.g. 0° no rotation scanning strategy), for both 1 mm model and 3 mm model. The computational modelling results of the maximum principal stress support this experimental finding.

- The 45° rotation scanning strategy could produce the least directional stress and is highly recommended in PBF-LB manufacturing. While the island scanning and 0° no rotation scanning obtained higher stress than other scanning strategies, which should be avoided.
- Computational modelling results of the maximum principal stress indicate that a higher gradient in stress was formed in the thicker part than the thinner part after base plate removal, i.e. larger compressive stress occurred at the central area and larger tensile stress was formed at the edges of part.
- The layer-by-layer modelling method could approximately predict σ_{xx} RS by the 0° no rotation scanning strategy (e.g. within a marginally 4.65 % difference in the maximum σ_{xx} RS), but not the inclined scanning strategies.
- After releasing constraints of the base plate in PBF-LB manufacturing, RS of part reduced significantly compared to before base plate removal, due to stress relaxation.

This chapter applied stress measurement experiments to AM components with the objective of validating computational model predictions and has highlighted a number of factors that could improve accuracy of experimentally measured RS. Firstly, RS should be measured before base plate removal, however the ability to measure stress of the specimen only, while attached to the built plate maybe difficult. If achieved, this could better validate the final stress state of the as-built part and thus validate the manufacturing process of PBF. Secondly, for stress after base plate removal, future work would consider simulating the removing process of the base plate from the part by ways such as modelling the practical wire EDM cutting process on the PBF manufactured component. Thirdly, strategies to obtain stress free values of d_0 could include extensive stress relieving heat treatments followed by d_0 measurements *after* the original as-built stress measurements are taken.

5 Residual stress simulated by multi-laser beam build powder bed fusion additive manufacturing

5.1 Introduction

Through the computational process modelling and experimental measurements in **Chapter 4**, the scanning strategy has been shown to affect RS in the single laser beam PBF-LB. First generation PBF-MLB systems, containing more than one laser beams, have been marketed by the AM OEMs (original equipment manufacturers), including the dual-laser system of Concept Laser M2 Series 5 and the four-laser systems of EOS M 400-4 and Renishaw RenAM 500Q [217, 219]. It therefore follows, that PBF-MLB systems will have a different RS profile than single laser system. With multiple laser beams working simultaneously, the PBF-MLB offers a key industrial advantage of increasing production rate by reducing the time required to melt the required profile in each layer relative to the single beam PBF-LB [306]. The addition of multiple laser beams does not affect powder recoating time, and so the scale up time is not linear with increasing the number of lasers. It has been reported that the build time for solid cubes ($10 \times 10 \times 10$ mm^3) and cylinders (Ø 14 mm × 100 mm) on a four laser beam PBF-MLB (19 hours) is 36.54 % of the single laser beam PBF-LB manufacturing (52 hours) [224]. An overall comparison of RS profile between PBF-MLB and the single laser beam PBF-LB has never been reported in the literature. Thus, it is necessary to investigate the effect of the number of laser beams on RS, which can provide insight the optimum number of laser beams for mitigating stress of additively manufactured components.

With the proven link between scanning strategy, residual stress and part deflection [50], it is hypothesised that with the use of additional laser beams, the temperature of the powder bed is more uniform and has a lower temperature gradient, and thus it could offer the potential to reduce RS and deflection, thus making PBF-MLB more suitable for components manufacturing than the single laser beam PBF-LB. While there has been considerable progress in optimising single laser beam PBF-LB scanning strategies, the optimum PBF-MLB scanning strategy and laser interaction remain unclear [40, 216].

Thus, the effect of PBF-MLB scanning strategies on RS requires further investigation, specifically whether lasers should work together on a single part within a build (and if so, what scanning strategy is most beneficial) or whether each laser should work on separate parts within the same layer. In addition, the effect of base plate constraint on RS in PBF-MLB is also computational investigated in this chapter.

The aim of this chapter is to develop and apply thermo-mechanical coupled FEM of PBF-MLB in order to investigate the effects of different scanning strategies on thermal and RS behaviours. The objectives of this work are as follows:

a) Develop the computational process modelling capability for multiple laser beams in PBF-MLB manufacturing.
b) Predict the influence of the number of laser beams on production rate, temperature, RS, and deflection by using the coupled thermo-mechanical process modelling of PBF-MLB.
c) Predict the effects of scanning strategies on RS and deflection by using the dual laser beams PBF-MLB process modelling and predict the optimal scanning strategies that can result in the least RS and deflection.

The results of this work will be beneficial for PBF designers and manufacturers to obtain the manufactured parts with optimum properties in PBF-MLB.

5.2 Methods

5.2.1 Configuration of the case study

In this work, a rectangular additively manufactured part ($3 \times 3 \times 0.12$ mm^3) and a rectangular base plate ($6 \times 6 \times 1$ mm^3) were modelled (Figure 5.1a). Figure 5.2 shows the procedure for the PBF-MLB thermo-mechanical modelling procedures. The layer height of powder material was 40 μm. The converged mesh size of $20 \times 20 \times 20$ μm^3 (i.e. one - fifth of the laser beam diameter) was applied on the part while a relatively coarse mesh (i.e. $0.2 \times 0.2 \times 0.2$ mm^3) was adapted for the base plate. Mesh - independent results were achieved (shown in Figure 5.3) by sampling the stress at the left bottom node of the solid part (Figure 5.1a) and was found to be comparable to other similar scale models [50, 307].

The total element number was 139,500. To obtain the temperature, RS and displacement information, the 8-node trilinear displacement and temperature mesh element (C3D8T) in ABAQUS was chosen. The bottom of the base plate was fully constrained as the mechanical boundary condition during the whole process except for the base plate constraints releasing steps. All the nodes at the bottom of the base plate, except for the four extremity nodes, were unconstrained to allow the deformation of the part at the final steps [291]. In each step, the simulation models employ the 'model change' function in ABAQUS to simulate the addition of new layers, which has been described in **Chapter 3**. Then Gaussian power densities (Figure 5.1b), which applied in the integration points of the finite elements, were applied to scan the designed paths of each layer. The initial time step for Gaussian distributed heat source was 10^{-7} s and the maximum time increment for heating step time was 10^{-5} s.

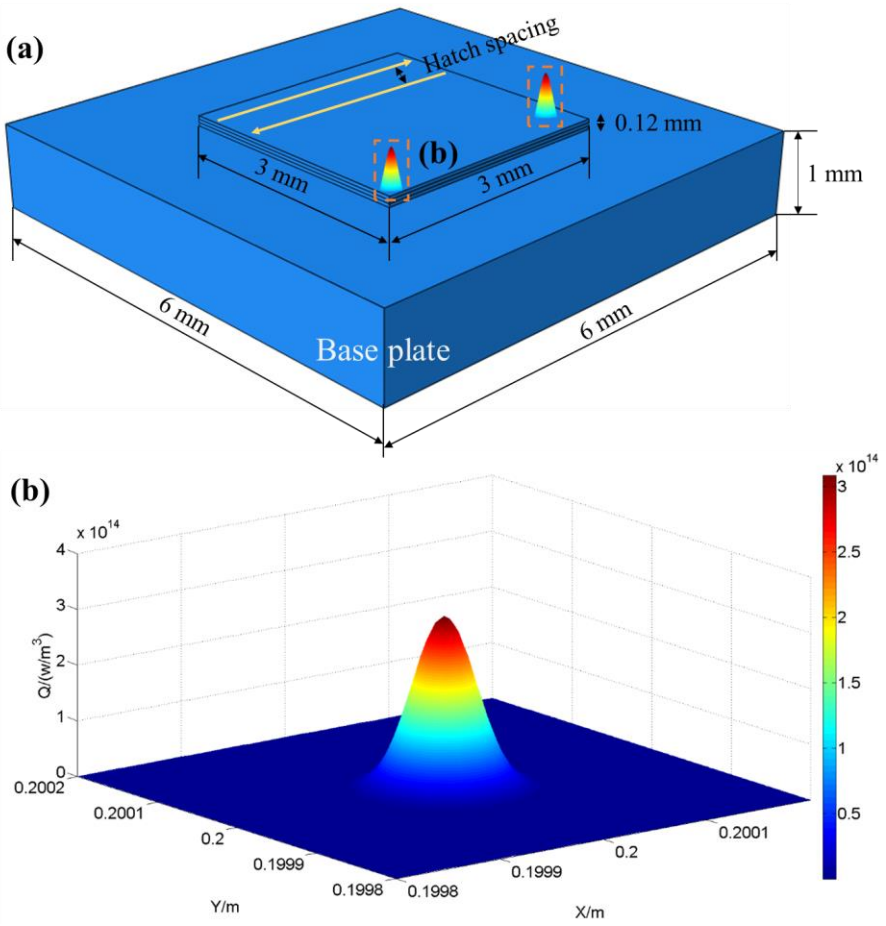

Figure 5.1. Model configurations: a) The computational model consists of rectangular part and base plate and b) The distribution contour of Gaussian energy source.

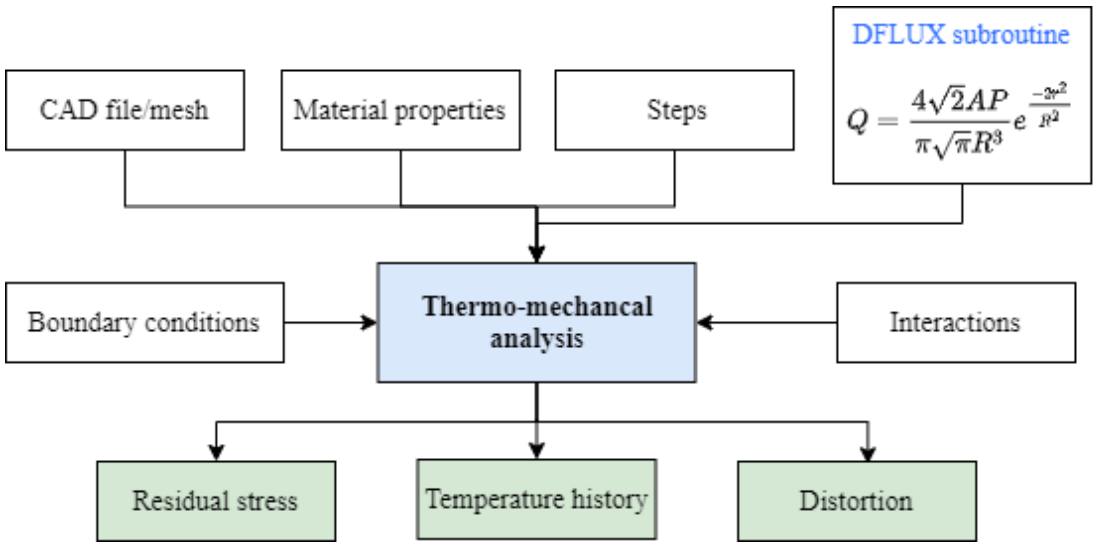

Figure 5.2. Flowchart of the PBF-MLB simulation procedure.

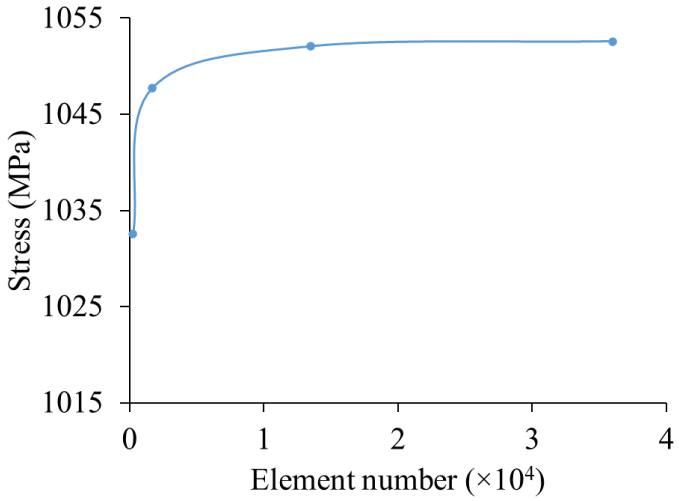

Figure 5.3. Mesh convergence validation at the left bottom node of the part.

The initial temperature of the whole system was set to be 293 K. The constant laser beam scanning speed, heat source spot diameter and hatch spacing were set as 0.6 m/s, 0.1 mm, and 0.1 mm, respectively. The three layers were deposited sequentially with an interval of recoating time of 10 s, which is the time for a new layer to be spread out on the powder bed prior to laser scanning [41]. The complete process modelling parameters are summarised on Table 5.1. Based on the predicted melt pool depth of 60 µm, trial builds and follow on µCT imaging at 1.5 µm resolution, the proposed process parameters will result in stable melting and approximately fully dense parts [308].

Table 5.1. Process parameters applied for PBF-LB process modelling [41, 309-312].

Symbol	Material	Ti-6Al-4V
	Base plate size (mm)	6 × 6 × 1
T_{bp}	Base plate preheating temperature (K)	293
	Part size (mm)	3 × 3 × 0.12
L_h	Layer height (mm)	0.04
	Recoating time (s)	10
P	Laser beam power (W)	95
A	Heat source absorption coefficient	0.4
R	Heat source spot radium (mm)	0.05
v_s	Laser scanning speed (m/s)	0.6
H_s	Hatch spacing (mm)	0.1
ε	Emissivity	0.35
h	Heat transfer coefficient (W/m^2/K)	12.7

The temperature dependent Ti-6Al-4V material properties (conductivity, density, specific heat, elastic modulus and yield stress) for both the solid part and the base plate have been described in **Chapter 3** (Figure 3.5) and **Chapter 4**.

5.2.2 Thermal and mechanical analysis

The fully coupled numerical thermal-stress simulations were performed using the general-purpose finite element software ABAQUS. The governing equation for the heat transfer process is formulated by using the energy equation (Eq. 2.1). The latent heat which describes the solid to liquid phase transition of the Ti-6Al-4V material was set as 370 kJ/kg [115]. The liquid fraction is calculated by Eq. 2.4 [153]. In this study, the PBF-MLB thermal cycles involve the laser beams heating process and the cooling processes. For the laser beams heating process, the Gaussian heat profile given in Eq. 2.5 is a widely adopted model to mathematically formulate the profile of laser heat source [154, 279, 313] and it is employed in this work, as shown in Figure 5.1b.

Details in terms of the thermal transfer mechanisms have been shown on Figure 3.2 of **Chapter 3** and previously published[149]. Briefly, the cooling process of the additively manufactured parts includes heat conduction to the solidified material and base plate, part-

powder interface conduction (approximated as free surface convection [149, 314], active layer (newly added and undergoing heat flux) convection and radiation from the top surface of active layer to the surrounding atmosphere until the finish of the final part. The influence of melt pool convection, radiation and evaporation were ignored due to the small size of the melt pool [38]. The heat transfer boundary conditions of radiation (Eq. 2.16) and convection (Eq. 2.17) occurred at the top surface of the active layer until the next layer was added. The mechanical mechanisms related theory has been introduced from Eq. 2.18 to Eq. 2.22 in **Chapter 2**.

5.2.3 Scanning strategies

To investigate the scanning strategies influence on the local thermal distribution resulted RS and deformation in the dual laser beams PBF-MLB [41], twelve different scanning strategies devised from reference [83, 216] were employed in the computational modelling (Figure 5.4). Case (a) is the opposite S scanning, where the two laser beams move parallel to the bottom edge of the part, parallel to each other but in opposite directions with a constant offset of hatch spacing H at any one time. The 'S' scanning means the laser beam heat source reverses scan direction after finishing each hatch. Case (b) and case (c) are parallel S scanning, where the two laser beams move parallel to the bottom edge but in the same direction. For case (b), the laser beams scan direction rotates 90° for the next layer while no layer rotation for case (c). Case (d) is the 0° approaching beam scanning and the two laser beams scan from respective top and bottom sides and close to each other gradually while case (e) is the 45° rotation approaching beam scanning that the laser beams move with a 45° angle with respective to the x direction. Case (f) is the opposite halves scanning that two laser beams responsible for the left and right halves of the model, respectively. Case (g) is the parallel halves scanning, where the two beams keep working parallel with a specific offset distance of half of the part width. Case (h) is the island approaching beam scanning, where two laser beams scan individual islands. Case (i) is the island mixed scanning that two laser beams move parallel to each other but in opposite directions within each individual island. For island scanning of case (h) and (i), the whole scanning domain has been divided into 9 islands and rotates 90° for the sequence island scanning. Cases (j) and (k) are the contour fill scanning that case (j) scans the outside

contour first while case (k) scans the part central area first. Case (l) is the delayed scanning that the secondary laser follows the first laser and post-heating the powder bed, which aims to slow down the cooling rate along the laser moving direction. The delayed laser beam applied half of the first melting laser power and the constant offset was set as 90 μm based on literature [83]. Except case (c), all the scanning strategies rotate 90° for the next layer.

A user defined subroutine DFLUX (Figure 5.2) was programmed using Fortran to implement the moving dual laser beams by applying two Gaussian heat profiles (Figure 5.1b) of the laser beams to the powder bed according to the respective scanning speed and scanning strategies as shown in Figure 5.4.

In order to establish overall trends due to increased number of lasers, three additional PBF process models were simulated for the above geometry using one, four and thirty laser beams. In the four and thirty laser models, all laser beams were set to simultaneously scan the above part using the same opposite S scanning strategy (Figure 5.4a) only. Thus, two comparative studies were produced, first the optimum number of lasers for a given laser scanning strategy and second, the optimum laser scanning strategy for dual laser beams PBF-MLB manufacturing.

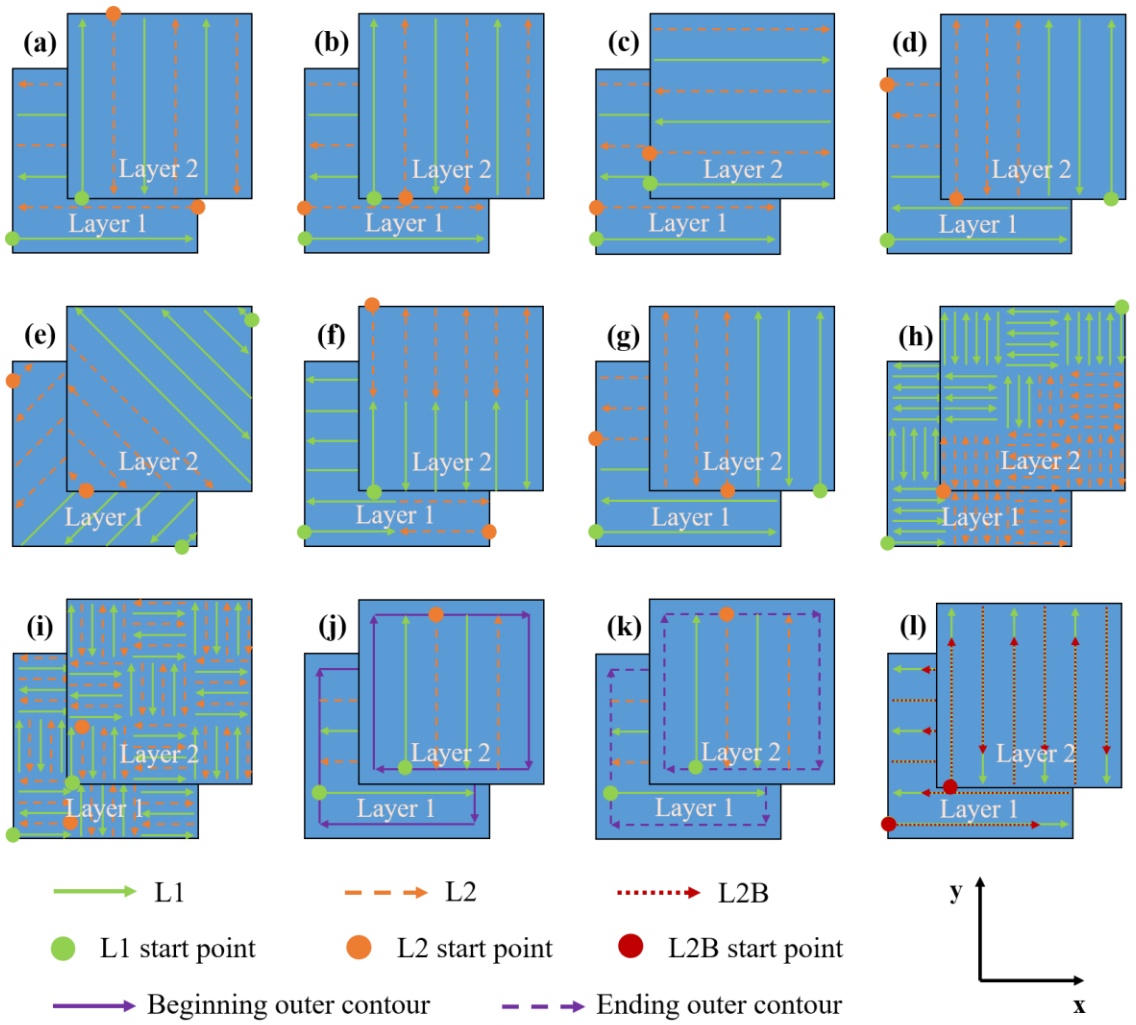

Figure 5.4. Different scanning strategies arrangement for dual laser beams PBF-MLB: a) Opposite S scanning. b) Parallel S 90° rotation scanning. c) Parallel S no rotation scanning. d) 0° approaching beam scanning. e) 45° rotation approaching beam scanning. f) Opposite halves scanning. g) Parallel halves scanning. h) Island approaching beam scanning. i) Island mixed scanning. j) Beginning contour fill. k) Ending contour fill and l) Delayed laser scanning. For illustration, the hatch spacing has been magnified.

5.3 Results and discussions

5.3.1 Influence of the number of laser beams on residual stress

In these computations, the single laser beam, dual laser beams, four laser beams and thirty laser beams were separately employed as the heat source. Figure 5.5 shows the computational modelling results of the von Mises stress distributions for different numbers of laser beams by using the opposite S scanning pattern (Figure 5.4a) at the

interface of the part with the base plate. Von Mises stress is a theoretical measure of (average) stress used to estimate yield failure criteria in ductile materials such as metals. It takes into account the principle and shear stresses and is used to determine if a given material will yield or fracture. The disadvantage of von Mises stress is it is always positive and cannot predict stress state (tensile or compressive) within manufactured components. The study shows that the maximum von Mises stress for the single laser beam, dual laser beams, four laser beams and thirty laser beams were 1438 MPa, 1379 MPa, 1303 MPa and 1201 MPa, respectively. The average von Mises stress (the average value of all the nodes at the bottom surface) of the dual laser, four laser and thirty laser beams PBF-MLB were 3.39 %, 4.63 % and 9.53 % lower than that of the single laser beam PBF-LB. The maximum von Mises stress and average von Mises stress results (Figure 5.5) indicate that to manufacture a single part, an increase in the number of laser beams reduces the magnitude and lower average RS distribution for the larger number of laser beams than that of the single beam PBF-LB modelling. The maximum *z* direction deflections for the single laser beam, dual laser beams, four laser beams and thirty laser beams PBF-MLB modelling were 3.61 μm, 3.49 μm, 3.26 μm and 2.25 μm, respectively. The lower RS and *z* direction deflection were formed for the larger number of laser beams PBF-MLB, which was due to the lower temperature gradient [50] caused by the multiple laser beams.

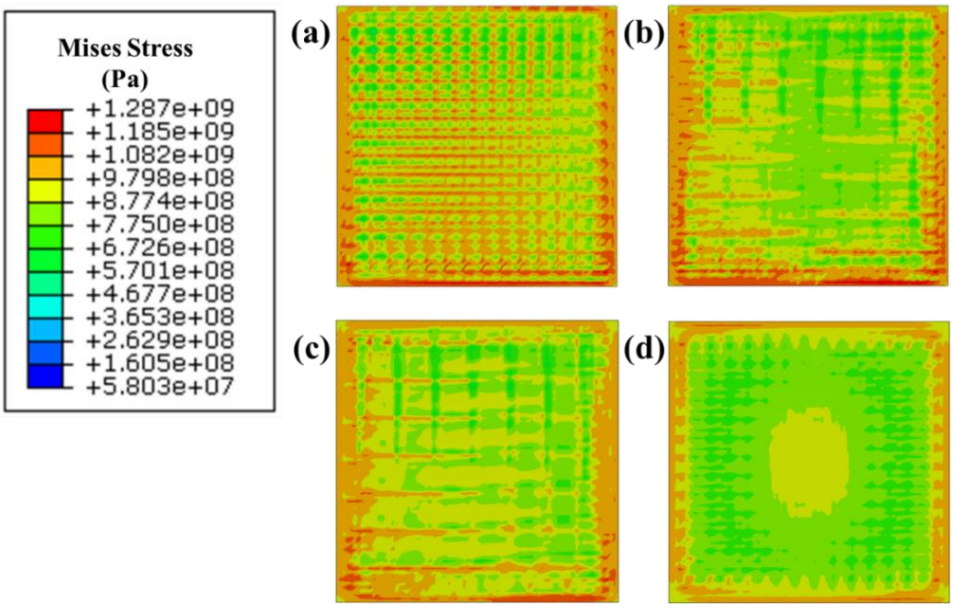

Figure 5.5. Computational final von Mises RS at the interface of the part and base plate (before releasing base plate constraints) for different numbers of laser beams: a) Single laser beam. b) Dual laser beams. c) Four laser beams and d) Thirty laser beams.

Temperature gradients (calculated per [50]) were sampled at two locations- the last element of the melt pool in the first and the last element in the last layer, at the same time i.e. when the final layer laser is complete. At the top layer, the temperature gradients were 48.18 K/µm, 56.47 K/µm, 59.28 K/µm and 65.863K/µm, and at the bottom layer the temperature gradients were 6.63 K/µm, 9.64 K/µm, 9.61 K/µm and 8.61 K/µm, for the single laser beam, dual laser beams, four laser beams and thirty laser beams models, respectively. The increase in temperature gradient causes a higher stress at the top surface for the larger number of laser beams. It is interesting to note that by the time the laser has completed the final layer, the trend in temperature gradients at the interface of the part and the build plate had almost reversed resulting in a lower stress at the build plate interface for multi-laser systems.

Processes with additional laser beams apply more energy at a given time and thus resulting in more heat to be conducted to the previously solidified layers and increasing the overall temperature of the powder bed [83]. For multiple laser beams PBF-MLB, the part was fabricated faster and there was less time for the heat to be dispersed compared with the single laser beam PBF-LB, resulting in a higher average temperature, initially a higher

temperature gradient in the most recent built layer, but overall a more uniform cooling and eventual lower temperature gradient in older previously solidified layers.

The effectiveness of PBF-MLB over single beam PBF-LB in terms of shorter build times, faster building rates, lower residual stresses and deflections, is detailed at Table 5.2. Though the laser exposure time for four laser beams PBF-MLB is 25 % of the single beam PBF-LB [216, 225], the building rate is just 2.74 times faster due to time overhead required for material spreading for each layer. The peak temperature increases with the number of laser beams, as there is more heat input at any given time and less time for the energy to be lost through conduction, convection, or radiation, therefore, the temperature gradient decreases and the cooling rate slows down, causing a reduction in RS and deflection.

Table 5.2. Comparison of multiple laser beams PBF-MLB with the single beam PBF-LB in this study.

Items	PBF-LB (single laser)	PBF-MLB (dual lasers)	PBF-MLB (four lasers)	PBF-MLB (thirty lasers)
Laser exposure time (s)	100% (0.45)	~ 50% (0.225)	~ 25% (0.1125)	~ 3.33% (0.015)
Max power density ($\times 10^{14}$ W/m^3)	100% (3.08)	~ 200% (6.16)	~ 400% (12.3)	~ 3000% (92.4)
Peak temperature (K)	100% (4145)	101.71% (4216)	103.04% (4271)	105.16% (4359)
Von Mises stress (MPa)	100% (1438)	95.90% (1379)	90.61% (1303)	83.5% (1201)
Deflection (μm)	100% (3.61)	96.68% (3.49)	90.30% (3.26)	62.33% (2.25)

5.3.2 Influence of scanning strategy on the thermal profile

The computational modelling results for the temperature fields of the additively manufactured parts using various different scanning strategies are demonstrated in Figure 5.6. The maximum temperature (called peak temperature in this chapter) of the layer of the material in relation to respective scanning strategies is shown by using the value on top of each image in Figure 5.6. Note that the predicted peak temperature of material exceeded the boiling temperature (3133 K) of Ti-6Al-4V material [315], which also occurred during physical manufacturing [316]. The predicted peak temperature of the majority of material was below the boiling temperature of material. Different scanning strategies obtained their peak temperatures at different time points, and the temperature contours at the half of the total time needed for a layer scanning of the top layer was

plotted to show the temperature fields of all the scanning strategies [41]. Comparing all the scanning strategies, the island mixed scanning strategy (Figure 5.4i and Figure 5.6i) obtained the highest peak temperature, which is due to the dual laser beams locally scanning a very small area of material simultaneously. This conclusion agrees with the single laser beam PBF-LB research outcomes by Cheng et.al. [41]. While the delayed laser scanning (Figure 5.4l and Figure 5.6l) obtained the second highest temperature which may due to the shorter distance (90 μm) of the two beams compared with other scanning cases (100 μm), even though the secondary laser beam was with a reduced laser power. The parallel halves scanning strategy (Figure 5.4g), in which the two laser beams were maintained farthest apart from each other, obtained the lowest peak temperature.

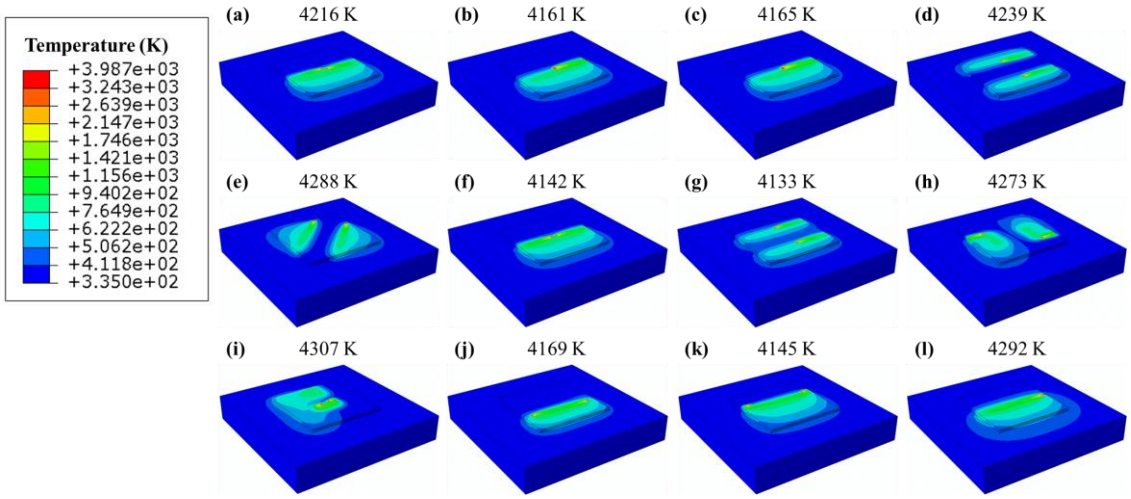

Figure 5.6. Computational results of temperature contours of the twelve different scanning strategies (logarithmic scale) before releasing base plate constraints.

5.3.3 Influence of scanning strategy on residual stress

The final RS refers to the RS of part after the build manufacture is completed and has been allowed to cool for 2000 s. The multiple cut views of RS (von Mises stress, *x* direction stress σ_{xx}, *y* direction stress σ_{yy}, *z* direction stress σ_{zz}, maximum principal stress and minimum principal stress) are presented in Figure 5.7. The *x* (transverse direction) and *y* (longitudinal) directions have been shown in Figure 5.4 and the *z* direction (build direction) is vertical to the *x*-*y* plane. Figure 5.7a shows that the maximum von Mises stress occurs at the interface between the part and the base plate, indicated by the red arrows (Figure 5.7a). At the interface, the von Mises stress is higher at the edges than that

at the central area. Figure 5.7b illustrates that the centre of the *x* direction stress contour is tensile stress while stress at the two edges in the *x* direction is compressive. For the *y* direction stress σ_{yy}, the highest tensile stress occurs at the central areas of the interface (Figure 5.7c). The high σ_{xx} and σ_{yy} RS located at the interface between the part and the base plate was also found in the computation for the single laser beam PBF-LB process [41]. Figure 5.7d shows the highest σ_{zz} can be found at the interface between the part and the base plate. The maximum principal tensile stress also occurs at the interface (Figure 5.7e). While the least minimum principal stress occurs at the top surface of the part and the minimum principal stress has the highest value along the trajectories of the laser beam scanning (Figure 5.7f). The high RS at the interface between the part and the base plate has potential to cause cracking of the manufactured part either during manufacturing (hot cracking) or in service (cold cracking).

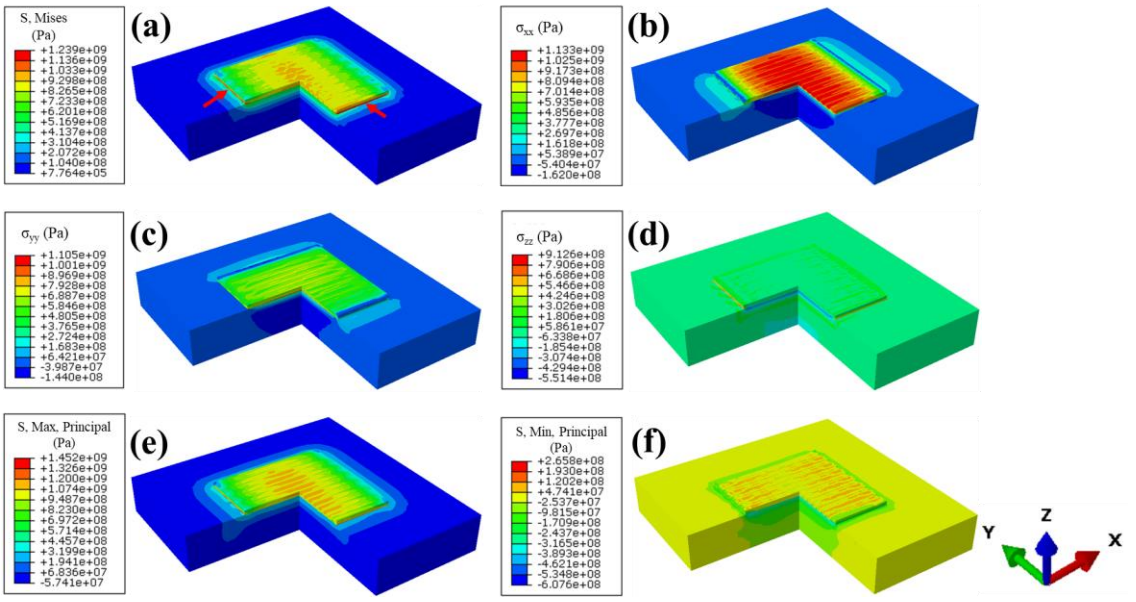

Figure 5.7. Multiple cut views of predicted residual stress by scanning case (a) (see Figure 5.4a) after cooling down for 2000 s (before releasing base plate constraints): a) von Mises stress. b) σ_{xx} RS along the *x* direction. c) σ_{yy} RS along the *y* direction. d) σ_{zz} RS along the *z* direction. e) The maximum principal stress and f) The minimum principal stress.

Figure 5.8 shows the modelling results of the maximum principal stress contours for the twelve different parts that were manufactured using respective scanning strategies before releasing constraints at the bottom of base plate (Figure 5.4). The sub-figures in Figure 5.8 and contour figures thereafter in this work shared the same legend scale in each

individual figure. The scanning patterns (both the scan directions and the scan vectors) can determine the stress distributions (Figure 5.8) and the average of the maximum principal stress (Figure 5.9). The results show the parallel S no rotation scanning (Figure 5.8c, Figure 5.9c and Figure 5.4c) produced the highest average maximum principal stress (900.57 MPa). The parallel S 90° rotation scanning (Figure 5.8b, Figure 5.4b) resulted in a lower and more uniform distribution of the maximum principal stress than that of the parallel S no rotation scanning (Figure 5.8c, Figure 5.4c), demonstrating the importance of rotating the laser scan direction by 90° after finishing each layer. The delayed laser scanning (Figure 5.8l, Figure 5.9l and Figure 5.4l) produced the lowest average maximum principal stress (772.30 MPa) among all the scanning strategies and it can be seen that the secondary delayed laser helps to mitigate the RS. Figure 5.9 illustrates 45° approaching beam scanning (Figure 5.9e) caused a marginal 3.12 % lower RS than 0° approaching beam scanning (Figure 5.9d). Island scanning (Figure 5.8h and Figure 5.8i) produced a higher RS at the island interface than the island central areas. It can be seen that regardless of the specific laser scanning strategy, high maximum principal stress always occurs at the interface between the part and the base plate. At the central area of the part, the residual maximum principal stress is always higher than that at the edges of the part. It can be seen from Figure 5.8 that the maximum principal stress of both beginning (Figure 5.8j) and ending (Figure 5.8k) contour fill scanning are slightly lower than that of the opposite S scanning (Figure 5.8a), which indicates that the contour fill scanning strategy is beneficial for mitigating the RS. The RS of opposite S scanning strategy (Figure 5.8a) is higher than that of parallel S 90° rotation scanning strategy (Figure 5.8b) due to the peak temperature of the opposite S scanning strategy (Figure 5.6a, 4216 K) being higher than that of the parallel S 90° rotation scanning strategy (Figure 5.6b, 4161 K). The case (a) and case (b) had larger residual stresses than the case (d), case (f) and case (g), which indicates that laser proximity influences the final RS that two laser beams closed to each other obtained larger RS than two laser beams kept far away. This is assumed to be caused by laser beams close to each other had larger temperature gradients.

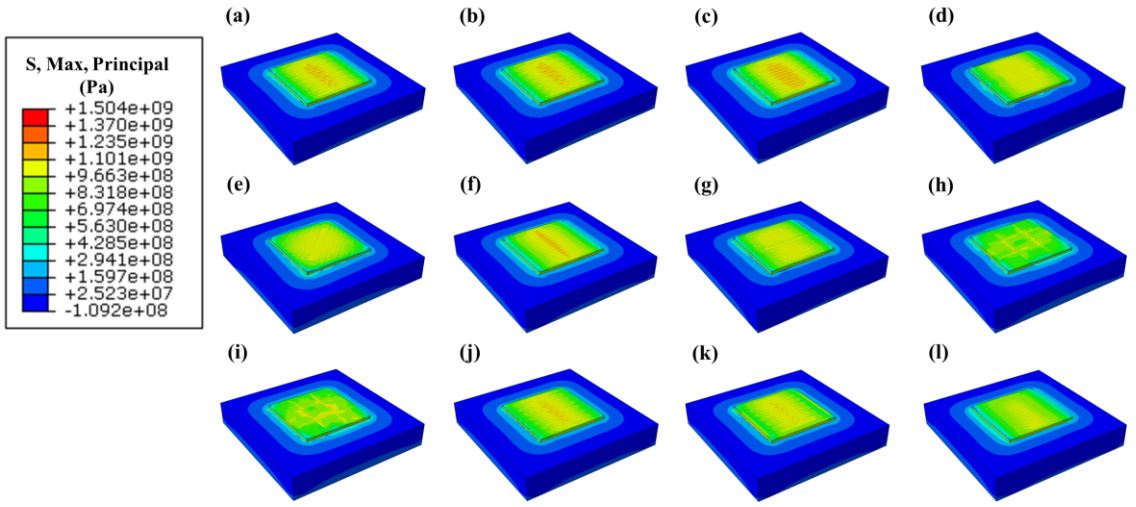

Figure 5.8. The predicted final maximum principal stress for the twelve different scanning strategies before releasing base plate constraints.

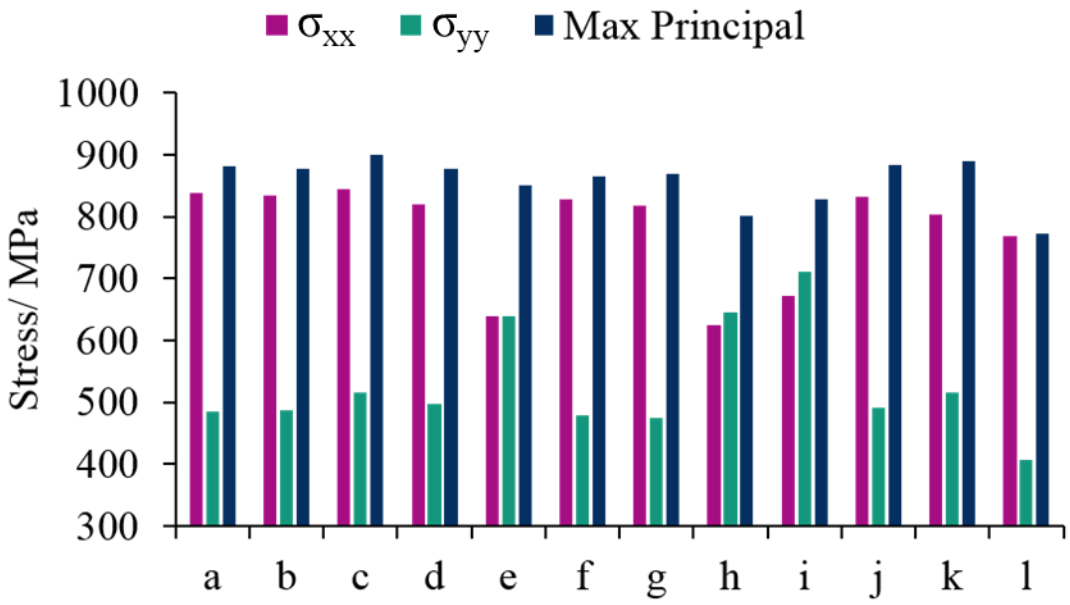

Figure 5.9 Predicted final average RS statistics for the different scanning strategies before releasing base plate constraints (σ_{xx}, σ_{yy} and maximum principal stress).

The σ_{xx} RS before releasing constraints at the bottom of base plate is presented in Figure 5.10 by using the contour plots and the average σ_{xx} (of all the nodes at the top surface) shown in Figure 5.9. Figure 5.10 shows the σ_{xx} stress at the central area of the part is always higher than that at the edges of the part. The results from Figure 5.9c and Figure 5.10c show the maximum σ_{xx} stress (844.85 MPa) occurs at parallel S no rotation scanning,

which is 1.28 % larger than the parallel S scanning with 90° layer rotation (Figure 5.10b). Figure 5.10e and Figure 5.9e illustrate the 45° rotation approaching beam scanning (Figure 5.4e) resulted in the minimum average σ_{xx} RS (624.14 MPa) and the approaching beam scanning (Figure 5.9h) generated the second lowest average σ_{xx} RS (671.23 MPa). The lowest average σ_{xx} of the 45° rotation approaching beam scanning (Figure 5.10e) is 26.12 % lower than that of the highest σ_{xx} of the parallel S no rotation scanning (Figure 5.10c). The σ_{xx} stress distribution pattern by scanning strategies of (Figure 5.4a - d and Figure 5.4f - g) are consistent with results of literature [39, 288]. The delayed laser scanning (Figure 5.10l) obtained significant reduced (8.35 % lower) σ_{xx} RS compared with the opposite S 90° rotation scanning (Figure 5.10a).

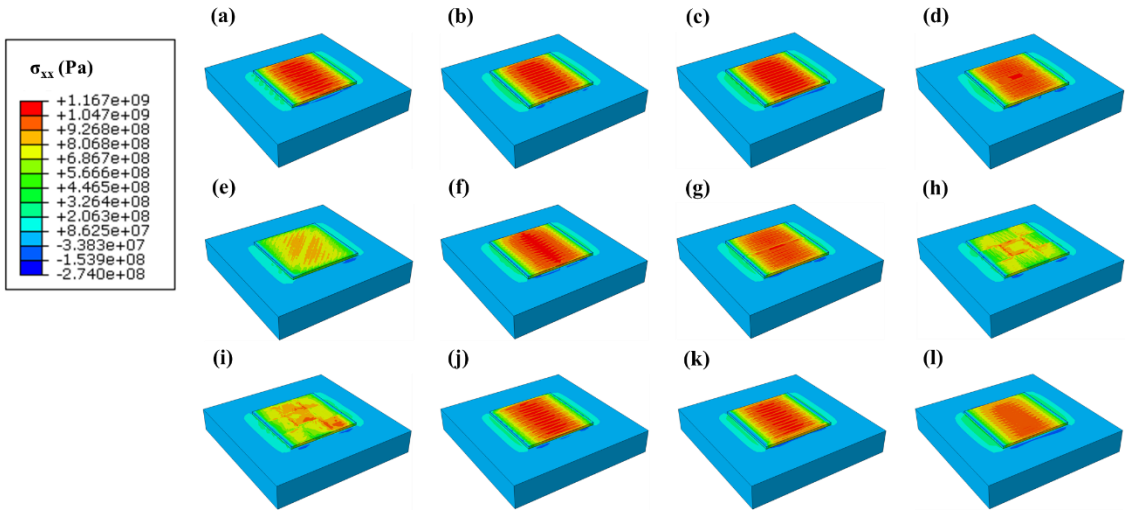

Figure 5.10. Computational final RS along the *x* direction σ_{xx} for the different scanning strategies before releasing base plate constraints.

Figure 5.11 shows the *y* direction RS σ_{yy} for all the twelve scanning strategies. Being different with the results for σ_{xx} (Figure 5.10), the σ_{yy} for the island scanning (Figure 5.11i, Figure 5.4i and Figure 5.11h, Figure 5.4h) and the 45° rotation approaching beam scanning (Figure 5.11e, Figure 5.4e) produced higher σ_{yy} residual stresses than other scanning strategies. The island mixed scanning (Figure 5.11i and Figure 5.12i) had the maximum σ_{yy} stress of 710.81 MPa due to that the scan direction of the islands rotates 90° for subsequent island. The 45° rotation approaching beam scanning (Figure 5.11e, Figure 5.4e) had the minimum σ_{xx} stress but had comparative higher σ_{yy} stress may be caused by the comparatively more uniform temperature gradient variance in *x* and *y* directions [41].

The scanning cases (e), case (h) and case (i) had larger σ_{yy} stress at the part central fields than the edges. Except case (e), case (h) and case (i), all other scanning strategies had similar low σ_{yy} stress distribution and quite uniform σ_{yy} stress distribution at the central areas and the edges.

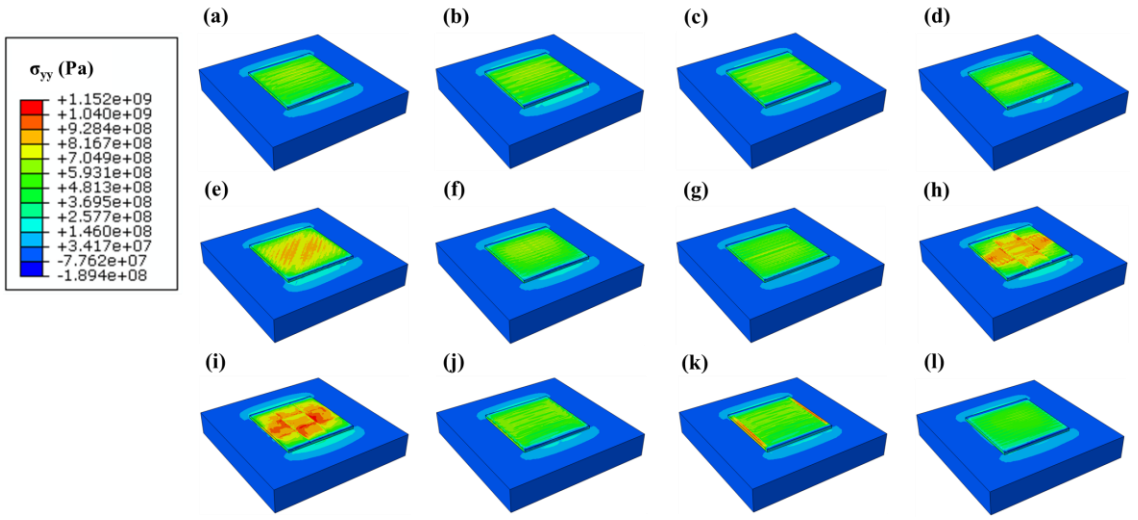

Figure 5.11. Computational final RS along the *y* direction σ_{yy} for the different scanning strategies before releasing base plate constraints.

Figure 5.12 shows the maximum RS (σ_{xx}, σ_{yy} and maximum principal stress) statistics for all the twelve scanning strategies. Combining the results of Figure 5.9, Figure 5.10 and Figure 5.12, the parallel S no rotation scanning (Figure 5.4c and Figure 5.12c) obtained the highest maximum principal stress (1504 MPa) and highest average maximum principal stress while the 45° rotation approaching beam scanning (Figure 5.4e) had both the least σ_{xx} average distribution and the least maximum *x* direction RS (1005 MPa). The least maximum principal stress occurs at the delayed laser scanning of 1447 MPa (Figure 5.12l), which validated the assumption that the addition of a second laser could reduce stress. Figure 5.12 states the maximum σ_{yy} (1154 MPa) occurred on the island mixed scanning (case i) and the delayed laser scanning (Figure 5.12l) had the lowest maximum σ_{yy} RS (861.5 MPa) among all scanning cases (Figure 5.4). The highest σ_{yy} stress (Figure 5.12i) was 33.95 % higher than the lowest maximum σ_{yy} stress (Figure 5.12l). The ending contour fill (Figure 5.12k) caused a 16 MPa lower maximum principal stress than the beginning contour fill (Figure 5.12j), which indicates the ending contour fill scanning strategy could be beneficial for reducing RS. The higher maximum principal RS compared

to σ_{xx}, σ_{yy} stresses in Figure 5.12 is also influenced by factors such as σ_{zz} and shear stresses. As the focus of this study is on normal residual stresses, the computational modelling results of shear stresses were not explicitly presented but could be in future work.

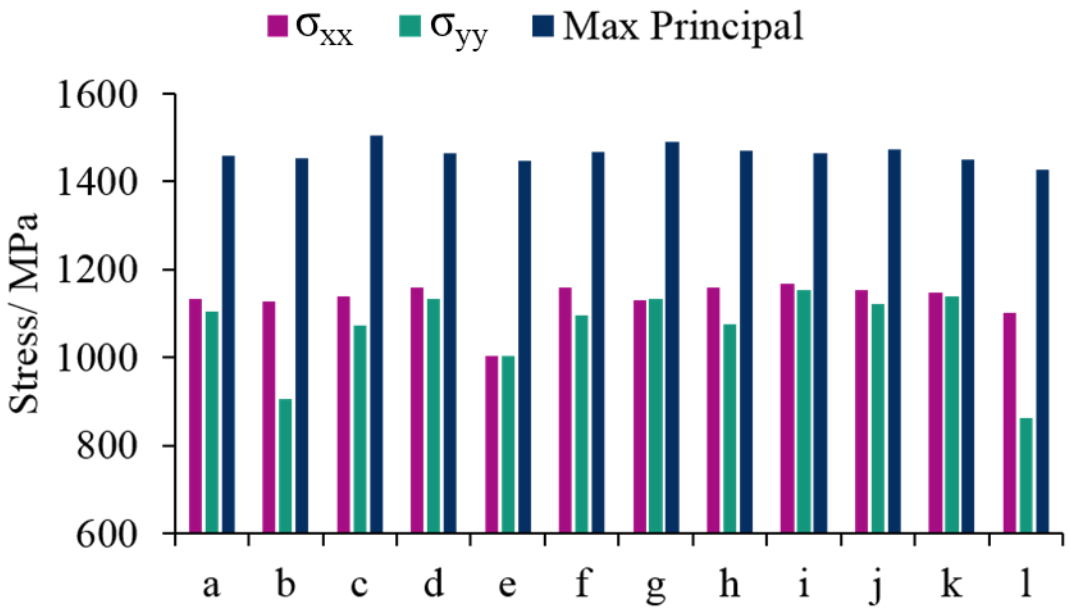

Figure 5.12. Computational final maximum RS (σ_{xx}, σ_{yy} and maximum principal stress) statistics for the different scanning strategies before releasing base plate constraints.

5.3.4 Influence of scanning strategy on the *z* direction deflection

Figure 5.13 illustrates the final *z* direction deflection of the parts for the five typical scanning strategies (Figure 5.4b-e, i and l). The deflection contours show significant influences of the scanning strategies on the final *z* direction deflection. The *z* direction deflection distributions resemble the laser beams scanning paths (Figure 5.13i). It can be seen that the positive *z* direction deflection is predicted in the laser beam path, with negative *z* direction deflection predicted between neighbouring laser paths (Figure 5.13). A similar distribution of *z* direction deflection (i.e. positive in the laser beam trajectories and negative at laser intervals, Figure 5.13) was observed in the literature [173, 195, 317]. The *z* direction deflection of parallel S 90° rotation scanning (Figure 5.13b, Figure 5.4b) is lower than the parallel S no rotation scanning (Figure 5.13c, Figure 5.4c), which is consistent with the maximum principal stress results (Figure 5.8).

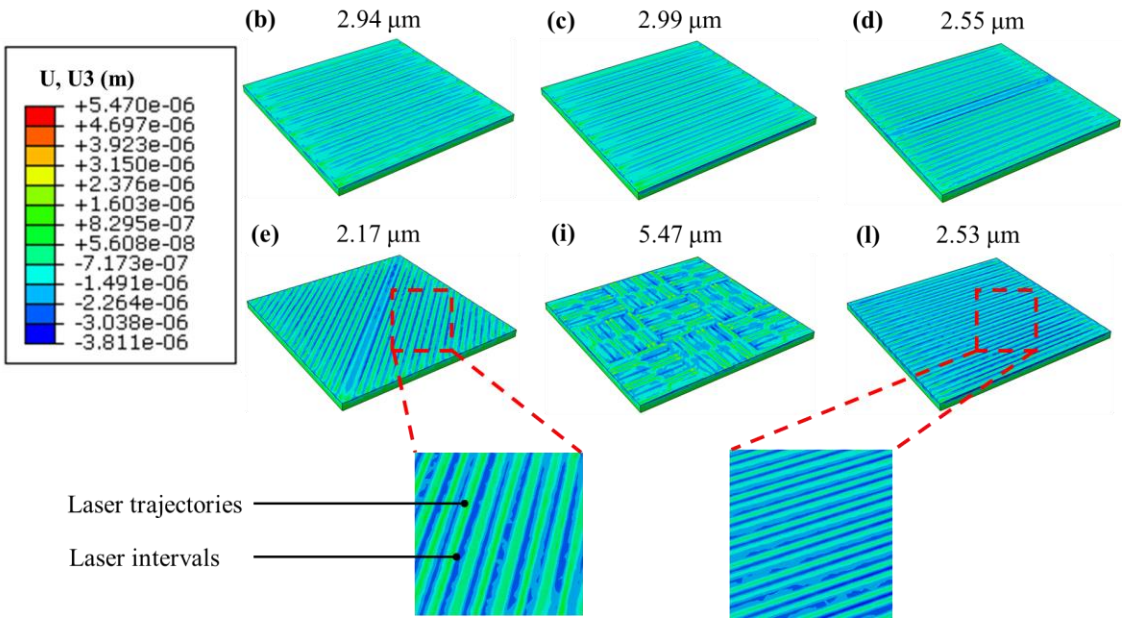

Figure 5.13. Computational final *z* direction deflections for the different scanning strategies before releasing base plate constraints.

Figure 5.14 shows the maximum *z* direction deflection of the parts that were manufactured using different scanning strategies. It can be found that the largest maximum *z* direction deflection occurred at the island mixed scanning (5.47 µm) (Figure 5.14i) was 152 % higher than the lowest maximum *z* direction deflection that was occurred at the 45° rotation approaching beam scanning (2.17 µm) (Figure 5.14e). The island mixed scanning had the maximum *z* direction deflection, which was due to the energy concentration of the two laser beams focused on one island simultaneously and the residual heat effect [41]. The peak temperature of the island mixed scanning (Figure 5.6i) is the highest among all cases which also causes a higher temperature gradient that further increased the deflection. The case (j) and case (k) had higher *z* direction deflections than case (a), which indicates that the contour fill scanning leads to higher deflection than no contour fill. A possible reason is that case (j) and case (k) had shorter scanning vectors than case (a), which caused more energy concentrated at the part central areas during the same time period. It can be seen from Figure 5.14 that the case (a) and case (b) had larger maximum *z* direction deflections than case (d), case (f) and case (g), which indicates that laser proximity also influenced the *z* direction deflection that laser beams closer to each other got larger *z* direction deflection, which is the consistent with the influences of laser proximity to the

temperatures and residual stresses (Figure 5.8). There were minor differences of the maximum z deflections for the 0° approaching beam scanning (case d), opposite halves scanning (case f), parallel halves scanning (case g) due to that the dual laser beams kept far away from each other during scanning.

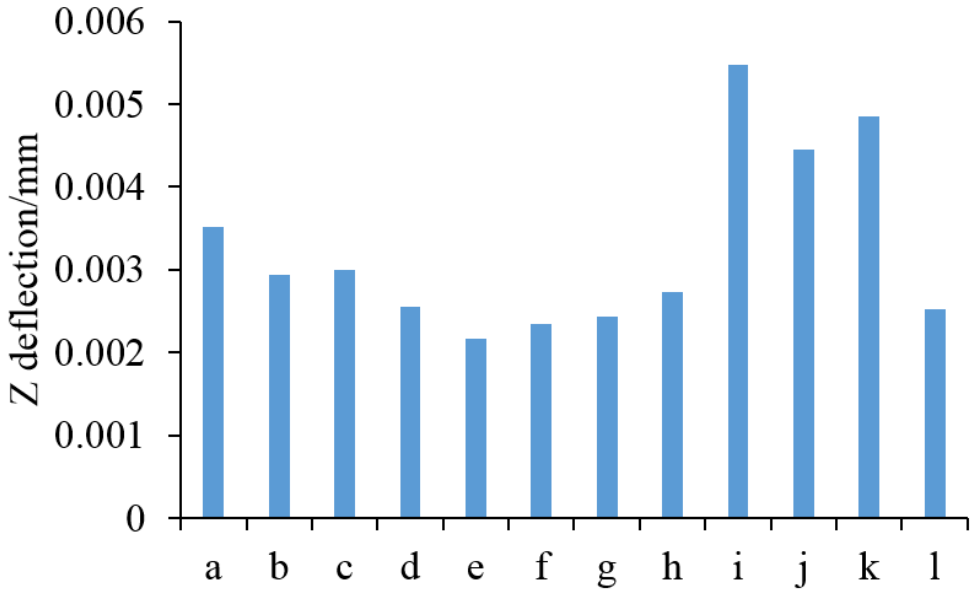

Figure 5.14. Computational results of maximum *z* direction deflection statistics for all cases before releasing base plate constraints.

Figure 5.15a illustrates the maximum *z* direction deflection of the base plate for all the scanning strategies and Figure 5.15b shows the contour plot for *z* direction deflection of the base plate for scanning strategy case a. In Figure 5.15a, it can be seen that the 0° approaching beam scanning (case d), the 45° rotation approaching beam scanning (case e), the island approaching beam scanning (case h) and the island mixed scanning (case i) resulted in comparatively higher maximum *z* direction deflection on the base plate than other cases. The difference of *z* direction deflection between the part and the base plate illustrates the final component's deflection is not only determined by the base plate deflection, but also influenced by the part deposition process. Figure 5.15b states the base plate deformation focused on the edges of the base plate interface contacted with the part as well as the part central area on the base plate. The laser scanning paths centres also deformed more than other fields. A similar base plate *z* direction deflection was found in prediction [196].

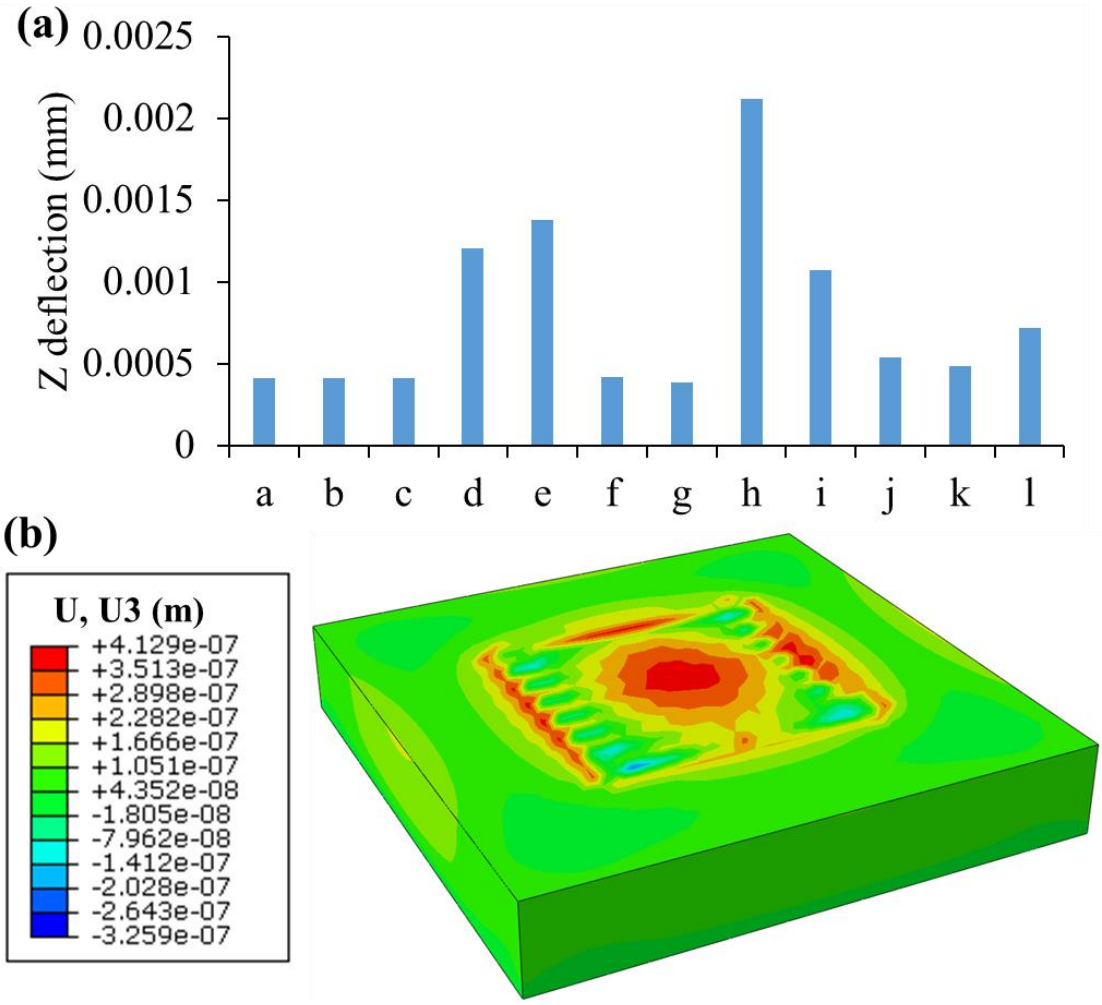

Figure 5.15. Computational results of *z* direction deflection on the base plate before releasing base plate constraints: a) Maximum z direction deflection statistics for the twelve scanning strategies and b) Contour of the opposite S scanning pattern (a).

5.3.5 Influence of base plate constraints on residual stress and deflection

The final maximum RS (σ_{xx}, σ_{yy} and principal stress) statistics for the different scanning strategies after releasing constraints at the bottom of the base plate are shown in Figure 5.16. RS after removing the constraint is more important than those with the constraint of base plate. The maximum RS (σ_{xx}, σ_{yy} and principal stress) reduced after removing constrain of base plate (Figure 5.12) compared to before base plate removal (Figure 5.16), due to stress releasing. Releasing these constraints resulted in some reordering of the scanning strategies in terms of stress and deflection behaviour. The lowest σ_{xx} RS occurred at the 45° rotation approaching beam scanning (Figure 5.16e) and the delayed laser

scanning (Figure 5.16l) had the lowest σ_{yy} RS, which is consistent with the modelling results before releasing the base plate constraints. However, the largest maximum principal stress occurred at the parallel halves scanning (Figure 5.12g) after releasing the base plate constraints while the largest maximum principal stress occurred at case (c) before releasing constraints of the base plate. Directly comparable results were obtained for the maximum principal stress before (Figure 5.12) and after (Figure 5.16) releasing constraints at the bottom of the base plate for this thin plate structure. In this study, the part removal process (e.g. wire electrical discharge machining) and post heat treatments were not involved.

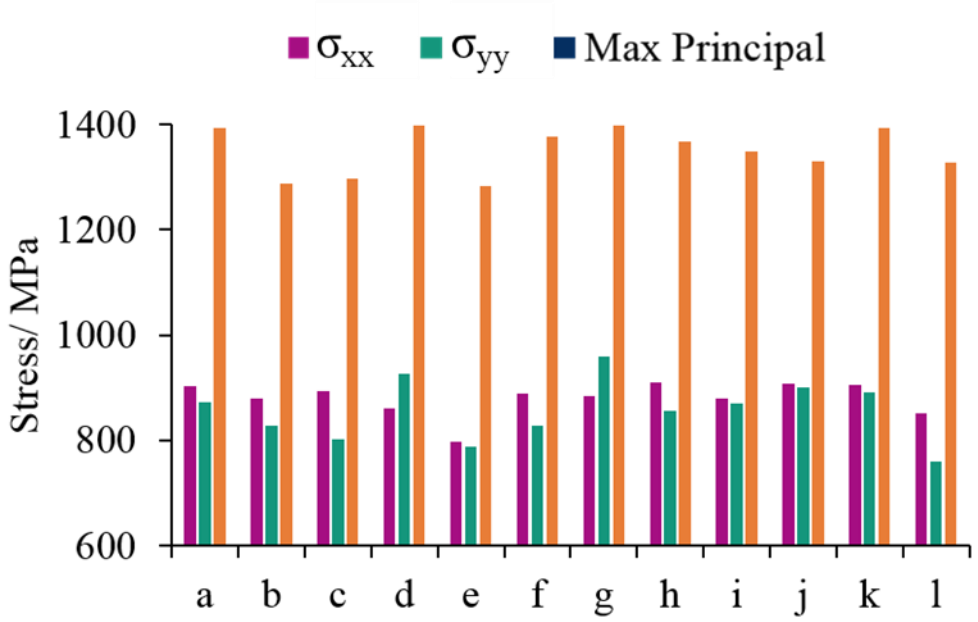

Figure 5.16. Computational results of final maximum RS (σ_{xx}, σ_{yy} and maximum principal stress) statistics for the different scanning strategies after releasing constraints at the bottom of base plate.

The *z* direction deflections of the part for the different scanning strategies after releasing constraints at the bottom of the base plate are shown in Figure 5.17. The *z* direction deflections became negative after releasing constraints at the bottom of the base plate (Figure 5.13). This is caused by the negative deflections at the base plate [39, 291] and there were less constraints at the bottom surface of the base plate and thus the part has more freedoms to deform. Due to thin plate (i.e. three layers) was predicted, the *z* direction deflections after releasing base plate constraints are tiny. The parallel halves scanning (case g) had significant deflection compared with other scanning cases. The 0°

approaching beam scanning (case d) had the least *z* direction deflection. The parallel S no rotation scanning (case c) had larger *z* direction deflection compared with parallel S 90° rotation scanning (case b), which is consistent with the experimental measurements that single *x* direction scanning caused larger deformation compared with the 90° rotation scanning strategy [164].

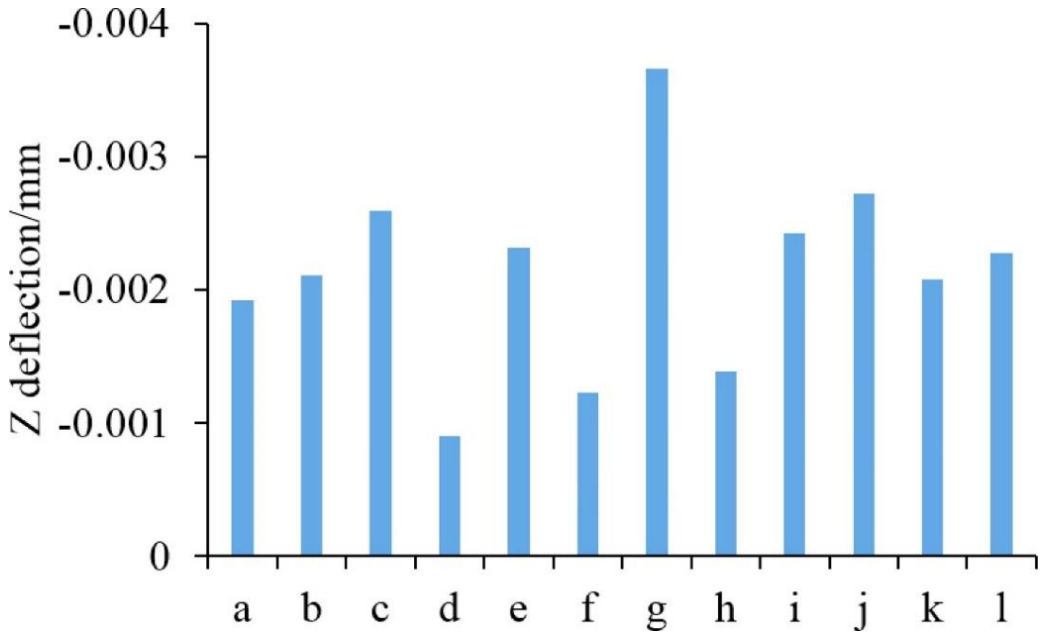

Figure 5.17. The predicted final *z* direction deflection statistics for the different scanning strategies after releasing base plate constraints.

5.4 Summary

Full coupled thermo-mechanical modelling was employed to computationally predict the thermal process and the RS of Ti-6Al-4V alloy parts that were manufactured by multiple laser beams PBF-MLB. Twelve different scanning strategies were used in the modelling. The results show scanning strategies influence the final RS and deformation significantly for the PBF-MLB. Based on the above thermal, RS and deflection results, the general guidelines for optimizing the scanning strategies on dual laser beams PBF-MLB are as follows:

- The lower RS and *z* direction deflection were formed for the larger number of laser beams PBF-MLB.

- To obtain the lowest peak temperature, the two laser beams need to be spaced apart from each other. Laser proximity influences peak temperatures, which is due to that the energy concentration and shorter scanning vectors led to higher peak temperatures.
- The parallel S no rotation scanning (Figure 5.4c) produced the highest maximum RS and larger stress than the parallel S 90° rotation scanning (Figure 5.4b), which indicates that 90° layer rotation after each layer is also necessary for minimising the final RS in PBF-MLB. This is likely due to perpendicular laser trajectories between each layer balancing the directional residual stresses.
- The delayed scanning strategy (Figure 5.4l) is beneficial for reducing RS because the secondary delayed laser slows down the cooling speed and thus mitigating RS.
- The 45° rotation approaching beam scanning obtained the second least RS and the parallel S no rotation scanning should be avoided as it resulted the highest RS.
- The island mixed scanning strategy gives the highest peak temperature and the parallel halves scanning strategy obtained the lowest peak temperature.
- The 45° rotation approaching beam scanning had the lowest *z* direction deflection.
- The results of higher residual stresses occurred along the interface between the base plate and the part for the dual laser beams PBF-MLB simulation is consistent with the single laser beam PBF-LB simulation in **Chapter 4**.
- After releasing constraints at the bottom of the base plate, a decrease in RS was found. The parallel halves scanning had the largest RS (maximum principal stress) and the lowest stress was occurred at the 45° rotation approaching beam scanning.
- After releasing constraints of the base plate, the 0° approaching beam scanning had the least *z* direction deflection.

6 Temperature and residual stress in multi-part build by laser beam powder bed fusion additive manufacturing

6.1 Introduction

PBF-LB operators have reported the inconsistent properties between identical specimens produced in a single build (i.e. batch manufacturing) despite uniform material, consistent manufacturing process parameters, and an equal number of laser beams in use [23, 84]. A change of the number of parts per build or the order in which the parts are printed (in each layer) may produce significantly different thermal histories and thus RS, microstructure and mechanical properties, between identical specimens in the same build [236]. The primary reason for variation in properties for the multi-part fabrication is the temperature history during the physical PBF-LB manufacturing. For multi-part manufacturing, there are two significant parameters that distinguish it from single part builds; total energy input and inter layer dwell time (ILDT). For a PBF-LB build with a larger number of parts (Figure 6.1), there will be more energy input into the powder bed compared with a build with a single part produced. The change of the number of parts per build would also result in different ILDTs, which indicates different layer cooling step times for different batch sizes of parts manufacturing, e.g. 20 s for the single part build and 55 s for the multi-part manufacturing [236], permitting a greater temperature fluctuation in recently printed layers as new layers are added. The larger ILDT indicates a longer overall duration of printing and cooling during multi-part PBF-LB manufacturing. In addition, for parts to be manufactured in the same build plate, the first part to be printed per layer has a longer time to cool before spreading and deposition of the new material. In contrast, the last part to be printed in each layer is immediately covered with new powder. However, the multi-part build effects on temperature and RS and variance between parts within a multi-part build have yet to be widely investigated in PBF-LB [221].

A previous study by Yakout et al. [318] reported that the location of the part on the base plate affected microstructure and RS in PBF-LB manufacturing. However, Robinson et

al. [195] stated the location of the part on the base plate had no significant effects on the resulting stress of parts in PBF-LB. Also, different locations of the base plate will have different in-plane depths of powder surrounding the part and different distances from other parts and distances to the build chamber wall. It has been shown that the cooling of parts at the centre of the base plate is dependent on the heat from the surrounding parts [318]. In addition, for the multi-part build, part spacing (i.e. the distance between adjacent parts) can also affect the cooling and resultant mechanical properties of PBF-LB manufactured parts [319]. Parts built with tighter spacing within the build volume have a more concentrated thermal mass which results in potential slower cooling [319]. However, the part spacing effects on RS in a multi-part build have yet to be widely investigated in PBF-LB [221].

Figure 6.1. Multiple orthopaedic hip stem implants printing in the same build plate by EOS [320].

Most of the metal AM process simulation models found in the literature (and in previous chapters of this thesis) are focused on the PBF-LB manufacturing of a single part, or a small portion of a single part [36, 45, 133, 143]. Although most of the real printing consists of a batch of samples (Figure 6.1), there is limited process FEM of multi-part build and thus multi-build effects on the thermal and mechanical behaviours of part have been largely ignored [228]. Prabhakar et al. [196] simulated RS formation of five cubic shaped Inconel 718 samples during the PBF-EB process but did not investigate the influence of sample number on RS of parts. In addition, for the convenience of computation, all the parts in the same layer were simplified to melting and cooling simultaneously in

Prabhakar's research, which is inconsistent with the practical manufacturing. To accurately simulate the practical manufacturing process of multi-part build in PBF-LB, the printing order of components and the ILDT of each layer should be considered. The ability to accurately simulate the physical PBF-LB manufacturing process of multi-part build and predict the temperature evolution and RS of parts would further advance the development of PBF-LB process modelling.

The aim of this research is to investigate the multi-part build effects on temperature and stress in PBF-LB manufacturing by computational finite element modelling. The key objectives of this study are:

a) Development of a 3D coupled thermo-mechanical modelling capability for the multi-part build PBF-LB manufacturing.
b) To investigate the influence of the sample numbers per build on temperature and RS in PBF-LB manufacturing.
c) Investigating effect of part printing order in the same build plate effects on RS in multi-part.
d) Computationally predicting effects of part spacing on RS in multi-part PBF-LB build.

This research could be beneficial for informing PBF-LB machine operators of the optimum build-plate configuration for minimising component RS.

6.2 Methods

6.2.1 Setup of the process finite element modelling

A 50 mm long, 10 mm wide and 60 mm high prism-shaped model of Ti-6Al-4V material is simulated above a build plate with dimension of 250 × 250 × 25 mm^3 [44, 87], as shown in Figure 6.2. Previous chapters (**Chapter 3 - 5**) investigated RS of rectangular square geometry, a complex prism geometry was chosen in this study. The cross-sectional area of the prism decreases along the build direction, which causes the total heat input and ILDT per layer to decrease as build height increases. To obtain the temperature and stress information for the multi-part build, the sequentially coupled thermo-mechanical

modelling is performed by the FEM software ABAQUS package (Dassault Systems, USA, 2019) [133]. For the mechanical analysis, the bottom of the build plate is fully constrained during the whole manufacturing process except for the build plate constraints releasing steps. At these final steps, all the nodes at the bottom surface of the build plate, except for the four extremity nodes, are unconstrained to allow deformation of the part, simulating part removal from the build plate [291, 292]. In this work, the layer-by-layer process simulation method described in **Chapters 3** and **4** is utilised, where all finite elements at each whole layer of a part are heating, melting, and solidification simultaneously.

The custom written Python script (Figure 3.1) for ABAQUS utilised in **Chapters 3** and **4** for the single part AM modelling is adapted for the multi-part build simulation to section the 3D macroscale parts into thin layers in the FEM model. The 'model change' function described in **Chapters 3** and **4** is applied to simulate the gradual deposition of new layers [149, 160, 292]. Due to the symmetry characteristic of the FEM model (along the XZ plane in Figure 6.2) and the layer-by-layer modelling approach (which models the printing of a whole layer instantly), half of the prediction model is built to save the computational cost (Figure 6.2). However, in this study, the layer-by-layer modelling approach is adapted to deposit the layer for each part separately (not instantaneously printing the full layer of all parts).

To investigate the influence of the number of samples on temperature and RS, three sets of modelling varying the number of prisms (1, 2 and 4) are performed in the same build plate by ABAQUS (Figure 6.2). The total seven prisms are labelled with '1-1', '2-1', '2-2', '4-1', '4-2', '4-3' and '4-4' (Figure 6.2), respectively, where the first number of the symbol indicates the total number of samples in a single build and the second number means the printing order of part in the same build plate during manufacturing. For the single prism modelling (Figure 6.2b), the prism locates at the centre of the build plate. For the two prisms (Figure 6.2c) and four prisms (Figure 6.2d) modelling, the prisms are positioned symmetrically with a 40 mm space (d_{ps} in Figure 6.2) between two adjacent parts. To investigate the influence of part spacing on the final RS, the two parts PBF-LB process modelling with part spacing of 80 mm and 120 mm are also utilised. Note that the

prism ‘2-1’ and ‘2-2’ with a part spacing of 120 mm in two-part build is at the same location of the build plate with the part ‘4-1’ and ‘4-4’ in the four-part build, respectively.

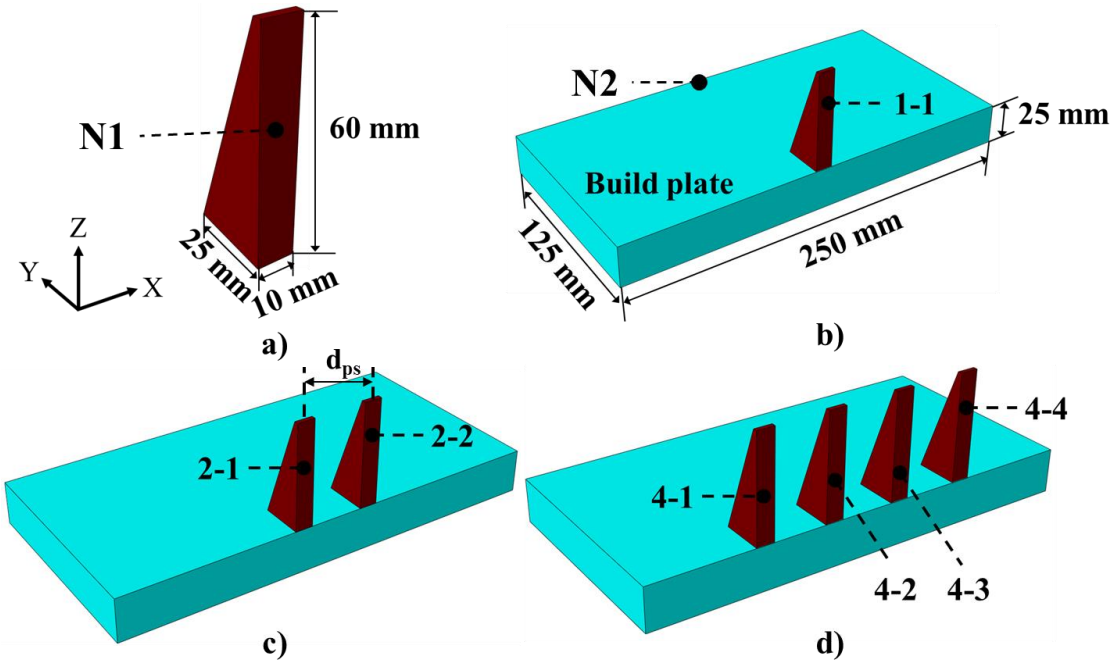

Figure 6.2. Illustration of the computational FEM model: a) Geometry of prism [87]. b) Single prism model. c) Two prisms model and d) Four prisms model.

In this work, it is assumed that the thin layers of each part are manufactured sequentially for the two and four prims manufacturing. For instance, the active layer of the part ‘2-1’ on the powder bed is fabricated first and then the layer of part ‘2-2’ is manufactured. The build direction is along the positive *z* direction and the prisms manufacturing sequence is along the *x* direction (Figure 6.2), which is opposite to the assuming gas flow direction along the negative *x* direction.

To simulate the practical PBF-LB manufacturing process that has been described in **Chapter 1** and for the convenience of computational FEM, the computational process for the single prism modelling consists of the following processes:

a) The heating step is the step in which the material is heated up to above the melting temperature. By using the layer-by-layer simulation method, each active (top) layer of the part is heated simultaneously for a period of heating step time t_m.

b) Layer cooling step represents the cooling and solidification process of the material, which is in response with the time for powders spread over the powder bed during practical PBF-LB manufacturing. The layer cooling step time t_c is based on the converged results of **Chapter 3**.

The above two steps are repeated for each layer until the 3D part is completed. After completion manufacturing of the part, there is a final long-time cooling step (e.g. 6 hours) for the part to be completely cooled to room temperature with no more deposition of powder material and no more heat input. For the two prisms process modelling, it consists of the following steps:

a) The heating step for the first part '2-1' (Figure 6.2c) to be heated and melted for a period of heating step time t_m, which is the same as the heating step for the single prism modelling.
b) Cooling step of the first part '2-1' (Figure 6.2c) for a period of cooling time interval t_i, which is before fabrication of the active layer of the second part '2-2' (Figure 6.2c). The cooling time interval t_i is defined as the time to manufacture the active layer of the first part (or any part in the layer) [143].
c) The heating step for the active layer of the second part '2-2' for a period of heating step time t_m, where the corresponding top layer of the second part is heated.
d) Layer cooling step for a period of t_c. During this t_c time, all the two parts continue to cool through thermal disseminations.

The above four steps are repeated for each layer until finish manufacturing of the two parts. At the end of the computational process modelling, there is a final cooling step for the two prisms to cool to room temperature. The process modelling of the four prisms consists of the following steps and is shown in Figure 6.3:

a) The heating step for the first part '4-1' (Figure 6.2d) to be manufactured for a period of heating step time t_m.
b) The first part '4-1' cooling step for a period of cooling time interval t_i. This step is after manufacturing of the active layer of the first part '4-1' and before melting of

the active layer of another three parts. The first part '4-1' begins to cool from the beginning of this cooling step.

c) The heating step for the second part '4-2' (Figure 6.2d) for a period of heating step time t_m.

d) The second part cooling step for a period of cooling time interval t_i. The second part starts to cool from the beginning of this step.

e) The heating step for the third part '4-3' (Figure 6.2d) for a period of t_m.

f) The third part cooling step for a period of cooling time interval t_i. The third part begins to cool from the beginning of this step.

g) The fourth part '4-4' (Figure 6.2d) heating step for a period of time t_m.

h) Layer cooling step for a period of time t_c, where all the four parts continue to cool through this layer cooling step.

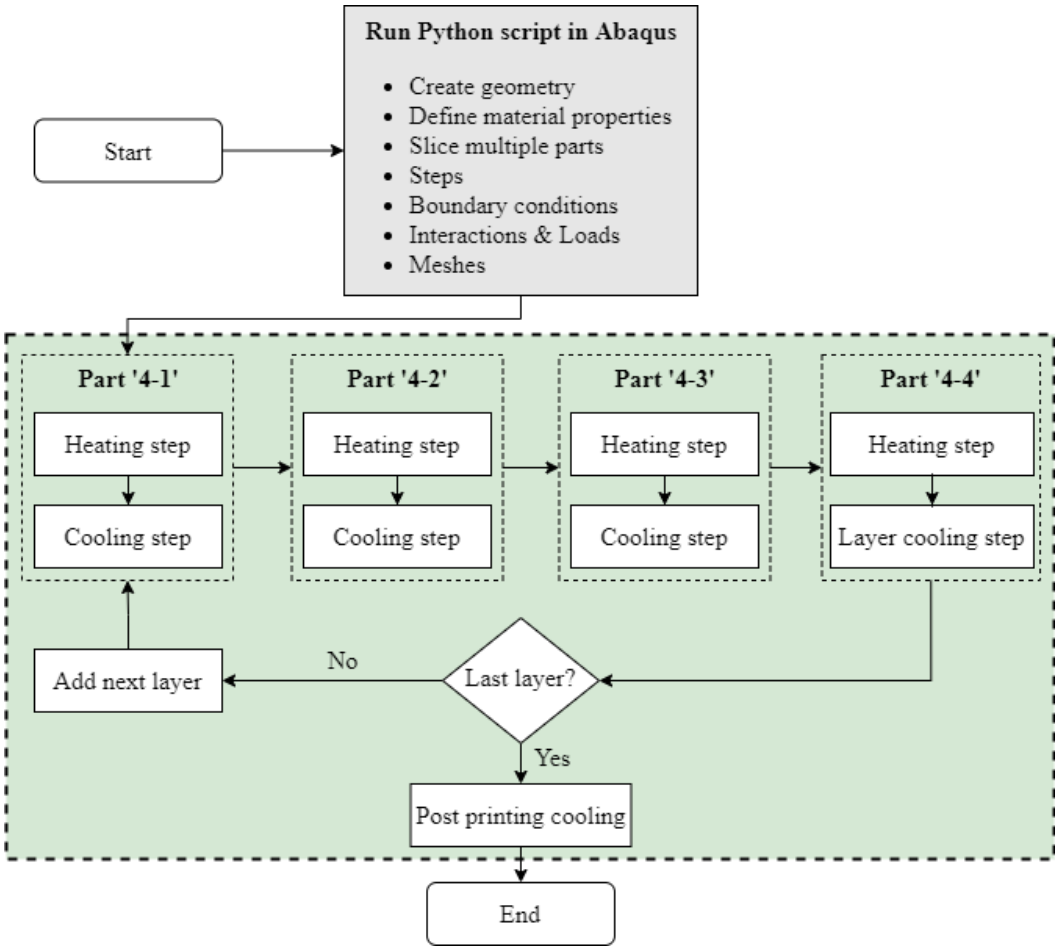

Figure 6.3. Flowchart for four-part thermo-mechanical PBF-LB modelling.

The above steps are repeated for each layer until completing the manufacturing process of all the four parts on the build plate, then all the parts are cooled to room temperature during the final post-printing process.

The effect of the number of parts per build on the temperature of the part is investigated via the temperature evolution at the central node of the part, which is labelled with 'N1' in Figure 6.2a. To investigate influence of the number of parts in a single build on the temperature of the build plate, temperature evolution at the node labelled 'N2' (Figure 6.2b) on the build plate is monitored for each simulation.

6.2.2 Thermal mechanisms

For the computational laser beam heating process in PBF-LB, the layer-by-layer approach with equivalent heat source (Eq. 2.6) is employed in this work, which has been described in **Chapters 3** and **4**. The governing equation for the computational finite element modelling using ABAQUS CAE is given based on the energy balance (Eq. 2.1).

The part cooling time interval t_i can be calculated based on the total scanning length of the active layer of a part and the laser beam scanning speed and can be defined as [143]:

$$t_i = \frac{L_t}{v_s} \tag{6.1}$$

where L_t is the total scanning length of the specific active layer of part and v_s is the laser beam scanning speed during the material melting process.

The ILDT for each layer is defined as the sum of part heating step time t_m, cooling time interval t_i and layer cooling step time t_c of all parts during manufacturing of a specific layer. As the cross-sectional area of the prism decreases along the build z direction, the ILDT per layer decreases with the number of layers of material deposited. For different numbers of the prisms manufacturing per build, the ILDT also differs from each other [236], as shown in Table 6.1.

Table 6.1. The ILDT for different numbers of prisms printing.

Number of prisms	ILDT of first layer (s)	Total ILDT of a part (s)
1	18.3	5572.71
2	26.6	6145.42
4	43.2	7290.84

In this multi-part process modelling work, the thermal transfer mechanisms described in Section 2.3.1 are applied. Briefly, heat conduction (Eq. 2.15) to the previously deposited material and the build plate, heat conduction from the solidified material to the surrounding powder bed, heat radiation (Eq. 2.16) and convection (Eq. 2.17) from the top surface of the active layer to the surrounding atmosphere (chamber) until the next layer is added. The initial predefined temperature of the whole powder bed model is set to be 293 K [321]. The equilibrium for the mechanical analysis has been given from Eq. 2.18 to Eq. 2.22.

6.2.3 Material properties and process parameters

The temperature dependent Ti-6Al-4V material properties described in Section 3.2.3 and Section 4.2.2 are utilised [285]. The temperature dependent plastic property with isotropic hardening law is original from [250], as shown in Figure 4.4. The process parameters for the computational multi-part PBF-LB modelling are summarised in Table 6.2.

Table 6.2. Process parameters applied in multi-part PBF-LB modelling [44, 149, 292].

Symbol	Material	Ti-6Al-4V
	Build plate size (m)	0.25 × 0.25 × 0.025
T_{bp}	Build plate preheat temperature (K)	293
L_h	Layer height (mm)	0.48
t_c	Cooling step time each layer (s)	40
P	Laser beam power (W)	95
A	Heat source absorption coefficient	0.4
R	Heat source spot radium (mm)	0.05
v_s	Laser scanning speed (m/s)	0.6
ε	Emissivity	0.35
h	Heat transfer coefficient (W/m^2/K)	12.7
L	Latent heat of fusion (kJ/kg)	370

6.3 Results and discussions

6.3.1 The batch size effects on temperature of build plate

The temperature history of the build plate influences the temperature history and RS of the manufactured parts [322, 323]. Therefore, the temperature evolution with time at the N2 node (Figure 6.2b) of the build plate is computationally investigated for the single prism, two prisms and four prisms PBF-LB manufacturing (Figure 6.4). To accurately predict temperature evolution during the actual printing, the dimension of the computational build plate is exactly the same as that of the real practical PBF-LB manufacturing [44]. In this work, the sample location effect on the temperature evolution of the build plate is ignored. For different numbers of prisms, all the N2 nodal temperature histories follow the same overall trend. The temperature of the build plate gradually increases with the deposition of layers during the manufacturing process (Figure 6.4a) before reaching the peak temperature after the last layer of powder is deposited (Figure 6.4b), and then monotonically decreases to room temperature during the post-printing process (Figure 6.4c). The same temperature trend of the build plate is also experimentally observed elsewhere [27]. Figure 6.4 indicates that the larger number of the same parts printed in the same build plate, the significantly higher temperature of the build plate. The

peak temperature at the N2 node of the build plate for the two prisms (369.64 K) and four prisms (420.03 K) PBF-LB during the entire manufacturing process are 10.62 % and 25.70 % higher than that of the single prism (334.15 K) PBF-LB printing. Processes with additional parts apply more energy and thus resulting in more heat to be conducted to the previously solidified layers and significantly increasing the overall temperature of the powder bed in a single build.

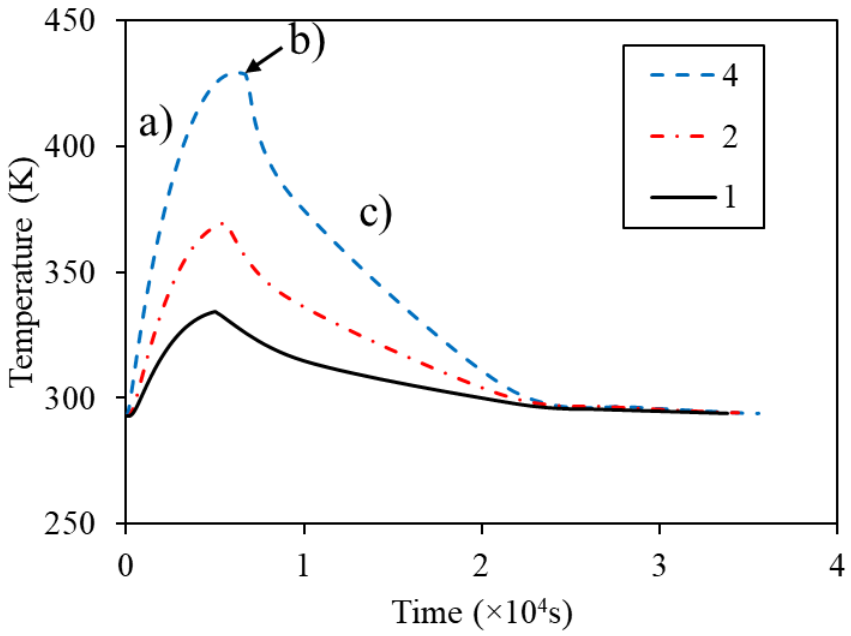

Figure 6.4. Influence of the number of the same prisms (1, 2 and 4) per build on temperature evolution of the build plate: a) Manufacturing process. b) Peak temperature and c) Post-printing cooling process.

6.3.2 The batch size effects on temperature of part

To investigate the effect of the number of samples per build on the temperature history of parts, the temperature evolution with time at the central node of N1 (Figure 6.2a) of the parts '1-1', '2-1' and '4-1' (Figure 6.2) is plotted (Figure 6.5). To make the temperature evolutions more feasible to compare for different numbers of parts printing, the time zero in Figure 6.5 is set to be at the time point when the middle layer (where the N1 node locates, Figure 6.2a) is printed for parts. For all the modelling cases, the repeated deposition, melting and solidification of the subsequent layers of material causes periodic fluctuations of nodal temperature at N1, but the overall trend of temperature is decreasing

with time. The IDLT, including melting time and cooling time for each layer, is different for different numbers of parts printing. The larger number of parts printing at the same build plate, the larger of IDLT, which causes a larger oscillation interval of temperature (Figure 6.5).

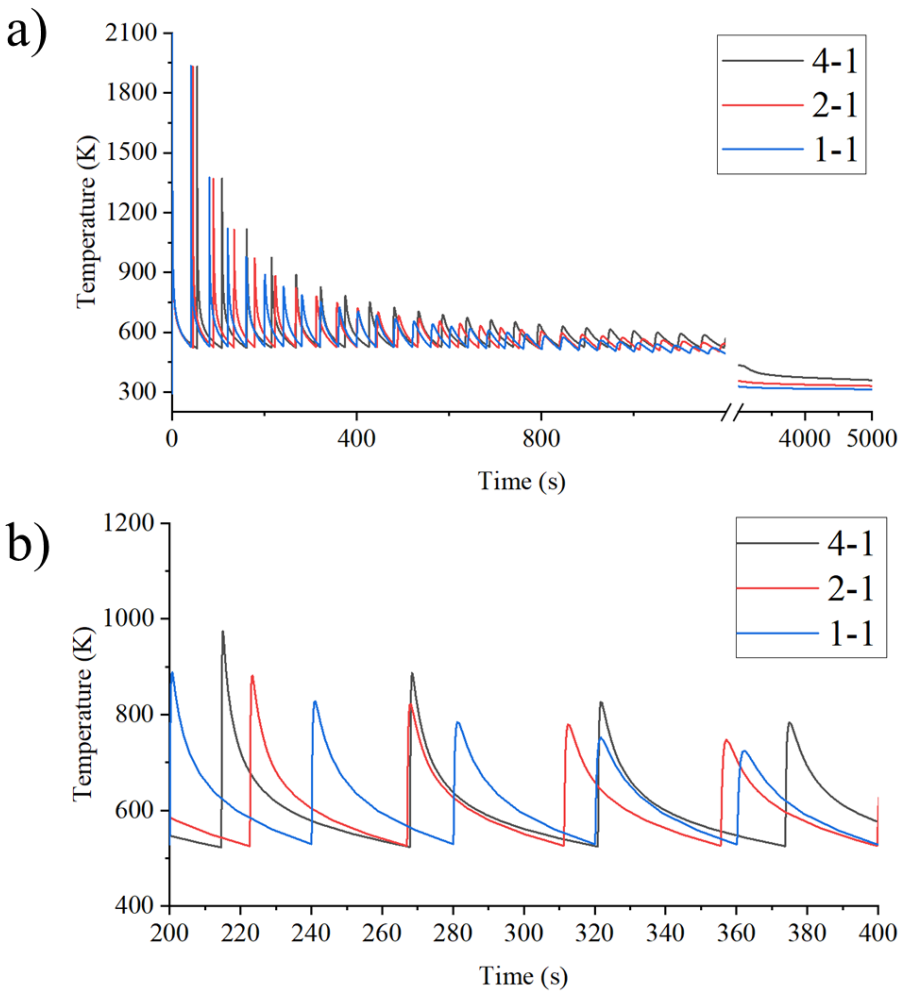

Figure 6.5. Computational temperature evolution with time at the central node N1 of the prisms for different numbers of the prisms printing (1, 2 and 4): a) Original figure and b) Magnified figure.

It can be seen from Figure 6.5a that the overall trend in temperature with time is consistent for all cases, but with different magnitudes of temperature. Figure 6.5b indicates that the overall temperature and temperature increment (TI) of the four prisms printing are always the highest comparing with that of the two prisms and single prism manufacturing for each layer. For the multiple parts PBF-LB manufacturing, more energy (e.g. four times for the

four-part build comparing with the single part manufacturing) is input into the powder bed that results in a higher temperature than the single part printing. The upward slope (for the heating process) for the three computational models is identical, due to the same process parameters are employed (Table 6.2). However, the downward slope (for the cooling process) is different for the different numbers of parts manufacturing, e.g. the downward slope for the four-part build '4-1' is lower than that of the single part build '1-1' (Figure 6.5).

To investigate influence of the number of parts on the temperature of prism, the computational modelling results of the temperature contours for the single prism, two prisms and four prisms after completing printing and cooling for 40 s are demonstrated in Figure 6.6. For all the temperature fields with different numbers of prisms, the top areas of the prisms always have a higher temperature than that of the bottom of the part. This is because the heat energy is input from the top layer of parts and the thermal dissemination is mainly from the top to bottom of the parts. The temperature contours indicate that the higher temperature is formed for the larger number of prisms printing (e.g. the overall temperature of the part '4-1' is significantly higher than that of the part '1-1'), which is in consistence with the study by Yılmaz et al. [44]. The temperature of four-part and two-part printing is 2.97 % and 8.11 % than the single part manufacturing, respectively, after the manufacturing process is complete and cooling for 40 s. The higher temperature of prisms for the larger number of samples is caused by more energy input into the powder bed per build. While for the two prisms and four prisms manufacturing on the same build plate, the effect of the prisms printing order on temperature is found to be minimum, (i.e. less than 0.85 % temperature difference, Figure 6.6b and Figure 6.6c), which indicates that the prisms and powder bed tend to form a uniform temperature distribution in the same build plate during PBF-LB manufacturing.

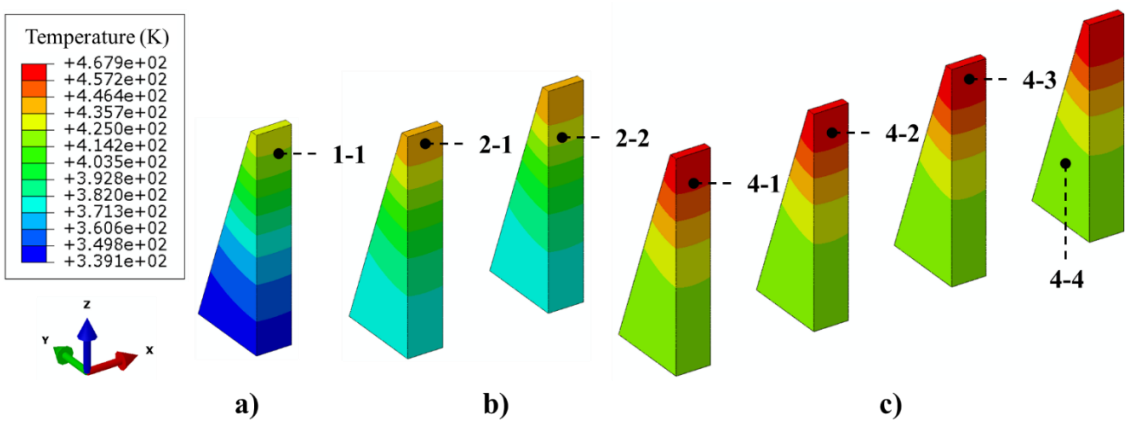

Figure 6.6. Computational temperature contours of prisms after completing printing and cooling for 40 s for different numbers of prisms: a) Single prism. b) Two prisms and c) Four prisms.

To quantify the temperature difference for different numbers of prisms PBF-LB manufacturing, the peak temperatures of parts after completing printing and cooling for 40 s for different numbers of the prisms are summarized in Figure 6.7. It can be seen from both the temperature contours (Figure 6.6) and temperature magnitudes (Figure 6.7) that the more prisms manufacturing at the same build plate, the higher the peak temperature is of the part after build completion and cooling for 40 s. For instance, the temperature of four prisms printing part '4-1' is 8.11 % higher than that of the single prism printing part '1-1' (Figure 6.2 and Figure 6.7). In addition, for the four-part manufacturing, the lowest peak temperature (463.86 K for part '4-1') of part for the four prisms printing is 0.85 % lower than that of the highest temperature (467.84 K for part '4-4'), which also indicates that the part printing order included in this model in the same build plate has minimum effects on the temperature of parts. The conclusion from the temperature histogram (Figure 6.7) is consistent with the temperature contours of parts (Figure 6.6).

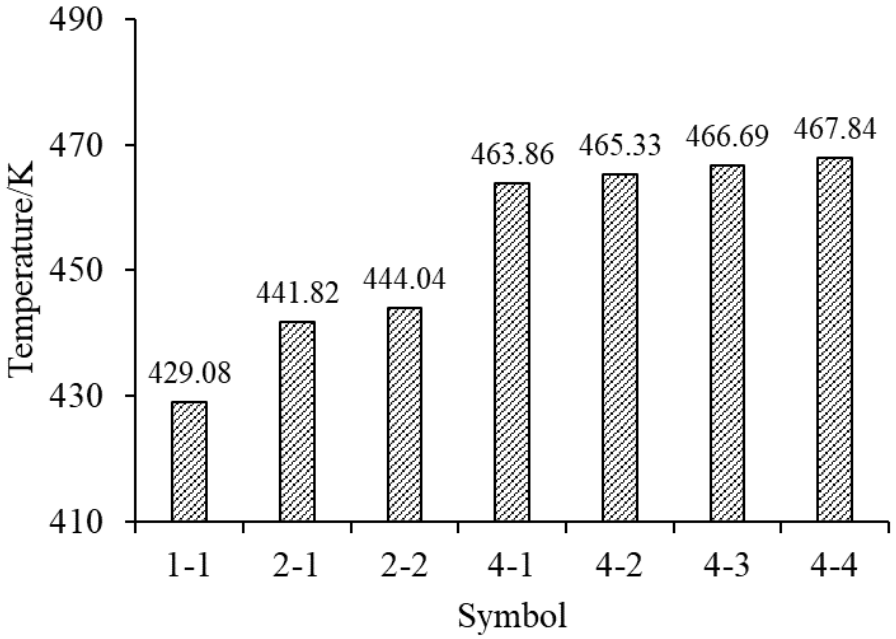

Figure 6.7. The computational peak temperatures statistics of parts after completing printing and cooling for 40 s for different numbers and different printing orders of prisms in a single build.

6.3.3 The batch size effects on residual stress

The final RS refers to stress of the part after the build is completed and has been allowed to cool for 6 hours to room temperature. Figure 6.8 shows the final maximum principal RS contours of the parts '1-1', '2-1' and '4-1' (Figure 6.2), which represent the single prism, two prisms and four prisms manufacturing, respectively. It can be seen that regardless of the number of parts printing at the same build plate, the edges of prisms are consistently in tensile RS while stresses at the central areas of prisms are compressive, which is in good agreement with the results of simulation and experiment by other studies [36, 149, 196]. For all the computational cases, the largest tensile RS occurs at the bottom of the part (i.e. the interface between the part and the build plate), and the same phenomena are also found elsewhere [41, 292]. The single prism modelling (Figure 6.8a) has a larger maximum stress (594.63 MPa) than the two prisms (577.93 MPa) and four prisms modelling (558.90 MPa), which indicates that the multi-part build in the same build plate is beneficial for mitigating RS of parts.

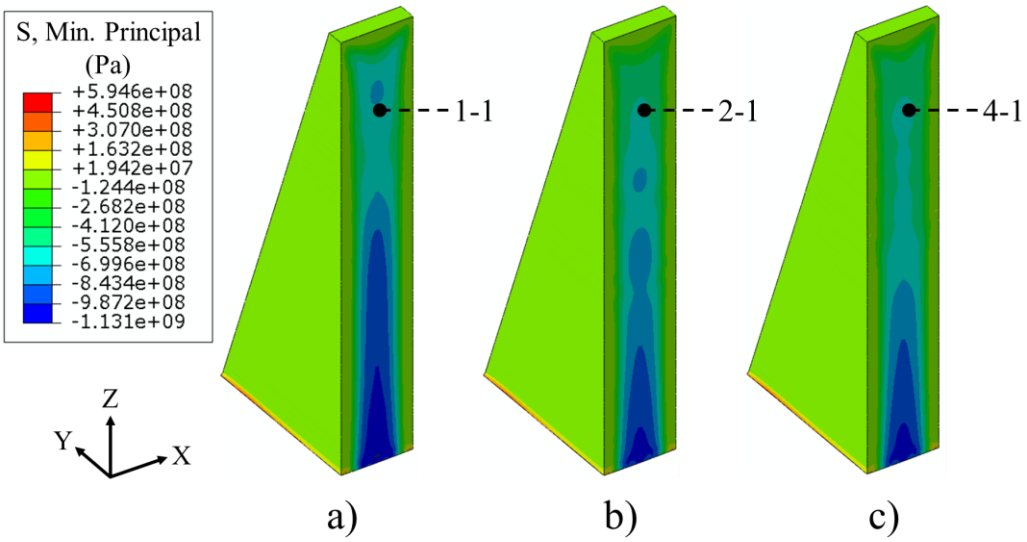

Figure 6.8. The computational modelling results of final RS contours for different number of prisms printing at the same build plate: a) Single prism. b) Two prisms and c) Four prisms.

The final maximum RS (maximum principal stress and minimum principal stress) of the single prism, two prisms and four prisms manufacturing are shown in Figure 6.9. Both the maximum principal RS and the minimum principal RS results (Figure 6.9) indicate that an increase in the number of parts at the same build plate reduces the maximum RS magnitude of parts. The maximum principal RS for the single prism, two prisms and four prisms modelling are 1711.30 MPa, 1658.42 MPa and 1613.89 MPa, respectively. The thermal behaviours of parts (Figure 6.6 and Figure 6.7) during the PBF-LB manufacturing influence the final RS of the parts. The decrease of RS of parts with increasing the number of prisms is because the temperature of the build plate increases (Figure 6.4) with the number of prisms printing in the same build plate, which results in a potential lower thermal gradient and thus a lower RS of parts [324].

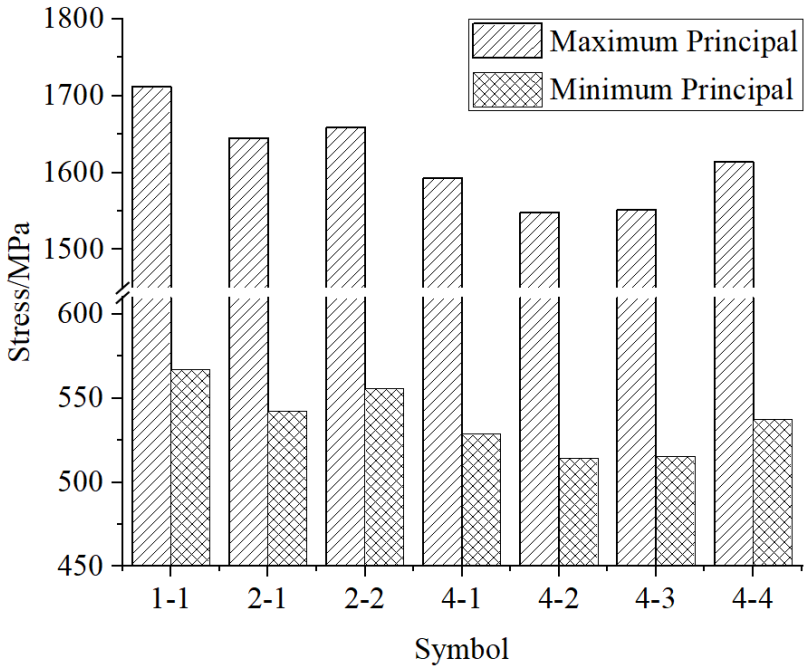

Figure 6.9. The predicted final RS (maximum principal stress and minimum principal stress) for different numbers and printing orders of prisms modelling.

6.3.4 The part printing order and location effects on residual stress

Figure 6.10 shows the modelling results of the minimum principal RS contours of the four prisms modelling with different printing orders within the same build plate. Similar RS distributions of prisms are formed for the different printing orders, which is assumed to be caused by similar temperature histories (Figure 6.6 and Figure 6.7). Both the final maximum principal RS magnitudes (Figure 6.9) and RS contours (Figure 6.10) of prisms for the different printing orders indicate that the printing order of samples on the same build plate have minimum influences on RS of samples. This conclusion agrees with the research outcomes by other research [44].

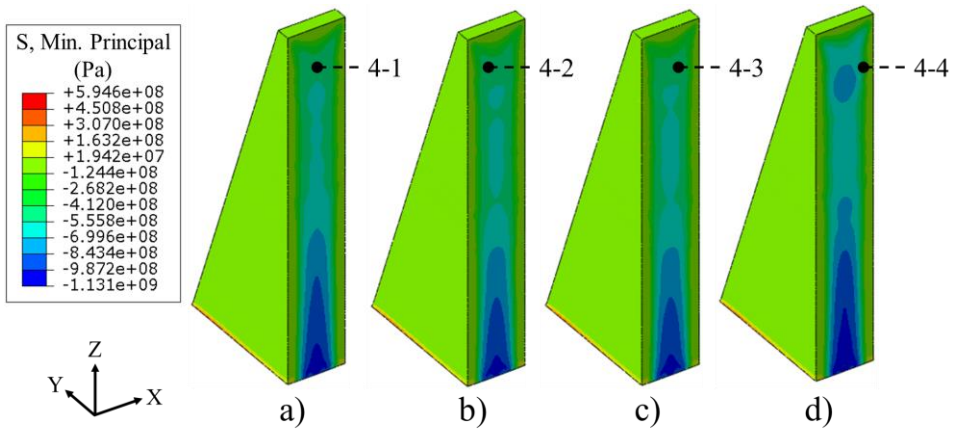

Figure 6.10. Printing order influence on RS contours of prisms in four-part build modelling.

Figure 6.11 illustrates the histogram distributions statistics of the maximum principal stress of prims for the four prisms printing with different printing orders at the same build plate. For all cases, RS for most regions with the prisms low- ranging from -200 MPa to 200 MPa (Figure 6.11). For the four prisms printing, the prisms located toward the edges of the build plate (i.e. part '4-4') have the largest maximum RS (Figure 6.9), but also have a wider RS distribution compared with other parts in the same build plate. It is noted that the prisms locates at central areas of the build plate (prisms '4-2' and '4-3', Figure 6.2) have comparatively lower RS than that of the parts locate at the edges (parts '4-1' and '4-4', Figure 6.2), which is in consistence with study [44]. This is assumed to be caused by the outer parts being connected to cooler regions of the build plate than the centrally located parts, thus the cooling rate of parts at the edges of the build plate is higher than that at the centre of the build plate [44].

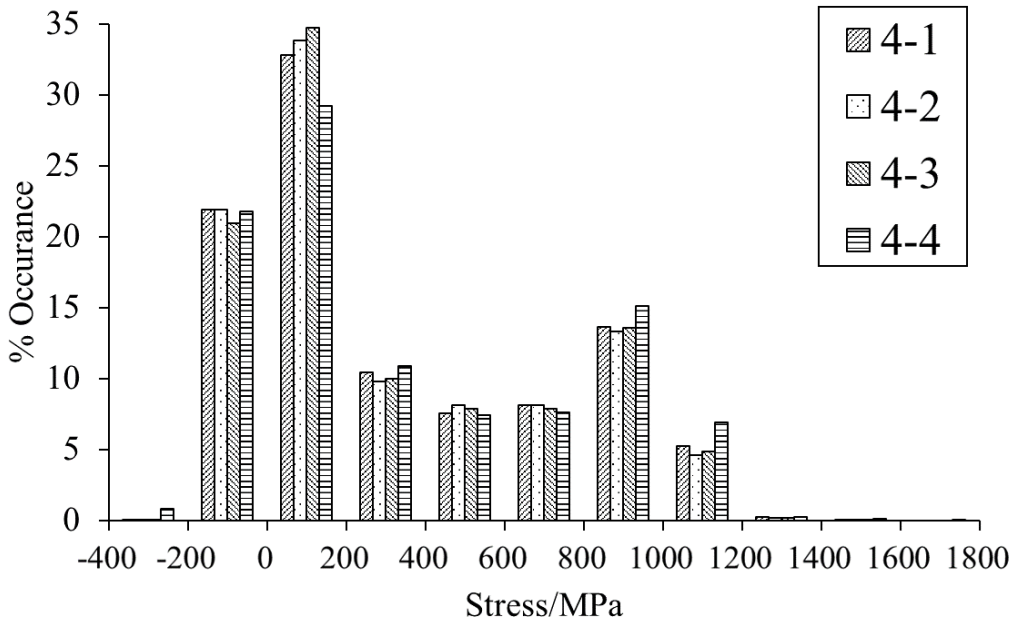

Figure 6.11. Histograms and distributions of predicted maximum principal stress statistics for four prisms printing with different printing orders.

Figure 6.12 shows the minimum RS for a two-part build with different spacings (40 mm, 80 mm, and 120 mm). The results indicate, for 40 mm and 80 mm parts spacing, the larger the spacing between parts, the lower the RS resulted. Then part spacing has an insignificant effect on RS (Figure 6.12c-f). Note that in the multi-part process modelling, the heat conduction between the solid part to the surrounding powder material is simplified as the part-interface convection (shown in **Chapter 3**). Therefore, the specific part heating and cooling influenced by the surrounding parts is not considered in the multi-part manufacturing in this work. In future, the convection approximation (i.e. the heat sink temperature and the depth of surrounding powder) should be further modified for multiple parts build in PBF-LB process modelling.

For parts that at exactly the same location of the base plate, but with different numbers of parts fabrication per build (i.e. part '2-1' with a part spacing of 120 mm and part '4-1', part '2-2' with a part spacing of 120 mm and part '4-4'), the lower stress of part is obtained for the larger number of parts build (Figure 6.9 and Figure 6.12). This further proves that the multiple part build is beneficial for mitigating RS. This work investigated the part spacing effects on RS by using a two-part build. As the number of parts can also influence

RS, part spacing effect RS on multiple (over two) parts should also be investigated in future work. This also provides guidance for the design of builds for experimental measurements of RS, demonstrating that repeated builds of single-part-only builds may give more repeatable experimental RS results than a single build with multiple parts.

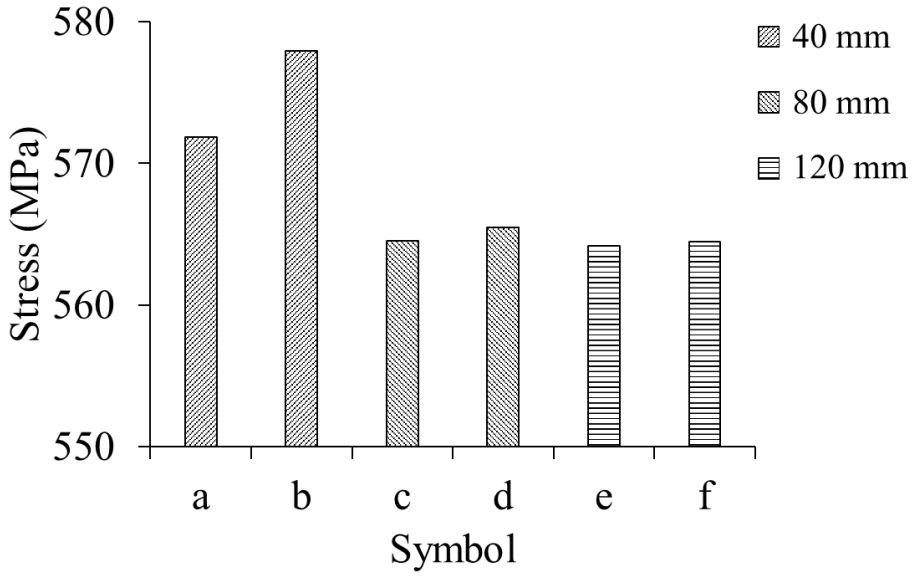

Figure 6.12. Part spacing effects on stress of part for the two prisms printing: a) Part '2-1' with a part spacing of 40 mm. b) Part '2-2' with a part spacing of 40 mm. c) Part '2-1' with a part spacing of 80 mm. d) Part '2-2' with a part spacing of 80 mm. e) Part '2-1' with a part spacing of 120 mm and f) Part '2-2' with part spacing of 120 mm.

6.4 Summary

In summary, the computational thermo-mechanical finite element modelling framework for macroscale multi-part build by single laser beam PBF-LB for Ti-6Al-4V is presented. The influences of the number of prisms per build, part spacing and part location on temperature and RS of parts are predicted in multi-part PBF-LB manufacturing. The key conclusions of this chapter are as follows:

- Coupled thermo-mechanical process modelling capability was developed for multi-part PBF-LB manufacturing for predicting temperature and RS of Ti-6Al-4V material.
- The temperature of the base plate and part by different numbers of parts manufacturing is quantitively compared. The more samples manufacturing in a

single build in PBF-LB, the higher temperature of both the part and the build plate. The temperature of the build plate increases with time during the multi-part manufacturing process.

- A multi-part build produces a 6 % lower residual stress than the single part build and the maximum RS of parts decreases with the number of (same) parts per build.
- In multi-part PBF-LB build, non-uniform stress profiles in parts at the same base plate are obtained. Parts located at the central areas of the build plate have a lower RS than parts that are located at the edges of the base plate in multi-part build.
- The larger the part spacing in multi-part PBF-LB manufacturing, the lower RS the part resulted before stabilisation.
- For multi-part printing, the largest stress occurred at the interface of the part and the base plate, and tensile stress occurs at the surface areas of parts while compressive stress forms at the central area of the part, which is identical with the single part PBF-LB manufacturing.

7 Application to electron beam powder bed fusion additive manufacturing

This chapter extends the process modelling tools developed in previous chapters (**Chapter 3** – **Chapter 6**) for PBF-LB of Ti-6Al-4V material to the PBF-EB category AM for Ti2448 material. The layer-by-layer process modelling technique described in **Chapter 3** is employed to characterise the thermal history and microstructure of the electron-beam variant of PBF (PBF-EB) and for a new titanium alloy Ti2448. This PBF-EB study in **Chapter 7** is a collaboration study with Institute of Metal Research, Chinese Academic of Sciences (IMR-China), and the collaborators from IMR-China are Qiushuang Wang, Shujun Li, W.T. Hou, H. Wang, Y.L. Hao, R. Yang. The author completed thermomechanical process modelling of PBF-EB. IMR-China completed all sample fabrication and experimental measurements. All experimental results (and Figures 7.3, 7.10, 7.11, 7.12, 7.13 and 7.14) that are presented in this chapter of thesis belong to Qiushuang Wang and are included in this thesis with the permission of Qiushuang Wang and Shujun Li in order to support the discussion relating to the computational modelling results of this chapter.

7.1 Introduction

As reviewed in Section 2.3.7, mechanical properties of PBF manufactured metallic parts are closely related to their microstructures. In order to manufacture PBF-EB products with desirable mechanical properties, it is important to understand the process-microstructure relationship. As described in Section 2.2, Ti2448 alloy is a nontoxic β-type titanium alloy and has a wide application in medical-device manufacturing. AM technology has been used to successfully manufacture Ti2448 medical products, such as hip stems, acetabular cups and interbody fusion cages [325]. Hernandez et al. [326] indicated that columnar β grains and α''-martensite plates were observed in the PBF-EB manufactured Ti2448 solid part. Yang et al. [327] showed that columnar β grains were surrounded by equiaxed β grains near the boundary of the melt pool in PBF manufactured Ti2448 alloy. The hard-wraps-soft effect caused by this kind of microstructure can improve the mechanical

performances of titanium alloy [327]. Liu et al. [82] found that the microstructure characteristics of PBF-LB and PBF-EB manufactured Ti2448 alloy were different and could significantly influence the mechanical behaviour of manufactured parts: the microstructures of PBF-LB and PBF-EB manufactured porous samples were composed of different phases due to the difference in powder bed temperature, and the single β phase of PBF-LB Ti2448 alloy resulted in a higher compressive strength and lower Young's modulus than that of PBF-EB manufactured parts.

In **Chapters 5** and **6,** effects of multi-beam PBF-LB and multi-part build on Ti-6Al-4V RS have been computationally investigated. The results indicate that the largest RS occurs at the bottom surface of the part (i.e. the interface of part with base plate). To prevent failure of PBF manufacturing process, strategies to reduce stress of part (especially at the interface of part with base plate) need to be explored. In addition, all the previous chapters of this work are focused on RS studies of Ti-6Al-4V material. However, examining the existing literature, there is no research on RS of PBF-EB manufactured Ti2448 parts. Computational investigation of RS of PBF-EB produced Ti2448 full scale parts is thus necessary and can inform AM designers and operators of the optimum process configuration for successful parts printing.

The overall aim of this work is to apply the process thermo-mechanical modelling techniques described and previously developed from **Chapter 3** to **Chapter 6** for PBF-LB of Ti-6Al-4V material to PBF-EB manufacturing of Ti2448 material. The objectives of this chapter are:

a) To computationally predict the temperature evolution of Ti2448 material during PBF-EB and its influence on microstructure by comparison with IMR-China's experimental results of material microstructure.
b) To computationally predict RS of PBF-EB AM of Ti2448 alloy at the scale of overall additively manufactured component.
c) To support the computational layer-by-layer thermal process modelling approach described in **Chapters 3** and **4** by experimental microstructure characterisations.
d) Investigate process parameter effects on RS and explore strategies to mitigate RS and improve mechanical performances of parts in PBF.

7.2 Research methods for PBF-EB

7.2.1 Computational modelling methods

To simulate the practical PBF-EB manufacturing process (described in section 1.1 and other studies [19, 20]) and for the convenience of computational modelling in this study, the PBF-EB AM process was simplified to include the following four steps in computation:

i. Preheating step is the step in which the heat source preheats the powders to below melt temperature for a period of time that is defined as the preheating step time t_p, which represents the time spent on preheating the entire powder layer of part by using the low power mode of electron beam during the preheating step.
ii. Preheating cooling step time t_{pc} represents the time delay between when the pre-heating ends and melting starts, due to for example, other regions of the powder bed being pre-heated. The total preheating time t_l is the sum of t_{pc} and t_p.
iii. Active layer heating step is when the finely focused electron beam operates in melt mode heating the newly added layer of powder to above liquidus temperature. The active layer heating step time t_m (Eq. 2.7) can be calculated as the electron beam spot diameter divided by the electron beam moving speed for melting the powder [143], and assumes a constant beam scanning speed within a layer.
iv. Melting cooling step is the step in which the electron beam deactivates, and the roller/coater spreads a new thin layer of powders on the powder bed.

The above four computational steps (i-iv) were repeated for each layer of the PBF-EB thermo-mechanical modelling process. After finishing manufacturing of the final layer, there was an additional final cooling step in which there was no further addition of heat into the model and the part was allowed to cool to room temperature for 8 hours 43 mins, corresponding to the experimental PBF-EB manufacturing.

A computational model of a cylindrical sample of Ø 20 mm × 20 mm, with a 10 mm thick base plate was created. As shown in Figure 7.1, a 2D axisymmetric simulation domain was employed in the thermo-mechanical process modelling to save the computational

cost. In the experimental PBF-EB manufacturing process, the temperature of base plate was approximately constant (around 773 K). In the computational modelling, the priority is the thermal history of the part, rather than the whole base plate. To reduce computational complexity of modelling, isothermal boundary condition (constant temperature of 773 K) was applied at the base plate and the size of the base plate in the model was 20 mm × 10 mm as shown in Figure 7.1. However, the influence of thermal boundary condition of the base plate on RS in PBF-EB is discussed in Section 7.6.1, where only a predefined temperature of 773 K was defined on the base plate in case 1 and a constant temperature was defined at the bottom surface of the base plate for case 2. Axisymmetric boundary conditions were applied on the left boundary of the simulation domain (as shown in Figure 7.1). The Python-based script (Figure 3.1) and 'model change' technique described in **Chapter 3** were employed on the sequentially coupled thermo-mechanical modelling as described in **Chapter 2**. The converged (less than 0.19 % nodal temperature difference) mesh size of 23 μm × 23 μm was employed for the part. The four-node linear axisymmetric heat transfer quadrilateral mesh type of DCAX4 was employed for the thermal analysis and the four-node bilinear axisymmetric quadrilateral mesh type of CAX4R was applied for the mechanical modelling.

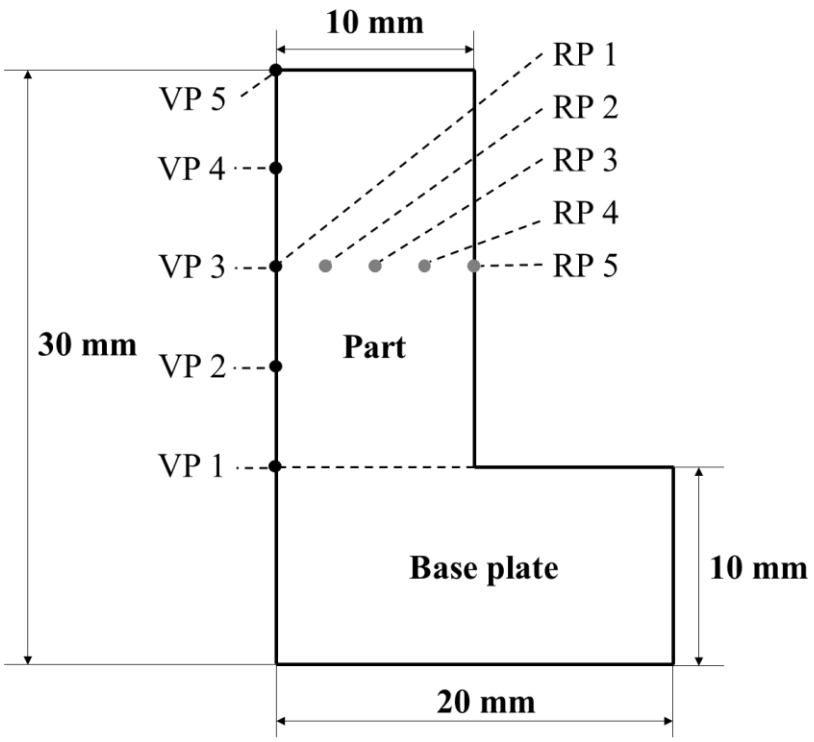

Figure 7.1. Geometry of the simulation domain and position of sampling points.

To compare RS induced by PBF-EB with that of PBF-LB, the process modelling of both PBF-LB and PBF-EB were performed on the model shown in Figure 7.1. The PBF-LB process modelling methods have been introduced in **Chapter 3**. To investigate the optimum strategy to mitigate RS and stress at the interface of part with the base plate in PBF-LB, effects of the preheating temperature of the base plate and the powder bed, surface convection at the active layer, energy density input for each layer on RS were investigated. The overall analysis models and process parameters applied for both PBF-LB and PBF-EB are summarised in Table 7.1.

The results of thermal modelling were analysed at 10 different sampling points, including 5 evenly distributed sampling points (the VP points) along the height of the 2D part at its centre and 5 sampling points (the RP points) along the radius of the 2D part at its mid height as shown in Figure 7.1. The 5 VP points responding to layer 1, layer 72, layer 143, layer 214 and layer 285 in the modelling, respectively. Note that the RP1 and VP3 are at the same position.

Table 7.1. Comparison of PBF-LB and PBF-EB and models to mitigate RS.

Model	Process	Material	Power density $\times 10^{13}$ (W/m^3)	Heating time per layer (s)	Preheating temperature of base plate and powder bed (K)	Top surface convection
1	PBF-EB	Ti2448	7.65	1.173×10^{-4}	773	No
2	PBF-LB	Ti-6Al-4V	9.5	1.67×10^{-4}	293	Yes
3	PBF-LB	Ti-6Al-4V	9.5	1.67×10^{-4}	293	No
4	PBF-LB	Ti-6Al-4V	5.37	1.67×10^{-4}	293	Yes
5	PBF-LB	Ti-6Al-4V	9.5	1.67×10^{-4}	373	Yes
6	PBF-LB	Ti-6Al-4V	9.5	1.67×10^{-4}	573	Yes
7	PBF-LB	Ti-6Al-4V	9.5	1.67×10^{-4}	773	Yes
8	PBF-LB	Ti2448	7.65	1.173×10^{-4}	773	No

The coupled thermo-mechanical modelling described in Section 2.3 was implemented by computationally solving the governing equation (Eq. 2.2) using finite element method with ABAQUS. For the layer-by-layer modelling method described in **Chapter 3**, the uniformly distributed volumetric heat sources (Eq. 2.6) for both preheating step and active layer heating step were applied for each whole active layer during PBF-EB. The heating step time t_m in the thermo-mechanical modelling was described in Eq. 2.7 [143]. Eq. 2.2 was computationally solved for t_m seconds for the active layer melting process. The computational melting cooling step time for each active layer was 10.45 s, corresponding to the practical PBF-EB manufacturing process.

The heat losses during PBF-EB process that were considered in the thermo-mechanical modelling is shown in Figure 7.2. Briefly, heat conduction (Eq. 2.15) between the active layer and the solidified material of the previous layer (Figure 7.2i) and the base plate (Figure 7.2ii), heat radiation (Eq. 2.16) at the top surface of the active layer to the chamber (Figure 7.2iv). The heat transfer between the powder bed and the side of the solidified part was dealt with in a way similar to heat convection (Figure 7.2iii), as has been described in **Chapter 3**. Due to the fact that the PBF-EB process is normally conducted in a vacuum environment, the heat convection at the top surface of the active layer was not considered in the computational PBF-EB modelling.

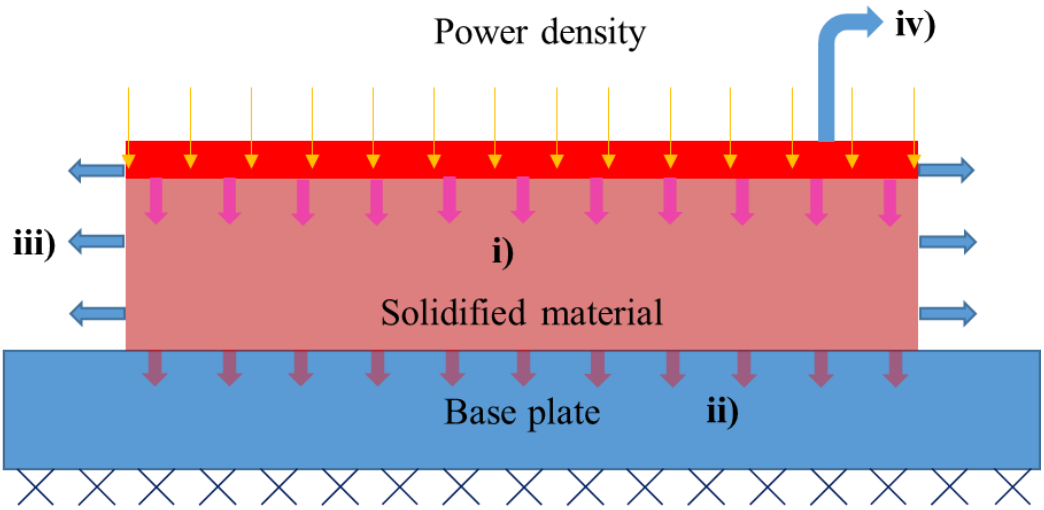

Figure 7.2. Illustration of thermal transfer mechanisms during the PBF-EB process: i) Solid conduction. ii) Base plate conduction. iii) Part-powder conduction and iv) Active layer radiation.

For the PBF-EB thermo-mechanical modelling, the material of both the part and the base plate was defined as Ti2448 to avoid thermal expansion mismatch [285]. The temperature dependent Ti2448 material properties that were employed in the computation were assumed to vary linearly with temperature between the values that are presented in Table 7.2. The temperature dependent plastic material property (i.e. yield strength) of Ti2448 with isotropic hardening law for PBF modelling is shown in Table 7.2, which is experimentally measured and provided by IMR-China. The temperature dependent Ti-6Al-4V material properties used for the PBF process modelling (Table 7.1) in this chapter have been descried in **Chapters 3** and **4**. The process manufacturing parameters used for the PBF process modelling are summarised in Table 7.3.

Table 7.2. Ti2448 material properties for PBF-EB modelling.

Temperature (K)	Thermal expansion (10^{-5}/K)	Thermal conductivity (W/m^2/K)	Specific heat (J/kg/K)	Yield strength (MPa)
333	0.87			
370		8.35	478	
573				870
673				945
773				665
873		15.8	445	210
923				95
983	1.06			
1273		19	470	
1928	1.35			

Table 7.3. PBF-EB process parameters [247].

Symbol	Modelling parameters	Unit	Value
U	Acceleration voltage	V	60000
I_p	Current for preheating	mA	14.6
I_m	Current for melting	mA	8.5
P	Energy beam power	W	510
v_s	Scanning speed for melting	mm/s	1704.3
v_p	Preheating scanning speed	mm/s	10000
T_{bp}	Build plate preheat temperature	K	773
A	Heat source absorption coefficient		0.9
d_s	Heat source spot diameter for melting	μm	200
d_m	Melt pool depth	μm	150
H_s	Hatch spacing	μm	200
	Powder layer thickness	μm	70

7.2.2 Experimental methods for PBF-EB

Collaborators at IMR-China used an Arcam A1 PBF-EB system to fabricate dense samples in this work. The pre-alloyed powder (particle diameter ranges from 45 to 106 μm) used in the PBF-EB process was produced by using argon atomization of a Ti2448 ingot. The chemical composition of the Ti2448 powder was (wt.%) Nb-24.43, Zr-3.93,

Sn-8.22, O-0.22 and the balance was Ti. The CAD model of samples with a size of Ø 20 × 20 mm was designed using Magics software (Materialise, Leuven, Belgium), and then the model was sliced and imported into PBF-EB equipment for parameter setting. The printing started after the vacuum in the sample chamber and in the electron gun dropped below 5.0×10^{-4} mbar and 5.0×10^{-6} mbar, respectively. The electron beam preheated the base plate with dimension of $170 \times 170 \times 10$ mm^3 to 773 K for 20 minutes, and the first layer of 70 µm thickness was laid. The electron beam moved by tracing out the designed geometry to melt the powders in the active layer of the powder bed and then the base plate decreased one layer thickness. These processes were repeated until the completion of the part. It was noted that the printing time of each layer was influenced by the melting area, and the printing procedure ended after 8 hours. When the base plate cooled to room temperature, the non-melted powder could be removed by compressed air to obtain the as-fabricated sample (Figure 7.3a).

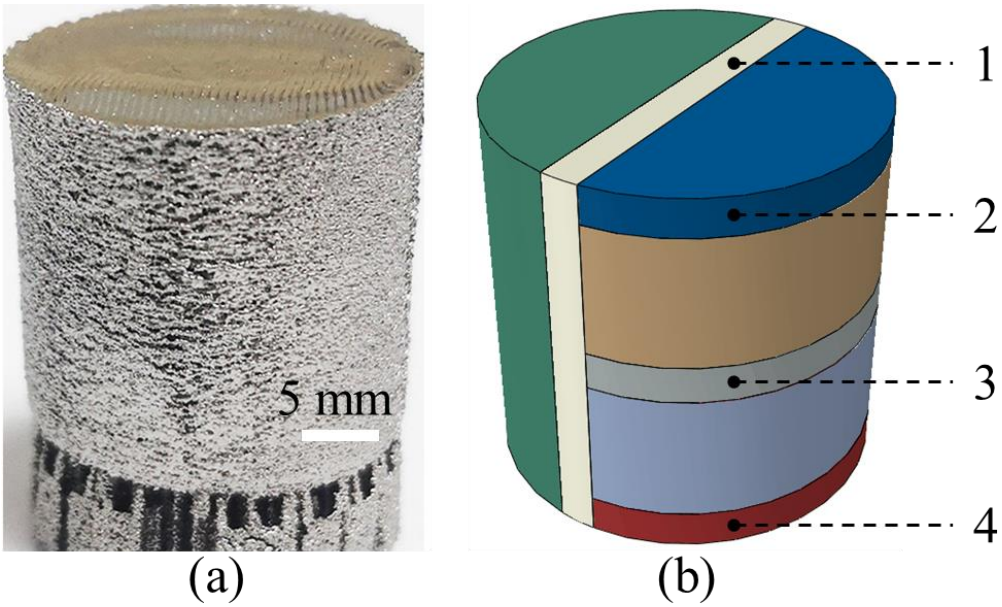

Figure 7.3. Model illustration: a) The Ti2448 sample manufactured by PBF-EB and b) Sketch illustrating how the sample was sectioned for metallographic analysis. This figure is provided by Qiushuang Wang from IMR-China. The sampling points VP1, VP3 and VP5 (Figure 7.1) in the computational domain corresponding to the section 4, 3 and 2 of the manufactured sample. The sampling points RP1 - RP5 (Figure 7.1) in the computational domain corresponding to positions from central line to the side surface of the manufactured sample in the section 3.

The samples were sectioned using wire EDM by collaborators at IMR-China as shown in Figure 7.3b. The metallographic specimens were made at segments 1 - 4, respectively, so as to characterise the microstructure from the cross-section and the vertical section at the top, middle and bottom positions of the samples. Note that the centre of section 2, 3 and 4 in Figure 7.3b for microstructure experiments is close to the sampling point of VP1, VP3 and VP5 (Figure 7.1) in the computational modelling domain, respectively. The sampling point RP1 - 5 (Figure 7.1) is at the mid layer where section 3 in Figure 7.3b locates. The microstructural features of the prepared samples were analysed by using ZEISS-AXIO optical microscope (OM), MIRA3 TESCAN SEM and Talos Transmission electron microscope (TEM) at IMR-China. Image Tool package (UTHSCSA, San Antonio, USA) was used by collaborators at IMR-China for quantitative analysis of phase based on metallographic pictures in different areas of the sample.

7.2.3 Computation of phase equilibrium

The equilibrium phase diagram of Ti2448 was calculated by collaborators at IMR-China with the PANDAT package in association with the Ti-Nb-Zr-Sn-O thermal and mobility database covering the temperature range of 273 - 1273 K. The two basic phases of Ti2448, i.e. α and β, were considered in the computation of phase equilibrium.

7.3 Results for PBF-EB

7.3.1 Thermal modelling results

In the PBF-EB modelling, the part was virtually sliced into 286 layers and each layer was deposited on top of the previous layer step by step. The thermal modelling was implemented for 11 hours 46.28 mins of the PBF-EB process, including 3 hours 3.28 mins of the layering and heating process and the post-manufacturing cooling process of 8 hours 43 mins. The predicted temperature histories of the five vertical sampling points (VP1, VP2, VP3, VP4 and VP5, shown in Figure 7.1) are illustrated in Figure 7.4. In this figure, zone (a) illustrates the predicted temperature of the active layer in question at the end of the corresponding melting process (step 3 in the simulation process). The maximum predicted temperature is above 3200 K, corresponding to the first peak of temperature for

each curve (e.g. the curve corresponding to VP3). The deposition, preheating, melting, and cooling processes of the subsequent layers of material caused periodic oscillation of temperature at the vertical sampling point in question with the predicted peak temperature (a) associated with the active layer melting, and subsequent lower peaks associated with deposition of later layers (b).

Figure 7.4 details how the temperature at the five vertical sampling points was predicted to change with time for the first 12000 s of the PBF-EB process. The predicted maximum temperatures at VP1 are the lowest compared with the maximum temperature at other four vertical sampling points, while the five vertical sampling points share similar temperature history (Figure 7.4). Overall, the predicted peak temperature increases from bottom towards the top of the manufactured part during the PBF-EB process. The first deposition layer has the lowest temperature, because of the heat conduction from the solid part to the base plate. With the sequential deposition of material, during the layer-by-layer PBF-EB process, the thermal influence of the base plate on the newly laid layer of material gradually becomes less significant. Therefore, the predicted temperature temporal evolution near the mid height of the part (e.g. VP2, VP3 and VP4) becomes relatively unaffected by the height of the vertical sampling points, and the corresponding three curves in Figure 7.4 are similar, which agrees with related findings in other experimental measurement of temperature during PBF-EB process of Ti-6Al-4V rectangular structure [328]. The predicted temperature temporal evolution at VP5 is relatively different from that of other four vertical sampling points, as no further layers are added after deposition of the final layer. The temperature at VP5 only oscillates two cycles, and it quickly starts to monotonically decrease. After finishing the manufacturing of the part, the predicted temperature of the part eventually cooled to room temperature during the simulation of post-printing cooling process.

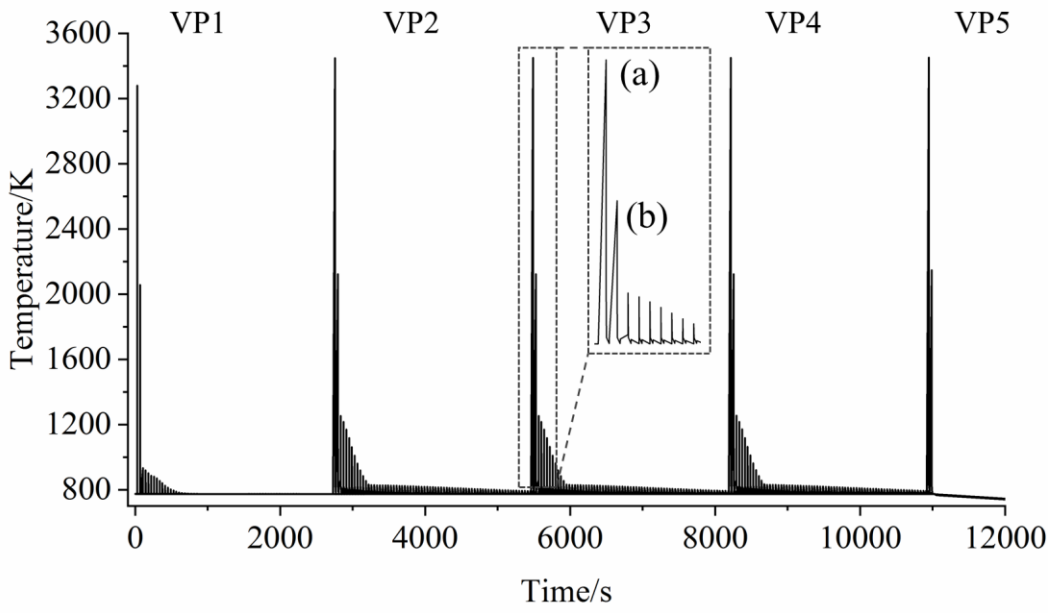

Figure 7.4. Computational modelling results of temperature evolution at the five vertical sampling points of part (VP1, VP2, VP3, VP4 and VP5) with time.

In order to characterise the temperature variation of the part in the vertical direction during the PBF-EB process, the vertical temperature difference (TD) is predicted, which is the difference between the temperatures at the sampling points VP2, VP3, VP4 and VP5 (Figure 7.1) and the temperature at VP1. The evolution of four TDs along the height of the part is shown in Figure 7.5. It can be seen that the values are all positive, which further confirms that the temperature of material near the base plate is the lowest in the overall part. The temporal evolution of the TD at VP2, VP3 and VP4 are very similar to one another. At VP2 for example, during the deposition, preheating, melting, and cooling of the active layer, the TD decreases from approximately 3000 K to ~ 1 K. Such process is not monotonic but significantly oscillates up and down, because the deposition, preheating, melting, and cooling of PBF-EB is repetitive.

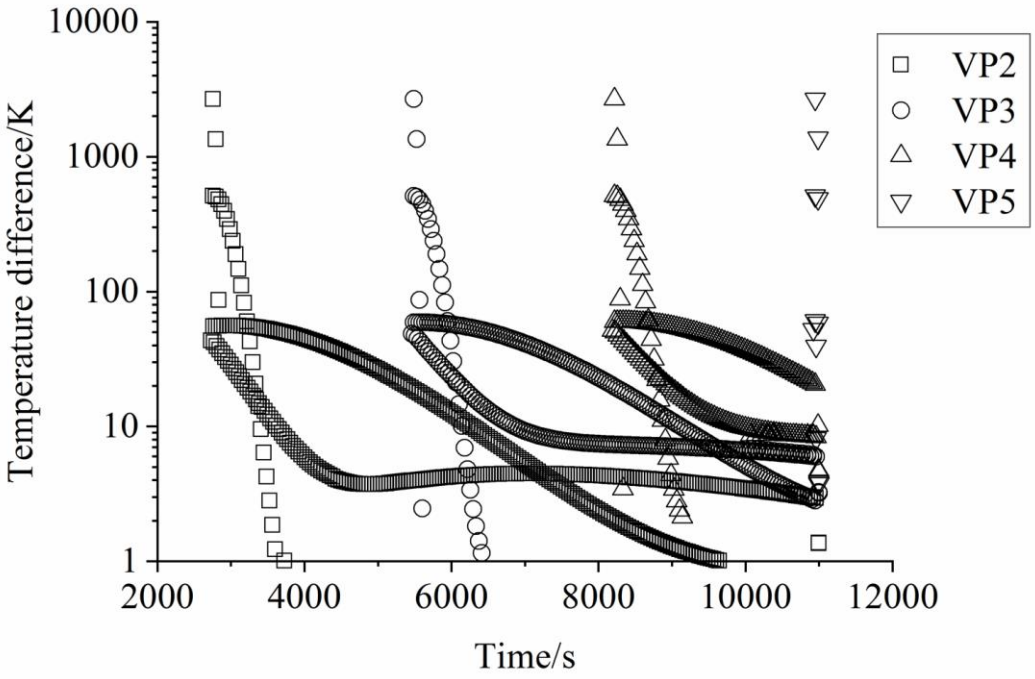

Figure 7.5. Predicted evolution of temperature difference at the 4 vertical sampling points of part during manufacturing process with time.

The cooling rate at the five vertical sampling points (Figure 7.1) was calculated based on the temperature history that is shown in Figure 7.4. Figure 7.6a illustrates the maximum CR at the vertical sampling point in question at the end of the heating step of each relevant sampling point layer (as shown in Figure 7.4a). Figure 7.6b illustrates the maximum CR at the vertical sampling point in question, which results from remelting and the influence of the subsequent layers (as shown in Figure 7.4b). It can be seen that the highest level of CR is in the order of magnitude of 10^5 K/s, which is calculated based on the time required for the temperature of VP1 - 5 to cool from the melting point to the β - transus temperature [329] and is in line with other PBF-EB work [330]. Figure 7.6a indicates that the peak CR takes place immediately after the completion of the heating step (Figure 7.4a) of the active layer. During the process of the subsequent layers (Figure 7.4b), the CR at the vertical sampling point in question significantly decreases. It can be seen, as shown in Figure 7.6, that the CR at the sampling point VP1 is the highest. It is higher than the CR at VP2, VP3, VP4 and VP5 by approximately 3×10^4 K/s. This is due to the heat conduction from the part at its bottom to the base plate during the PBF-EB process. A decrease in CR along the building direction of 718 alloy thin wall structures with height of 8 mm was found in other PBF-EB work [243].

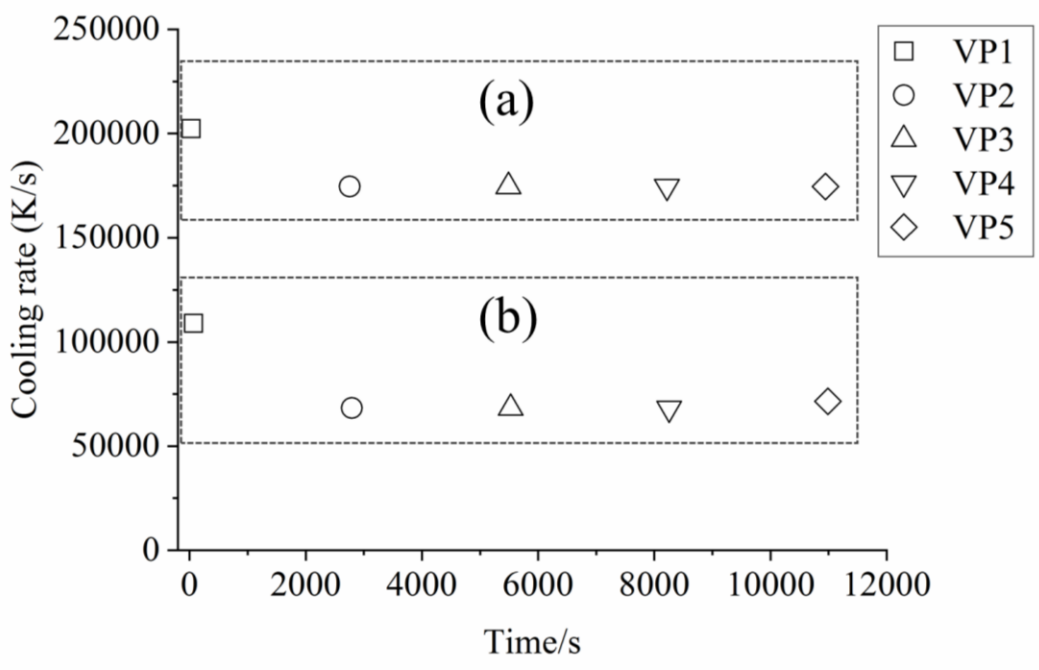

Figure 7.6. Predicted maximum cooling rate at the 5 vertical sampling points: a) at the end of the melting process of the layer in question and b) Resulting from the thermal processes of subsequent layers.

The radial temperature difference in the manufactured part is defined to be the temperature at the four sampling points RP2, RP3, RP4, RP5 minuses the temperature at the sampling point RP1 (as shown at Figure 7.1), at the mid height of the manufactured part. Its evolution with time is shown in Figure 7.7. It can be seen that the value of TD is negative, which means that the temperature at RP2, RP3, RP4 and RP5 is lower than that at RP1 during the PBF-EB process. TD has the highest absolute value at RP5. Overall, the temperature near the side surface of the part is lower than that near the centreline of the part, and there is a decreasing profile of temperature along the radius of the part. This phenomenon is caused by the heat loss of the part to the surrounding powder bed [149, 160]. The TD in the radial direction decreases with time at all the sampling points (RP2 to RP5). This is because that the heat conduction process in the part tends to make the temperature profile uniform, as increasingly more materials are deposited above the mid height of the part.

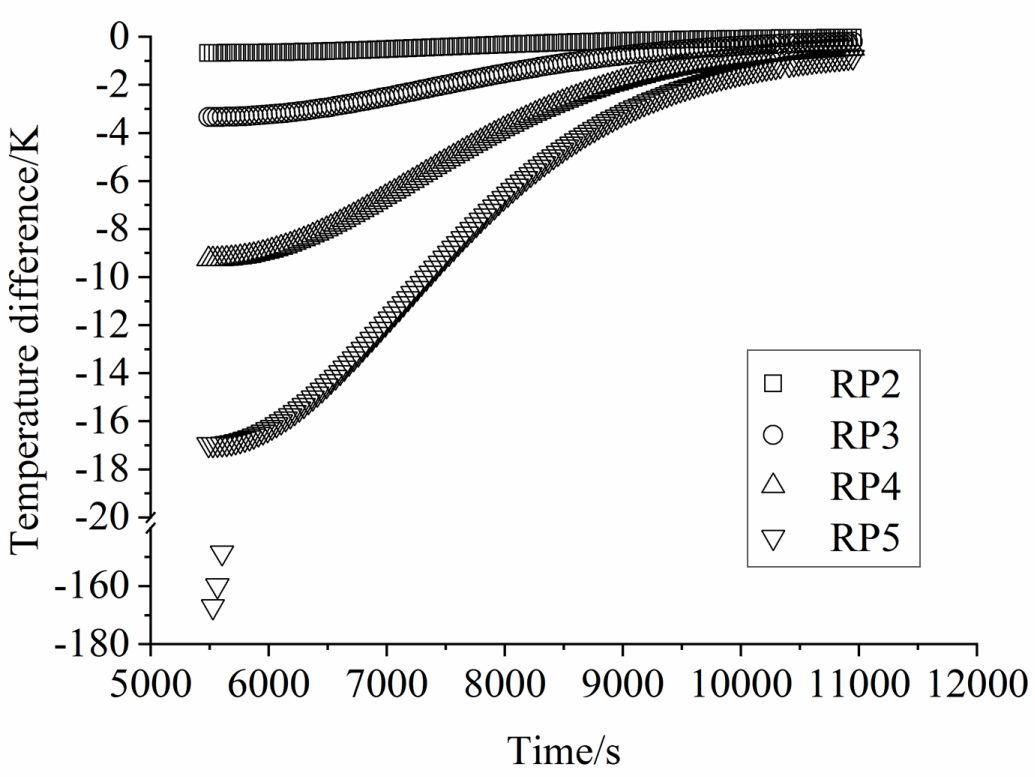

Figure 7.7. Predicted evolution of radial temperature difference at the 4 radial sampling points with time.

The cooling rate at the five radial sampling points RP1, RP2, RP3, RP4 and RP5 is shown in Figure 7.8. During the processes of deposition, preheating and melting of the layer at the mid height of the part, the highest CR is in the order of magnitude of 10^5 K/s. It can be seen that, as shown in Figure 7.8, the surface of the part (i.e. at RP5) has the highest level of CR, which is higher than the CR at RP1, RP2, RP3 and RP4 by approximately 1×10^4 K/s. As the subsequent layers are deposited on the part above its mid height, the CR at the sampling points RP1, RP2, RP3 and RP4 significantly decreases to the order of magnitude of 7×10^4 K/s, while the CR at RP5 decreases to the order of magnitude of 9×10^4 K/s (Figure 7.8b).

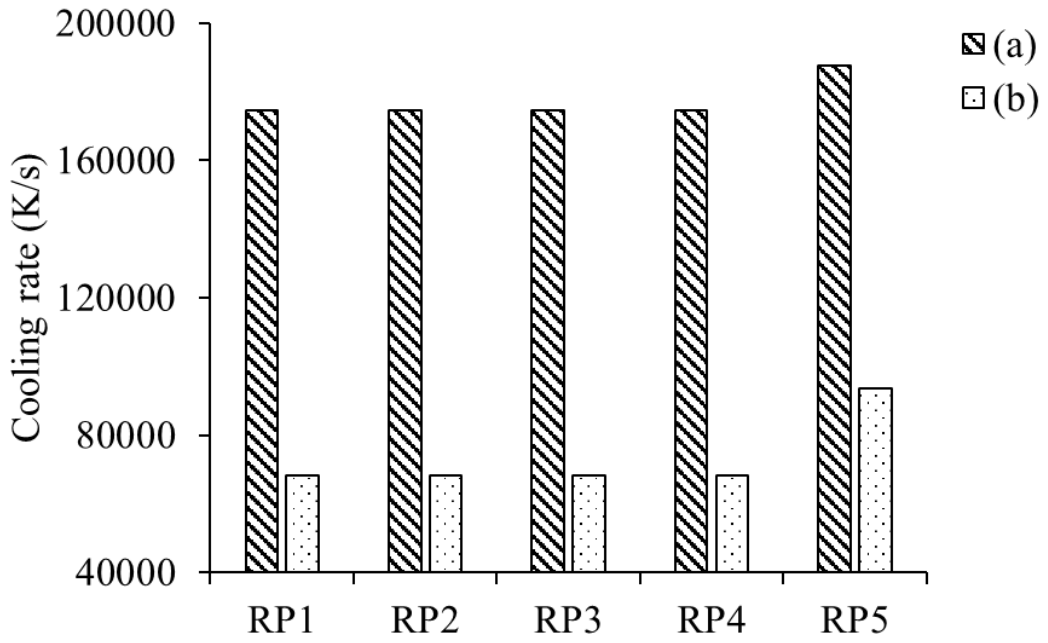

Figure 7.8. Predicted maximum cooling rate at the 5 radial sampling points: a) at the end of the melting process of the layer in question and b) Resulting from the thermal processes of subsequent layers.

In the thermal modelling results that were analysed in above, the data analysis was focused on the manufacturing process. After the manufacturing process was completed, the manufactured part was left in the build chamber to cool for 8 hours 43 mins before it could be taken out. Figure 7.9 illustrates the thermal modelling results of the temperature evolution of the part at the five vertical sampling positions (VP1 - VP5) with time during the natural cooling process post manufacturing. It can be seen that, at vertical sampling point VP1 in this figure, the material temperature continuously decreases from 774 K to 426 K between 3 hours 3.28 mins and 11 hours 46.28 mins. The temperature evolutions at the five different vertical sampling points are very close to one another, and the maximum difference in temperature is 7.3 K. In the radial direction of the sample, the temperature profile turns out to be relatively uniform from 3 hours 3.28 mins. The maximum difference in temperature between the five radial sampling positions is 0.87 K.

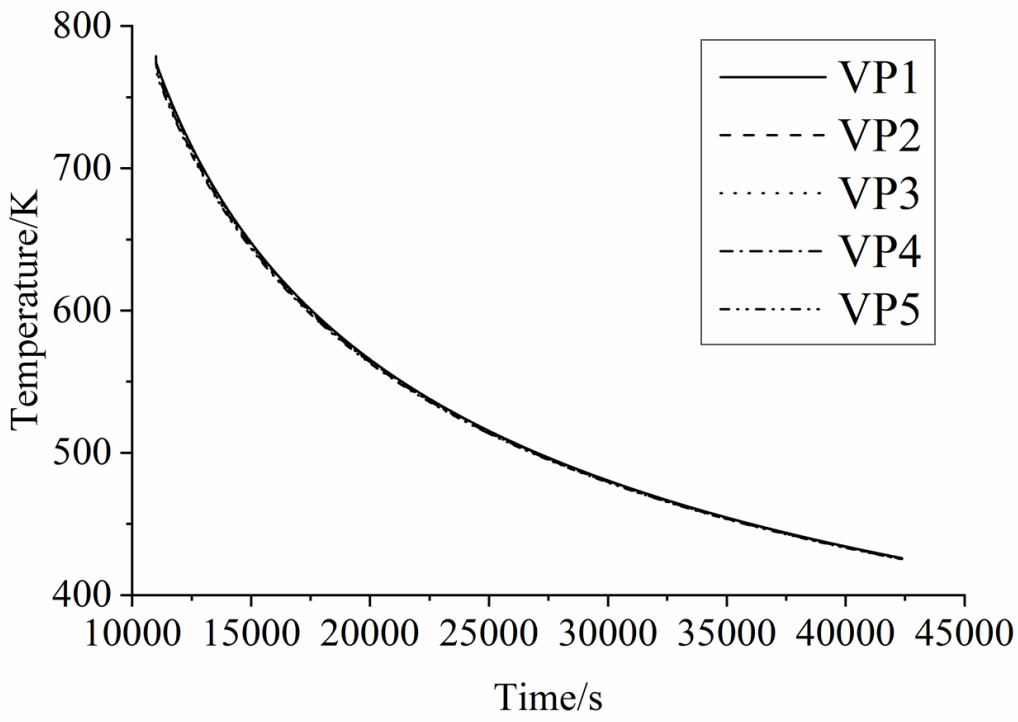

Figure 7.9. Predicted evolution of temperature of the part at the five vertical sampling points (VP1 - VP5) with time during natural cooling process post manufacturing.

7.3.2 Material characterization results

Sample microscopy images provided by Qiushuang Wang from IMR-China are shown in Figure 7.10 to Figure 7.12. Figure 7.10 shows the microstructure characteristics of the PBF-EB produced Ti2448 sample. The PBF-EB sample displays a microstructure with coarse columnar grains and acicular phases (Figure 7.10a). There is plenty of acicular phase distributed on the grain boundaries and inside the grains according to the SEM images of the cross-section of the sample. It is verified by TEM observation that the acicular phase is α'' phase with orthorhombic crystal structure precipitated from β columnar grains (Figure 7.10b).

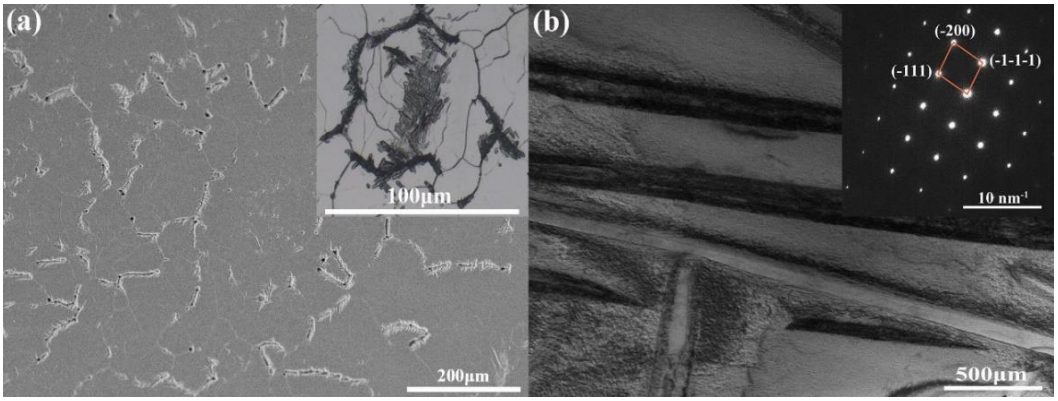

Figure 7.10. Cross-section observations of the manufactured Ti2448 sample: a) SEM image and b) TEM image with diffraction patterns, all provided by Qiushuang Wang from IMR-China.

Comparing the microstructure of material at the cross-section (Figure 7.11) and vertical section (Figure 7.12), it can be seen that coarse columnar β grains tend to form parallel to the building direction, and a layer of equiaxed grains is distributed near the base plate. Such a microstructure is the inherent feature of AM process and is consistent with the results elsewhere [331]. Observing the distribution trend of α'' phase at the positions 2-4 (Figure 7.3b), it can be seen that the content of acicular phase decreases from the bottom to the top along the building direction of the sample, and only very limited acicular grains can be seen on the top of part (Figure 7.11C-2). In addition, it can be seen that more acicular phase exists near the side surface of sample than that around the centre line of sample at the same height (Figure 7.11B-2 and Figure 7.11C-2). To confirm this, the phase content and grain size within 0.5 mm from the side surface, and separately near the centre line of the sample were measured using the metallographic pictures in conjunction with metallographic quantitative analysis by Qiushuang Wang from IMR-China.

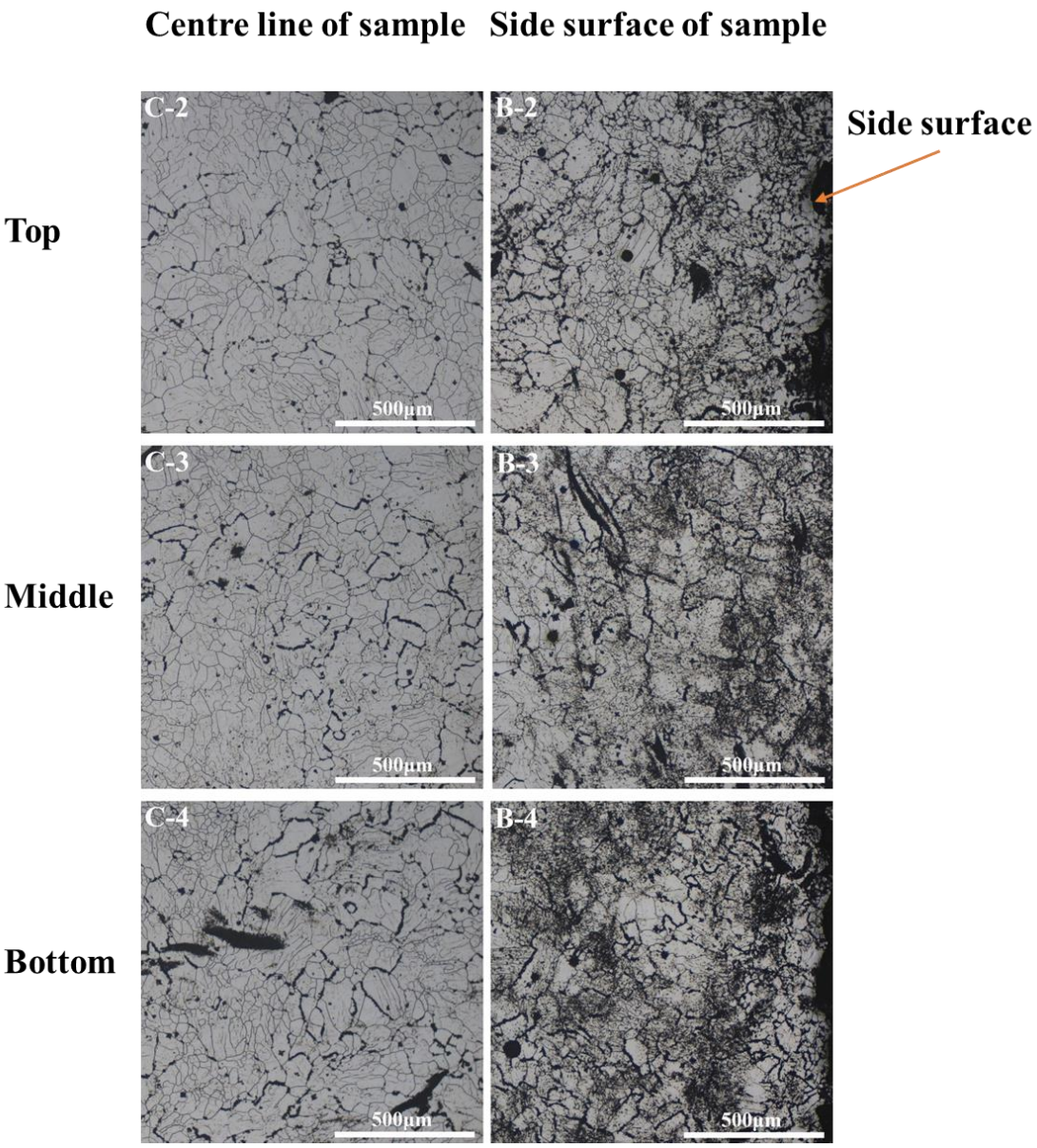

Figure 7.11. Optical image of cross-section in different segments of sample. The picture with letter "C" represents cross-section around centre line of sample, and the picture with letter "B" represents cross-section of sample near its side surface. Number 2-4 on the pictures represents segment 2-4 as illustrated in Figure 7.3b. This figure is provided by Qiushuang Wang from IMR-China.

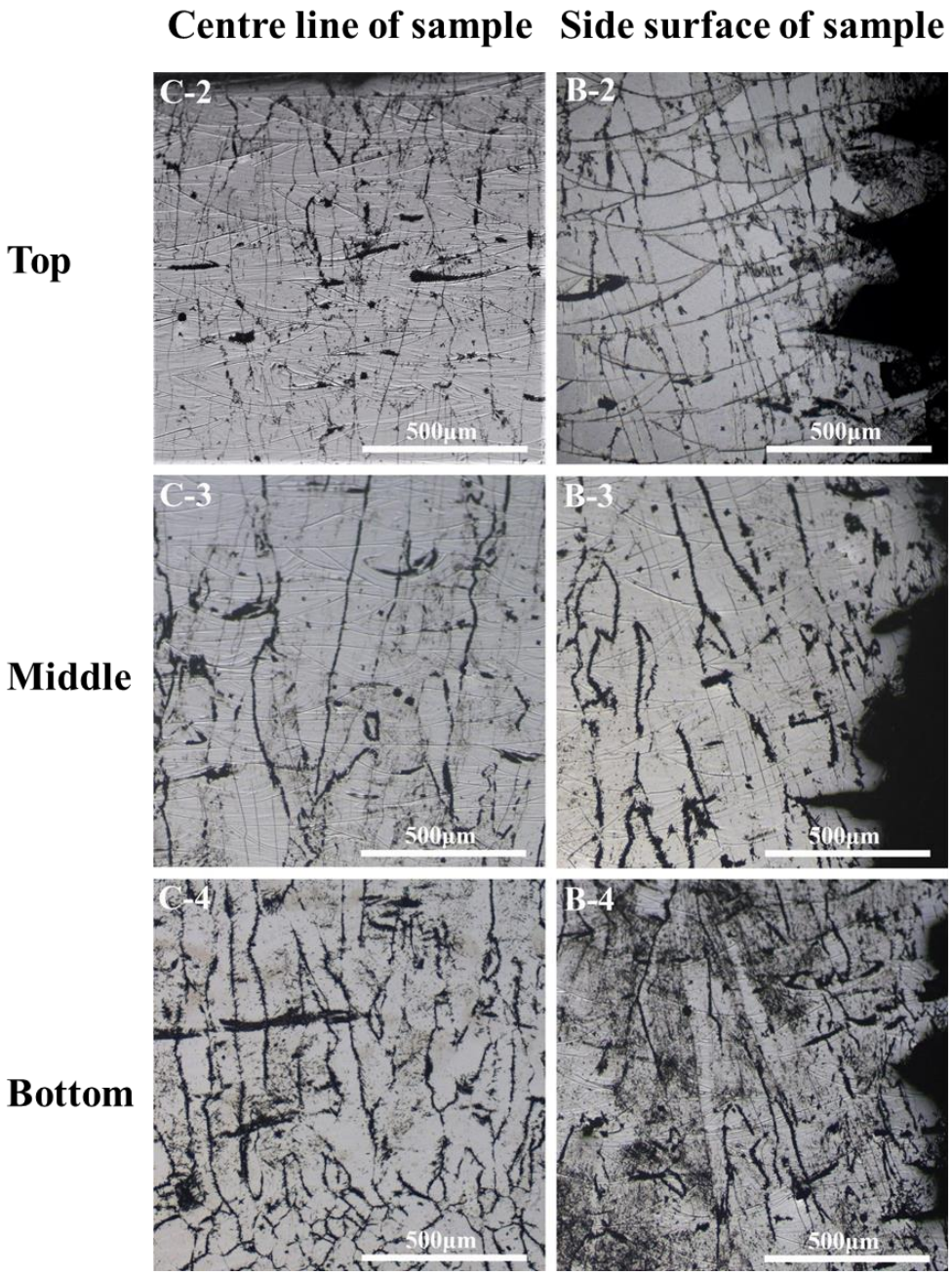

Figure 7.12. Optical image of vertical section in different segments of sample. The picture with letter "C" represents vertical section around centre line of sample, and the picture with letter "B" represents vertical section of sample near its side surface. Number 2-4 on the pictures represents segment 2-4 as illustrated in Figure 7.3b. This figure is provided by Qiushuang Wang from IMR-China.

Experimental results of α'' phase fraction and β grain size from Qiushuang Wang can be seen in Figure 7.13 and Figure 7.14. Figure 7.13 clearly presents the decreasing profile of content of α" phase along the building direction near either the centre line or side surface

of sample. It can be seen from Figure 7.14 that the β grain size increases along the building direction of the sample. Meanwhile, the β grain size near the centre line of the sample is significantly greater than that near the side surface of sample.

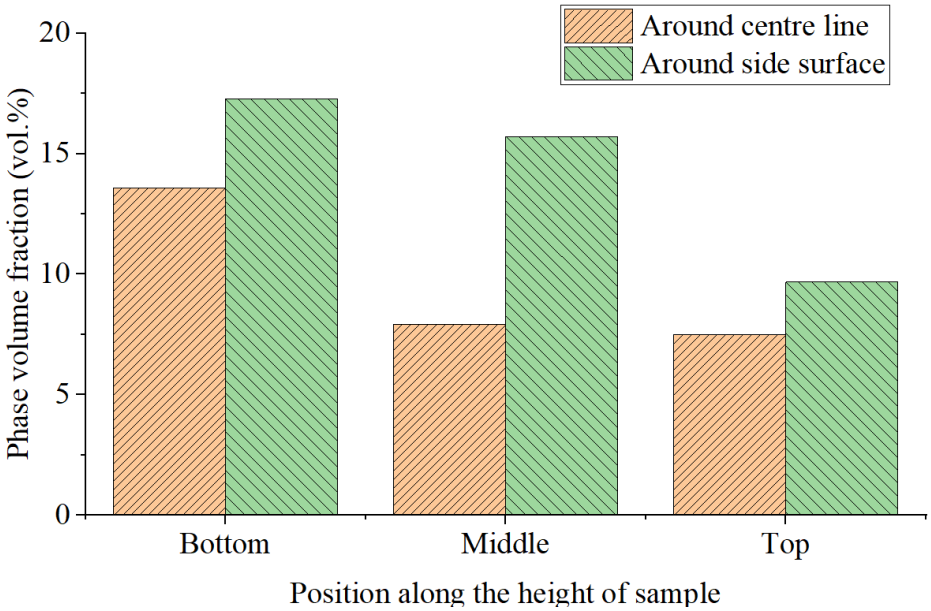

Figure 7.13. Experimentally measured α'' phase volume fraction (vol.%) at different segments of the sample provided by Qiushuang Wang from IMR-China.

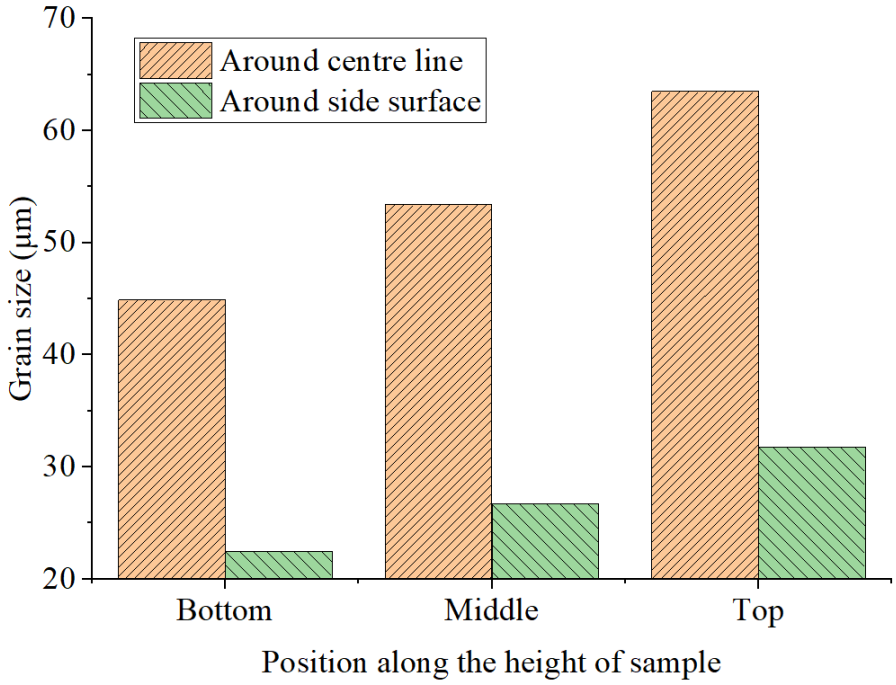

Figure 7.14. Experimentally measured β Grain size (μm) at different segments of the sample, provided by Qiushuang Wang from IMR-China.

7.3.3 Mechanical modelling results and strategies to mitigate stress

Figure 7.15a shows the computational modelling result of the maximum principal stress contour of part after cooling to room temperature for the typical PBF-EB manufacturing by using process parameters listed in Table 7.1 (model 1). The RS contour indicates that the RS state evolutions from tensile to compressive from the side surface to the centreline of part [87]. The largest RS occurs at the interface of the part with the build plate, which is consistent with conclusions from **Chapters 3**, **4**, **5** and studies elsewhere [48, 332]. Plastic deformation occurs since the maximum RS exceeds the yield stress of titanium material [38, 41, 288]. Figure 7.15a also reveals that, apart from RS at the interface of part with the base plate, most areas of RS of PBF-EB manufactured part is with a low level of magnitude (i.e. less than 200 MPa).

To quantifiably compare RS of parts manufactured by PBF-EB with that of PBF-LB, the RS contour produced by the typical PBF-LB process on the same cylinder part with parameters of model 2 in Table 7.1 is shown in Figure 7.15b. It can be seen from Figure 7.15 that similar RS distribution is resulted in PBF-LB and PBF-EB that both of their tensile RS occurs at the side surface while compressive RS forms at the central area of sample. However, significantly higher maximum principal RS of part is formed by PBF-LB than that of the PBF-EB, which is in line with other studies [333, 334]. Several factors (e.g. temperature of the base plate) may influence the RS of part and can cause the significantly RS difference between PBF-LB and PBF-EB manufacturing, which have been introduced in **Chapter 1**. It is therefore necessary to reduce RS in PBF manufacturing, especially at the interface of the part with the base plate.

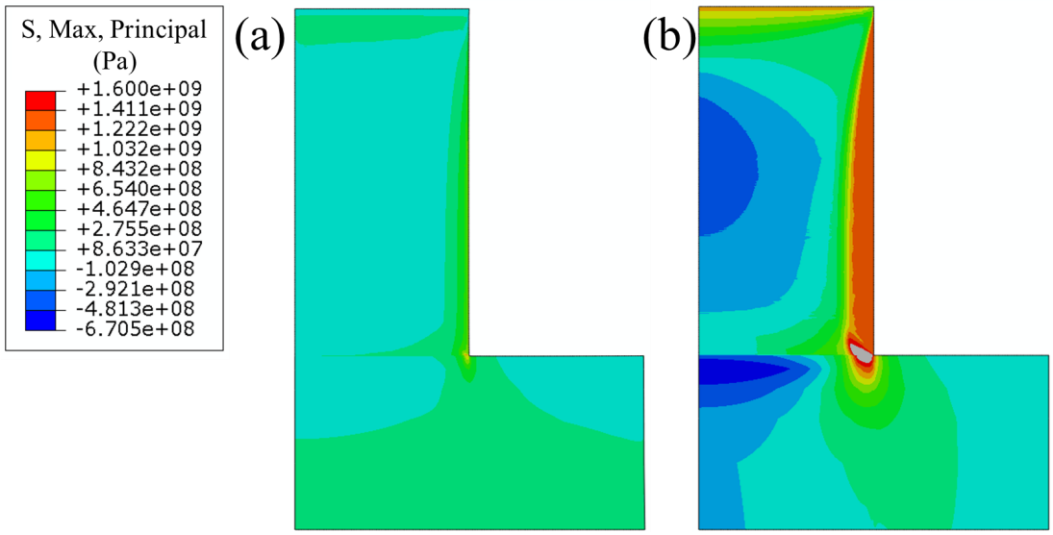

Figure 7.15. The computational modelling results of final RS contours of part at room temperature by a) PBF-EB (case 1 in Table 7.1) and b) PBF-LB (case 2 in Table 7.1).

7.3.4 Strategies to mitigate residual stress in PBF

To explore the effective strategies to mitigate RS in PBF, a set of the computational PBF-LB process modelling varying preheating temperatures of the base plate (as well as the powder bed), top surface convection heat loss at the active layer and energy densities were performed by using the corresponding process modelling parameters listed in Table 7.1. Figure 7.16 indicates RS contours with different computational modelling conditions by PBF-LB, such as Figure 7.16b and Figure 7.16c reveal RS contour without the top surface convection (model 3 in Table 7.1) and the RS contour with a lower energy density (model 4 in Table 7.1) comparing with model 2 in Table 7.1, respectively. The similar RS contour with (Figure 7.16a) and without (Figure 7.16b) the top surface convection was formed, which indicates the top surface convection has minimum effects on RS and is consistent with studies of literature [280, 335]. Comparing RS resulted by different energy densities, Figure 7.16a (with a higher energy density) and Figure 7.16c (with a lower energy density) indicate similar RS distribution that stress at the surface of part is tensile. However, the maximum principal stress of part manufactured with the higher energy density (Figure 7.16a) is marginally (17 MPa) lower than that with the lower energy density (Figure 7.16c), which indicates the higher energy density applied in the PBF-LB manufacturing potentially results a lower RS. This phenomenon is because that the uniformity of the

powder bed causes a lower temperature gradient and cooling rate and is consistent with studies elsewhere [42, 87, 121].

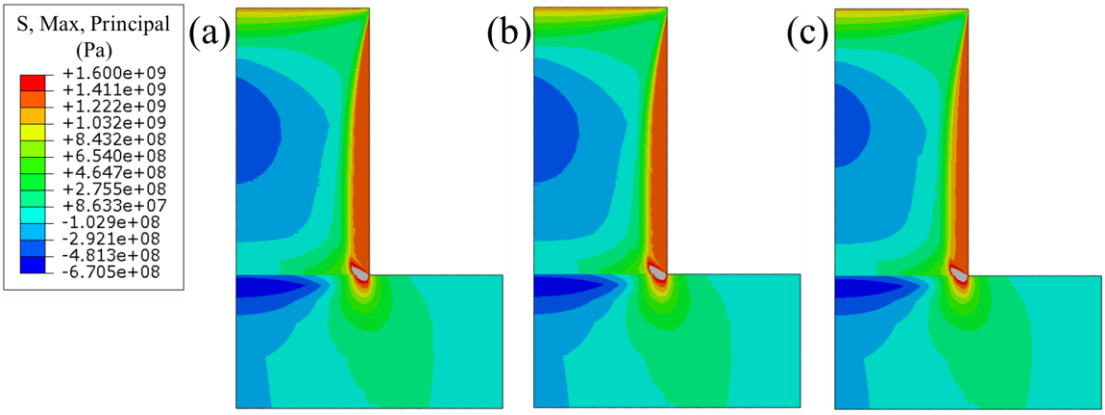

Figure 7.16. Predicted RS contours manufactured by PBF-LB: a) Typical process modelling (model 2 in Table 7.1). b) Without top surface convection (model 3 in Table 7.1) and c) With lower energy density (model 4 in Table 7.1).

Figure 7.17 shows the corresponding RS contours for different preheating temperatures (293 K, 353 K, 573 K and 773 K) of the base plate and the powder bed, where the RS contours differ significantly. Figure 7.17 indicates the higher preheating temperatures of the base plate and the powder bed, the significantly lower RS of the final manufactured parts, which is consistent with studies elsewhere [336, 337]. For instance, the maximum RS with preheating temperature of base plate and powder bed of 773 K (1271 MPa) was 41.37 % lower than that of the computational modelling without preheating the base plate and powder bed (293 K). This phenomenon is because the higher temperature of the base plate and the powder bed, the lower thermal gradient between the melted layers and the base plate and the powder bed [338].

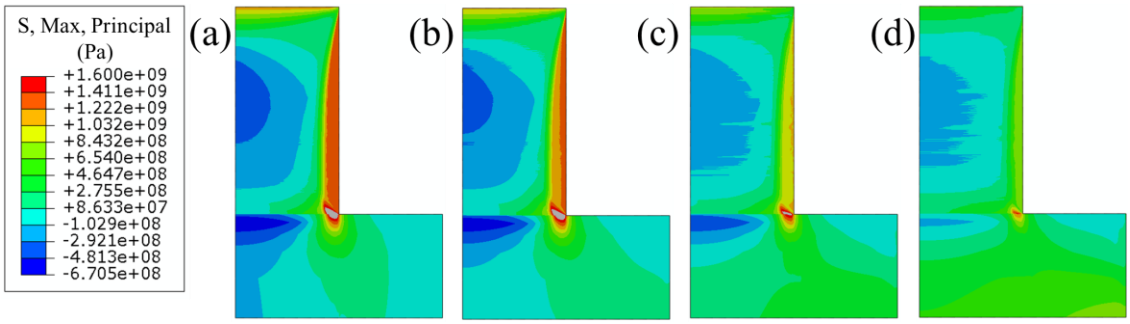

Figure 7.17. Predicted RS contours of part manufactured with different preheating temperatures of the base plate and the powder bed in PBF-LB: a) 293 K. b) 373 K. c) 573 K and d) 773 K.

In order to get a similar RS magnitude and contour by PBF-LB with that of the PBF-EB, the RS mitigation strategies mentioned above were applied for PBF-LB process modelling. Figure 7.18b shows the computational PBF-LB process modelling with the base plate and powder bed preheating temperature of 773 K (model 8 in Table 7.1). By modifying these process parameters for the PBF process modelling, the similar RS distribution and magnitude by PBF-LB with that of the PBF-EB was achieved. It should be noted that the maximum principal RS for PBF-LB (1271.50 MPa, Figure 7.18b) was still marginally (3.37 %) higher than that of the PBF-EB (1228.69 MPa, Figure 7.18b).

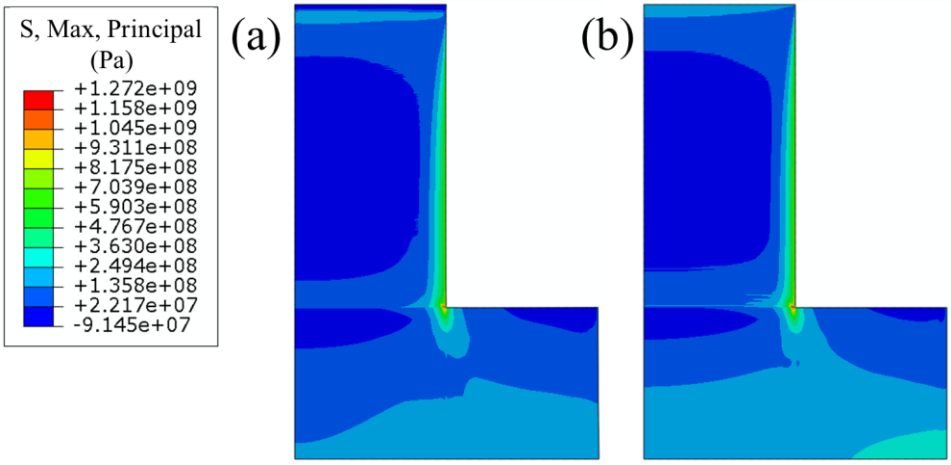

Figure 7.18. The computational final RS contours by a) PBF-EB (model 1 in Table 7.1) and b) PBF-LB with base plate and powder bed preheating to 773 K (model 8 in Table 7.1).

This study indicates that the RS can be effectively reduced via modifications of process parameters in PBF manufacturing. For the development of PBF technology, the strategies below are recommended to mitigate RS based on results of this study:

a) The preheating temperature of the base plate and the powder bed can significantly affect RS of the manufactured parts in PBF. The higher of the preheating temperature of the base plate and the powder bed in PBF-LB, the lower magnitude of RS induced, which is consistent with research elsewhere [322, 339].
b) The higher energy density applied on each layer in PBF manufacturing, the marginal lower (e.g. 17 MPa) RS resulted. The higher energy density can be induced by increasing energy power input, decreasing energy beam moving speed etc.
c) The top surface convection from the active layer to the surrounding atmosphere employed in PBF process modelling has minimum effects on RS.

It should be noted that the typical preheating temperature of the base plate in the first-generation physical PBF-LB manufacturing is up to 473 K due to the PBF machine design, while the most recently developed PBF-LB systems is able to preheat the temperature of the base plate to a higher temperature [21, 337]. For instance, Ali et al. [324] designed a preheating platform by integrating with a Renishaw SLM125 system that enabled to preheat Ti-6Al-4V powder bed up to 1073 K.

7.4 Discussions

7.4.1 Effects of boundary conditions of base plate on residual stress

In this study, to keep the computational temperature of the base plate consistent with that of the practical PBF-EB manufacturing, the computational temperature and RS resulted by isothermal boundary condition (constant temperature of 773 K) at the base plate was used. The influence of thermal boundary condition of the base plate on RS is discussed in this section. Three case studies with different thermal boundary conditions of the base plate were performed for the thermo-mechanical PBF-EB modelling: 1) isothermal boundary condition (constant temperature of 773 K) at the whole base plate; 2) isothermal boundary condition (constant temperature of 773 K) at the bottom of the base plate and 3) predefined boundary condition (initial temperature of 773 K) at the whole base plate. For the case 3, temperature of both the part and the base plate is influenced by thermal input and heat dissipation mechanisms in PBF-EB. Figure 7.19 indicates the largest RS occurred

at the interface of the part with the base plate for all the three modelling cases. The largest maximum principal stress for case 1, case 2 and case 3 was 1228.69 MPa, 1203.59 MPa and 1111.12 MPa, respectively, which indicates the isothermal boundary condition (case 1 and case 2) had a larger RS than that applying a predefined initial temperature at the base plate. This is because, for the isothermal boundary condition at the base plate or at the bottom of the base plate, the base plate takes the role of a powerful heat sink that effectively extracts heat by conduction from the part (where the temperature is higher than the base plate) at its bottom during the PBF-EB process. In this study, for the convenience of PBF-EB modelling, the dimension of the base plate is smaller than the real practical PBF-EB manufacturing, which can also influence the resulting RS. In addition, multiple parts were built in the same base plate during the practical PBF-EB manufacturing. As indicated in **Chapter 6**, the multi-part build can further reduce stress of PBF manufactured part.

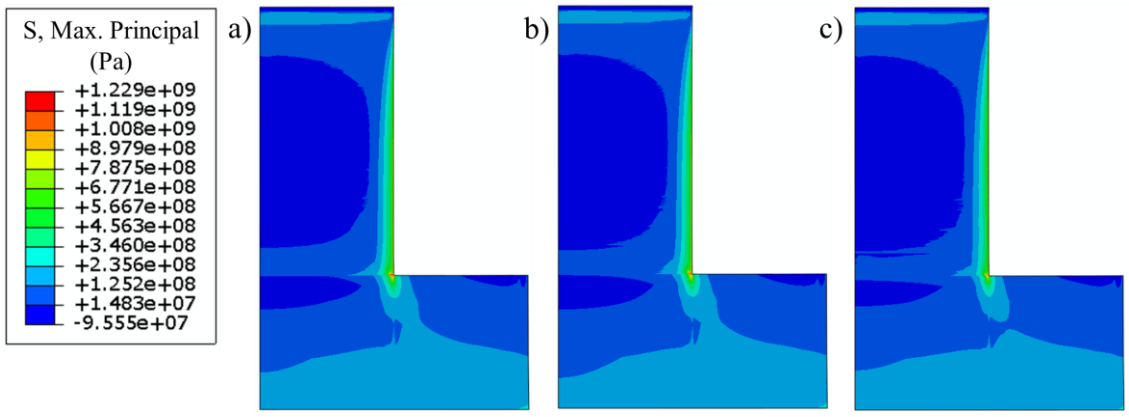

Figure 7.19. Residual stress predicted by different boundary conditions of the base plate in PBF-EB: a) Isothermal boundary condition (constant temperature of 773 K) of the whole base plate. b) Isothermal boundary condition (constant temperature of 773 K) at the bottom of the base plate and c) Predefined temperature of 773 K at the whole base plate.

7.4.2 Variation of α'' phase

The Ti2448 alloy manufactured by PBF-EB process mainly consists of α'' phase and β phase. The transition α'' phase precipitates from the super saturated β phase in solid state during the cooling process of Ti2448 alloy in additive manufacturing. The transition α'' phase can gradually transform to equilibrium α phase at long aging time [340, 341]. It is obvious that the content of α'' phase increases along the radial direction and decreases

along the build direction. The reasons for the variation of α'' phase content can be summarized as follows: firstly, aging time can significantly affect the content of precipitates. According to Figure 7.4, the temperatures of the sampling points VP1 - 4 are approximately stable at 773 K after several cycles of drastic temperature fluctuations. This stage is similar to the aging process, which is conducive to the precipitation of α'' phase. The longer the aging time at precipitation temperature range of α" phase, the more α" phase will be precipitated. In the PBF-EB process, the aging time of the sampling points decreases from VP1 to VP4 in the building direction (Figure 7.4), which is the main reason for the content of α'' phase decreases along the building direction. Secondly, aging temperature is also an important factor that affects the content of precipitates. The content of α phase decreases with the increase of temperature before the transus point (~ 1023 K, provided by Qiushuang Wang from IMR-China), while the content of β phase decreases with the increase of temperature. Because α'' phase is the intermediate phase of β-to-α transformation, the change of α'' phase content with temperature is similar to that of α phase. Therefore, the positive temperature gradient of VP1 - VP5 (Figure 7.5, Figure 7.20) and negative temperature gradient of RP5 - RP1 (Figure 7.7, Figure 7.20) cause the decreasing profile of α'' phase in the building direction and increasing profile of α'' phase from centre line to side surface of sample in the radial direction, respectively.

7.4.3 Variation of β grain size

It is reported that the equiaxed grain layer near the base plate is formed by heterogeneous nucleation due to comelting and alloying of deposited powder material close to the base plate [342]. PBF-EB process has a high cooling rate which causes a large thermal gradient on the solidification front. The thermal gradient promotes the epitaxial growth (a process of growing one crystal type of material on top of another crystal and the growing orientation is determined by the underlying material [343]) of β grains upon the equiaxed grain layer and then forms coarse columnar crystals [331]. It is known that the effect of aging temperature on grain size is larger than the effect of aging time. Figure 7.20 shows the temperature profiles along the building direction and the radial direction at 10986.9 s, when the last layer of the sample has been melted and before the completion of the manufacturing process. The temperature at the top of the sample is 58 K higher than that

at the bottom, which is conducive to the rapid growth of grains, making the grain size at the top of the sample slightly larger than that at the bottom (Figure 7.20b). Due to the decreasing temperature profile from RP1 to RP5 along the radial direction (Figure 7.20a), the β grains around side surface of the sample are smaller than those around the sample centre line.

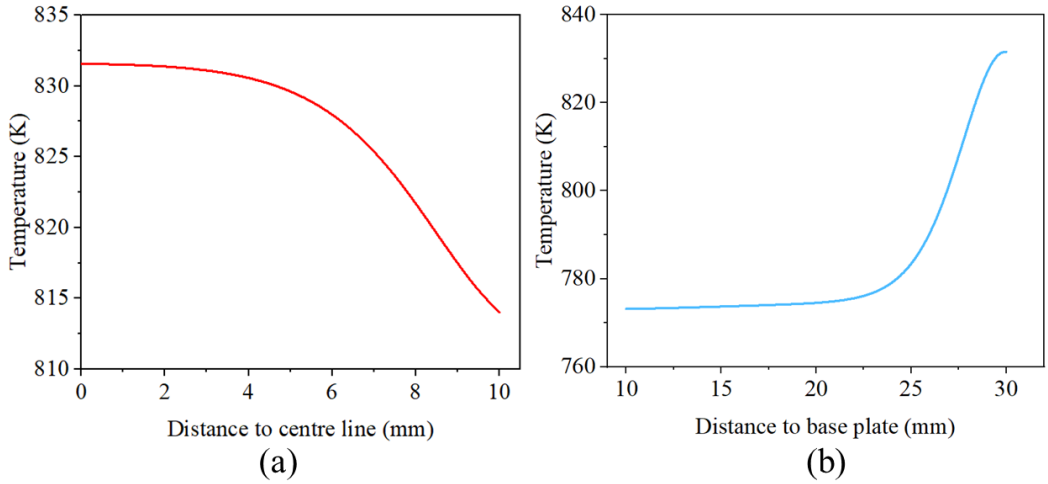

Figure 7.20. Computational modelling results of temperature profile at 10986.9 s: a) At the top surface of sample along the radial direction and (b) Along the centre line of sample.

7.5 Summary

In this study, PBF-EB manufactured Ti2448 alloy at the scale of overall additively manufactured component was computationally predicted by using the layer-by-layer 2D modelling method described in **Chapter 3**. Thermal history and microstructure of manufactured components were characterised using computational and experimental methods, respectively. The stress in PBF-EB manufactured Ti2448 was computationally investigated and strategies to mitigate RS in PBF were recommended. The main conclusions for PBF-EB are as follows:

a) For PBF-EB manufactured Ti2448 alloy component, the content of α" phase decreases along the building direction and increases from the centre line to side surface of sample along the radial direction.
b) The computational modelling results of temperature history, temperature difference and cooling rate along the height and radius of a cylinder component

have revealed the driving factors behind the experimentally observed profiles of α'' phase fraction and β grain size in multiple directions.

c) Variation in thermal history from location to location of a PBF-EB manufactured sample results in non-uniform profile of grain size. The grain size of β phase at the top of the sample is larger than that at the bottom. The β grains at around the side surface of sample are smaller than those around the sample centre line.

d) The computational modelling proves to be an effective tool that can help experimentalists to understand the influence of macroscopic processes on material microstructural evolution and hence potentially optimise the process parameters of PBF-EB to eliminate or otherwise modify such microstructure gradients.

e) Improving the preheating temperature of the base plate and the powder bed is the key strategy to reduce RS. By preheating the base plate and powder bed temperature to 773 K in PBF-LB, it is able to obtain the similar RS with that of the PBF-EB. The higher of energy input into the PBF process modelling, the lower RS resulted in the manufactured part.

f) It is presented in this chapter that the computational modelling in conjunction with practical PBF-EB manufacturing as well as experimental material characterisation can contribute to establish the link between process parameters and material microstructure. Such link can be used by experimentalists and industries to optimise the design of PBF-EB process parameters with the purpose of achieving optimal material microstructure.

8 Application to directed energy deposition additive manufacturing

This chapter aims to expand the finite element process modelling tools developed in previous chapters (**Chapter 3** - **Chapter 6**) for PBF-LB of Ti-6Al-4V material to another application and material, such as DED manufacturing of aluminium alloy. The computational bead-by-bead modelling technique described in **Chapter 2** is employed to predict the thermal and stress behaviours of Al-4(wt %)Si alloy during DED manufacturing. This is a collaborative research with Dr. Wajira Mirihanage's research group (Da Guo and Wajira Mirihanage) at the University of Manchester. *In-situ* RS characterisation of Al-4(wt %)Si alloy during practical DED (i.e. wire arc AM) manufacturing process is completed by the University of Manchester using the high energy X-ray diffraction method. To interpret the *in-situ* measured RS raw data from Dr. Wajira Mirihanage's group at the University of Manchester, a custom written code to calculate through thickness residual stress and computational finite element DED process thermo-mechanical modelling is performed by the author.

8.1 Introduction

In-situ measurement of RS enables to obtain RS state evolution during the physical DED manufacturing process. Due to that the non-destructive RS measurement facility is worldwide limited, as has been described in Section 2.4, *in-situ* measurement of RS for DED manufacturing of Al-4(wt %)Si Aluminium alloy is challenging and is investigated by the collaborators at the University of Manchester for the first time. The comparisons between DED manufacturing (which is the focus of this chapter) and previously investigated PBF manufacturing from **Chapter 2** to **Chapter 7** have been described in **Chapter 1** and summarised in Table 1.1.

Predicting thermal history and the resulting RS in DED could better understand the practical manufacturing process and interpret the experimentally measured temperature and stress behaviours. Song et al. [131] predicted stress of DED manufactured Inconel

718 thin wall structure and the results indicated that the largest stress was formed at the interface of the thin wall with the base plate and resulting symmetric stress distribution along the scanning direction. Lu et al. [27] computationally investigated temperature and distortion of Ti-6Al-4V material in DED by using the fully coupled thermo-mechanical method and the in - house Comet FEM software. The results indicated an over 60 % increase of distortion at the end of post - manufacturing natural cooling process, comparing with distortion after completing manufacturing of the last layer of part in DED manufacturing.

The aim of this work is to interpret the experimental RS measurement and to apply the process thermo-mechanical modelling techniques described and previously developed from **Chapter 2** to **Chapter 6** for PBF-LB of Ti-6Al-4V material to DED process of aluminium material. The objectives of this chapter are as follows:

a) To interpret the *in-situ* observation of stress during the practical DED manufacturing, which was performed by collaborators at the University of Manchester.
b) To adapt the thermo - mechanical modelling capability developed for PBF-LB to DED manufacturing process for macroscopic aluminium component.
c) To computationally investigate thermal behaviours (i.e. temperature, temperature gradient and cooling rate) and RS state evolutions with time at different positions of part during DED manufacturing process.
d) Investigation of bead increment length effect on RS in DED manufacturing by using the computational bead-by-bead modelling method.

8.2 Research methods for DED modelling

8.2.1 Computational modelling methods

To simulate the practical DED manufacturing process that was performed by collaborators at the University of Manchester, an Al-4(wt %)Si thin trapezoidal plate (353.2 mm long at the top surface and 255 mm long at the bottom surface, 49.1 mm height, 8.4 mm thickness) was created on a rigid body of fixture in the computational DED process

modelling (Figure 8.1). The bead-by-bead (i.e. element-by-element) modelling approach introduced in **Chapter 2** was employed for the transient fully coupled thermo-mechanical process modelling of DED by computationally solving the governing equation (Eq. 2.1) using ABAQUS (Dassault Systems, USA, 2019). A Python script (Figure 3.1) was adapted from the PBF-LB modelling in **Chapter 3** to slice the 3D model into separate bead increment based on the layer height (Table 8.1) and bead increment length (Figure 8.1b) in DED modelling. All the bead increments were deactivated at the initial step and then each bead increment was sequentially activated by following the predefined scanning path and using the 'model change' function (described in **Chapter 3**) in ABAQUS. Due to the symmetric characteristic of the part with respective to the XZ plane (Figure 8.1a), half of the width of the system was employed in FEM to save the computational cost. The 'S' shape scanning strategy (shown as the purple arrow in Figure 8.1b) was applied in DED modelling, corresponding to the practical DED manufacturing process. To investigate effect of the computational bead increment length (Figure 8.1a) on stress in DED process, different finite element bead increment lengths (10 mm, 20 mm, and 40 mm) were applied in the bead-by-bead modelling. Considering the computational capabilities, the 8-node displacement and temperature mesh element (C3D8T) and converged (less than 0.99 % RS difference) mesh size of $80 \times 80 \times 80$ μm^3 were applied on the solid part. The similar mesh scales were also adopted in other DED simulations [27, 344]. Temperature and stress state evolutions at four different positions (P1, P2, P3 and P4, as shown in Figure 8.1b) during DED manufacturing process were monitored. The first layer is deposited on the fixture along the negative *x* direction and then the scanning direction reverses for the next deposition layer. There are totally 58 layers of material were deposited for manufacturing the thin wall structure, each with one track wide. To compare with the experimentally measured RS, the computational maximum time increment in ABAQUS for each step was set as 0.2 s during the DED manufacturing process.

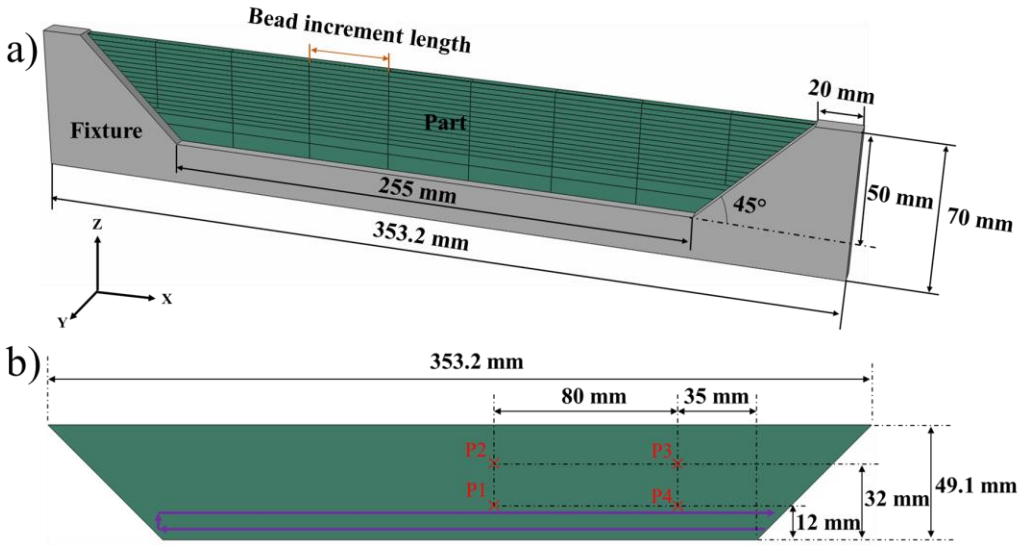

Figure 8.1. a) Computational DED model consisting of part and fixture and b) Position illustration for temperature and stress.

To simulate energy input in DED modelling, the initial (predefined) temperature of material of each bead increment was calculated based on the actual process of energy input during DED manufacturing (as shown in Section 8.2.2). After applying the predefined temperature, each bead increment began to cool for a period of cooling step time, which was calculated by the bead increment length divided by the moving speed of deposition nozzle [345]. The layer cooling step time during computational process modelling was set as a constant of 25 s. The height for the first layer, the second layer and the remaining layers (3^{rd} - 58^{th}) is 2.6 mm, 1.7 mm, and 0.8 mm, respectively. The overall DED process modelling parameters are summarised in Table 8.1, corresponding to the practical DED manufacturing process of Da Guo and Wajira Mirihanage at the University of Manchester.

Table 8.1. Parameters applied for DED process modelling.

Layer	Layer height (mm)	Moving speed (mm/s)	Power (w)	Layer cooling time (s)
First layer	2.6	6.67	3160	25
Second layer	1.7	16.67	3260	25
Other layers	0.8	16.67	3260	25

For the convenience of DED process modelling, the corresponding thermal transfer mechanisms (shown in Figure 8.2) are as follows:

i) Heat conduction (Eq.2.15) within the solid part;

ii) Heat conduction from part to the fixture;

iii) Free surface convection (Eq. 2.17) to environment at top surface of each active layer and front surface of part (Figure 8.1);

iv) Free surface radiation (Eq. 2.16) to environment at the top surface of each active layer.

v) Free surface convection from fixture to the surrounding atmosphere.

The convective heat transfer coefficient of aluminium to surrounding environment (heat losses of Figure 8.2iii and Figure 8.2v) was set as 10 W/m^2/K [142] and the emissivity coefficient for radiation (Figure 8.2iv) was set as 0.4 [346].

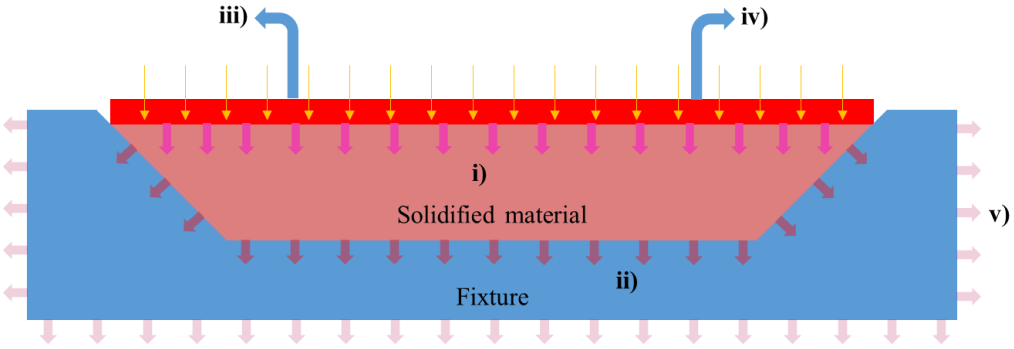

Figure 8.2. Illustration of thermal boundary conditions applied for the computational DED process modelling: i) Solid conduction. ii) Part-fixture conduction. iii) Active layer and front surface (Figure 8.1) convection. iv) Active layer radiation and v) Free surface convection between fixture and the surrounding atmosphere.

In DED process modelling, energy is input to newly born bead increment using a predefined temperature, which has been reviewed in **Chapter 2**. For all the bead increments of the computational model, the temperature increase ΔT is calculated based on the DED manufacturing process parameters shown in Table 8.1. After overall calculation based on Eq. 2.8 to Eq. 2.13, the predefined temperatures for bead increments in the first layer, second layer and the rest layers of the computational DED model were set as 3773.68 K, 2483.03 K and 4969.32 K, respectively.

8.2.2 Material properties for DED modelling

The temperature dependent thermal and mechanical material properties (e.g. density, specific heat, expansion coefficient, conductivity, elastic modulus and yield strength) of aluminium alloy were applied for the coupled thermo-mechanical DED process modelling, which are shown in Table 8.2. The Poisson's ratio of aluminium was set as 0.33 and the latent heat (described in Eq. 2.4) coefficient was set as 387 kJ/kg [347, 348].

Table 8.2. Material properties of aluminium material applied for the DED process modelling [347, 348].

Temperature (K)	Density (kg/m^3)	Specific heat (J/kg/K)	Expansion coefficient $\times 10^{-5}$ (1/K)	Conductivity (W/m/K)	Elastic Modulus $\times 10^4$ (MPa)	Yield strength (MPa)
273	2703	917	2.24	162	6.97	277.7
371	2685	978	2.461	177	6.62	264.6
474	2657	1028	2.66	192	5.92	218.6
589	2630	1078	2.76	207	4.778	66.2
701	2602	1133	2.96	223	3.172	17.9
844	2574	1230	3.42	253		

8.3 Results

The influence of finite element bead increment length (Figure 8.1) on RS was analysed and RS contours with different bead increment lengths (10 mm, 20 mm, and 40 mm) after the part was cooled to room temperature are shown in Figure 8.3. For all the simulation cases with different bead increment lengths, a larger RS was formed at the interface of the part with the fixture (i.e. the bottom and side surfaces of part) than that at the central area of part (Figure 8.3). This is assumed to be caused by the high cooling rate at the part-fixture interface and the same phenomena was also found in other DED work [27]. The maximum von Mises stress for the 10 mm, 20 mm, and 40 mm bead increment lengths DED process modelling was 479.21 MPa, 498.80 MPa and 505.54 MPa, respectively, which indicates the larger the bead increment length utilised for DED process modelling, the larger the resulting RS. Based on the maximum RS and contour (Figure 8.3), the RS of part converged at the 20 mm bead increment. Thus, temperature and RS results produced by the 20 mm bead increment modelling were utilised thereafter. Symmetric

stress distribution along the scanning direction was obtained, which is caused by the 'S' scanning strategy (Figure 8.1) in DED manufacturing.

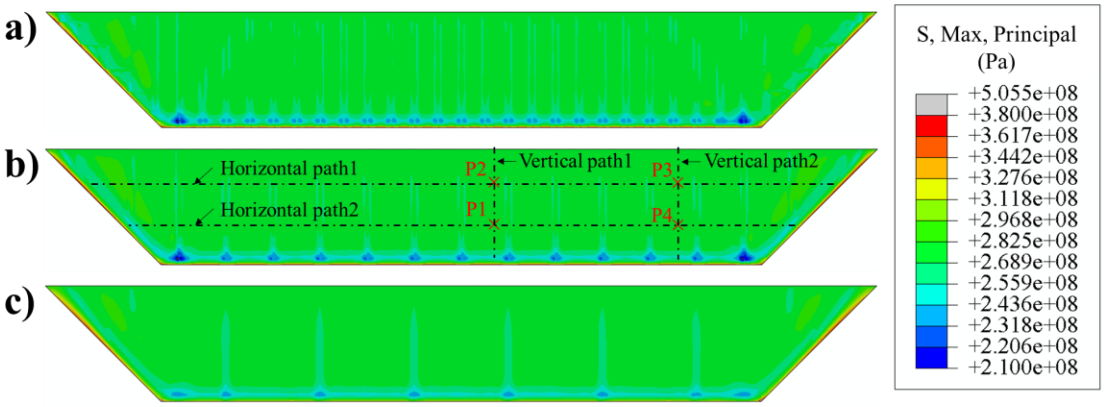

Figure 8.3. Computational modelling results of RS contours at the surface of part by using different bead increment lengths: a) 10 mm. b) 20 mm and c) 40 mm.

The computational modelling results of temperature evolution during the entire DED manufacturing process at four different positions of part (P1 - P4, Figure 8.1) with time is shown in Figure 8.4. The average temperature and RS (i.e. average temperature of all the 6 nodes along the *y* direction, as shown in Figure 8.1) in the computational domain was analysed in this work. Figure 8.4 indicates the temperature oscillated up and down repeatedly with the deposition, heating, and cooling of newly added material. The magnitude of temperature fluctuation decreased with subsequent layers of material deposited. For both central area and around side surface of part (Figure 8.1), the overall temperature at upper position of part (e.g. P2 and P3, Figure 8.4) was higher than at the bottom area (i.e. close to the base plate) of part (e.g. P1 and P4, Figure 8.4). It indicates that the temperature of part increases with the number of layers of material deposited, which has been reported in [290]. In addition, at the same height of part during DED, the temperature near the central line of part (e.g. P1) was slightly higher than that near side surface (e.g. P4). This is caused by the strong heat conduction loss from side surface of part to the fixture. Note that the peak temperature of material exceeded the evaporation temperature of aluminium material, which also occurred during the practical DED manufacturing [316].

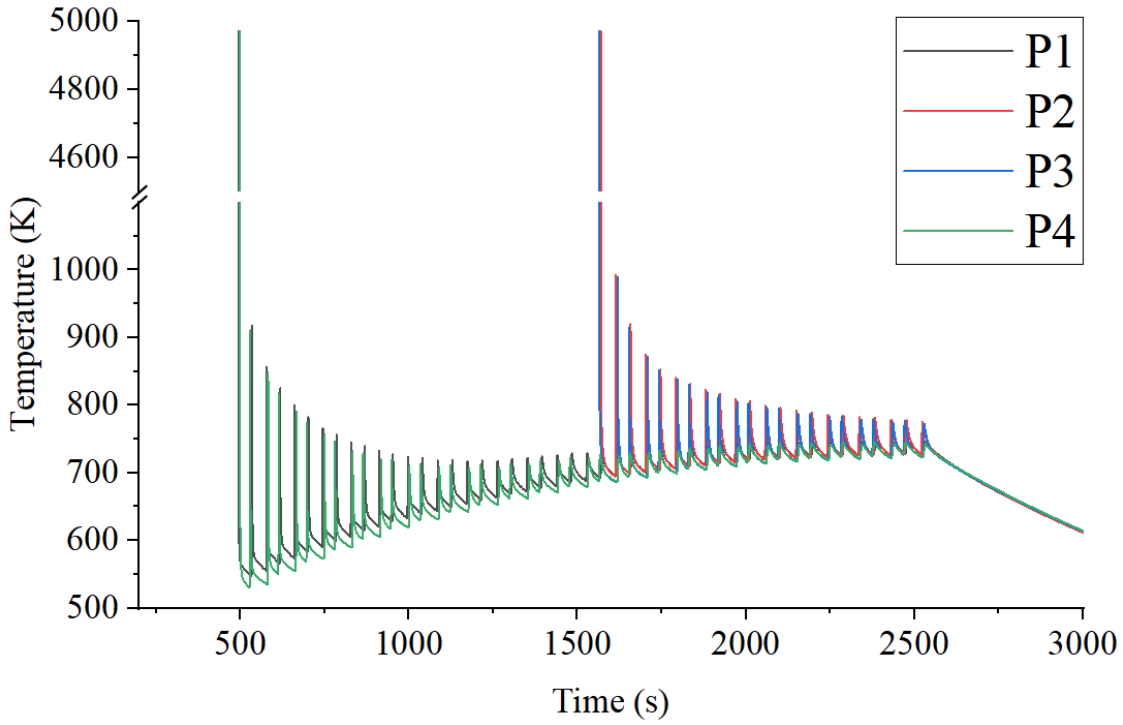

Figure 8.4. Computational modelling results of temperature evolution during the DED manufacturing process at four different positions of part (P1 - P4, as shown in Figure 8.1) with time.

Temperature gradient (TG) at different positions of part (P1 - P4, Figure 8.1) with time is also examined, as shown in Figure 8.5. The TG is calculated based on the temperature history in Figure 8.4 by using the following second-order central difference equation [50]:

$$\|\nabla T\| = \left\|\left(\frac{T(x+\Delta x,y,z)-T(x,y,z)}{2\Delta x}, \frac{T(x,y+\Delta y,z)-T(x,y,z)}{2\Delta y}, \frac{T(x,y,z+\Delta z)-T(x,y,z)}{2\Delta z}\right)\right\| \quad (8.1)$$

Figure 8.5 reveals that TG is the largest at the time point when the newly born molten material is firstly deposited. Then TG gradually decreased with time to a low level of magnitude (e.g. 0.2 K/μm), during subsequent deposition, re-melting and solidification processes of the material. The TG at the bottom of part (e.g. P1 and P4) is higher than that at upper area of part (e.g. P2 and P3). This is because the base plate takes the role as a powerful heat sink that very effectively extracts heat by conduction from the solid part to cool the part during the DED process. The similar results were reported in study [27]. At the same level of part, TG at the side surface (e.g. P4) is higher than at the central area of

part (P1), which is caused by the conduction heat loss from part-fixture interface to the fixture.

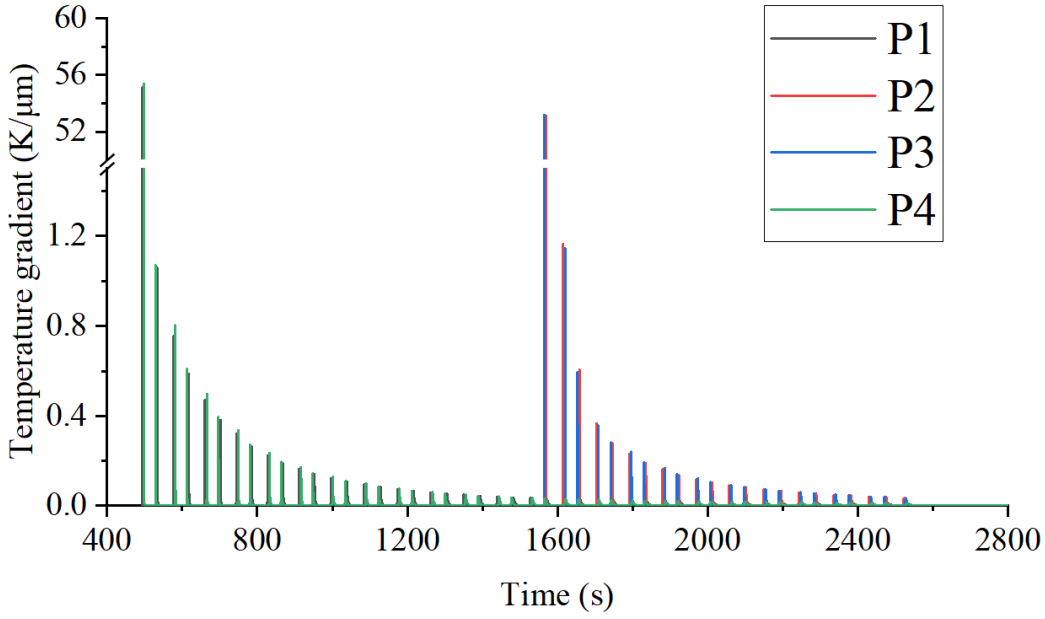

Figure 8.5. Computational results of temperature gradient evolution at four different positions of part (P1 - P4, Figure 8.1) during DED with time.

The von Mises stress state evolution at four positions of part (P1 - P4, Figure 8.1) during the manufacturing and post-manufacturing processes with time is shown in Figure 8.6, by using the average stress through the thickness of part. The stress state fluctuated up and down with the deposition, melting and cooling of material, and the similar stress state evolution with time was also observed in study elsewhere [349]. The decrease trend of stress from P1 to P2 during the manufacturing process is caused by the decrease trend of TG with subsequent layers deposited (Figure 8.5). Figure 8.6 reveals stress at around side surface (e.g. P4) was higher than that around the central area of part (e.g. P1) at the same height of part, which is caused by the higher TG at P4 than P1 (Figure 8.5). During the post manufacturing natural cooling process, stress gradually increased to 274.80 MPa before stabilisation, due to that the shrinkage of part was constrained by the base plate during the cooling process to room temperature [349]. It is therefore recommended to mitigate stress in DED by controlling the post manufacturing cooling process, by such as reducing the cooling rate by controlling environmental temperatures.

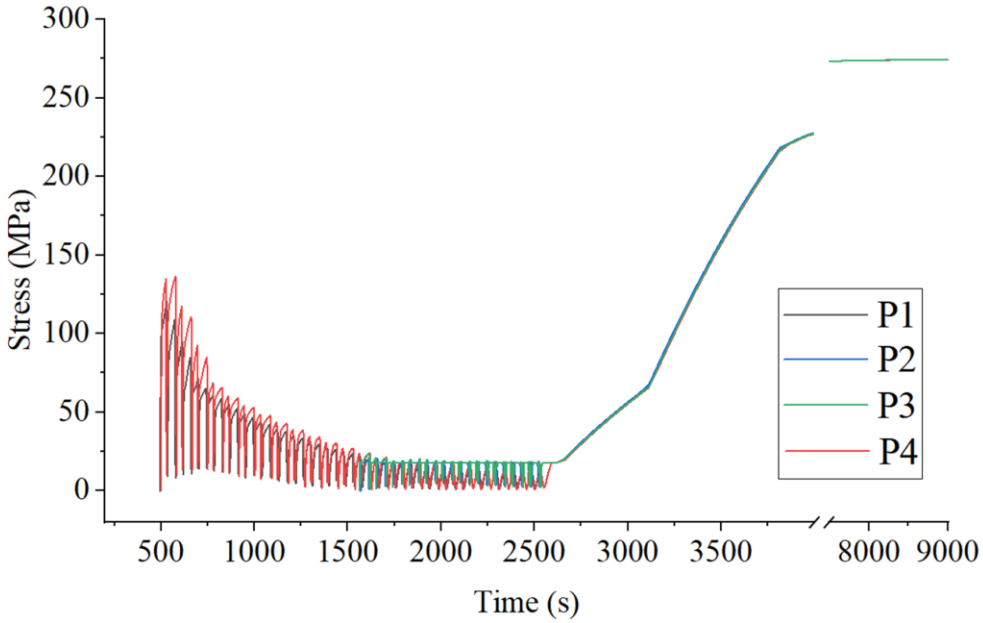

Figure 8.6. Computational modelling results of von Mises stress state evolution during DED process at four positions (P1 - P4, as shown in Figure 8.1) with time.

Cooling rate at four different positions (P1 - P4) of part is shown in Table 8.3, which is calculated based on the average temperature history through thickness of part. The CR is calculated based on the time required for the temperature of P1 - P4 to cool from the melting point to the β - transus temperature, by following the calculation method in study [329]. Table 8.3 indicates CR varied from location to location in DED modelling and is in the magnitude of 10^5 K/s. Generally, CR at the bottom (e.g. P1 and P4) of part was higher than that at upper location (e.g. P2 and P3) of part, which is caused by the heat conduction loss from the bottom surface of part to the fixture and thus the initial deposition temperature at the bottom area is lower than that at the upper location of part (Figure 8.4). CR at around the side surface (e.g. P4) was marginal 2.82 % higher than that at the central area of part (e.g. P1) at the same height of part, which is caused by the heat conduction from the side surface of part to the fixture.

Table 8.3. Computational modelling results of cooling rate at four different positions (P1 - P4) during DED.

Position	P1	P2	P3	P4
Cooling rate (K/s)	17139.00	16725.20	16742.29	17622.32

Figure 8.7 shows the resulting stress at room temperature along the build direction of part (Figure 8.3b): vertical path 1 along direction P1 to P2 and vertical path 2 along direction

P4 to P3. For both vertical paths, the largest stress (~ 370 MPa) occurred at the bottom of the part. With increasing the printing height of part, the stress became stable along the build direction of part, which was around 100 MPa lower than the largest stress at the bottom of part. Similar stress distribution along the vertical direction was observed in other DED study [26]. Figure 8.8 indicates the resulting stress along the horizontal direction of part (Figure 8.3b): horizontal path 1 along P2 to P3 and horizontal path 2 along P1 to P4 (Figure 8.3b), respectively. For both horizontal paths, stress along the side surface of part was significantly higher than at the central area of part, which is caused by the constraint of the fixture and heat dissipation from part to the fixture.

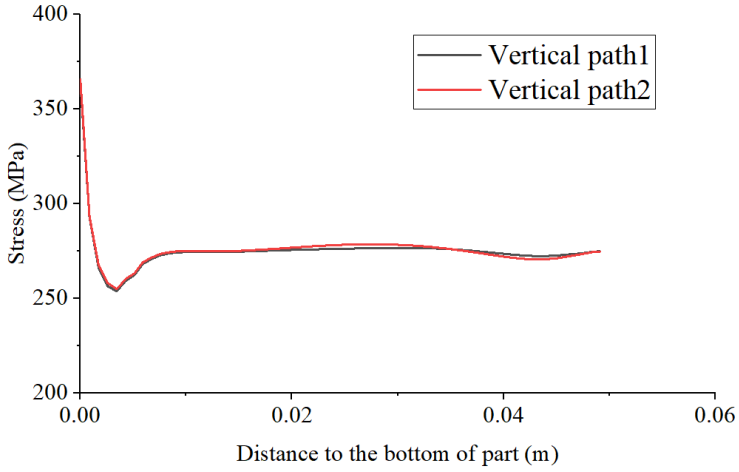

Figure 8.7. Predicted residual stress along vertical paths (Figure 8.3b) of part.

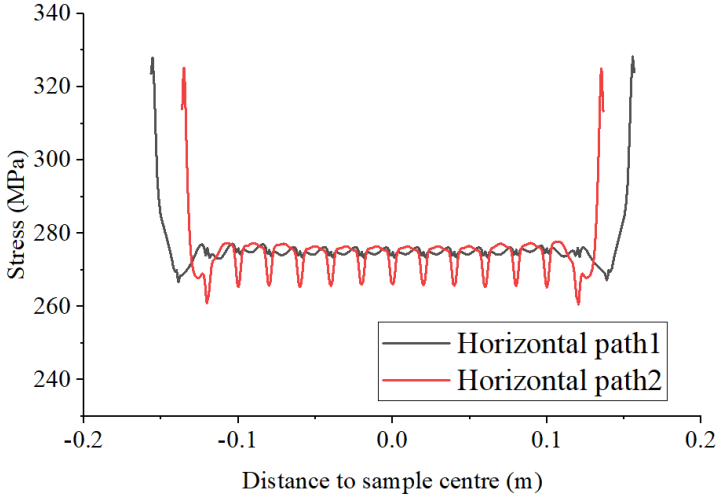

Figure 8.8. Computational modelling results of residual stress along horizontal paths (Figure 8.3b) of part.

Figure 8.9 shows the computational modelling results of σ_{xx} (along the x direction as shown in Figure 8.1), σ_{zz} stress (along the z direction as shown in Figure 8.1) and the maximum principal state evolutions during the DED manufacturing process with time at the P1 position of part (Figure 8.1). As can be seen in Figure 8.9, the compressive σ_{xx} stress state is formed when the material is heated, due to thermal expansion, which has been described in **Chapter 2**. During the cooling process of each layer, the tensile stress state was generated due to thermal contraction of material [41]. During the entire DED manufacturing, the maximum σ_{xx} stress at P1 was always larger than the σ_{zz} stress, which is in good agreement with another DED study [349] for different numbers of layers. Figure 8.1 shows the magnitude of the maximum principal stress close to the σ_{xx} stress, but with a lower magnitude of fluctuation.

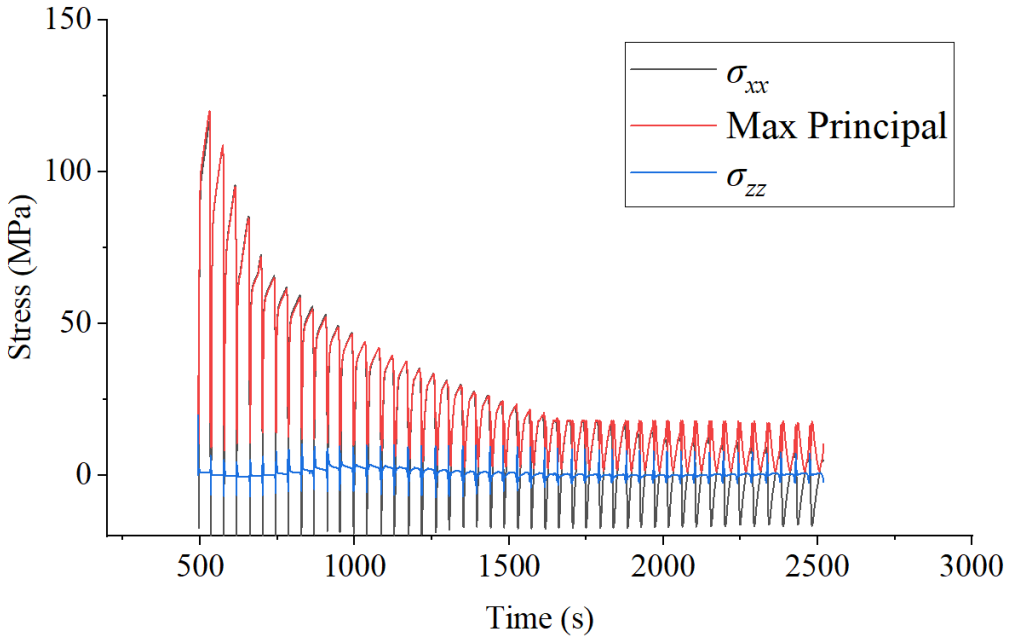

Figure 8.9. Computational modelling results of σ_{xx} and σ_{zz} stress state evolution during DED with time at the P1 position (Figure 8.1).

8.4 Discussions

In this chapter, the process modelling capability developed for PBF-LB in **Chapter 3** – **Chapter 6** was extended to DED process modelling for a macroscopic aluminium thin trapezoidal plate. Both the thermal and stress behaviours at different positions (P1 - P4, Figure 8.1b) of part was investigated and analysed.

The computational modelling results indicate that the maximum RS of DED manufactured part was formed at the interface of part with the fixture (Figure 8.3). Guo et al. [290] experimentally measured RS of DED manufactured 316L stainless steel thin plate (i.e. 200 × 2.4 × 125 mm^3) on a rectangular base plate by the high energy X-ray diffraction experiment. The results indicated that the maximum tensile RS (i.e. ~ 250 MPa) occurred at the bottom of the part, followed by the compressive stress that was slightly lower than zero at the middle of the part, and finally tensile stress (i.e. ~ 100 MPa) formed at the top area along the build direction of the part. The predicted maximum stress (~ 370 MPa, Figure 8.7) at the interface of part with the fixture is larger than that was experimentally measured in Guo's study (~ 250 MPa). In addition, the predicted maximum *x* direction stress in this chapter is ~ 290 MPa, which is also 80 MPa higher than that of DED manufactured 100 mm length aluminium component [350]. The higher computational results of RS than the experimental measurement is induced by the trapezoidal shape of the fixture, which causes additional mechanical constraints of part from the interface of part with the fixture.

Multiple factors can influence the computational modelling results of temperature and RS, and further causing differences between simulation and experimental results. Firstly, the heat input profile influences the computational thermal and mechanical results. For the convenience of DED process modelling, a constant predefined temperature over the entire bead increment (Figure 8.1) was employed, and the temperature gradient inside the single bead increment was not specifically involved. To better simulate the heat input during practical DED manufacturing, future work would consider the bead-by-bead modelling method but with a non-uniformly distributed moving heat profile (e.g. Gaussian (Eq. 2.5) or Goldak double ellipsoid [351]). The non-uniformly distributed heat profile is expected to produce different temperatures along the thickness of the part (along the *y* direction in Figure 8.1), i.e. a higher temperature at the central field while a lower temperature at the front surface of part (Figure 8.1) [117]. The gradient temperature inside the bead increment could possibly cause a larger difference in RS along the thickness direction of part. Note that the Gaussian or double ellipsoid moving heat input has a potential to provide accurate temperature history, however, this would significantly expand the computational cost. One feasible solution is to perform DED modelling by using the AM

Modeler plugin [131], as reviewed in **Chapter 2**. Secondly, the melt pool flow and arc pressure were not involved in the DED process modelling in this chapter. In the practical DED manufacturing, the high arc pressure induces a large depression in the central field of the melt pool [23, 352]. To accurately simulate the melt pool shape and thus the temperature profile of the melt pool, in the future, there is a need to consider the influences of melt pool flow and arc pressure in DED process modelling. Thirdly, in this study, different bead increment lengths (10 mm, 20 mm, and 40 mm) were employed for DED modelling and the results indicated temperature and stress results converged at the 20 mm bead increment length. However, the converged bead increment size is still larger than the diameter of wire that was used in the practical DED manufacturing (i.e. 1.2 mm). The variation of bead increment size that was employed in DED modelling would further influence the temperature gradient and cooling rate. A Python code has been developed for slicing the thin wall part (Figure 8.1) into a smaller bead increment length of 1.2 mm for DED manufacturing. But the computational thermo-mechanical DED modelling exacerbates the computational time, if using smaller bead increment length (i.e. 1.2 mm). As the computational time is largely depending on the number of the total finite elements involved in computational modelling, adaptive mesh technique [207] is an alternative solution to be developed and employed, to reduce the number of finite elements and shorten the computational modelling time. More details in terms of DED process modelling can be found in [23, 117].

8.5 Summary

In this study, computational thermo-mechanical modelling of DED process for aluminium alloy was developed by using the bead-by-bead modelling approach. The influence of bead increment length on RS was computationally predicted. The thermal and mechanical behaviours at different positions of part were computationally investigated. The key summaries for DED work are as follows:

a) The DED process modelling capability for Al-4(wt %)Si alloy is developed for temperature and stress by using the computational bead-by-bead modelling method.

b) The temperature increases along the build direction, while temperature gradient and cooling rate decrease with the deposition height.
c) Residual stress of part decreases with more layers of material deposited during the DED manufacturing process and gradually increases at the post - printing process before stabilisation.
d) At the same height of part, the temperature at around the side surface of part is lower than at the central area of part, while temperature gradient, cooling rate and RS are higher.
e) RS along the scanning direction (σ_{xx}) is similar with the maximum principal stress, and is always larger than RS in the build direction (σ_{zz}) during the DED manufacturing process.

9 Conclusions and future work

9.1 Summary

This thesis aimed to improve the ability and efficiency of computationally predictions of RS in additively manufactured macroscale components, in order to help mitigate RS formation and provide insights into optimum process configuration in metal AM. The overall thermo-mechanical AM process modelling fundamental features and capabilities for macroscale metal component were developed by using the concept of 'layer scaling' technique. The indirect quantitative comparison indicated consistent trend between predicted temperature in FE model and experimental microstructure characterisation of a cylinder specimen in PBF-EB, based on assumptions. RS of parts with varying scanning strategies and part heights in PBF-LB was compared to non-destructive high energy X-ray diffraction measurements of RS . The computational finite element model for temperature and RS was further extended to PBF-MLB, multi-part PBF-LB and DED printing processes. The majority of the objectives described in **Chapter 1** were accomplished. The summaries of the main content of this thesis are as following:

In **Chapter 3**, a thermo-mechanical process finite element modelling tool was presented and applied to predict temperature and RS of PBF-LB manufactured Ti-6Al-4V macroscale component. The objective of creating a rapid automated FEM capability was achieved by developing a Python script and 'layer scaling' approach. A computationally efficient concept and model which approximates part-powder conduction as part-interface convection was presented. Process parameters such as heating step time and cooling step time effects on the final temperature and RS were characterised by using the 'layer scaling' technique. The feasible solution to simulate temperature and RS of a higher resolution (i.e. thinner layer height) by using a lower resolution (i.e. thicker layer height) was presented and the corresponding process parameters needed to be adjusted were recommended.

To expand application of PBF-LB to other AM processes, PBF-EB process thermo-mechanical modelling was performed in **Chapter 7** for a novel biomedical Ti2448 material. The predicted temperature history of sampling points along both the radial and

build directions of a Ti2448 cylinder was indirectly compared to microstructure (e.g. grain size) characterisation of material, which was performed by collaborators at IMR-China. Residual stress of PBF-EB manufactured Ti2448 material was computationally investigated. In addition, RS of part manufactured by PBF-LB and PBF-EB was computationally compared and RS mitigation approaches in PBF were recommended.

In order to validate the predicted RS and finite element prediction model, non-destructive high energy X-ray diffraction experiments were performed at Diamond Light Source on PBF-LB manufactured Ti-6Al-4V components in **Chapter 4**. Effects of scanning strategy and sample height on RS were experimentally assessed in the single laser beam PBF-LB manufacturing. The coupled thermo-mechanical hatch-by-hatch modelling method was employed for predicting influences of scanning strategies on stress for macroscale component. The results indicate a fit between the computational modelling RS results and experimental measurements (e.g. predicted σ_{yy} RS was 35.05 % lower than the experimentally measured for the 0° no rotation scanning strategy), but highlighted difficulties with non-destructive stress measurement techniques and the concept of through-thickness averaged directional stresses. This work completed the objective of experimental comparison of the computational finite element prediction model.

To improve the production rate of AM, coupled thermo-mechanical PBF-MLB process modelling capability was developed in **Chapter 5** by programming a FORTRAN subroutine for simulating simultaneous movement of multiple laser beams. Twelve different scanning strategies effect on RS and *z* direction deflection was quantified assessed in dual laser beams PBF-MLB. The guideline for optimizing the scanning strategies on dual laser beams PBF-MLB was presented. Different numbers of laser beams PBF-MLB effects on temperature, RS and deformation were overall compared. This work completed the objective of exploring approaches to improve the build rate and optimize fabrication quality of PBF-MLB manufactured parts.

In **Chapter 6**, multi-part process modelling was performed by adapting the finite element model and Python script developed in **Chapter 3** for 2D single part to multiple 3D parts build in PBF-LB. The converged solution of ‘layer scaling’ technique described in **Chapter 3** was applied for the multi-part thermo-mechanical process modelling in

Chapter 6. The number of parts per build and arrangement of parts in multi-part build (e.g. part spacing) effect on RS were investigated. The optimum setting up for multi-part PBF-LB build was recommended. For another application, process DED thermo-mechanical modelling for a thin wall structure of Al-4(wt %)Si aluminium alloy was developed and performed in **Chapter 8**. Temperature, temperature gradient, cooling rate and RS state evolutions at different positions of the part were computationally investigated.

The computational finite element model, experimental RS measurements and findings in this work could provide insights into the optimum printing setup for mitigating RS in metal AM.

9.2 Conclusions

The main findings for each chapter of the main content of this work (**Chapter 3** to **Chapter 8**) are summarised as following:

9.2.1 Macroscale PBF modelling framework

1) The part-scale component process PBF-LB finite element modelling capability was built in a layer-by-layer manner by developing a custom written Python script for use with the general-purpose finite element software ABAQUS.
2) A novel efficient method for simulating solid-powder heat conduction by powder-interface convection from the solid part to surrounding atmosphere was presented and applied in PBF-LB for Ti-6Al-4V.
3) Key parameter interdependencies of resolution, energy and time were investigated in a series of 'layer scaling' thermo-mechanical process models.
4) The final temperature and RS were found to be strongly dependent on 'layer scaling' (i.e. layer height in the simulation domain) and 'time scaling' (i.e. cooling step time after each layer).
5) Temperature and RS of PBF-LB manufactured part-scale component could be predicted with reasonable balance of accuracy and computational efficiency by using 'layer scaling' technique, but up to a limit of 4 times layer scaling. To computationally simulate the temperature and RS results of a thinner layer height

by using a thicker layer height, the cooling step time after each layer should be scaled up based on the ratio of the computational layer height to the practical layer thickness.

9.2.2 Computational residual stress and experimental validation

1) The influences of scanning strategy and sample height on stress were measured by the non-destructive high energy X-ray diffraction experiments on a series of Ti-6Al-4V square plates that were manufactured by the single laser beam PBF-LB.
2) The computational results of the directional stresses (σ_{xx} and σ_{yy}) were compared to the experimental RS measurements for PBF-LB manufactured Ti-6Al-4V part.
3) Experimental RS measurements show the 90° layer rotation is beneficial for mitigating RS in PBF-LB that 90° rotation scanning strategy produced a marginal 46.36 % lower σ_{yy} stress than the no rotation scanning strategy.
4) Both the computational modelling and experimental measurement reveal the inclined scanning strategy could balance and thus reduce the directional stresses than the no inclined scanning strategy.
5) The 45° rotation scanning strategy obtained the least directional stress in PBF-LB manufactured part, while the island scanning and 0° rotation scanning strategy produced higher residual stress than other scanning strategies.
6) The computational model indicates RS of part reduced significantly after releasing constraints of the base plate in PBF-LB manufacturing.

9.2.3 Multi-laser beam PBF build process modelling

1) The influence of the number of laser beams (1, 2, 4 and 30) on temperature, RS, and deflection of Ti-6Al-4V PBF-MLB was characterised. Higher numbers of laser beams lead to a higher peak temperature while a lower RS and deflection of part. The laser exposure time for the four-laser beam PBF-MLB manufacturing was 25 % of the single beam PBF-LB while RS in PBF-MLB can be mitigated by 9.39 % comparing with that of the single laser beam PBF-LB.
2) The overall influence of scanning strategy on temperature, RS, and deflection for dual laser beams PBF-MLB was computationally investigated for the first time.

Varying the scanning strategies was predicted to lead to a up to 4.21 % and 26.98 % variation in peak temperature and RS in dual laser beams PBF-MLB, respectively.

3) The 90° layer rotation is predicted to be beneficial for mitigating RS in dual laser beams PBF-MLB manufacturing. The 'following but time delayed' laser scanning strategy is predicted to lead to the lowest RS of the final geometry simulated.
4) The maximum RS occurred at the interface of the part with the build plate in PBF-MLB manufacturing. This computational finding confirms the similar trend found in single laser beam PBF-LB.
5) The model developed in this thesis could be used as a guideline for both PBF-MLB modelling designers and machine operators.

9.2.4 Multi-part build process modelling

1) Printing batch size effect on temperature and RS was computationally investigated by the developed multi-part build PBF-LB model. The more parts printing in a single build, the higher temperatures of both the build plate and the part, while the lower of RS resulted. Part manufactured by four-part PBF-LB manufacturing had a 6.01 % reduction in maximum RS comparing with that of the single part PBF-LB manufacturing.
2) Part printing order in the same build plate had a minimum effect on temperature and RS. Parts located at the central areas of the build plate had lower residual stresses than parts that located at the edges of the build plate.
3) Part spacing effects on RS was computationally investigated on the two-part PBF-LB manufacturing. The larger of part spacing employed, the lower of RS resulted before stabilisation.

9.2.5 PBF-EB modelling and microstructure validation

1) The predicted temperature histories along both the vertical and radial directions of Ti2448 cylinder were indirectly compared to the microstructure experiments in PBF-EB. The peak temperature increased along the building direction while decreased from the centre line to the side surface of sample.

2) The computational PBF-EB process model was used to infer same trends that were compared to microscopy characterisations of grain sizes. These findings provide a theoretical guidance for the control of microstructure and properties of the solid Ti2448 parts produced by PBF-EB.
3) Modelling results, based on common PBF-EB and PBF-LB process parameters, predicted a 42.85 % lower RS in PBF-EB compared to PBF-LB, highly influenced by the preheating temperature of the powder bed [333]. Strategies to mitigate RS in PBF-LB were presented and preheating base plate is the most effective way to reduce RS.

9.2.6 DED modelling

1) The higher the number of layers of material deposited in DED, the higher the temperature of the thin trapezoidal plate part, while resulting in a lower temperature gradient, cooling rate and RS.
2) The temperature on the side surface of the part was lower than that at the central area, but the temperature gradient, cooling rate and RS on the side surface was higher than that at the central area.
3) During the DED manufacturing process, the RS along travelling direction (σ_{xx}) is close to the maximum principal stress and is always higher than RS along building direction (σ_{zz}). RS gradually decreased during manufacturing process and then increased during post manufacturing process before stabilisation.

9.3 Recommendations for future work

Further work will be focused on developing further computational tools and capabilities for AM process modelling and experimental RS validation on parts manufactured by multi-laser beam and multi-part AM. Computational model such as microstructure evolution prediction model and microstructure observation in multi-part PBF-LB should also be investigated and examined [5, 246, 353, 354]. The main recommendations for future work are summarised as following:

9.3.1 Computational tools for process AM modelling

1) This thesis applied a static mesh for AM process modelling and developed a Python script for 'layer scaling' method to computational efficiency model the macroscale part. However, to further save the computational modelling costs, the dynamic remesh strategy and corresponding algorithm and code to simulate the physical PBF manufacturing process are recommended to be developed in future. In addition, future investigations might be focused on exploring approaches to speed up AM modelling by ways such as machine learning [355].
2) Finite element software companies released their own modules such as AM Modeler in ABAQUS [131], after the start of this PhD project, which provides an opportunity to combine the process modelling tool developed in this thesis with the released modelling plugin AM Modeler or program on the basis of AM Modeler plugin. By combing the computational tool developed in this work with AM Modeler, the process AM modelling has a potential to be further accelerated for macroscale model in PBF-MLB.

9.3.2 AM process modelling

1) In this work, the temperature history was indirectly compared with the microstructure characterisation of Ti2448 material in PBF-EB. However, future work needs to predict microstructure evolution (e.g. grain growth and phase), such as developing an integrated through-process thermal history based microstructural evolution model, similar to recent computational PBF-LB [5, 246] and weld [353, 354] manufacturing.
2) This work investigated scanning strategies effect on RS by the dual laser beams PBF-MLB. Multiple laser beams PBF-MLB system has been developed and released recently, including such as four-laser beams and twelve-laser beams [217, 219]. Scanning strategies effects on RS and deflection by multiple (four and twelve) laser beams PBF-MLB manufacturing need to be investigated by computational modelling approach.
3) This work investigated multi-part build by using the single laser beam PBF-LB and a single part print by PBF-MLB. Future work would consider investigating

multi-part build by multi-laser beam in metal AM. For instance, it is recommended to investigate whether multiple laser beams should work on a macroscale component together or independently on separate component in multi-part and PBF-MLB manufacturing.

4) Development of PBF process modelling capability includes support structure and optimisation of build support structure to mitigate stress of part. During the practical AM, part (especially lattice or porous structure) is supported to prevent warping and distortion of parts and aid dissipation heat from parts. This work aims to contribute to better build configuration and process parameters and fewer support is needed; thus, support is not considered. By following the results of this work, the support structure and specific finite element for support can now be examined, i.e. better design of build support for heat transfer for RS mitigation in PBF-LB process modelling. The support structure should be optimised to mitigate RS and one of the feasible solution is to design graded lattice structures for support [356].

9.3.3 Experimental measurements

1) To complete the RS experimental measurements, which were initiated prior to the Covid-19 lockdown in 2020 but were halted due to travel and facility access limitations. These RS measurements include stress-free lattice spacing measurement on small Ti-6Al-4V cubes (e.g. $3 \times 3 \times 3$ mm^3) for RS calculation in **Chapter 4** and experimental RS measurement on PBF-LB manufactured Ti-6Al-4V components with different batch sizes of samples for **Chapter 6**. In addition, future work would consider experimentally measure RS contours at macroscale component by non-destructive technique such as neutron diffraction at world class facilities such as Diamond and ISIS.
2) This work computationally investigated RS in PBF-MLB. Experimental measurements of RS and deflection in PBF-MLB might be considered in future work to validate the predicted RS and deflection of part. The experimentally measured RS and deformation of PBF-MLB manufactured parts could also be compared with that of the single laser beam PBF-LB manufacturing.

3) Investigation of post build treatment effects on Ti6Al4V RS in PBF-LB. In order to reduce RS and internal defects of PBF manufactured parts, parts are normally post treated after completing the printing process. Thus, future work might computationally investigate post treatment effects on RS mitigation of PBF-LB manufactured part.

The current metal AM in industry is towards faster production rates and better mechanical properties of the manufactured component. There is a great demand on the next generation of the AM modelling capability to simulate components on an overall industrial scale and to fit with the latest developed commercial AM system, such as twelve-laser beams PBF-MLB. Through exploring computational efficiency tools and capabilities for macroscale component, the knowledge obtained could provide insights into better setting up for AM and manufacturing metal components with desirable performances.

References

1. ISO, *DIN EN ISO/ASTM 52900 Additive Manufacturing—General Principles—Terminology*. 2018.
2. Sun, L., G. Hua, T.C.E. Cheng, and Y. Wang, *How to price 3D-printed products? Pricing strategy for 3D printing platforms.* International Journal of Production Economics, 2020: p. 107600.
3. Bartlett, J.L. and X. Li, *An overview of residual stresses in metal powder bed fusion.* Additive Manufacturing, 2019. **27**: p. 131-149.
4. Krishnakumar, A., K. Suresh, and A. Chandrasekar, *Towards Assembly-Free Methods for Additive Manufacturing Simulation*. 2015.
5. Yang, X., R.A. Barrett, M. Tong, N.M. Harrison, and S.B. Leen, *Towards a process-structure model for Ti-6Al-4V during additive manufacturing.* Journal of Manufacturing Processes, 2021. **61**: p. 428-439.
6. Druzgalski, C.L., A. Ashby, G. Guss, W.E. King, T.T. Roehling, and M.J. Matthews, *Process optimization of complex geometries using feed forward control for laser powder bed fusion additive manufacturing.* Additive Manufacturing, 2020. **34**: p. 101169.
7. Harun, W.S.W., M.S.I.N. Kamariah, N. Muhamad, S.A.C. Ghani, F. Ahmad, and Z. Mohamed, *A review of powder additive manufacturing processes for metallic biomaterials.* Powder Technology, 2018. **327**: p. 128-151.
8. Deckard Carl, R., *Method And Apparatus For Producing Parts By Selective Sintering*. 1989, The University of Texas System: US.
9. Seifi, M., A. Salem, J. Beuth, O. Harrysson, and J.J. Lewandowski, *Overview of Materials Qualification Needs for Metal Additive Manufacturing.* JOM, 2016. **68**(3): p. 747-764.
10. King, W.E., A.T. Anderson, R.M. Ferencz, N.E. Hodge, C. Kamath, S.A. Khairallah, and A.M. Rubenchik, *Laser powder bed fusion additive manufacturing of metals; physics, computational, and materials challenges.* Applied Physics Reviews, 2015. **2**(4): p. 041304.
11. Chatham, C.A., T.E. Long, and C.B. Williams, *A review of the process physics and material screening methods for polymer powder bed fusion additive manufacturing.* Progress in Polymer Science, 2019. **93**: p. 68-95.
12. Grossin, D., A. Montón, P. Navarrete-Segado, E. Özmen, G. Urruth, F. Maury, D. Maury, C. Frances, M. Tourbin, P. Lenormand, and G. Bertrand, *A review of additive manufacturing of ceramics by powder bed selective laser processing (sintering / melting): Calcium phosphate, silicon carbide, zirconia, alumina, and their composites.* Open Ceramics, 2021. **5**: p. 100073.
13. Calignano, F., M. Galati, and L. Iuliano, *A Metal Powder Bed Fusion Process in Industry: Qualification Considerations.* Machines, 2019. **7**(4).
14. K G, P., S. Kolla, and J. Eckert, *Additive Manufacturing Processes: Selective Laser Melting, Electron Beam Melting and Binder Jetting—Selection Guidelines.* Materials, 2017. **10**.
15. Zhang, B., P. Wang, Y. Chew, Y. Wen, M. Zhang, P. Wang, G. Bi, and J. Wei, *Mechanical properties and microstructure evolution of selective laser melting*

Inconel 718 along building direction and sectional dimension. Materials Science and Engineering: A, 2020. **794**: p. 139941.
16. Maconachie, T., M. Leary, B. Lozanovski, X. Zhang, M. Qian, O. Faruque, and M. Brandt, *SLM lattice structures: Properties, performance, applications and challenges.* Materials & Design, 2019. **183**: p. 108137.
17. Dev Singh, D., T. Mahender, and A. Raji Reddy, *Powder bed fusion process: A brief review.* Materials Today: Proceedings, 2020.
18. Frazier, W.E., *Metal Additive Manufacturing: A Review.* Journal of Materials Engineering and Performance, 2014. **23**(6): p. 1917-1928.
19. Yan, W., W. Ge, J. Smith, S. Lin, O.L. Kafka, F. Lin, and W.K. Liu, *Multi-scale modeling of electron beam melting of functionally graded materials.* Acta Materialia, 2016. **115**: p. 403-412.
20. Shen, N. and K. Chou, *Thermal Modeling of Electron Beam Additive Manufacturing Process: Powder Sintering Effects*. 2012. p. 287.
21. Caprio, L., A.G. Demir, G. Chiari, and B. Previtali, *Defect-free laser powder bed fusion of Ti–48Al–2Cr–2Nb with a high temperature inductive preheating system.* Journal of Physics: Photonics, 2020. **2**(2): p. 024001.
22. Fousová, M., D. Vojtěch, K. Doubrava, M. Daniel, and C.F. Lin, *Influence of Inherent Surface and Internal Defects on Mechanical Properties of Additively Manufactured Ti6Al4V Alloy: Comparison between Selective Laser Melting and Electron Beam Melting.* Materials (Basel), 2018. **11**(4).
23. DebRoy, T., H.L. Wei, J.S. Zuback, T. Mukherjee, J.W. Elmer, J.O. Milewski, A.M. Beese, A. Wilson-Heid, A. De, and W. Zhang, *Additive manufacturing of metallic components – Process, structure and properties.* Progress in Materials Science, 2018. **92**: p. 112-224.
24. Thompson, S.M., L. Bian, N. Shamsaei, and A. Yadollahi, *An overview of Direct Laser Deposition for additive manufacturing; Part I: Transport phenomena, modeling and diagnostics.* Additive Manufacturing, 2015. **8**: p. 36-62.
25. Pirch, N., S. Linnenbrink, A. Gasser, and H. Schleifenbaum, *Laser-aided directed energy deposition of metal powder along edges.* International Journal of Heat and Mass Transfer, 2019. **143**: p. 118464.
26. Lu, X., X. Lin, M. Chiumenti, M. Cervera, Y. Hu, X. Ji, L. Ma, H. Yang, and W. Huang, *Residual stress and distortion of rectangular and S-shaped Ti-6Al-4V parts by Directed Energy Deposition: Modelling and experimental calibration.* Additive Manufacturing, 2019. **26**: p. 166-179.
27. Lu, X., X. Lin, M. Chiumenti, M. Cervera, J. Li, L. Ma, L. Wei, Y. Hu, and W. Huang, *Finite element analysis and experimental validation of the thermomechanical behavior in laser solid forming of Ti-6Al-4V.* Additive Manufacturing, 2018. **21**: p. 30-40.
28. Saboori, A., A. Aversa, G. Marchese, S. Biamino, M. Lombardi, and P. Fino, *Application of Directed Energy Deposition-Based Additive Manufacturing in Repair.* Applied Sciences, 2019. **9**: p. 3316.
29. Vyatskikh, A., S. Delalande, A. Kudo, X. Zhang, C.M. Portela, and J.R. Greer, *Additive manufacturing of 3D nano-architected metals.* Nature Communications, 2018. **9**(1): p. 593.
30. Arısoy, Y.M., L.E. Criales, T. Özel, B. Lane, S. Moylan, and A. Donmez, *Influence of scan strategy and process parameters on microstructure and its*

optimization in additively manufactured nickel alloy 625 via laser powder bed fusion. The International Journal of Advanced Manufacturing Technology, 2017. **90**(5): p. 1393-1417.
31. Gao, W., Y. Zhang, D. Ramanujan, K. Ramani, Y. Chen, C.B. Williams, C.C.L. Wang, Y.C. Shin, S. Zhang, and P.D. Zavattieri, *The status, challenges, and future of additive manufacturing in engineering.* Computer-Aided Design, 2015. **69**: p. 65-89.
32. Harrison, N., P.E. McHugh, W. Curtin, and P. Mc Donnell, *Micromotion and friction evaluation of a novel surface architecture for improved primary fixation of cementless orthopaedic implants.* Journal of the Mechanical Behavior of Biomedical Materials, 2013. **21**: p. 37-46.
33. Harrison, N., J.R. Field, F. Quondamatteo, W. Curtin, P.E. McHugh, and P. Mc Donnell, *Preclinical trial of a novel surface architecture for improved primary fixation of cementless orthopaedic implants.* Clinical Biomechanics, 2014. **29**(8): p. 861-868.
34. Associates, W. *Wohlers Report*. 2019.
35. Poyraz, Ö. and M.C. Kuşhan, *Residual Stress-induced Distortions in Laser Powder Bed Additive Manufacturing of Nickel-based Superalloys.* Journal of Mechanical Engineering, 2019. **65**(6): p. 8.
36. Williams, R.J., C.M. Davies, and P.A. Hooper, *A pragmatic part scale model for residual stress and distortion prediction in powder bed fusion.* Additive Manufacturing, 2018. **22**: p. 416-425.
37. Liu, S. and Y.C. Shin, *Additive manufacturing of Ti6Al4V alloy: A review.* Materials & Design, 2019. **164**: p. 107552.
38. Li, C., C.H. Fu, Y.B. Guo, and F.Z. Fang, *A multiscale modeling approach for fast prediction of part distortion in selective laser melting.* Journal of Materials Processing Technology, 2016. **229**(Supplement C): p. 703-712.
39. Cao, J., M.A. Gharghouri, and P. Nash, *Finite-element analysis and experimental validation of thermal residual stress and distortion in electron beam additive manufactured Ti-6Al-4V build plates.* Journal of Materials Processing Technology, 2016. **237**: p. 409-419.
40. Heeling, T. and K. Wegener, *Computational Investigation of Synchronized Multibeam Strategies for the Selective Laser Melting Process.* Physics Procedia, 2016. **83**: p. 899-908.
41. Cheng, B., S. Shrestha, and K. Chou, *Stress and deformation evaluations of scanning strategy effect in selective laser melting.* Additive Manufacturing, 2016. **12**: p. 240-251.
42. Levkulich, N.C., S.L. Semiatin, J.E. Gockel, J.R. Middendorf, A.T. DeWald, and N.W. Klingbeil, *The effect of process parameters on residual stress evolution and distortion in the laser powder bed fusion of Ti-6Al-4V.* Additive Manufacturing, 2019. **28**: p. 475-484.
43. Pal, D., N. Patil, K. Zeng, C. Teng, and B. Stucker, *An Efficient Multi-Scale Simulation Architecture for the Prediction of Performance Metrics of Parts Fabricated Using Additive Manufacturing*. Vol. 46. 2015.
44. Yılmaz, N. and M.Y. Kayacan, *Effect of single and multiple parts manufacturing on temperature-induced residual stress problems in SLM.* International Journal of Material Forming, 2020.

45. Li, C., Y. Guo, X. Fang, and F. Fang, *A scalable predictive model and validation for residual stress and distortion in selective laser melting.* CIRP Annals, 2018. **67**(1): p. 249-252.
46. Withers, P.J. and H.K.D.H. Bhadeshia, *Residual stress. Part 2 – Nature and origins.* Materials Science and Technology, 2001. **17**(4): p. 366-375.
47. Zaza, D., M. Ciavarella, and G. Zurlo, *Strain incompatibility as a source of residual stress in welding and additive manufacturing.* European Journal of Mechanics - A/Solids, 2021. **85**: p. 104147.
48. Zafar, M.Q., C.C. Wu, H. Zhao, J. Wang, and X. Hu, *Finite element framework for electron beam melting process simulation.* The International Journal of Advanced Manufacturing Technology, 2020. **109**(7): p. 2095-2112.
49. Roehling, J.D., W.L. Smith, T.T. Roehling, B. Vrancken, G.M. Guss, J.T. McKeown, M.R. Hill, and M.J. Matthews, *Reducing residual stress by selective large-area diode surface heating during laser powder bed fusion additive manufacturing.* Additive Manufacturing, 2019. **28**: p. 228-235.
50. Masoomi, M., S.M. Thompson, and N. Shamsaei, *Laser powder bed fusion of Ti-6Al-4V parts: Thermal modeling and mechanical implications.* International Journal of Machine Tools and Manufacture, 2017. **118**: p. 73-90.
51. Li, C., J.F. Liu, X.Y. Fang, and Y.B. Guo, *Efficient predictive model of part distortion and residual stress in selective laser melting.* Additive Manufacturing, 2017. **17**: p. 157-168.
52. Ahmad, B., S.O. van der Veen, M.E. Fitzpatrick, and H. Guo, *Residual stress evaluation in selective-laser-melting additively manufactured titanium (Ti-6Al-4V) and inconel 718 using the contour method and numerical simulation.* Additive Manufacturing, 2018. **22**: p. 571-582.
53. Kruth, J.P., L. Froyen, J. Van Vaerenbergh, P. Mercelis, M. Rombouts, and B. Lauwers, *Selective laser melting of iron-based powder.* Journal of Materials Processing Technology, 2004. **149**(1): p. 616-622.
54. Yasa, E., J.P. Kruth, and J. Deckers, *Manufacturing by combining Selective Laser Melting and Selective Laser Erosion/laser re-melting.* CIRP Annals, 2011. **60**(1): p. 263-266.
55. Bobbio, L.D., S. Qin, A. Dunbar, P. Michaleris, and A.M. Beese, *Characterization of the strength of support structures used in powder bed fusion additive manufacturing of Ti-6Al-4V.* Additive Manufacturing, 2017. **14**: p. 60-68.
56. Calignano, F., *Design optimization of supports for overhanging structures in aluminum and titanium alloys by selective laser melting.* Materials & Design, 2014. **64**: p. 203-213.
57. Tripathi, V., A. Armstrong, X. Gong, G. Manogharan, T. Simpson, and E. De Meter, *Milling of Inconel 718 block supports fabricated using laser powder bed fusion.* Journal of Manufacturing Processes, 2018. **34**: p. 740-749.
58. Singla, A.K., M. Banerjee, A. Sharma, J. Singh, A. Bansal, M.K. Gupta, N. Khanna, A.S. Shahi, and D.K. Goyal, *Selective laser melting of Ti6Al4V alloy: Process parameters, defects and post-treatments.* Journal of Manufacturing Processes, 2021. **64**: p. 161-187.
59. Syed, A.K., B. Ahmad, H. Guo, T. Machry, D. Eatock, J. Meyer, M.E. Fitzpatrick, and X. Zhang, *An experimental study of residual stress and direction-dependence*

of fatigue crack growth behaviour in as-built and stress-relieved selective-laser-melted Ti6Al4V. Materials Science and Engineering: A, 2019. **755**: p. 246-257.
60. Yan, X., S. Yin, C. Chen, C. Huang, R. Bolot, R. Lupoi, M. Kuang, W. Ma, C. Coddet, H. Liao, and M. Liu, *Effect of heat treatment on the phase transformation and mechanical properties of Ti6Al4V fabricated by selective laser melting.* Journal of Alloys and Compounds, 2018. **764**: p. 1056-1071.
61. Tsai, M.-T., Y.-W. Chen, C.-Y. Chao, J.S.C. Jang, C.-C. Tsai, Y.-L. Su, and C.-N. Kuo, *Heat-treatment effects on mechanical properties and microstructure evolution of Ti-6Al-4V alloy fabricated by laser powder bed fusion.* Journal of Alloys and Compounds, 2020. **816**: p. 152615.
62. Qiu, C., N.J.E. Adkins, and M.M. Attallah, *Microstructure and tensile properties of selectively laser-melted and of HIPed laser-melted Ti–6Al–4V.* Materials Science and Engineering: A, 2013. **578**: p. 230-239.
63. Du Plessis, A., B. Yelamanchi, C. Fischer, J. Miller, C. Beamer, K. Rogers, P. Cortes, J. Els, and E. MacDonald, *Productivity enhancement of laser powder bed fusion using compensated shelled geometries and hot isostatic pressing.* Advances in Industrial and Manufacturing Engineering, 2021: p. 100031.
64. Acevedo, R., P. Sedlak, R. Kolman, and M. Fredel, *Residual stress analysis of additive manufacturing of metallic parts using ultrasonic waves: State of the art review.* Journal of Materials Research and Technology, 2020. **9**(4): p. 9457-9477.
65. Eskandari Sabzi, H., *Powder bed fusion additive layer manufacturing of titanium alloys.* Materials Science and Technology, 2019. **35**(8): p. 875-890.
66. Fang, Z.Z., J.D. Paramore, P. Sun, K.S.R. Chandran, Y. Zhang, Y. Xia, F. Cao, M. Koopman, and M. Free, *Powder metallurgy of titanium – past, present, and future.* International Materials Reviews, 2018. **63**(7): p. 407-459.
67. Brika, S.E., M. Letenneur, C.A. Dion, and V. Brailovski, *Influence of particle morphology and size distribution on the powder flowability and laser powder bed fusion manufacturability of Ti-6Al-4V alloy.* Additive Manufacturing, 2020. **31**: p. 100929.
68. Tian, Y., W.S. Gora, A.P. Cabo, L.L. Parimi, D.P. Hand, S. Tammas-Williams, and P.B. Prangnell, *Material interactions in laser polishing powder bed additive manufactured Ti6Al4V components.* Additive Manufacturing, 2018. **20**: p. 11-22.
69. Vastola, G., G. Zhang, Q.X. Pei, and Y.-W. Zhang, *Active Control of Microstructure in Powder-Bed Fusion Additive Manufacturing of Ti6Al4V.* Advanced Engineering Materials, 2017: p. 1700333.
70. Antonysamy, A.A., J. Meyer, and P.B. Prangnell, *Effect of build geometry on the β-grain structure and texture in additive manufacture of Ti6Al4V by selective electron beam melting.* Materials Characterization, 2013. **84**(Supplement C): p. 153-168.
71. Ali, H., H. Ghadbeigi, and K. Mumtaz, *Effect of scanning strategies on residual stress and mechanical properties of Selective Laser Melted Ti6Al4V.* Materials Science and Engineering: A, 2018. **712**: p. 175-187.
72. Fu, C.H. and Y.B. Guo, *3-Dimensional Finite Element Modeling of Selective Laser Melting TI6Al4V Alloy*. 2014.
73. Gu, H., H. Gong, J.J.S. Dilip, D. Pal, A. Hicks, H. Doak, and B. Stucker, *Effects of Powder Variation on the Microstructure and Tensile Strength of Ti6Al4V Parts Fabricated by Selective Laser Melting.* 2014.

74. Acquesta, A. and T. Monetta, *As-Built EBM and DMLS Ti-6Al-4V Parts: Topography–Corrosion Resistance Relationship in a Simulated Body Fluid.* Metals, 2020. **10**: p. 1015.
75. Wang, X., X. Gong, and K. Chou, *Scanning Speed Effect on Mechanical Properties of Ti-6Al-4V Alloy Processed by Electron Beam Additive Manufacturing.* Procedia Manufacturing, 2015. **1**(Supplement C): p. 287-295.
76. Bartolomeu, F., S. Faria, O. Carvalho, E. Pinto, N. Alves, F.S. Silva, and G. Miranda, *Predictive models for physical and mechanical properties of Ti6Al4V produced by Selective Laser Melting.* Materials Science and Engineering: A, 2016. **663**: p. 181-192.
77. Valoppi, B., S. Bruschi, and A. Ghiotti, *Modelling of Fracture Onset in Ti6Al4V Sheets Deformed at Elevated Temperature.* Procedia Manufacturing, 2016. **5**: p. 248-258.
78. Shipley, H., D. McDonnell, M. Culleton, R. Coull, R. Lupoi, G. O'Donnell, and D. Trimble, *Optimisation of process parameters to address fundamental challenges during selective laser melting of Ti-6Al-4V: A review.* International Journal of Machine Tools and Manufacture, 2018. **128**: p. 1-20.
79. Vock, S., B. Klöden, A. Kirchner, T. Weißgärber, and B. Kieback, *Powders for powder bed fusion: a review.* Progress in Additive Manufacturing, 2019. **4**(4): p. 383-397.
80. Sun, Y., M. Aindow, and R.J. Hebert, *Comparison of virgin Ti-6Al-4V powders for additive manufacturing.* Additive Manufacturing, 2018. **21**: p. 544-555.
81. Liu, Y.J., H.L. Wang, S.J. Li, S.G. Wang, W.J. Wang, W.T. Hou, Y.L. Hao, R. Yang, and L.C. Zhang, *Compressive and fatigue behavior of beta-type titanium porous structures fabricated by electron beam melting.* Acta Materialia, 2017. **126**: p. 58-66.
82. Liu, Y.J., S.J. Li, H.L. Wang, W.T. Hou, Y.L. Hao, R. Yang, T.B. Sercombe, and L.C. Zhang, *Microstructure, defects and mechanical behavior of beta-type titanium porous structures manufactured by electron beam melting and selective laser melting.* Acta Materialia, 2016. **113**: p. 56-67.
83. Heeling, T. and K. Wegener, *The effect of multi-beam strategies on selective laser melting of stainless steel 316L.* Additive Manufacturing, 2018. **22**: p. 334-342.
84. Mohr, G., S.J. Altenburg, and K. Hilgenberg, *Effects of inter layer time and build height on resulting properties of 316L stainless steel processed by laser powder bed fusion.* Additive Manufacturing, 2020. **32**: p. 101080.
85. Ahmadi, A., R. Mirzaeifar, N.S. Moghaddam, A.S. Turabi, H.E. Karaca, and M. Elahinia, *Effect of manufacturing parameters on mechanical properties of 316L stainless steel parts fabricated by selective laser melting: A computational framework.* Materials & Design, 2016. **112**: p. 328-338.
86. Ronneberg, T., C.M. Davies, and P.A. Hooper, *Revealing relationships between porosity, microstructure and mechanical properties of laser powder bed fusion 316L stainless steel through heat treatment.* Materials & Design, 2020. **189**: p. 108481.
87. Wu, A.S., D.W. Brown, M. Kumar, G.F. Gallegos, and W.E. King, *An Experimental Investigation into Additive Manufacturing-Induced Residual Stresses in 316L Stainless Steel.* Metallurgical and Materials Transactions A, 2014. **45**(13): p. 6260-6270.

88. Williams, R.J., F. Vecchiato, J. Kelleher, M.R. Wenman, P.A. Hooper, and C.M. Davies, *Effects of heat treatment on residual stresses in the laser powder bed fusion of 316L stainless steel: Finite element predictions and neutron diffraction measurements.* Journal of Manufacturing Processes, 2020. **57**: p. 641-653.
89. Zhang, B., M. Xiu, Y.T. Tan, J. Wei, and P. Wang, *Pitting corrosion of SLM Inconel 718 sample under surface and heat treatments.* Applied Surface Science, 2019. **490**: p. 556-567.
90. Kusoglu, I.M., B. Gökce, and S. Barcikowski, *Research trends in laser powder bed fusion of Al alloys within the last decade.* Additive Manufacturing, 2020. **36**: p. 101489.
91. Oliveira, J.P., A.D. LaLonde, and J. Ma, *Processing parameters in laser powder bed fusion metal additive manufacturing.* Materials & Design, 2020. **193**: p. 108762.
92. Han, C., Q. Fang, Y. Shi, S.B. Tor, C.K. Chua, and K. Zhou, *Recent Advances on High-Entropy Alloys for 3D Printing.* Advanced Materials, 2020. **32**(26): p. 1903855.
93. Gallmeyer, T.G., S. Moorthy, B.B. Kappes, M.J. Mills, B. Amin-Ahmadi, and A.P. Stebner, *Knowledge of process-structure-property relationships to engineer better heat treatments for laser powder bed fusion additive manufactured Inconel 718.* Additive Manufacturing, 2020. **31**: p. 100977.
94. *Additive Manufacturing: Siemens uses innovative technology to produce gas turbines*. 2018; Available from: https://press.siemens.com/global/en/feature/additive-manufacturing-siemens-uses-innovative-technology-produce-gas-turbines.
95. Lindgren, L.-E. and A. Lundbäck, *Approaches in computational welding mechanics applied to additive manufacturing: Review and outlook.* Comptes Rendus Mécanique, 2018. **346**(11): p. 1033-1042.
96. Fisk, M., J.C. Ion, and L.E. Lindgren, *Flow stress model for IN718 accounting for evolution of strengthening precipitates during thermal treatment.* Computational Materials Science, 2014. **82**: p. 531-539.
97. Barros, R., F.J.G. Silva, R.M. Gouveia, A. Saboori, G. Marchese, S. Biamino, A. Salmi, and E. Atzeni, *Laser Powder Bed Fusion of Inconel 718: Residual Stress Analysis Before and After Heat Treatment.* Metals, 2019. **9**(12).
98. Altıparmak, S.C., V.A. Yardley, Z. Shi, and J. Lin, *Challenges in additive manufacturing of high-strength aluminium alloys and current developments in hybrid additive manufacturing.* International Journal of Lightweight Materials and Manufacture, 2021. **4**(2): p. 246-261.
99. Svetlizky, D., B. Zheng, T. Buta, Y. Zhou, O. Golan, U. Breiman, R. Haj-Ali, J.M. Schoenung, E.J. Lavernia, and N. Eliaz, *Directed energy deposition of Al 5xxx alloy using Laser Engineered Net Shaping (LENS®).* Materials & Design, 2020. **192**: p. 108763.
100. Sélo, R.R.J., S. Catchpole-Smith, I. Maskery, I. Ashcroft, and C. Tuck, *On the thermal conductivity of AlSi10Mg and lattice structures made by laser powder bed fusion.* Additive Manufacturing, 2020. **34**: p. 101214.
101. *Copper for 3D Printing*. Available from: https://www.eos.info/en/additive-manufacturing/3d-printing-metal/dmls-metal-materials/copper.

102. Zhang, Y., *Multi-Scale Multi-Physics Modeling of Laser Powder Bed Fusion Process of Metallic Materials With Experiment Validation*. 2018, Purdue University: Ann Arbor. p. 158.
103. Sun, C., Y. Wang, M.D. McMurtrey, N.D. Jerred, F. Liou, and J. Li, *Additive manufacturing for energy: A review.* Applied Energy, 2021. **282**: p. 116041.
104. Schoinochoritis, B., D. Chantzis, and K. Salonitis, *Simulation of metallic powder bed additive manufacturing processes with the finite element method: A critical review.* Proceedings of the Institution of Mechanical Engineers, Part B: Journal of Engineering Manufacture, 2015. **231**(1): p. 96-117.
105. Lu, X., M. Chiumenti, M. Cervera, J. Li, X. Lin, L. Ma, G. Zhang, and E. Liang, *Substrate design to minimize residual stresses in Directed Energy Deposition AM processes.* Materials & Design, 2021. **202**: p. 109525.
106. Zhang, J., Y. Zhang, W.H. Lee, L. Wu, H.-H. Choi, and Y.-G. Jung, *A multi-scale multi-physics modeling framework of laser powder bed fusion additive manufacturing process.* Metal Powder Report, 2018. **73**(3): p. 151-157.
107. Haeri, S., Y. Wang, O. Ghita, and J. Sun, *Discrete element simulation and experimental study of powder spreading process in additive manufacturing.* Powder Technology, 2017. **306**: p. 45-54.
108. Fouda, Y.M. and A.E. Bayly, *A DEM study of powder spreading in additive layer manufacturing.* Granular Matter, 2019. **22**(1): p. 10.
109. Zhang, Y. and J. Zhang, *Modeling of solidification microstructure evolution in laser powder bed fusion fabricated 316L stainless steel using combined computational fluid dynamics and cellular automata.* Additive Manufacturing, 2019. **28**: p. 750-765.
110. Markl, M. and C. Körner, *Multiscale Modeling of Powder Bed–Based Additive Manufacturing.* Annual Review of Materials Research, 2016. **46**(1): p. 93-123.
111. Khairallah, S.A., A.T. Anderson, A. Rubenchik, and W.E. King, *Laser powder-bed fusion additive manufacturing: Physics of complex melt flow and formation mechanisms of pores, spatter, and denudation zones.* Acta Materialia, 2016. **108**: p. 36-45.
112. Lee, Y., Y. Bandari, P. Nandwana, B.T. Gibson, B. Richardson, and S. Simunovic, *Effect of Interlayer Cooling Time, Constraint and Tool Path Strategy on Deformation of Large Components Made by Laser Metal Deposition with Wire.* 2019.
113. Lindwall, J., V. Pacheco, M. Sahlberg, A. Lundbäck, and L.-E. Lindgren, *Thermal simulation and phase modeling of bulk metallic glass in the powder bed fusion process.* Additive Manufacturing, 2019. **27**: p. 345-352.
114. Galati, M. and L. Iuliano, *A literature review of powder-based electron beam melting focusing on numerical simulations.* Additive Manufacturing, 2018. **19**: p. 1-20.
115. Zhao, X., A. Iyer, P. Promoppatum, and S.-C. Yao, *Numerical modeling of the thermal behavior and residual stress in the direct metal laser sintering process of titanium alloy products.* Additive Manufacturing, 2017. **14**: p. 126-136.
116. Li, Y., K. Zhou, P. Tan, S.B. Tor, C.K. Chua, and K.F. Leong, *Modeling temperature and residual stress fields in selective laser melting.* International Journal of Mechanical Sciences, 2018. **136**: p. 24-35.

117. Wei, H.L., T. Mukherjee, W. Zhang, J.S. Zuback, G.L. Knapp, A. De, and T. DebRoy, *Mechanistic models for additive manufacturing of metallic components.* Progress in Materials Science, 2020: p. 100703.
118. Roberts, I.A., *Investigation of Residual Stresses in the Laser Melting of Metal Powders in Additive Layer Manufacturing*. 2012, University of Wolverhampton. p. 246.
119. Galati, M., L. Iuliano, A. Salmi, and E. Atzeni, *Modelling energy source and powder properties for the development of a thermal FE model of the EBM additive manufacturing process.* Additive Manufacturing, 2017. **14**: p. 49-59.
120. Dong, L., A. Makradi, S. Ahzi, and Y. Remond, *Three-dimensional transient finite element analysis of the selective laser sintering process.* Journal of Materials Processing Technology, 2009. **209**(2): p. 700-706.
121. Mukherjee, T., W. Zhang, and T. DebRoy, *An improved prediction of residual stresses and distortion in additive manufacturing.* Computational Materials Science, 2017. **126**: p. 360-372.
122. Tian, X., G. Peng, M. Yan, S. He, and R. Yao, *Process prediction of selective laser sintering based on heat transfer analysis for polyamide composite powders.* International Journal of Heat and Mass Transfer, 2018. **120**: p. 379-386.
123. Acharya, R., J.A. Sharon, and A. Staroselsky, *Prediction of microstructure in laser powder bed fusion process.* Acta Materialia, 2017. **124**: p. 360-371.
124. Bandyopadhyay, A. and K.D. Traxel, *Invited review article: Metal-additive manufacturing—Modeling strategies for application-optimized designs.* Additive Manufacturing, 2018. **22**: p. 758-774.
125. Chiumenti, M., E. Neiva, E. Salsi, M. Cervera, S. Badia, J. Moya, Z. Chen, C. Lee, and C. Davies, *Numerical modelling and experimental validation in Selective Laser Melting.* Additive Manufacturing, 2017. **18**: p. 171-185.
126. Malmelöv, A., A. Lundbäck, and L.-E. Lindgren, *History Reduction by Lumping for Time-Efficient Simulation of Additive Manufacturing.* Metals, 2020. **10**(1).
127. Lindgren, L.-E., A. Lundbäck, M. Fisk, R. Pederson, and J. Andersson, *Simulation of additive manufacturing using coupled constitutive and microstructure models.* Additive Manufacturing, 2016. **12**: p. 144-158.
128. Chiumenti, M., X. Lin, M. Cervera, L. Wei, Y. Zheng, and W. Huang, *Numerical simulation and experimental calibration of additive manufacturing by blown powder technology. Part I: Thermal analysis.* 2017. **23**: p. 448-463.
129. Bayat, M., C.G. Klingaa, S. Mohanty, D. De Baere, J. Thorborg, N.S. Tiedje, and J.H. Hattel, *Part-scale thermo-mechanical modelling of distortions in Laser Powder Bed Fusion – Analysis of the sequential flash heating method with experimental validation.* Additive Manufacturing, 2020. **36**: p. 101508.
130. Zhang, Q., J. Xie, Z. Gao, T. London, D. Griffiths, and V. Oancea, *A metallurgical phase transformation framework applied to SLM additive manufacturing processes.* Materials & Design, 2019. **166**: p. 107618.
131. Song, X., S. Feih, W. Zhai, C.-N. Sun, F. Li, R. Maiti, J. Wei, Y. Yang, V. Oancea, L. Romano Brandt, and A.M. Korsunsky, *Advances in additive manufacturing process simulation: Residual stresses and distortion predictions in complex metallic components.* Materials & Design, 2020. **193**: p. 108779.

132. Zhang, Q., J. Xie, T. London, D. Griffiths, I. Bhamji, and V. Oancea, *Estimates of the mechanical properties of laser powder bed fusion Ti-6Al-4V parts using finite element models.* Materials & Design, 2019. **169**: p. 107678.
133. Yang, Y., M. Allen, T. London, and V. Oancea, *Residual Strain Predictions for a Powder Bed Fusion Inconel 625 Single Cantilever Part.* Integrating Materials and Manufacturing Innovation, 2019. **8**(3): p. 294-304.
134. Peter, N., Z. Pitts, S. Thompson, and A. Saharan, *Benchmarking build simulation software for laser powder bed fusion of metals.* Additive Manufacturing, 2020. **36**: p. 101531.
135. Li, M., J. Li, D. Yang, and B. He, *Dimensional Deviation Management for Selective Laser Melted Ti6Al4V Alloy Blade.* Frontiers in Materials, 2020. **7**(42).
136. Wang, L., X. Jiang, Y. Zhu, X. Zhu, J. Sun, and B. Yan, *An approach to predict the residual stress and distortion during the selective laser melting of AlSi10Mg parts.* The International Journal of Advanced Manufacturing Technology, 2018. **97**(9): p. 3535-3546.
137. Chen, Q., X. Liang, D. Hayduke, J. Liu, L. Cheng, J. Oskin, R. Whitmore, and A.C. To, *An inherent strain based multiscale modeling framework for simulating part-scale residual deformation for direct metal laser sintering.* Additive Manufacturing, 2019. **28**: p. 406-418.
138. Li, C., M.F. Gouge, E.R. Denlinger, J.E. Irwin, and P. Michaleris, *Estimation of part-to-powder heat losses as surface convection in laser powder bed fusion.* Additive Manufacturing, 2019. **26**: p. 258-269.
139. Soylemez, E., E. Koç, and M. Coşkun, *Thermo-mechanical simulations of selective laser melting for AlSi10Mg alloy to predict the part-scale deformations.* Progress in Additive Manufacturing, 2019. **4**(4): p. 465-478.
140. Liang, X., D. Hayduke, and A.C. To, *An enhanced layer lumping method for accelerating simulation of metal components produced by laser powder bed fusion.* Additive Manufacturing, 2021: p. 101881.
141. Promoppatum, P. and V. Uthaisangsuk, *Part scale estimation of residual stress development in laser powder bed fusion additive manufacturing of Inconel 718.* Finite Elements in Analysis and Design, 2021. **189**: p. 103528.
142. Foteinopoulos, P., A. Papacharalampopoulos, and P. Stavropoulos, *On thermal modeling of Additive Manufacturing processes.* CIRP Journal of Manufacturing Science and Technology, 2018. **20**: p. 66-83.
143. Zhang, Y., G. Guillemot, M. Bernacki, and M. Bellet, *Macroscopic thermal finite element modeling of additive metal manufacturing by selective laser melting process.* Computer Methods in Applied Mechanics and Engineering, 2018. **331**: p. 514-535.
144. Shahabad, S.I., Z. Zhang, A. Keshavarzkermani, U. Ali, Y. Mahmoodkhani, R. Esmaeilizadeh, A. Bonakdar, and E. Toyserkani, *Heat source model calibration for thermal analysis of laser powder-bed fusion.* The International Journal of Advanced Manufacturing Technology, 2020. **106**(7): p. 3367-3379.
145. Lindgren, L.E., *Numerical modelling of welding.* Computer Methods in Applied Mechanics and Engineering, 2006. **195**(48): p. 6710-6736.
146. Lindgren, L.-E., *Computational Welding Mechanics: Thermomechanical and Microstructural Simulations.* Computational Welding Mechanics: Thermomechanical and Microstructural Simulations, 2007: p. 1-231.

147. Mirkoohi, E., J. Ning, P. Bocchini, O. Fergani, K.-N. Chiang, and S.Y. Liang, *Thermal Modeling of Temperature Distribution in Metal Additive Manufacturing Considering Effects of Build Layers, Latent Heat, and Temperature-Sensitivity of Material Properties.* Journal of Manufacturing and Materials Processing, 2018. **2**(3).
148. Michaleris, P., *Modeling metal deposition in heat transfer analyses of additive manufacturing processes.* Finite Elements in Analysis and Design, 2014. **86**: p. 51-60.
149. Zhang, W., M. Tong, and N.M. Harrison, *Resolution, energy and time dependency on layer scaling in finite element modelling of laser beam powder bed fusion additive manufacturing.* Additive Manufacturing, 2019. **28**: p. 610-620.
150. Chiumenti, M., M. Cervera, N. Dialami, B. Wu, L. Jinwei, and C. Agelet de Saracibar, *Numerical modeling of the electron beam welding and its experimental validation.* Finite Elements in Analysis and Design, 2016. **121**: p. 118-133.
151. *Abaqus Theory Guide*. Providence RI, USA: Dassault Systèmes.
152. Chiumenti, M., M. Cervera, C. Agelet de Saracibar, and N. Dialami, *Numerical modeling of friction stir welding processes.* Computer Methods in Applied Mechanics and Engineering, 2013. **254**: p. 353-369.
153. Bayat, M., S. Mohanty, and J.H. Hattel, *A systematic investigation of the effects of process parameters on heat and fluid flow and metallurgical conditions during laser-based powder bed fusion of Ti6Al4V alloy.* International Journal of Heat and Mass Transfer, 2019. **139**: p. 213-230.
154. Zhang, Z., Y. Huang, A. Rani Kasinathan, S. Imani Shahabad, U. Ali, Y. Mahmoodkhani, and E. Toyserkani, *3-Dimensional heat transfer modeling for laser powder-bed fusion additive manufacturing with volumetric heat sources based on varied thermal conductivity and absorptivity.* Optics & Laser Technology, 2019. **109**: p. 297-312.
155. Li, C., J.F. Liu, and Y.B. Guo, *Prediction of Residual Stress and Part Distortion in Selective Laser Melting.* Procedia CIRP, 2016. **45**: p. 171-174.
156. Barrett, R.A., T. Etienne, C. Duddy, and N.M. Harrison, *Residual stress prediction in a powder bed fusion manufactured Ti6Al4V hip stem.* AIP Conference Proceedings, 2017. **1896**(1): p. 040018.
157. Lindwall, J., A. Malmelöv, A. Lundbäck, and L.E. Lindgren, *Efficiency and Accuracy in Thermal Simulation of Powder Bed Fusion of Bulk Metallic Glass.* JOM, 2018. **70**(8): p. 1598-1603.
158. Zhang, Z., Z. Wan, L.-E. Lindgren, T. Zhijun, and X. Zhou, *The Simulation of Precipitation Evolutions and Mechanical Properties in Friction Stir Welding with Post-Weld Heat Treatments.* Journal of Materials Engineering and Performance, 2017. **26**: p. 5731-5740.
159. Li, C., C.H. Fu, Y.B. Guo, and F.Z. Fang, *A multiscale modeling approach for fast prediction of part distortion in selective laser melting.* Journal of Materials Processing Technology, 2016. **229**: p. 703-712.
160. Zhang, W., M. Tong, and N.M. Harrison, *Data on a computationally efficient approximation of part-powder conduction as surface free convection in powder bed fusion process modelling.* Data in Brief, 2019. **27**: p. 104559.
161. Masoomi, M., S.M. Thompson, and N. Shamsaei, *Laser powder bed fusion of Ti-6Al-4V parts: Thermal modeling and mechanical implications.* International

Journal of Machine Tools and Manufacture, 2017. **118-119**(Supplement C): p. 73-90.
162. Liu, W.K., P. Cheng, O.L. Kafka, W. Xiong, and Z. Liu, *Linking Process , Structure , and Property in Additive Manufacturing Applications through Advanced Materials Modelling.* COMPLAS XIII: proceedings of the XIII International Conference on Computational Plasticity: fundamentals and applications, 2015: p. 23-39.
163. Yang, Y.P., M. Jamshidinia, P. Boulware, and S.M. Kelly, *Prediction of microstructure, residual stress, and deformation in laser powder bed fusion process.* Computational Mechanics, 2017.
164. Zaeh, M.F. and G. Branner, *Investigations on residual stresses and deformations in selective laser melting.* Production Engineering, 2010. **4**(1): p. 35-45.
165. Roberts, I.A., *Investigation of residual stresses in the laser melting of metal powders in additive layer manufacturing*. University of Wolverhampton.
166. Raghavan, A., H.L. Wei, T.A. Palmer, and T. DebRoy, *Heat transfer and fluid flow in additive manufacturing.* Journal of Laser Applications, 2013. **25**(5): p. 052006.
167. Khairallah, S.A. and A. Anderson, *Mesoscopic simulation model of selective laser melting of stainless steel powder.* Journal of Materials Processing Technology, 2014. **214**(11): p. 2627-2636.
168. Chen, T. and Y. Zhang, *Numerrical simulation of two-dimentional melting and resolidification of a two-component metal powder layer in Selective Laser Sintering process.* Numerical Heat Transfer, Part A: Applications, 2004. **46**(7): p. 633-649.
169. Hodge, N.E., R.M. Ferencz, and J.M. Solberg, *Implementation of a thermomechanical model for the simulation of selective laser melting.* Computational Mechanics, 2014. **54**(1): p. 33-51.
170. Hodge, N.E., R.M. Ferencz, and R.M. Vignes, *Experimental comparison of residual stresses for a thermomechanical model for the simulation of selective laser melting.* Additive Manufacturing, 2016. **12**: p. 159-168.
171. Hebert, R.J., *Viewpoint: metallurgical aspects of powder bed metal additive manufacturing.* Journal of Materials Science, 2016. **51**(3): p. 1165-1175.
172. Keller, T., G. Lindwall, S. Ghosh, L. Ma, B.M. Lane, F. Zhang, U.R. Kattner, E.A. Lass, J.C. Heigel, Y. Idell, M.E. Williams, A.J. Allen, J.E. Guyer, and L.E. Levine, *Application of finite element, phase-field, and CALPHAD-based methods to additive manufacturing of Ni-based superalloys.* Acta Materialia, 2017. **139**: p. 244-253.
173. Dunbar, A.J., E.R. Denlinger, M.F. Gouge, and P. Michaleris, *Experimental validation of finite element modeling for laser powder bed fusion deformation.* Additive Manufacturing, 2016. **12**: p. 108-120.
174. Ma, L., J. Fong, B. Lane, S. Moylan, J. Filliben, A. Hecket, and L. Levine, *Using Design of Experiments in Finite Element Modeling to Identify Critical Variables for Laser Powder Bed Fusion*, in *Solid Freeform Fabrication Symposium*. 2015.
175. Li, C., J.F. Liu, Y.B. Guo, and Z.Y. LI, *A Temperature-Thread Multiscale Modeling Approach for Efficient Prediction of Part Distortion by Selective Laser Melting*. 2015.

176. Pal, D., N. Patil, M. Nikoukar, K. Zeng, H. Kutty, and B. Stucker, *An Integrated Approach to Cyber-Enabled Additive Manufacturing using Physics based, Coupled Multi-scale Process Modeling*. 2013.
177. Denlinger, E.R., V. Jagdale, G.V. Srinivasan, T. El-Wardany, and P. Michaleris, *Thermal modeling of Inconel 718 processed with powder bed fusion and experimental validation using in situ measurements.* Additive Manufacturing, 2016. **11**: p. 7-15.
178. Afazov, S., W.A.D. Denmark, B. Lazaro Toralles, A. Holloway, and A. Yaghi, *Distortion prediction and compensation in selective laser melting.* Additive Manufacturing, 2017. **17**(Supplement C): p. 15-22.
179. Brika, S.E., Y.F. Zhao, M. Brochu, and J. Mezzetta, *Multi-Objective Build Orientation Optimization for Powder Bed Fusion by Laser.* Journal of Manufacturing Science and Engineering, 2017. **139**(11): p. 111011-111011-9.
180. Li, C., Z.Y. Liu, X.Y. Fang, and Y.B. Guo, *On the Simulation Scalability of Predicting Residual Stress and Distortion in Selective Laser Melting.* Journal of Manufacturing Science and Engineering, 2018. **140**(4): p. 041013-041013-10.
181. Rubenchik, A.M., W.E. King, and S.S. Wu, *Scaling laws for the additive manufacturing.* Journal of Materials Processing Technology, 2018. **257**: p. 234-243.
182. Qiu, Q. and D. Lau, *A novel approach for near-surface defect detection in FRP-bonded concrete systems using laser reflection and acoustic-laser techniques.* Construction and Building Materials, 2017. **141**: p. 553-564.
183. Cunningham, R., S.P. Narra, C. Montgomery, J. Beuth, and A.D. Rollett, *Synchrotron-Based X-ray Microtomography Characterization of the Effect of Processing Variables on Porosity Formation in Laser Power-Bed Additive Manufacturing of Ti-6Al-4V.* JOM, 2017. **69**(3): p. 479-484.
184. Kasperovich, G., J. Haubrich, J. Gussone, and G. Requena, *Correlation between porosity and processing parameters in TiAl6V4 produced by selective laser melting.* Materials & Design, 2016. **105**: p. 160-170.
185. Gusarov, A.V., I. Yadroitsev, P. Bertrand, and I. Smurov, *Model of Radiation and Heat Transfer in Laser-Powder Interaction Zone at Selective Laser Melting.* Journal of Heat Transfer, 2009. **131**(7): p. 072101-072101-10.
186. Vastola, G., G. Zhang, Q.X. Pei, and Y.W. Zhang, *Modeling the Microstructure Evolution During Additive Manufacturing of Ti6Al4V: A Comparison Between Electron Beam Melting and Selective Laser Melting.* JOM, 2016. **68**(5): p. 1370-1375.
187. Shukla, M. and M. Shukla, *Finite Element Simulation and Analysis of Laser Metal Deposition*, in *6th Int'l Conference on Mechanical, Production & Automobile Engineering*. 2014.
188. Vastola, G., G. Zhang, Q.X. Pei, and Y.W. Zhang, *Controlling of residual stress in additive manufacturing of Ti6Al4V by finite element modeling.* Additive Manufacturing, 2016. **12, Part B**: p. 231-239.
189. Matsumoto, M., M. Shiomi, K. Osakada, and F. Abe, *Finite element analysis of single layer forming on metallic powder bed in rapid prototyping by selective laser processing.* International Journal of Machine Tools and Manufacture, 2002. **42**(1): p. 61-67.

190. Kreitcberg, A., V. Brailovski, and S. Prokoshkin, *New biocompatible near-beta Ti-Zr-Nb alloy processed by laser powder bed fusion: process optimization.* Journal of Materials Processing Technology, 2018. **252**: p. 821-829.
191. Romano, J., L. Ladani, J. Razmi, and M. Sadowski, *Temperature distribution and melt geometry in laser and electron-beam melting processes – A comparison among common materials.* Additive Manufacturing, 2015. **8**(Supplement C): p. 1-11.
192. Zhang, Y. and J. Zhang, *Finite element simulation and experimental validation of distortion and cracking failure phenomena in direct metal laser sintering fabricated component.* Additive Manufacturing, 2017. **16**: p. 49-57.
193. Cheng, B., S. Shrestha, and K. Chou, *Stress and deformation evaluations of scanning strategy effect in selective laser melting*. 2016.
194. Vignesh, R.K.R., M. Kiriti, R. Bharath, F. Behzad, A. Amirhesam, and M. Narges Shayesteh. *Determination of residual stress for Inconel 718 samples fabricated through different scanning strategies in selective laser melting*. in *Proc.SPIE*. 2020.
195. Robinson, J., I. Ashton, P. Fox, E. Jones, and C. Sutcliffe, *Determination of the effect of scan strategy on residual stress in laser powder bed fusion additive manufacturing.* Additive Manufacturing, 2018. **23**: p. 13-24.
196. Prabhakar, P., W.J. Sames, R. Dehoff, and S.S. Babu, *Computational modeling of residual stress formation during the electron beam melting process for Inconel 718.* Additive Manufacturing, 2015. **7**: p. 83-91.
197. Zhang, Z., Y. Huang, A. Rani Kasinathan, S. Imani Shahabad, U. Ali, Y. Mahmoodkhani, and E. Toyserkani, *3-Dimensional heat transfer modeling for laser powder-bed fusion additive manufacturing with volumetric heat sources based on varied thermal conductivity and absorptivity.* Optics & Laser Technology, 2018. **109**: p. 297-312.
198. Parimi, L.L., *Additive manufacturing of nickel based superalloys for aerospace applications*. 2014.
199. Yavari, M.R., K.D. Cole, and P.K. Rao, *Design Rules for Additive Manufacturing – Understanding the Fundamental Thermal Phenomena to Reduce Scrap.* Procedia Manufacturing, 2019. **33**: p. 375-382.
200. Pant, P., S. Proper, V. Luzin, S. Sjöström, K. Simonsson, J. Moverare, S. Hosseini, V. Pacheco, and R.L. Peng, *Mapping of residual stresses in as-built Inconel 718 fabricated by laser powder bed fusion: A neutron diffraction study of build orientation influence on residual stresses.* Additive Manufacturing, 2020. **36**: p. 101501.
201. Koeck, F.X., L. Perlick, C. Luring, M. Handel, J. Beckmann, O. Linhardt, and J. Grifka, *Leg axis correction with ConforMIS iForma™ (interpositional device) in unicompartmental arthritis of the knee.* International Orthopaedics, 2008. **33**(4): p. 955.
202. Ding, J., P. Colegrove, J. Mehnen, S. Williams, F. Wang, and P.S. Almeida, *A computationally efficient finite element model of wire and arc additive manufacture.* The International Journal of Advanced Manufacturing Technology, 2014. **70**(1): p. 227-236.

203. Papadakis, L., A. Loizou, J. Risse, and J. Schrage, *Numerical Computation of Component Shape Distortion Manufactured by Selective Laser Melting.* Procedia CIRP, 2014. **18**: p. 90-95.
204. Bugatti, M. and Q. Semeraro, *Limitations of the inherent strain method in simulating powder bed fusion processes.* Additive Manufacturing, 2018. **23**: p. 329-346.
205. Ferro, P., F. Berto, and L. Romanin, *Understanding powder bed fusion additive manufacturing phenomena via numerical simulation.* Frattura ed Integrità Strutturale, 2020. **14**(53): p. 252-284.
206. Liang, X., L. Cheng, Q. Chen, Q. Yang, and A.C. To, *A modified method for estimating inherent strains from detailed process simulation for fast residual distortion prediction of single-walled structures fabricated by directed energy deposition.* Additive Manufacturing, 2018. **23**: p. 471-486.
207. Olleak, A. and Z. Xi, *A scan-wise adaptive remeshing framework for thermal simulation of the selective laser melting process.* The International Journal of Advanced Manufacturing Technology, 2020. **107**(1): p. 573-584.
208. Gouge, M., E. Denlinger, J. Irwin, C. Li, and P. Michaleris, *Experimental validation of thermo-mechanical part-scale modeling for laser powder bed fusion processes.* Additive Manufacturing, 2019. **29**: p. 100771.
209. *Abaqus Analysis User's Manual, Version 6.8*. Providence RI, USA: Dassault Systèmes.
210. Hajializadeh, F. and A. Ince, *Finite element–based numerical modeling framework for additive manufacturing process.* Material Design & Processing Communications, 2019. **1**(1): p. e28.
211. Wiesner, A. and D. Schwarzea, *Multi-Laser Selective Laser Melting*, in *8th International Conference on Photonic Technologies*. 2014.
212. Buchbinder, D., H. Schleifenbaum, S. Heidrich, W. Meiners, and J. Bültmann, *High Power Selective Laser Melting (HP SLM) of Aluminum Parts.* Physics Procedia, 2011. **12**: p. 271-278.
213. Weingarten, C., D. Buchbinder, N. Pirch, W. Meiners, K. Wissenbach, and R. Poprawe, *Formation and reduction of hydrogen porosity during selective laser melting of AlSi10Mg.* Journal of Materials Processing Technology, 2015. **221**: p. 112-120.
214. Li, F., Z. Wang, and X. Zeng, *Microstructures and mechanical properties of Ti6Al4V alloy fabricated by multi-laser beam selective laser melting.* Materials Letters, 2017. **199**: p. 79-83.
215. Mejia-Parra, D., D. Montoya-Zapata, A. Arbelaiz, A. Moreno, J. Posada, and O. Ruiz-Salguero, *Fast Analytic Simulation for Multi-Laser Heating of Sheet Metal in GPU.* Materials (Basel, Switzerland), 2018. **11**(11): p. 2078.
216. Masoomi, M., S.M. Thompson, and N. Shamsaei, *Quality part production via multi-laser additive manufacturing.* Manufacturing Letters, 2017. **13**: p. 15-20.
217. Taheri Andani, M., R. Dehghani, M.R. Karamooz-Ravari, R. Mirzaeifar, and J. Ni, *Spatter formation in selective laser melting process using multi-laser technology.* Materials & Design, 2017. **131**: p. 460-469.
218. *Sandvik acquires Renishaw 3D printers.* Metal Powder Report, 2019. **74**(2): p. 102.

219. *The ultra-fast four-laser system*. Available from: https://www.eos.info/en/additive-manufacturing/3d-printing-metal/eos-metal-systems/eos-m-400-4.
220. Sutton, B., E. Herderick, R. Thodla, M. Ahlfors, and A. Ramirez, *Heat Treatment of Alloy 718 Made by Additive Manufacturing for Oil and Gas Applications.* JOM, 2019. **71**(3): p. 1134-1143.
221. Williams, R.J., A. Piglione, T. Rønneberg, C. Jones, M.-S. Pham, C.M. Davies, and P.A. Hooper, *In situ thermography for laser powder bed fusion: Effects of layer temperature on porosity, microstructure and mechanical properties.* Additive Manufacturing, 2019. **30**: p. 100880.
222. Zou, S., H. Xiao, F. Ye, Z. Li, W. Tang, F. Zhu, C. Chen, and C. Zhu, *Numerical analysis of the effect of the scan strategy on the residual stress in the multi-laser selective laser melting.* Results in Physics, 2020. **16**: p. 103005.
223. Chen, C., Z. Xiao, H. Zhu, and X. Zeng, *Distribution and evolution of thermal stress during multi-laser powder bed fusion of Ti-6Al-4 V alloy.* Journal of Materials Processing Technology, 2020. **284**: p. 116726.
224. Wong, H., K. Dawson, G.A. Ravi, L. Howlett, R.O. Jones, and C.J. Sutcliffe, *Multi-Laser Powder Bed Fusion Benchmarking—Initial Trials with Inconel 625.* The International Journal of Advanced Manufacturing Technology, 2019. **105**(7): p. 2891-2906.
225. Liu, B., Z. Kuai, Z. Li, J. Tong, P. Bai, B. Li, and Y. Nie, *Performance Consistency of AlSi10Mg Alloy Manufactured by Simulating Multi Laser Beam Selective Laser Melting (SLM): Microstructures and Mechanical Properties.* Materials (Basel, Switzerland), 2018. **11**(12): p. 2354.
226. Criales, L.E. and T. Özel, *Temperature profile and melt depth in laser powder bed fusion of Ti-6Al-4V titanium alloy.* Progress in Additive Manufacturing, 2017. **2**(3): p. 169-177.
227. Parry, L.A., I.A. Ashcroft, and R.D. Wildman, *Geometrical effects on residual stress in selective laser melting.* Additive Manufacturing, 2019. **25**: p. 166-175.
228. Ganeriwala, R.K., M. Strantza, W.E. King, B. Clausen, T.Q. Phan, L.E. Levine, D.W. Brown, and N.E. Hodge, *Evaluation of a thermomechanical model for prediction of residual stress during laser powder bed fusion of Ti-6Al-4V.* Additive Manufacturing, 2019. **27**: p. 489-502.
229. Yadollahi, A., N. Shamsaei, S.M. Thompson, and D.W. Seely, *Effects of process time interval and heat treatment on the mechanical and microstructural properties of direct laser deposited 316L stainless steel.* Materials Science and Engineering: A, 2015. **644**: p. 171-183.
230. Mahmoudi, M., *Mechanical properties and microstructural characterization of selective laser melted 17-4 PH stainless steel.* Rapid Prototyping Journal, 2017. **23**(2): p. 280-294.
231. Denlinger, E.R., J.C. Heigel, P. Michaleris, and T.A. Palmer, *Effect of inter-layer dwell time on distortion and residual stress in additive manufacturing of titanium and nickel alloys.* Journal of Materials Processing Technology, 2015. **215**: p. 123-131.
232. Foster, B.K., A.M. Beese, J.S. Keist, E.T. McHale, and T.A. Palmer, *Impact of Interlayer Dwell Time on Microstructure and Mechanical Properties of Nickel and*

Titanium Alloys. Metallurgical and Materials Transactions A, 2017. **48**(9): p. 4411-4422.
233. Li, R. and J. Xiong, *Influence of interlayer dwell time on stress field of thin-walled components in WAAM via numerical simulation and experimental tests.* Rapid Prototyping Journal, 2019.
234. Ge, J., J. Lin, H. Fu, Y. Lei, and R. Xiao, *Tailoring microstructural features of wire arc additive manufacturing 2Cr13 part via varying inter-layer dwelling time.* Materials Letters, 2018. **232**: p. 11-13.
235. Babu, B., A. Lundbäck, and L.-E. Lindgren, *Simulation of Ti-6Al-4V Additive Manufacturing Using Coupled Physically Based Flow Stress and Metallurgical Model.* Materials, 2019. **12**(23): p. 3844.
236. Yadollahi, A. and N. Shamsaei, *Additive manufacturing of fatigue resistant materials: Challenges and opportunities.* International Journal of Fatigue, 2017. **98**: p. 14-31.
237. Jacob, G., A. Donmez, J. Slotwinski, and S. Moylan, *Measurement of powder bed density in powder bed fusion additive manufacturing processes.* Measurement Science and Technology, 2016. **27**(11): p. 115601.
238. Zhang, Y., Q. Chen, G. Guillemot, C.-A. Gandin, and M. Bellet, *Numerical modelling of fluid and solid thermomechanics in additive manufacturing by powder-bed fusion: Continuum and level set formulation applied to track- and part-scale simulations.* Comptes Rendus Mécanique, 2018. **346**(11): p. 1055-1071.
239. Murgau, C.C., R. Pederson, and L.E. Lindgren, *A model for Ti–6Al–4V microstructure evolution for arbitrary temperature changes.* Modelling and Simulation in Materials Science and Engineering, 2012. **20**(5): p. 055006.
240. Baykasoğlu, C., O. Akyildiz, M. Tunay, and A.C. To, *A process-microstructure finite element simulation framework for predicting phase transformations and microhardness for directed energy deposition of Ti6Al4V.* Additive Manufacturing, 2020. **35**: p. 101252.
241. Collins, P.C., D.A. Brice, P. Samimi, I. Ghamarian, and H.L. Fraser, *Microstructural Control of Additively Manufactured Metallic Materials.* Annual Review of Materials Research, 2016. **46**(1): p. 63-91.
242. Calta, N.P., V. Thampy, D.R.C. Lee, A.A. Martin, R. Ganeriwala, J. Wang, P.J. Depond, T.T. Roehling, A.Y. Fong, A.M. Kiss, C.J. Tassone, K.H. Stone, J. Nelson Weker, M.F. Toney, A.W. Van Buuren, and M.J. Matthews, *Cooling dynamics of two titanium alloys during laser powder bed fusion probed with in situ X-ray imaging and diffraction.* Materials & Design, 2020. **195**: p. 108987.
243. Karimi, P., E. Sadeghi, P. Åkerfeldt, J. Ålgårdh, and J. Andersson, *Influence of successive thermal cycling on microstructure evolution of EBM-manufactured alloy 718 in track-by-track and layer-by-layer design.* Materials & Design, 2018. **160**: p. 427-441.
244. Sames, W.J., K.A. Unocic, R.R. Dehoff, T. Lolla, and S.S. Babu, *Thermal effects on microstructural heterogeneity of Inconel 718 materials fabricated by electron beam melting.* Journal of Materials Research, 2014. **29**(17): p. 1920-1930.
245. Lars-Erik, Rannar, Andrey, Koptyug, Jon, Olsen, Kamran, Saeidi, Zhijian, and Shen, *Hierarchical structures of stainless steel 316L manufactured by Electron Beam Melting.* Additive Manufacturing, 2017.

246. Yang, X., R.A. Barrett, M. Tong, N.M. Harrison, and S.B. Leen, *Prediction of Microstructure Evolution for Additive Manufacturing of Ti-6Al-4V.* Procedia Manufacturing, 2020. **47**: p. 1178-1183.
247. Ding, X., Y. Koizumi, D. Wei, and A. Chiba, *Effect of process parameters on melt pool geometry and microstructure development for electron beam melting of IN718: A systematic single bead analysis study.* Additive Manufacturing, 2019. **26**: p. 215-226.
248. Todaro, C.J., M.A. Easton, D. Qiu, D. Zhang, M.J. Bermingham, E.W. Lui, M. Brandt, D.H. StJohn, and M. Qian, *Grain structure control during metal 3D printing by high-intensity ultrasound.* Nature Communications, 2020. **11**(1): p. 142.
249. Brailovski, V., *The Average Grain Size and Grain Aspect Ratio in Metal Laser Powder Bed Fusion: Modeling and Experiment.* Journal of Manufacturing and Materials Processing, 2020. **4**.
250. Ahn, J., E. He, L. Chen, R.C. Wimpory, J.P. Dear, and C.M. Davies, *Prediction and measurement of residual stresses and distortions in fibre laser welded Ti-6Al-4V considering phase transformation.* Materials & Design, 2017. **115**: p. 441-457.
251. Crespo, A.n., *Modelling of Heat Transfer and Phase Transformations in the Rapid Manufacturing of Titanium Components*, in *Convection and Conduction Heat Transfer*. 2011. p. 315-340.
252. Zitelli, C., Folgarait, and A. Schino, *Laser Powder Bed Fusion of Stainless Steel Grades: A Review.* Metals, 2019. **9**: p. 731.
253. Koepf, J.A., M.R. Gotterbarm, M. Markl, and C. Körner, *3D multi-layer grain structure simulation of powder bed fusion additive manufacturing.* Acta Materialia, 2018. **152**: p. 119-126.
254. Arısoy, Y.M., L.E. Criales, and T. Özel, *Modeling and simulation of thermal field and solidification in laser powder bed fusion of nickel alloy IN625.* Optics & Laser Technology, 2019. **109**: p. 278-292.
255. Olleak, A. and Z. Xi, *Finite Element Modeling of the Selective Laser Melting Process for Ti-6Al-4V*. 2018.
256. Rossini, N.S., M. Dassisti, K.Y. Benyounis, and A.G. Olabi, *Methods of measuring residual stresses in components.* Materials & Design, 2012. **35**: p. 572-588.
257. Marchese, G., E. Atzeni, A. Salmi, and S. Biamino, *Microstructure and Residual Stress Evolution of Laser Powder Bed Fused Inconel 718 under Heat Treatments.* Journal of Materials Engineering and Performance, 2021. **30**(1): p. 565-574.
258. Withers, P.J. and H.K.D.H. Bhadeshia, *Residual stress. Part 1 – Measurement techniques.* Materials Science and Technology, 2001. **17**(4): p. 355-365.
259. Swain, D., A. Sharma, S.K. Selvan, B.P. Thomas, Govind, and J. Philip, *Residual stress measurement on 3-D printed blocks of Ti-6Al-4V using incremental hole drilling technique.* Procedia Structural Integrity, 2019. **14**: p. 337-344.
260. *Hole drilling for residual stress measurements and analyses*. Available from: https://sonats-et.com/en/residual-stress/hole-drilling-residual-stress-measurement/.
261. Vrancken, B., V. Cain, R. Knutsen, and J. Van Humbeeck, *Residual stress via the contour method in compact tension specimens produced via selective laser melting.* Scripta Materialia, 2014. **87**: p. 29-32.

262. Delbergue, D., D. Texier, M. Lévesque, and P. Bocher, *Comparison of Two X-Ray Residual Stress Measurement Methods: Sin2 ψ and Cos α, Through the Determination of a Martensitic Steel X-Ray Elastic Constant*. 2016.
263. Vemanaboina, H., G. Guruvaiah Naidu, D. Satya Abhinav, N. Krishna, and D. Ramachandra Reddy, *Evaluation of residual stress in multipass dissimilar butt joints using X-ray diffraction.* Materials Today: Proceedings, 2019. **19**: p. 283-288.
264. Anderoglu, O., *Residual Stress Measurement Using X-ray Diffraction*. 2004, Texas A&M University.
265. Fitzpatrick, M., A. Fry, P. Holdway, F.A. Kandil, J. Shackleton, and L. Suominen, *NPL Good Practice Guide no. 52: determination of residual stresses by x-ray diffraction*. 2002.
266. Hartunian, P. and M. Eshraghi, *Effect of Build Orientation on the Microstructure and Mechanical Properties of Selective Laser-Melted Ti-6Al-4V Alloy.* Journal of Manufacturing and Materials Processing, 2018. **2**(4).
267. Xu, L., S.Y. Zhang, W. Sun, D. McCartney, T. Hyde, J. James, and M. Drakopoulos, *Residual stress distribution in a Ti-6Al-4V T-joint weld measured using synchrotron X-ray diffraction.* The Journal of Strain Analysis for Engineering Design, 2015. **50**.
268. Szost, B.A., S. Terzi, F. Martina, D. Boisselier, A. Prytuliak, T. Pirling, M. Hofmann, and D.J. Jarvis, *A comparative study of additive manufacturing techniques: Residual stress and microstructural analysis of CLAD and WAAM printed Ti–6Al–4V components.* Materials & Design, 2016. **89**: p. 559-567.
269. Beese, A.M., Z. Wang, A.D. Stoica, and D. Ma, *Absence of dynamic strain aging in an additively manufactured nickel-base superalloy.* Nature Communications, 2018. **9**(1): p. 2083.
270. Sandmann, P., M.-A. Nielsen, S. Keller, E. Maawad, P. Staron, and B. Klusemann, *Combined experimental–numerical study on residual stresses induced by a single impact as elementary process of mechanical peening.* Strain, 2020. **56**(4): p. e12338.
271. Brown, D.W., J.D. Bernardin, J.S. Carpenter, B. Clausen, D. Spernjak, and J.M. Thompson, *Neutron diffraction measurements of residual stress in additively manufactured stainless steel.* Materials Science and Engineering: A, 2016. **678**: p. 291-298.
272. Xu, L., S.-Y. Zhang, W. Sun, D.G. McCartney, T.H. Hyde, J. James, and M. Drakopoulos, *Residual stress distribution in a Ti–6Al–4V T-joint weld measured using synchrotron X-ray diffraction.* The Journal of Strain Analysis for Engineering Design, 2015. **50**(7): p. 445-454.
273. Ganguly, S., M.E. Fitzpatrick, and L. Edwards, *Use of neutron and synchrotron X-ray diffraction for evaluation of residual stresses in a 2024-T351 aluminum alloy variable-polarity plasma-arc weld.* Metallurgical and Materials Transactions A, 2006. **37**(2): p. 411-420.
274. Vogel, S.C., *A Review of Neutron Scattering Applications to Nuclear Materials.* ISRN Materials Science, 2013. **2013**: p. 302408.
275. Scattering, N.R.C.P.o.N. and G. Rossi, *Neutron Scattering Facilities in Europe : Present Status and Future Perspectives*. 2016: University of Milan, $c2016.

276. Strantza, M., R.K. Ganeriwala, B. Clausen, T.Q. Phan, L.E. Levine, D. Pagan, W.E. King, N.E. Hodge, and D.W. Brown, *Coupled experimental and computational study of residual stresses in additively manufactured Ti-6Al-4V components.* Materials Letters, 2018. **231**: p. 221-224.
277. Song, X., M. Xie, F. Hofmann, T.S. Jun, T. Connolley, C. Reinhard, R.C. Atwood, L. Connor, M. Drakopoulos, S. Harding, and A.M. Korsunsky, *Residual stresses in Linear Friction Welding of aluminium alloys.* Materials & Design, 2013. **50**: p. 360-369.
278. Brown, D.W., M.A. Okuniewski, J.D. Almer, L. Balogh, B. Clausen, J.S. Okasinski, and B.H. Rabin, *High energy X-ray diffraction measurement of residual stresses in a monolithic aluminum clad uranium–10wt% molybdenum fuel plate assembly.* Journal of Nuclear Materials, 2013. **441**(1): p. 252-261.
279. Roberts, I.A., C.J. Wang, R. Esterlein, M. Stanford, and D.J. Mynors, *A three-dimensional finite element analysis of the temperature field during laser melting of metal powders in additive layer manufacturing.* International Journal of Machine Tools and Manufacture, 2009. **49**(12): p. 916-923.
280. Riedlbauer, D., M. Drexler, D. Drummer, P. Steinmann, and J. Mergheim, *Modelling, simulation and experimental validation of heat transfer in selective laser melting of the polymeric material PA12.* Computational Materials Science, 2014. **93**: p. 239-248.
281. Megahed, M., H.-W. Mindt, N. N'Dri, H. Duan, and O. Desmaison, *Metal additive-manufacturing process and residual stress modeling.* Integrating Materials and Manufacturing Innovation, 2016. **5**(1).
282. Keller, N. and V. Ploshikhin, *New method for fast predictions of residual stress and distortion of AM parts*, in *Solid Freeform Fabrication Symposium*. 2014: Austin Texas. p. 1229-1237.
283. Romano, J., L. Ladani, and M. Sadowski, *Thermal Modeling of Laser Based Additive Manufacturing Processes within Common Materials.* Procedia Manufacturing, 2015. **1**: p. 238-250.
284. Gong, H., H. Gu, K. Zeng, J.J.S. Dilip, D. Pal, and B. Stucker, *Melt Pool Characterization for Selective Laser Melting of Ti-6Al-4V Pre-alloyed Powder.* 2014.
285. Protasov, C.E., R.S. Khmyrov, S.N. Grigoriev, and A.V. Gusarov, *Selective laser melting of fused silica: Interdependent heat transfer and powder consolidation.* International Journal of Heat and Mass Transfer, 2017. **104**: p. 665-674.
286. Tolochko, N.K., M.K. Arshinov, A.V. Gusarov, V.I. Titov, T. Laoui, and L. Froyen, *Mechanisms of selective laser sintering and heat transfer in Ti powder.* Rapid Prototyping Journal, 2003. **9**(5): p. 314-326.
287. Zäh, M.F. and S. Lutzmann, *Modelling and simulation of electron beam melting.* Production Engineering, 2010. **4**(1): p. 15-23.
288. Denlinger, E.R., M. Gouge, J. Irwin, and P. Michaleris, *Thermomechanical model development and in situ experimental validation of the Laser Powder-Bed Fusion process.* Additive Manufacturing, 2017. **16**: p. 73-80.
289. Denlinger, E.R. and P. Michaleris, *Effect of stress relaxation on distortion in additive manufacturing process modeling.* Additive Manufacturing, 2016. **12**: p. 51-59.

290. Guo, D., K. Yan, M.D. Callaghan, D. Daisenberger, M. Chatterton, J. Chen, A. Wisbey, and W. Mirihanage, *Solidification microstructure and residual stress correlations in direct energy deposited type 316L stainless steel.* Materials & Design, 2021: p. 109782.
291. Ramos, D., F. Belblidia, and J. Sienz, *New scanning strategy to reduce warpage in additive manufacturing.* Additive Manufacturing, 2019. **28**: p. 554-564.
292. Zhang, W., M. Tong, and N.M. Harrison, *Scanning strategies effect on temperature, residual stress and deformation by multi-laser beam powder bed fusion manufacturing.* Additive Manufacturing, 2020. **36**: p. 101507.
293. Wang, M., Y. Wu, S. Lu, T. Chen, Y. Zhao, H. Chen, and Z. Tang, *Fabrication and characterization of selective laser melting printed Ti–6Al–4V alloys subjected to heat treatment for customized implants design.* Progress in Natural Science: Materials International, 2016. **26**(6): p. 671-677.
294. Woo, W., Z. Feng, X.l. Wang, and S.A. David, *Neutron diffraction measurements of residual stresses in friction stir welding: a review.* Science and Technology of Welding and Joining, 2011. **16**(1): p. 23-32.
295. Maimaitiyili, T., R. Woracek, M. Neikter, M. Boin, R.C. Wimpory, R. Pederson, M. Strobl, M. Drakopoulos, N. Schaefer, and C. Bjerk'en, *Residual Lattice Strain and Phase Distribution in Ti-6Al-4V Produced by Electron Beam Melting.* Materials, 2019. **12**.
296. Korsunsky, A.M., X. Song, F. Hofmann, B. Abbey, M. Xie, T. Connolley, C. Reinhard, R.C. Atwood, L. Connor, and M. Drakopoulos, *Polycrystal deformation analysis by high energy synchrotron X-ray diffraction on the I12 JEEP beamline at Diamond Light Source.* Materials Letters, 2010. **64**(15): p. 1724-1727.
297. Waqar, S., K. Guo, and J. Sun, *FEM analysis of thermal and residual stress profile in selective laser melting of 316L stainless steel.* Journal of Manufacturing Processes, 2021. **66**: p. 81-100.
298. Ghasri-Khouzani, M., H. Peng, R. Rogge, R. Attardo, P. Ostiguy, J. Neidig, R. Billo, D. Hoelzle, and M.R. Shankar, *Experimental measurement of residual stress and distortion in additively manufactured stainless steel components with various dimensions.* Materials Science and Engineering: A, 2017. **707**: p. 689-700.
299. Patil, N., R. Ganeriwala, J.M. Solberg, N.E. Hodge, and R.M. Ferencz, *Benchmark multi-layer simulations for residual stresses and deformation in small additively manufactured metal parts.* Additive Manufacturing, 2021: p. 102015.
300. Nycz, A., Y. Lee, M. Noakes, D. Ankit, C. Masuo, S. Simunovic, J. Bunn, L. Love, V. Oancea, A. Payzant, and C.M. Fancher, *Effective residual stress prediction validated with neutron diffraction method for metal large-scale additive manufacturing.* Materials & Design, 2021. **205**: p. 109751.
301. Mercelis, P. and J.P. Kruth, *Residual stresses in selective laser sintering and selective laser melting.* Rapid Prototyping Journal, 2006. **12**(5): p. 254-265.
302. Ivanov, S., E. Zemlyakov, K. Babkin, G. Turichin, I. Karpov, V. Em, and S. Rylov, *Stress distribution in laser metal deposited multi-layer thick-walled parts of Ti-6Al-4V.* Procedia Manufacturing, 2019. **36**: p. 240-248.
303. Huchings, M.T., P. Withers, T.M. Holden, and T. Lorentzen, *Introduction to the Characterization of Residual Stress by Neutron Diffraction, CRC Press.* Taylor & Francis, 2005: p. 149-202.

304. Lundbäck, A., R. Pederson, M.H. Colliander, C. Brice, A. Steuwer, A. Heralic, T. Buslaps, and L.-E. Lindgren, *Modeling And Experimental Measurement with Synchrotron Radiation of Residual Stresses in Laser Metal Deposited Ti-6Al-4V,* in *Proceedings of the 13th World Conference on Titanium*. 2016. p. 1279-1282.
305. Clausen, B., C.R. D'Elia, M.B. Prime, M.R. Hill, J.E. Bishop, K.L. Johnson, B.H. Jared, K.M. Allen, D.K. Balch, R.A. Roach, and D.W. Brown, *Complementary Measurements of Residual Stresses Before and After Base Plate Removal in an Intricate Additively-Manufactured Stainless-Steel Valve Housing.* Additive Manufacturing, 2020. **36**: p. 101555.
306. Masoomi, M., S.M. Thompson, and N. Shamsaei, *Laser powder bed fusion of Ti-6Al-4V parts: Thermal modeling and mechanical implications.* International Journal of Machine Tools and Manufacture, 2017. **118-119**: p. 73-90.
307. Luo, Z. and Y. Zhao, *A survey of finite element analysis of temperature and thermal stress fields in powder bed fusion Additive Manufacturing.* Additive Manufacturing, 2018. **21**: p. 318-332.
308. Zhao, C., N.D. Parab, X. Li, K. Fezzaa, W. Tan, A.D. Rollett, and T. Sun, *Critical instability at moving keyhole tip generates porosity in laser melting.* Science, 2020. **370**(6520): p. 1080.
309. Beese, A.M. and B.E. Carroll, *Review of Mechanical Properties of Ti-6Al-4V Made by Laser-Based Additive Manufacturing Using Powder Feedstock.* JOM, 2016. **68**(3): p. 724-734.
310. Mower, T.M. and M.J. Long, *Mechanical behavior of additive manufactured, powder-bed laser-fused materials.* Materials Science and Engineering: A, 2016. **651**: p. 198-213.
311. Tang, M., P.C. Pistorius, and J.L. Beuth, *Prediction of lack-of-fusion porosity for powder bed fusion.* Additive Manufacturing, 2017. **14**: p. 39-48.
312. Li, C., C.H. Fu, Y.B. Guo, and F.Z. Fang, *A multiscale modeling approach for fast prediction of part distortion in selective laser melting.* Journal of Materials Processing Tech, 2016. **229**: p. 703-712.
313. Li, Y. and D. Gu, *Thermal behavior during selective laser melting of commercially pure titanium powder: Numerical simulation and experimental study.* Additive Manufacturing, 2014. **1-4**: p. 99-109.
314. Zhang, W., M. Tong, and N.M. Harrison, *Data on a computationally efficient approximation of part-powder conduction as surface free convection in powder bed fusion process modelling.* Data in Brief, 2019: p. 104559.
315. Zhang, G., J. Chen, M. Zheng, Z. Yan, X. Lu, X. Lin, and W. Huang, *Element Vaporization of Ti-6Al-4V Alloy during Selective Laser Melting.* Metals, 2020. **10**(4).
316. Hertel, M., M. Trautmann, S. Jäckel, and U. Füssel, *The Role of Metal Vapour in Gas Metal Arc Welding and Methods of Combined Experimental and Numerical Process Analysis.* Plasma Chemistry and Plasma Processing, 2017. **37**(3): p. 531-547.
317. Dunbar, A.J., E.R. Denlinger, J. Heigel, P. Michaleris, P. Guerrier, R. Martukanitz, and T.W. Simpson, *Development of experimental method for in situ distortion and temperature measurements during the laser powder bed fusion additive manufacturing process.* Additive Manufacturing, 2016. **12**: p. 25-30.

318. Yakout, M., M.A. Elbestawi, and S.C. Veldhuis, *On the characterization of stainless steel 316L parts produced by selective laser melting.* The International Journal of Advanced Manufacturing Technology, 2018. **95**(5): p. 1953-1974.
319. Fitzgerald, E. and W. Everhart. *The Effect of Location on the Structure and Mechanical Properties of Selective Laser Melted 316 L Stainless Steel.* 2016.
320. Anderton, J. *Designing for Maximum Strength with Minimum Support in Metal Additive Manufacturing*. 2020; Available from: https://www.engineering.com/3DPrinting/3DPrintingArticles/ArticleID/20583/Designing-for-Maximum-Strength-with-Minimum-Support-in-Metal-Additive-Manufacturing.aspx.
321. Li, H., M. Ramezani, Z. Chen, and S. Singamneni, *Effects of Process Parameters on Temperature and Stress Distributions During Selective Laser Melting of Ti–6Al–4V*. Transactions of the Indian Institute of Metals, 2019. **72**(12): p. 3201-3214.
322. Malý, M., C. Höller, M. Skalon, B. Meier, D. Koutný, R. Pichler, C. Sommitsch, and D. Paloušek, *Effect of Process Parameters and High-Temperature Preheating on Residual Stress and Relative Density of Ti6Al4V Processed by Selective Laser Melting.* Materials (Basel, Switzerland), 2019. **12**(6): p. 930.
323. Lei, Y., J. Xiong, and R. Li, *Effect of inter layer idle time on thermal behavior for multi-layer single-pass thin-walled parts in GMAW-based additive manufacturing.* The International Journal of Advanced Manufacturing Technology, 2018. **96**(1): p. 1355-1365.
324. Ali, H., L. Ma, H. Ghadbeigi, and K. Mumtaz, *In-situ residual stress reduction, martensitic decomposition and mechanical properties enhancement through high temperature powder bed pre-heating of Selective Laser Melted Ti6Al4V*. Materials Science and Engineering: A, 2017. **695**.
325. Hao, Y.L., S.-J. Li, and R. Yang, *Biomedical titanium alloys and their additive manufacturing.* Rare Metals, 2016. **35**(9): p. 661-671.
326. *Microstructures and Hardness Properties for β-Phase Ti-24Nb-4Zr-7.9Sn Alloy Fabricated by Electron Beam Melting.* Journal of Materials Science & Technology, 2013(11): p. 1011-1017.
327. Yang, C., Z. Zhang, S. Li, Y. Liu, T. Sercombe, W. Hou, P. Zhang, Y. Zhu, Y. Hao, Z. Zhang, and R. Yang, *Simultaneous improvement in strength and plasticity of Ti-24Nb-4Zr-8Sn manufactured by selective laser melting.* Materials & Design, 2018. **157**: p. 52-59.
328. Price, S., J. Lydon, K. Cooper, and K. Chou, *Experimental temperature analysis of powder-based electron beam additive manufacturing.* 24th International SFF Symposium - An Additive Manufacturing Conference, SFF 2013, 2013: p. 162-173.
329. Thampy, V., A.Y. Fong, N.P. Calta, J. Wang, A.A. Martin, P.J. Depond, A.M. Kiss, G. Guss, Q. Xing, R.T. Ott, A. van Buuren, M.F. Toney, J.N. Weker, M.J. Kramer, M.J. Matthews, C.J. Tassone, and K.H. Stone, *Subsurface Cooling Rates and Microstructural Response during Laser Based Metal Additive Manufacturing.* Scientific Reports, 2020. **10**(1): p. 1981.
330. Al-Bermani, S.S., M.L. Blackmore, W. Zhang, and I. Todd, *The Origin of Microstructural Diversity, Texture, and Mechanical Properties in Electron Beam Melted Ti-6Al-4V*. Metallurgical and Materials Transactions A, 2010. **41**(13): p. 3422-3434.

331. Antonysamy, A.A., *Microstructure, Texture and Mechanical Property Evolution during Additive Manufacturing of Ti6Al4V Alloy for Aerospace Applications.* University of Manchester, 2012.
332. Chen, C., S. Chang, J. Zhu, Z. Xiao, H. Zhu, and X. Zeng, *Residual stress of typical parts in laser powder bed fusion.* Journal of Manufacturing Processes, 2020. **59**: p. 621-628.
333. Zhao, L., J.G. Santos Macías, A. Dolimont, A. Simar, and E. Rivière-Lorphèvre, *Comparison of residual stresses obtained by the crack compliance method for parts produced by different metal additive manufacturing techniques and after friction stir processing.* Additive Manufacturing, 2020. **36**: p. 101499.
334. Sochalski-Kolbus, L.M., E.A. Payzant, P.A. Cornwell, T.R. Watkins, S.S. Babu, R.R. Dehoff, M. Lorenz, O. Ovchinnikova, and C. Duty, *Comparison of Residual Stresses in Inconel 718 Simple Parts Made by Electron Beam Melting and Direct Laser Metal Sintering.* Metallurgical and Materials Transactions A, 2015. **46**(3): p. 1419-1432.
335. Loh, L.-E., C.-K. Chua, W.-Y. Yeong, J. Song, M. Mapar, S.-L. Sing, Z.-H. Liu, and D.-Q. Zhang, *Numerical investigation and an effective modelling on the Selective Laser Melting (SLM) process with aluminium alloy 6061.* International Journal of Heat and Mass Transfer, 2015. **80**: p. 288-300.
336. Maly, M., C. Höller, M. Skalon, B. Meier, D. Koutny, R. Pichler, C. Sommitsch, and D. Paloušek, *Effect of Process Parameters and High-Temperature Preheating on Residual Stress and Relative Density of Ti6Al4V Processed by Selective Laser Melting.* Materials, 2019. **12**: p. 930.
337. Ali, H., L. Ma, H. Ghadbeigi, and K. Mumtaz, *In-situ residual stress reduction, martensitic decomposition and mechanical properties enhancement through high temperature powder bed pre-heating of Selective Laser Melted Ti6Al4V.* Materials Science and Engineering: A, 2017. **695**: p. 211-220.
338. Dunbar, A.J., E.R. Denlinger, M.F. Gouge, T.W. Simpson, and P. Michaleris, *Comparisons of laser powder bed fusion additive manufacturing builds through experimental in situ distortion and temperature measurements.* Additive Manufacturing, 2017. **15**: p. 57-65.
339. Saewe, J., C. Gayer, A. Vogelpoth, and J.H. Schleifenbaum, *Feasability Investigation for Laser Powder Bed Fusion of High-Speed Steel AISI M50 with Base Preheating System.* BHM Berg- und Hüttenmännische Monatshefte, 2019. **164**(3): p. 101-107.
340. Ivasishin, O.M., R. Markovsky, S.L. Semiatin, and C.H. Ward, *Aging response of coarse- and fine-grained β titanium alloys.* Materials ence & Engineering A, 2005. **405**(1/2): p. 296-305.
341. Terlinde, G. and G. Fischer, *Beta Titanium Alloys.* Titanium and Titanium Alloys, 2003: p. 37-57.
342. Al-Bermani, S., M. Blackmore, W. Zhang, and I. Todd, *The Origin of Microstructural Diversity, Texture, and Mechanical Properties in Electron Beam Melted Ti6Al4V.* Metallurgical and Materials Transactions A-physical Metallurgy and Materials Science - METALL MATER TRANS A, 2010. **41**: p. 3422-3434.
343. Basak, A. and S. Das, *Epitaxy and Microstructure Evolution in Metal Additive Manufacturing.* Annual Review of Materials Research, 2016. **46**(1): p. 125-149.

344. Heigel, J.C., P. Michaleris, and E.W. Reutzel, *Thermo-mechanical model development and validation of directed energy deposition additive manufacturing of Ti–6Al–4V.* Additive Manufacturing, 2015. **5**: p. 9-19.
345. Lindgren, L.-E., *Finite Element Modeling and Simulation of Welding Part 1: Increased Complexity.* Journal of Thermal Stresses, 2001. **24**(2): p. 141-192.
346. Wei, Z. and J. Du, *Heat and Mass Transfer of Additive Manufacturing Processes for Metals*. 2019.
347. Seli, H., M. Awang, A. Ismail, E. Rachman, and Z. Ahmad, *Evaluation of Properties and FEM Model of the Friction Welded Mild Steel-Al6061-Alumina.* Materials Research, 2013. **16**: p. 453-467.
348. Li, L.Q., P. Genchen, J. Wang, J. Gong, and S. Meng, *Numerical and experimental study on keyhole and melt flow dynamics during laser welding of aluminium alloys under subatmospheric pressures.* International Journal of Heat and Mass Transfer, 2019. **133**: p. 812-826.
349. Li, R., J. Xiong, and Y. Lei, *Investigation on thermal stress evolution induced by wire and arc additive manufacturing for circular thin-walled parts.* Journal of Manufacturing Processes, 2019. **40**: p. 59-67.
350. Bock, F.E., J. Herrnring, M. Froend, J. Enz, N. Kashaev, and B. Klusemann, *Experimental and numerical thermo-mechanical analysis of wire-based laser metal deposition of Al-Mg alloys.* Journal of Manufacturing Processes, 2021. **64**: p. 982-995.
351. Ding, J., P. Colegrove, J. Mehnen, S. Ganguly, P.M. Sequeira Almeida, F. Wang, and S. Williams, *Thermo-mechanical analysis of Wire and Arc Additive Layer Manufacturing process on large multi-layer parts.* Computational Materials Science, 2011. **50**(12): p. 3315-3322.
352. Wang, C., W. Suder, J. Ding, and S. Williams, *The effect of wire size on high deposition rate wire and plasma arc additive manufacture of Ti-6Al-4V.* Journal of Materials Processing Technology, 2021. **288**: p. 116842.
353. Mac Ardghail, P., N. Harrison, and S.B. Leen, *A through-process, thermomechanical model for predicting welding-induced microstructure evolution and post-weld high-temperature fatigue response.* International Journal of Fatigue, 2018. **112**: p. 216-232.
354. Mac Ardghail, P., N. Harrison, and S.B. Leen, *A process-structure-property model for welding of 9Cr power plant components: The influence of welding process temperatures on in-service cyclic plasticity response.* International Journal of Pressure Vessels and Piping, 2019. **173**: p. 26-44.
355. Yuan, B., G.M. Guss, A.C. Wilson, S.P. Hau-Riege, P.J. DePond, S. McMains, M.J. Matthews, and B. Giera, *Machine-Learning-Based Monitoring of Laser Powder Bed Fusion.* Advanced Materials Technologies, 2018. **3**(12): p. 1800136.
356. Cheng, L., X. Liang, J. Bai, Q. Chen, J. Lemon, and A. To, *On utilizing topology optimization to design support structure to prevent residual stress induced build failure in laser powder bed metal additive manufacturing.* Additive Manufacturing, 2019. **27**: p. 290-304.